

---

[All ETDs from UAB](#)

[UAB Theses & Dissertations](#)

---

2017

## An Improved Contact Method for Multi-Material Eulerian Hydrocodes

Kenneth Cline Walls  
*University of Alabama at Birmingham*

Follow this and additional works at: <https://digitalcommons.library.uab.edu/etd-collection>

---

### Recommended Citation

Walls, Kenneth Cline, "An Improved Contact Method for Multi-Material Eulerian Hydrocodes" (2017). *All ETDs from UAB*. 3245.  
<https://digitalcommons.library.uab.edu/etd-collection/3245>

This content has been accepted for inclusion by an authorized administrator of the UAB Digital Commons, and is provided as a free open access item. All inquiries regarding this item or the UAB Digital Commons should be directed to the [UAB Libraries Office of Scholarly Communication](#).

AN IMPROVED CONTACT METHOD FOR MULTI-MATERIAL EULERIAN  
HYDROCODES

by

KENNETH CLINE WALLS, III

DAVID L. LITTLEFIELD, COMMITTEE CHAIR  
PURUSHOTHAM BANGALORE

DAVID CRAWFORD  
ROBERT DORGAN  
EUGENE HERTEL  
DEAN SICKING

A DISSERTATION

Submitted to the graduate faculty of The University of Alabama at Birmingham,  
in partial fulfillment of the requirements for the degree of  
Doctor of Philosophy

BIRMINGHAM, ALABAMA

2017

Copyright by  
Kenneth Cline Walls, III  
2017

# AN IMPROVED CONTACT METHOD FOR MULTI-MATERIAL EULERIAN HYDROCODES

KENNETH CLINE WALLS, III

INTERDISCIPLINARY ENGINEERING

## ABSTRACT

Realistic and accurate modeling of contact for problems involving large deformations and severe distortions presents a host of computational challenges. Due to their natural description of surfaces, Lagrangian finite element methods are traditionally used for problems involving sliding contact. However, problems such as those involving ballistic penetrations, blast-structure interactions, and vehicular crash dynamics, can result in elements developing large aspect ratios, twisting, or even inverting. For this reason, Eulerian, and by extension Arbitrary Lagrangian-Eulerian (ALE), methods have become popular. However, additional complexities arise when these methods permit multiple materials to occupy a single finite element.

Multi-material Eulerian formulations in computational structural mechanics are traditionally approached using mixed-element thermodynamic and constitutive models. These traditional approaches treat discontinuous pressure and stress fields that exist in elements with material interfaces by using a single approximated pressure and stress field. However, this approximation often has little basis in the physics taking place at the contact boundary and can easily lead to unphysical behavior. This work presents a significant departure from traditional Eulerian contact models by solving the conservation equations separately for each material and then imposing inequality constraints associated with contact to the solutions for each material with the appropriate tractions included.



The advantages of this method have been demonstrated with several computational examples. This work concludes by drawing a comparison between the method put forth in this work and traditional treatment of multi-material contact in Eulerian methods.

## ACKNOWLEDGEMENTS

I would like to express my gratitude to Dr. David Littlefield, my research advisor, for his guidance, understanding, and patience, which have enabled me to become an independent researcher. It was his ideas that served as the inspiration for this work, and without his expertise none of this would have been possible.

I am also grateful to Dr. Dean Sicking, Dr. Eugene Hertel, Dr. David Crawford, Dr. Puri Bangalore, and Dr. Robert Dorgan for serving on my committee and providing valuable feedback on this work.

I would also like to thank the faculty and staff of the Mechanical Engineering Department at the University of Alabama at Birmingham. During my time as a student and researcher in this department they have provided tremendous support and friendship. It has been a pleasure working with all of them.

Lastly, I would like to thank my family for the support and encouragement they have provided during this process. My late father, K.C., taught me the value of hard work and for that I am forever grateful. I would like to especially thank my mother, Jeanie, sister, Sarah, and in-laws, Steve, Angie, Kevin, Blake, and Heather for believing in me even when I doubted myself. I would also like to thank my daughter, Audrey, who is due to be born in August. She was the focus that motivated me to finish this dissertation. But

most importantly, I would like to thank my wife, Jana. Words cannot express how thankful I am for the love, patience, support, and constant encouragement that she has provided. She suffered through the frustrations and reveled in the successes right beside me and if not for her I would have never gotten to this point.

## TABLE OF CONTENTS

ABSTRACT.....	iii
ACKNOWLEDGEMENTS.....	v
LIST OF TABLES.....	x
LIST OF FIGURES.....	xi
LIST OF ABBREVIATIONS.....	xvii
CHAPTER	
<b>1</b> INTRODUCTION.....	<b>1</b>
Approaches to the Contact-Impact Problem.....	1
Hydrocode Modeling.....	2
Methods for Modeling Contact.....	5
History of the Finite Element Method.....	11
Background.....	12
Dissertation Organization.....	17
<b>2</b> MATHEMATICAL FOUNDATIONS.....	<b>19</b>
Mathematical Background for Continuum Mechanics.....	19
Notation.....	19
Conservation Equations.....	21
Operator Splitting.....	23
The Donor Cell Advection Algorithm.....	26
The Half-Index Shift (HIS) Momentum Advection Algorithm.....	27

<b>3</b>	<b>FORMULATIONS .....</b>	<b>29</b>
	Development of the Conservation Equations and Finite Element Formulation .....	<b>29</b>
	Conservation of Momentum in ALE Coordinates .....	30
	Conservation of Mass in ALE Coordinates.....	43
	Conservation of Energy in ALE Coordinates.....	50
	Summary of the ALE Finite Element Contact Formulation.....	59
	The Contact Enforcement Model.....	<b>63</b>
	Determining Interface Areas.....	<b>72</b>
	Interface Tracking Formulations .....	<b>81</b>
	Interface Tracking in Two Dimensions .....	<b>83</b>
	Triangle Intersection Condition.....	87
	Quadrilateral Intersection Condition .....	88
	Determining Material Specific Advection Volumes in Two-Dimensions.....	<b>89</b>
	Extensions to Interface Tracking in Three-Dimensions .....	<b>93</b>
	Triangular Pyramid Intersection Condition.....	99
	Quadrilateral Intersection Condition A .....	100
	Pentagonal Intersection Condition .....	103
	Hexagonal Intersection Condition.....	107
	Quadrilateral Intersection Condition B .....	110
	Determining Material Specific Advection Volumes in Three-Dimensions.....	<b>113</b>
	Advection in Directions other than the +1-Direction .....	<b>116</b>
	Limits on the Advection Volume Calculation .....	<b>118</b>
<b>4</b>	<b>SOFTWARE.....</b>	<b>120</b>
	ALEAS.....	<b>120</b>
	CTH .....	<b>122</b>
<b>5</b>	<b>VALIDATION AND VERIFICATION PROBLEMS.....</b>	<b>124</b>
	Frictionless Block Sliding.....	<b>125</b>
	The Taylor Impact Test.....	<b>128</b>
	Long Rod Penetration Problems .....	<b>131</b>
	Penetration by Projectiles with Combined Obliquity and Yaw .....	131
	Normal Impact of Long Rods into Steel Targets.....	134
	Sod Shock Tube Problem .....	<b>137</b>
<b>6</b>	<b>DISCUSSION AND RESULTS.....</b>	<b>140</b>
	Results of Numerical Validation and Verification Problems .....	<b>140</b>
	Frictionless Block Sliding.....	<b>141</b>
	Taylor Impact Tests .....	<b>154</b>
	Penetration by Projectiles with Combined Obliquity and Yaw .....	<b>165</b>

Normal Impact of Long Rods into Steel Targets .....	179
Long Rod Penetration of Semi-infinite Targets.....	185
Sod Shock Tube .....	195
Discussion of Results.....	201
<b>7 CONCLUSIONS .....</b>	<b>208</b>
Future Work.....	210
<b>REFERENCES .....</b>	<b>213</b>
<b>APPENDIX: INPUT FILES .....</b>	<b>223</b>

## LIST OF TABLES

<i>Table</i>	<i>Page</i>
5.1 Mie-Gruneisen equation-of-state parameters used in validation problems .....	125
5.2 Johnson-Cook strength parameters used in validation problems.....	125
5.3 Initial states for the Sod shock tube validation .....	139
6.1 Summary of measures of final deformation for the Taylor impact simulations ..	164
6.2 Summary of results from combined obliquity and yaw simulations and experiments .....	178
6.3 Summary of results for 5.08 cm plate penetration .....	184
6.4 Computational cost of the contact method.....	205

## LIST OF FIGURES

<i>Figure</i>	<i>Page</i>
1.1 A simple two-body contact problem.....	2
1.2 Lagrangian and Eulerian representations of the computational mesh .....	5
1.3 Treatment of sliding contact in an ALE element with mixture theory compared to the desired result .....	9
2.1 Geometric interpretation of operator splitting in an Eulerian framework .....	25
3.1 Lagrangian, Eulerian, and ALE coordinate systems.....	31
3.2 The multi-material contact process implemented in this work.....	62
3.3 Representation of excess volume determination.....	68
3.4 Schematic of choice for master and slave materials .....	73
3.5 Five possible intersection conditions for the unit cube.....	74
3.6 Projections of the five intersection conditions into the $\xi$ - $\eta$ plane.....	79
3.7 Interface tracking methods.....	82
3.8 Schematic of central cell and its 8 neighboring cells.....	85
3.9 Possible two-dimensional intersection conditions .....	87



3.10	Illustration of the normalization process for determining the material-specific advection volume .....	92
3.11	Schematic of central cell and its 26 neighboring cells.....	95
3.12	Schematic of neighboring cells used for determining $\phi_e$ .....	95
3.13	Triangular pyramid intersection condition.....	99
3.14	Quadrilateral intersection condition A.....	101
3.15	Pentagonal intersection condition .....	103
3.16	Hexagonal intersection condition .....	107
3.17	Quadrilateral intersection condition B.....	110
3.18	Limits on the advection calculation .....	119
5.1	Setup for the mesh aligned normal block sliding problem .....	127
5.2	Setup for the half-element offset normal block sliding problem .....	127
5.3	Setup for the angled block sliding problem .....	128
5.4	Schematic of Taylor impact specimen pre-deformation and post-deformation...	130
5.5	Setup for Taylor impact problem.....	130
5.6	Rod-plate geometries for oblique impacts at positive, zero, and negative yaws .	132
5.7	Initial conditions for 0° yaw case.....	133
5.8	Initial conditions for -9.3° yaw case .....	134

5.9	Initial conditions for +10.3° yaw case.....	134
5.10	Initial conditions for 5.08 cm plate penetration .....	135
5.11	Initial conditions for penetration of an L/D=10 tungsten rod into a semi-infinite steel target.....	137
5.12	Initial condition of the Sod shock tube validation .....	138
5.13	Sod shock tube at time $t > 0$ .....	138
6.1	ALEAS MMM normal block sliding problem with no initial mixed elements ...	144
6.2	ALEAS SMM normal block sliding problem with no initial mixed elements ....	145
6.3	CTH normal block sliding problem with no initial mixed elements .....	146
6.4	ALEAS MMM normal block sliding problem with layer of initial mixed elements .....	147
6.5	ALEAS SMM normal block sliding problem with layer of initial mixed elements .....	148
6.6	CTH normal block sliding problem with layer of initial mixed elements .....	149
6.7	ALEAS MMM angled block sliding problem .....	150
6.8	ALEAS SMM angled block sliding problem.....	151
6.9	CTH angled block sliding problem.....	152
6.10	Comparison of available sliding interface options in CTH .....	153
6.11	ALEAS MMM Taylor impact problem with no initial mixed cells .....	157
6.12	ALEAS SMM Taylor impact problem with no initial mixed cells.....	158

6.13	CTH Taylor impact problem with no initial mixed cells .....	159
6.14	ALEAS MMM Taylor impact problem with layer of initial mixed cells .....	160
6.15	ALEAS SMM Taylor impact problem with layer of initial mixed cells .....	161
6.16	CTH Taylor impact problem with layer of initial mixed cells.....	162
6.17	Comparison of deformation profile for ALEAS MMM, ALEAS SMM, CTH, and experiment for mesh aligned Taylor impact .....	163
6.18	Comparison of deformation profile for ALEAS MMM, ALEAS SMM, CTH, and experiment for Taylor impact with initial layer of mixed cells .....	163
6.19	Profile of ALEAS MMM Taylor impact at 5 $\mu$ s showing separation of the center of the bar from the rigid plate .....	164
6.20	ALEAS MMM penetration of uranium rod into steel plate with 0 $^{\circ}$ yaw.....	168
6.21	ALEAS SMM penetration of uranium rod into steel plate with 0 $^{\circ}$ yaw .....	169
6.22	CTH penetration of uranium rod into steel plate with 0 $^{\circ}$ yaw .....	170
6.23	ALEAS MMM penetration of uranium rod into steel plate with +10.3 $^{\circ}$ yaw .....	171
6.24	ALEAS SMM penetration of uranium rod into steel plate with +10.3 $^{\circ}$ yaw.....	172
6.25	CTH penetration of uranium rod into steel plate with +10.3 $^{\circ}$ yaw .....	173
6.26	ALEAS MMM penetration of uranium rod into steel plate with -9.3 $^{\circ}$ yaw .....	174
6.27	ALEAS SMM penetration of uranium rod into steel plate with -9.3 $^{\circ}$ yaw.....	175
6.28	CTH penetration of uranium rod into steel plate with -9.3 $^{\circ}$ yaw .....	176
6.29	Comparison of normalized exit velocity versus yaw angle .....	177

6.30	ALEAS MMM normal penetration of uranium rod into 5.08cm steel plate .....	180
6.31	ALEAS SMM normal penetration of uranium rod into 5.08cm steel plate.....	181
6.32	CTH normal penetration of uranium rod into 5.08cm steel plate .....	182
6.33	Comparison of normal penetration of uranium rod into 5.08cm steel plate at 98.1 $\mu$ s.....	183
6.34	ALEAS MMM penetration of L/D=10 tungsten alloy rod into steel target with $V_0=3000$ m/s .....	186
6.35	ALEAS SMM penetration of L/D=10 tungsten alloy rod into steel target with $V_0=3000$ m/s .....	187
6.36	CTH penetration of L/D=10 tungsten alloy rod into steel target with $V_0=3000$ m/s .....	188
6.37	Comparison of maximum penetration depth for L/D=10 tungsten alloy rods into steel targets with $V_0$ of 500 m/s.....	189
6.38	Comparison of maximum penetration depth for L/D=10 tungsten alloy rods into steel targets with $V_0$ of 1000 m/s.....	190
6.39	Comparison of maximum penetration depth for L/D=10 tungsten alloy rods into steel targets with $V_0$ of 1500 m/s.....	191
6.40	Comparison of maximum penetration depth for L/D=10 tungsten alloy rods into steel targets with $V_0$ of 2000 m/s.....	192
6.41	Comparison of maximum penetration depth for L/D=10 tungsten alloy rods into steel targets with $V_0$ of 3000 m/s.....	193
6.42	Comparison of normalized depth of penetration (P/L) for L/D=10 tungsten alloy rods into steel targets .....	194
6.43	ALEAS MMM Sod shock tube results for pressure, density, and velocity .....	196
6.44	ALEAS SMM Sod shock tube results for pressure, density, and velocity .....	197
6.45	CTH Sod shock tube results for pressure, density, and velocity .....	198

6.46	Comparison of pressure for Sod shock tube validation .....	199
6.47	Comparison of density for Sod shock tube validation .....	199
6.48	Comparison of velocity for Sod shock tube validation.....	200

## LIST OF ABBREVIATIONS

ALE	Arbitrary Lagrangian-Eulerian
CLE	Coupled Lagrangian-Eulerian
HIS	Half-Index Shift
MALE	Multi-material Arbitrary Lagrangian-Eulerian
MMM	Multi-material Momentum
SALE	Single-material Arbitrary Lagrangian-Eulerian
SMM	Single-material Momentum

## CHAPTER 1

### INTRODUCTION

#### Approaches to the Contact-Impact Problem

Dynamic contact is an extremely important event in many engineering applications, however, due to the complexity associated with these types of problems it is often simplified. Problems involving dynamic contact are, by their nature, highly nonlinear and involve many unknown boundary conditions including contacting interfaces as well as the stresses and displacements on the contacting surfaces. The behavior of contacting bodies is governed by the equations of motion, conservation equations, and the problem-specific initial conditions and boundary conditions. A number of unknowns arise from these governing equations that cannot be determined without solving the problem. Therefore, the mathematical models associated with contact involve difficult systems of inequalities or nonlinear equations.

As a basic example, consider the simple two-body problem shown in Figure 1.1. In this figure, external forces are applied to two bodies,  $\Omega_1$  and  $\Omega_2$ , causing an impact condition to occur along the interface boundary. This leads to complicated interactions taking place along the material interface boundary that must be modeled. In order to accomplish this, it is possible to simplify the dynamic contact into a series of discrete contact events.

Accurate modeling of contact problems while taking all of these variables into account is extremely difficult. However, it has become somewhat simplified with the introduction of sophisticated computational mechanics programs. Additionally, the finite element method has also simplified the numerical analysis of contact problems. These simplifications now make it possible to solve a wide range of problems with a fair amount of accuracy [101].

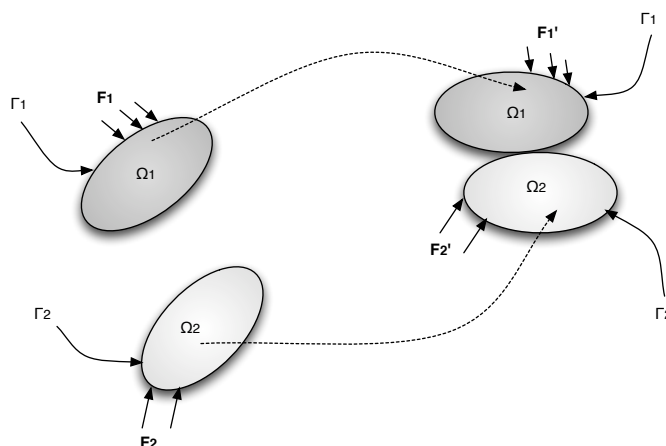


**Figure 1.1:** A simple two-body contact problem

### Hydrocode Modeling

The use of hydrocodes in the field of structural mechanics is vital for many applications, including hypervelocity impacts and penetrations, vehicular crashworthiness, fluid structure interactions, biomechanical injury analysis, and many more. Hydrocodes are defined as computer software packages for solving large deformation, finite strain transient problems that occur on short time scales. These codes were developed for the analysis of hypervelocity impacts in the mid-1960s as a result of work by Walsh and Johnson [96], as well as later work by Anderson [1]. Development of



these codes continues today in specialized codes such as CTH and ALEAS, which were used in this work, as well as many other commercial and research codes. The use of these shock physics codes have seen widespread implementation for both the solution of defense problems, for which they were originally developed, as well as a number of industrial applications. The ability of these codes to accurately represent a wide range of contact and impact events makes them very attractive due to the reduced need to conduct experiments, which are often very costly, time consuming, and yield limited data.

However, hydrocodes should be implemented carefully. One of the primary weaknesses of these codes is the validity of the material models used in the computation. They are also limited by the reliability of the numerical methods and algorithms being implemented. Despite these limitations, hydrocodes have been used to reliably replicate the details of stress, strain, and deformations in many dynamic events.

There are several features which are common to all hydrocodes. First, all hydrocodes represent a continuous physical system with discretized systems in which the material continuum is replaced with a computational mesh. Both finite element and finite difference techniques are used to evaluate system responses. Finite element methods use mathematical approximations to solve differential equations. The solutions within each element are then combined to model a continuum. Finite difference techniques evaluate the system using difference quotients to approximate differential equations to a given solution at discrete times.

Hydrocodes are categorized by the frame of reference of the computational mesh. Each method has advantages and disadvantages, which will be described in the next section, that the user must understand and take into account. For instance, due to the

mesh description of Lagrangian methods enforcement of the contact constraints is straightforward, however, since the mesh deforms along with the material these codes are limited to problems involving moderate stresses and deformations. Eulerian methods, on the other hand, naturally allow large stresses and deformations because the mesh is fixed in space. However, the Eulerian approach is traditionally hindered by its treatment elements containing more than one material since only one strain rate, velocity field, stress field, and pressure field are possible in an element. This makes it impossible to accurately model sliding interfaces. This work aims to bridge the gap between Lagrangian and Eulerian methods to develop an approach to accurately model problems that involve large stresses and deformations, but where the ability to model interface contact is still important.

In this work a new approach for modeling contact in an Eulerian framework is developed. It significantly differs from traditional Eulerian and ALE methods in that the conservation of mass, momentum, and energy equations are solved separately for each material and then specific contact inequalities and associated tractions are imposed. This eliminates the need for traditional mixed cell algorithms and consequently greatly improves the accuracy of the problem at hand. The advantages of this method are made clear using a variety of examples, including frictionless sliding problems, a Taylor impact test, and a series of oblique plate penetration problems, all of which can result in substantial error with traditional Eulerian methods but can be solved more accurately using the method developed in this work. Comparisons were also made to problems that traditional Eulerian methods handle well to examine the range of applicability of the method. As a result of this work, high stress and large deformation problems in which

sliding contact is important can now be carried out with greater accuracy than previously possible.

### Methods for Modeling Contact

Dynamic contact and impact problems are usually solved using explicit finite element and finite difference programs. In order to obtain an adequate degree of accuracy, impact problems require small time steps and a fine mesh, enabling the problem to model deformations with a fair degree of certainty. Explicit finite element and finite difference formulations are therefore extremely useful in modeling crash worthiness, shock responses, and a wide range of other problems. There are several methods for modeling dynamic contact-impact, including the Lagrangian method, the Eulerian method, and ALE methods.

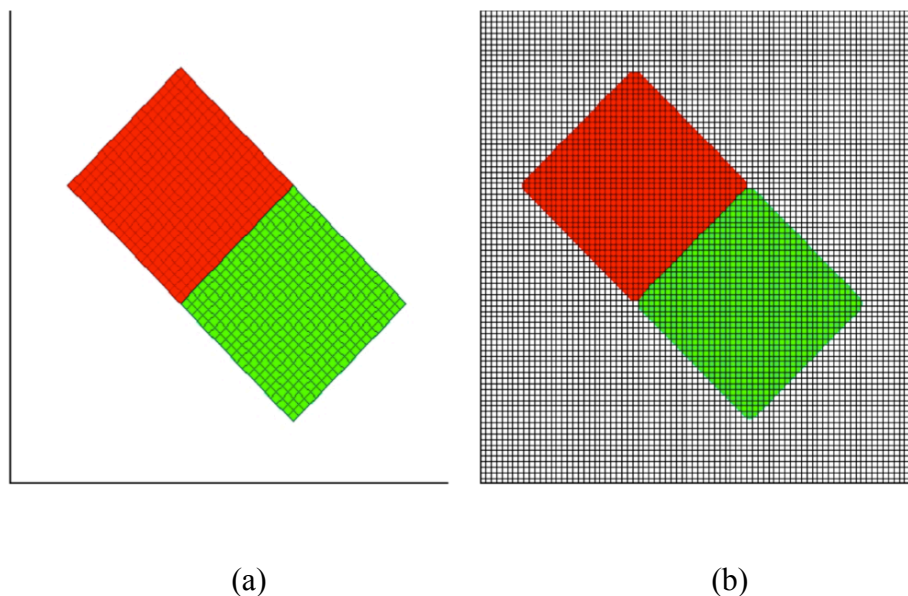


**Figure 1.2:** Lagrangian (a) and Eulerian (b) representations of the computational mesh

The Lagrangian formulation uses a computational mesh that is embedded in the material domain, as can be seen in Figure 1.2 (a), and movement of material is inferred directly from the motion of the mesh. Contact between materials is straightforward in that each computational element contains only a single material. Material surfaces are prevented from interpenetrating through the implementation of contact algorithms. These contact surfaces are typically referred to as “slide lines” in which one surface is defined as a master surface and the other is known as the slave, and the nodes contained on these surfaces are likewise referred to as master and slave nodes. A number of Lagrangian contact algorithms exist and are typically categorized based upon their method used for contact search, how the method handles contact and release conditions, and how contact forces are determined. Many Lagrangian hydrocodes have an extensive library of contact algorithms available including both automatic and manual surface to surface, node to surface, and single surface contact conditions.

However, because the computational grid is fixed to the body of interest, the mesh will deform along with the material. This will result in the time step decreasing as large deformations are introduced. Elements become stretched, the element thickness decreases, and, as a result, the time step size decreases with it. In a Lagrangian formulation, a mesh that has a large time step throughout the calculation that involves large deformations cannot be constructed. Therefore, in cases where large deformations are present, it is desirable for the material to be moved relative to the mesh during the calculation. This can be accomplished with Eulerian and ALE methods.

Eulerian formulations use a mesh that is fixed in space, as show in Figure 1.2 (b). The material interfaces present in each element are calculated at the beginning of each

time step, allowing the deformation of each material in the problem to occur naturally. Eulerian methods permit arbitrarily large deformations and automatically allow new free surfaces to form. Since the Eulerian mesh is fixed in space the problems that hinder Lagrangian formulations involving mesh distortion are eliminated. However, because material is allowed to move through the mesh, additional information is required to describe the contents of each element and update the calculations being performed. The addition of these material transport and advection calculations to Eulerian methods make them much more computationally expensive than Lagrangian methods, however, since the mesh is fixed in space and material is placed within the mesh the setup of these problems is trivial. For complex geometries Lagrangian computations can require a significant amount of setup time to achieve a good quality mesh, so this computational cost is offset by the reduced setup time for many simulations. Eulerian methods were originally developed for modeling fluid dynamics problems, however, Eulerian and ALE hydrocodes are distinguished from modern day Computational Fluid Dynamics (CFD) codes in that they typically include information about the strength of materials being modeled.

Additionally, in problems that involve the contact and separation of surfaces, contact forces between interacting materials must be accounted for. Typically, Eulerian hydrocodes treat subelement thermodynamics and stresses with mixture theory. In this work, the term mixture theory is used to describe a method used to approximate the stress and pressure field discontinuities that occur at interface boundaries within an element with a single pressure and stress field. Individual materials have their own sets of properties, and each material is assumed to occupy some portion of the element volume.

This requires the implementation of specific thermodynamic conditions to define a nonlinear system of equations where the volume fraction of each material within a cell acts as the unknown. Several mixture theories exist, however none of these methods are based in the physics taking place at the interface boundary and are thus considered to be ad hoc methods which will affect the accuracy of the solution.

Furthermore, traditional Eulerian methods require that a single velocity field is present for all materials in the problem space. This results in a single strain rate for each element, even in instance where multiple materials are present. Conservation of volume prevents multiple materials from occupying the same space at once. This implies that contact algorithms are unnecessary since the traction is accounted for by changes in the material stresses. However, this leaves Eulerian codes unable to properly account for the physics taking place at interface boundaries. This leads to artificial shear stresses developing as materials attempt to slide relative to one another, as can be seen in Figure 1.3. This is especially problematic in cases where the interaction is occurring between a liquid and a gas or a solid and a gas. This can ultimately lead to strain rates well above the actual values of the problem [11]. This is a major source of inaccuracy in these problems and removing this source of error is the principle scope of this work [13], [14], [19]. As a result, multi-material Eulerian formulations in the traditional sense have been limited to problems that involve large stresses and deformations that cannot be solved by other methods, but the generality of the formulation presented here makes it very appealing for a wide range of applications [17].

The Arbitrary Lagrangian-Eulerian (ALE) method has been developed to take advantage of the strengths of both the Lagrangian and Eulerian coordinate systems. In ALE methods, the mesh is permitted to deform as it would in a Lagrangian formulation,

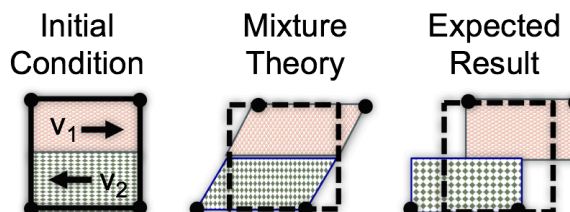


**Figure 1.3:** Treatment of sliding contact in an ALE element with mixture theory compared to the desired result

be remapped to its original location as it would in an Eulerian formulation, or be rezoned arbitrarily according to a specified algorithm. ALE methods allow for improved handling of distortions compared to Lagrangian methods while also providing more flexibility for handling material interfaces. ALE formulations are comprised of two steps, a Lagrangian step in which the solution is advanced in time and the mesh is distorted, and an advection, or remap, step in which the mesh is relaxed and material is transferred across element boundaries. This step can be simplified to restore the mesh to its original position and create the Eulerian formulation that was used in the validation of the contact approach developed for this work [90]. While ALE methods provide more flexibility in performing the calculation they still suffer from the same drawbacks as Eulerian methods when multiple materials are permitted to occupy the same element. These multi-material ALE formulations (MALE) uses the same mixture theory approach to mixed cells as Eulerian formulations. The finite element formulations in Chapter 3 are developed in the ALE coordinate system. For the validation problems shown in Chapters 5 and 6 the mesh is

remapped to its original position, eliminating the need for a mesh relaxation algorithm. This results in an ALE form of the Eulerian method.

A variety of other numerical techniques have also been developed to alleviate the difficulties associated with Lagrangian methods. These include  $r$ -adaptive or Single-material Arbitrary Lagrangian-Eulerian (SALE), Coupled Lagrangian-Eulerian (CLE), and Smoothed-Particle Hydrodynamics (SPH).  $r$ -adaptive and SALE techniques have been successfully used to improve Lagrangian calculations that involve moderate amounts of deformation. Since they do not allow multiple materials within a computational element they do not suffer from the drawbacks of mixture theory seen in traditional Eulerian and ALE formulations. These techniques allow for the independent movement of nodes, allowing element distortions to be controlled and, thus, dramatically increasing the time step required for numerical stability. SALE and  $r$ -adaptive methods, however, are not able overcome the difficulties associated with problems that involve large deformations and penetrations found in Lagrangian methods. Therefore, these techniques alone are insufficient to prevent severe mesh distortions [63].

It is possible to combine Eulerian and Lagrangian mesh systems into a single formulation. This method is referred to as the Coupled Eulerian-Lagrangian (CLE) method, and is implemented in several commercially available codes. These codes facilitate the modeling of fluid-structure and gas-structure interaction by allowing some of the materials or subgrids to be described using an Eulerian coordinate system while others are simultaneously modeled using a Lagrangian construction. CLE codes require special attention to be given to the interaction of subgrids, especially those comprising differing coordinate systems.



Another subset of methods for modeling dynamic contact that have recently become popular are meshless methods. These methods aim to alleviate the need for mesh regeneration in problems involving large deformations altogether. These methods rely on node connectivity that is bounded in time and depends completely on the total number of nodes in the domain. While this eliminates the need for complex mesh generation, the choice for nodal connectivity may be an unbounded problem, leading to similar difficulties associated with traditional problems that implement a computational mesh. While these methods hold a great deal of potential for simplifying contact modeling, development in this area is still in its early stages, and thus this method will not be further discussed in this work [51], [86].

### History of the Finite Element Method

The idea of representing a domain using a collection of discrete parts is not unique to computational mechanics or the finite element method. Ancient mathematicians were able to estimate the value of  $\pi$  to more than 40 significant figures by determining the perimeter of a polygon with a finite number of sides that had been inscribed within a circle [78]. The finite element method (FEM) has its origins in the late 19<sup>th</sup> century when Lord Rayleigh [61] used minimization of energy principles that were available at the time to solve structural design problems. In the early 20<sup>th</sup> century, Ritz [79] extended the theory by introducing multiple independent functions. In 1915, Galerkin [39] published the method of weighted residuals, which is the foundation of the modern finite element method. In 1941, Hrenikoff [49] introduced the frame-work method which involved replacing a continuum body with a finite number of bars that

express the mechanical properties of the body. The use of piecewise continuous functions defined over a subdomain to approximate an unknown function dates to 1943, with the work of Courant. Courant's method made use of a continuum body that was discretized using triangular elements and used the principles of minimum potential energy to solve the St. Venant torsion problem [28]. However, the formal presentation of the finite element method is attributed to Turner, Clough, Martin, and Topp in 1956 [89]. This work used triangular elements to obtain the solution of plane stress problems. Their work produced the direct stiffness method, and four years later the nomenclature "finite element method" appeared in a paper published by Clough [29].

Since its formal introduction, the popularity of the finite element method has grown significantly, as have its potential applications. With increased emphasis being placed on improving computing resources during the 1960s the finite element method became more accessible to both researchers and industry. As computing power increased and the FEM theory developed, the first commercial code, the so-called NASA STRuctural Analysis (NASTRAN) code came to the market. Other commercial codes such as SAP and ANSYS followed suit and today hundreds of finite element solvers are available for a variety of specialized purposes in industries such as defense, automotive safety, aerospace, and biomechanics [44], [50].

## Background

The simulation of contact in computational structural mechanics has a long history, going back over 50 years. It would be impossible to list all of the work that has

been published on this topic. However, in this section we consider several works that have had a major influence on this dissertation.

Some of the early work examining impacts using hydrocodes dates back to the mid-1980s. Holian and Burkett [47], Bjork [21], and Trucano and Asay [88] all produced work concerning phase transitions during hypervelocity impacts, while Holsapple [48], Bjorkman and Holsapple [22], and Schmidt and Housen [80] all studied the dynamics and final state of impact cratering. Still others, including Spillman [84], Arione and Bjorkman [5], Piekutowski [77], Trucano and Asay [88], and Schultz [82], studied the dynamics of debris clouds. While this work brought a tremendous amount of interest to the modeling of hypervelocity impacts, work in this area was also investigated much earlier during the late 1950s and 1960s when the first two-dimensional hydrocodes were developed by Evans and Harlow [35] and Johnson [53]. A history of the development of hydrocodes and their uses can be found in a paper by Johnson [54].

Much of this early work led the way for the development of the Eulerian and Arbitrary Lagrangian-Eulerian formulations that we use in this dissertation. A large summative work by Benson [11] presents numerous algorithms involving explicit finite element and finite difference methods that are used to solve transient, large deformation problems in solid mechanics. Among the many topics covered in this 200 page work are the detailed development of the Lagrangian and Eulerian methods, as well as operator splitting and interface tracking, all of which are of the utmost importance to the ALEAS hydrocode developed for this dissertation. Other more recent work by Benson, including his work on stable time step estimation for multi-material Eulerian hydrocodes [16] and

his implicit multi-material Eulerian formulation [17] have served as an important background for this work.

More recently, work by Lim and Taylor [62], Benson and Okazawa [19], Vitali and Benson [90], Okazawa, et al. [74], and Littlefield [64], [65], have focused on the specific treatment of contact in multi-material contact in Eulerian and ALE methods, while a book by Zhong [101] goes into tremendous detail involving finite element procedures for the contact-impact problem. Other work by Donea, et al. [31] gives an in-depth description of the ALE method.

Work by Benson and his student Vitali has also attempted to bypass the use of mixture theory in Eulerian hydrocodes [90], [91], [92]. The approach used in this work was an extension to the extended finite element method (XFEM) pioneered by Belytschko, et al. in the late 1990s [36], [73], [85]. While the goal of Vitali and Benson's work is the same as the subject of this dissertation, the approach used varies significantly. As mentioned previously, Vitali and Benson's work employed XFEM, in which nodes are "enriched" to provide additional degrees of freedom. In the case presented in these works, the enrichment allowed for the determination of independent velocity fields at the nodes for each material located within a mixed cell. This was accomplished by creating separate elements for each material that overlay one another. During the Lagrangian step each overlaying element is allowed to deform independently and a contact enforcement algorithm was implemented if the combined volume fractions of the cells exceeded 1.0. If this condition was violated the velocities and accelerations were coupled and the material surface normals were determined. While this work shows a great deal of promise, it requires the use of extended finite element algorithms that are not readily

available in many production Eulerian codes, and thus is limited to codes that make use of XFEM, and currently, to the knowledge of the author the use of these methods are currently limited to two-dimensions. In addition to the research code RAVEN discussed in Vitali and Benson's work, the Sandia National Laboratories hydrocode ALEGRA has also been recently updated to include an XFEM Eulerian contact algorithm in two-dimensions [75]. This implementation has proven to be very computationally expensive, resulting in run times three to four times greater than ALEGRA's traditional Eulerian approach, though Park points out that little optimization has been made to the code at this point, so this speed penalty will likely decrease with time.

Work involving rigid body contact and motion have also proven to be useful in the development of this dissertation. These works include a paper by Benson and Hallquist [18] in which rigid body algorithms were developed for structural dynamics programs. Other works of interest in this area include multi-rigid-body contact problems presented by Anitescu and Potra [4], an overview of rigid body contact by Mirtich [72], a thesis by Cline [26], as well as a study of rigid plate impact by a soft impactor by Jeng, et al. [52]. Other works involving penetration studies have also been a useful background and these include works by Anderson and Walker [2], Benson [13], Walker [93], Gee [40], Ben-Dor, et al. [10] and Daneshjou, et al. [30].

The Taylor impact test will also be simulated in this work. In order to draw a comparison between experimental results and the computational results obtained in this work, as well as to gain background knowledge of the Taylor impact test, many works from the literature were reviewed. Papers dealing with the theory of the Taylor impact test include papers by Jones, Maudlin, and Foster [56], Jones, Drinkard, Rule, and

Wilson, [58], and Lu, Wang, and Zhang [68]. Numerous papers giving experimental results have also been presented in the literature. These include works by Wilkins and Guinan [99], Jones, Maudlin, and Foster [57], Wang, Zhang, and Lu [97], Eakins and Thadhani [33], [34], Brunig and Driemeier [23], and Martin, Mishra, Meyers, and Thadhani [69].

The advection approach presented in this work was developed by Littlefield [66], which built on Youngs' method for interface tracking developed by Youngs [100]. Other works that were important to the development of this dissertation include an early paper on mixture theory and numerical procedures for hypervelocity impacts by Drumheller [32], a development of mixture theory for multi-material contact in Eulerian formulations by Benson [14], work involving the prioritization of material interfaces by Benson [15], and other advection approaches by Jun [59], and Fressmann and Wriggers [37].

This work is an extension of the work done by Littlefield [64], [65], [66], and while many of the works mentioned in this section provided valuable background information, the work developed by Littlefield and continued in this dissertation represents a significant departure from traditional treatments of contact in a multi-material Eulerian method. Namely, this work differs from traditional approaches in that no mixed-element thermodynamic or constitutive models are used in the formulation, but rather the governing equations are solved for each material, and are subject to the imposed contact constraints with the appropriate tractions included. In the formulation presented here, multiple velocity fields are required per cell, whereas traditionally only a single velocity field is used. Through the use of multiple velocity fields it becomes possible to enforce contact constraints along material interfaces. The interface tracking

methods discussed in later chapters are also repurposed for the contact approach. In addition to its traditional use in keeping track the content of advection volumes, it is also used to determine interface areas in the contact enforcement method developed in this work. The formulations developed for this work are presented in Chapter 3, and results of the implementation are reported in Chapter 6 to demonstrate the advantages of this method over traditional approaches of multi-material contact.

### Dissertation Organization

The layout of this dissertation is as follows:

In Chapter 1 we have presented the motivation for this work as well as an introduction to the topics to be covered and a broad overview of related works.

In Chapter 2, a brief introduction to the notation and mathematical background necessary to develop the ALE form of the conservation equations developed for this work is presented. This will be followed by an overview of the conservation equations in both the Lagrangian and Eulerian reference frames and an overview of operator splitting techniques.

In Chapter 3, the formulations for the conservation equations used in this work will be developed. This section will also present the contact constraints and the finite element formulations of the conservation of mass, momentum, and energy equations. This section will conclude with the development of the interface tracking formulation used in this work in both two- and three-dimensions, as well as a description of a number of other methods implemented in ALEAS.

Chapter 4 will provide an overview of the research code ALEAS, a multi-material hydrocode which will be used in this work and was initially developed by Littlefield in two-dimensions [63] and expanded to three-dimensions as part of this work. This section will also describe the Eulerian hydrocode CTH, which was used as a means of comparison in this work.

In Chapter 5, the setup of several validation and verification calculations that were performed to demonstrate the applicability and improvements seen in this method are described.

Chapter 6 presents the results of these example problems. By implementing the method developed in Chapter 3 it was possible to gain a significant improvement over traditional Eulerian approaches. The advantages of using the multi-material contact methods developed in this work are discussed. Additionally, solutions to complications that arise from this method are given.

Chapter 7 concludes this dissertation and makes recommendations for future areas of research with regards to Eulerian contact modeling.



## CHAPTER 2

## MATHEMATICAL FOUNDATIONS

## Mathematical Background for Continuum Mechanics

*Notation*

In continuum mechanics, physical quantities are expressed by mathematical representations in the form of tensors and vectors. The physical laws are also expressed by tensor and vector equations. Any physical process being represented in this form is the same regardless of the coordinate system being used, thus the expressions describing the process must be able to be expressed in any coordinate system. This law of vectors and tensors is known as the law of transformation.

Vectors are represented by both a magnitude and a direction, and are made up of both unit vectors and scalar coefficients. For example, the velocity vector in a three-dimensional Cartesian coordinate system can be expressed by:

$$\mathbf{v} = u\mathbf{i} + v\mathbf{j} + w\mathbf{k} = \sum_{i=1}^n v_i \hat{e}_i \quad (2.1)$$

where  $\mathbf{i}$ ,  $\mathbf{j}$ , and  $\mathbf{k}$  are the associated unit vectors, and  $u$ ,  $v$ , and  $w$  are scalar quantities for vector notation and  $\hat{e}_i$  is the unit vector and  $v_i$  is velocity component in indicial notation where  $n$  is the number of dimensions of the problem. This summation is implied in indicial notation when an index is repeated, so the summation symbol is often omitted, but shown here for clarity.

The gradient operator  $\nabla$  is frequently used in the conservation equations, contact approach, and interface tracking methods developed in this work. It is defined as:

$$\nabla = \mathbf{i} \frac{\partial}{\partial x} + \mathbf{j} \frac{\partial}{\partial y} + \mathbf{k} \frac{\partial}{\partial z} = \hat{e}_i \frac{\partial}{\partial x_i} \quad (2.2)$$

The product of  $\nabla$  and a scalar quantity, denoted here by  $\phi$ , results in a vector defined as:

$$\nabla \phi = \frac{\partial \phi}{\partial x} \mathbf{i} + \frac{\partial \phi}{\partial y} \mathbf{j} + \frac{\partial \phi}{\partial z} \mathbf{k} = \hat{e}_i \frac{\partial \phi}{\partial x_i} \quad (2.3)$$

The product of  $\nabla$  and a vector, such as the velocity vector  $\mathbf{v}$ , is known as the divergence and is defined as:

$$\nabla \cdot \mathbf{v} = \frac{\partial u}{\partial x} + \frac{\partial v}{\partial y} + \frac{\partial w}{\partial z} = \frac{\partial v_i}{\partial x_i} \quad (2.4)$$

The Cauchy stress, which is the only stress used in this dissertation, is denoted by  $\sigma$ , the specific internal energy is  $e$ , the density is  $\rho$ , the traction is  $\mathbf{t}$ , and the body force per unit mass is  $\mathbf{f}$ . In Chapter 3 the symbol  $\phi$  is used to denote the volume fraction of material within an element, but has other uses in this chapter.

The velocity gradient  $\nabla \mathbf{v}$ , which can also be denoted as  $L_{ij}$ , is divided into a symmetric component,  $D_{ij}$ , which is the deformation rate, and a skew component,  $W_{ij}$ , which is the spin. This is given by the following series of equations:

$$\begin{aligned}
 L_{ij} &= \frac{\partial v_i}{\partial x_j} \\
 D_{ij} &= \frac{1}{2}(L_{ij} + L_{ji}) \\
 W_{ij} &= \frac{1}{2}(L_{ij} - L_{ji})
 \end{aligned}
 \tag{2.5}$$

The deformation rate,  $D_{ij}$ , is commonly referred to as the strain rate,  $\dot{\epsilon}_{ij}$ , as is done in Chapter 3, because it is conjugate to the Cauchy stress. This is not strictly correct because the time integral of the deformation rate does not define a measure of large deformation strain, but this nomenclature is common and thus used here as well [11].

### Conservation Equations

The Lagrangian formulation of the conservation equations can be developed using the concept of a material volume where all points contained within the volume move at the velocity of the local continuum. The Eulerian formulation on the other hand, uses a volume fixed in space to solve the conservation equations. In an Eulerian formulation, the rate at which the quantity of each material decreases in the fixed space equals the material flux through the mesh. This section contains a brief description of the governing equations for mass, momentum, and energy in both the Lagrangian and Eulerian reference frames. Numerous publications and text books give detailed description of their derivations, so a full derivation is not presented here [25], [70], [98].

The conservation of mass equation in the Lagrangian reference frame is written as:

$$\frac{D\rho}{Dt} + \rho \frac{\partial v_i}{\partial x_i} = 0
 \tag{2.6}$$

where  $\rho$  is the density.

The conservation of momentum equation in the Lagrangian reference frame is:

$$\rho \frac{Dv_i}{Dt} = \frac{\partial}{\partial x_j} \sigma_{ji} + \rho f_i \quad (2.7)$$

where  $\sigma_{ji}$  is the Cauchy stress and  $f_i$  is the body force per unit mass.

The conservation of energy equation in the Lagrangian reference frame is:

$$\rho \frac{De}{Dt} = \sigma_{ij} \dot{\epsilon}_{ij} + \rho f_i v_i \quad (2.8)$$

where  $e$  is the internal energy and  $\dot{\epsilon}_{ij}$  is the strain rate.

Here the  $D/Dt$  term is known as the material derivative. This is the time rate of change associated with the material. It is defined as:

$$\frac{D}{Dt} (\ ) = \frac{\partial}{\partial t} (\ ) + v_i \frac{\partial}{\partial x_i} (\ ) \quad (2.9)$$

where the first term on the right-hand side is the local change and the second term is the convective change.

The Eulerian form of the conservation equations arise from the change of the material quantity in a control volume over time. The rate of increase of the material quantity in the volume is equal to the rate of the quantity flowing into the volume minus the rate of the quantity flowing out of the volume. The conservation of mass equation in the Eulerian reference frame is given by:

$$\frac{\partial \rho}{\partial t} + \frac{\partial}{\partial x_i} (\rho v_i) = 0 \quad (2.10)$$

The conservation of momentum equation in the Eulerian reference frame is given by:

$$\frac{\partial}{\partial t} (\rho v_i) + \frac{\partial}{\partial x_j} (\rho v_i v_j) = \frac{\partial}{\partial x_j} \sigma_{ji} + \rho f_i \quad (2.11)$$

The conservation of energy in the Eulerian reference frame is given by:

$$\frac{\partial}{\partial t} (\rho e) + \frac{\partial}{\partial x_j} (\rho e v_j) = \sigma_{ij} \dot{\epsilon}_{ij} + \rho f_i v_i \quad (2.12)$$

It is important to recognize that there is no generalized closed-form of these equations, so the solutions implemented in hydrocodes are approximate solutions.

In addition to the unknowns which are solved using the conservation equations, which include the density  $\rho$ , the velocity components  $v_i$ , and the specific internal energy  $e$ , the equations of state and constitutive laws for the materials of interest must be solved to determine the remaining unknowns, including the pressure and deviatoric stress components which combine to define the Cauchy stress. These types of formulations are commonly referred to as material models and are not discussed in this work, however extensive work can be found in the literature [27], [43].

### Operator Splitting

Operator splitting provides a convenient method for solving the ALE form of the conservation equations developed in this work. While the complete development of the ALE formulation can be found in Chapter 3, this section provides a useful background in

understanding how the ALE equations are split into Lagrangian and Eulerian parts. Unsplit methods are also available and can result in improved accuracy, however, they are typically more complicated to implement and are more computationally expensive. Operator splitting provides an efficient, robust, and simplified approach to solving the ALE form of the conservation equations and is used in a large majority of Eulerian and ALE hydrocodes under development today.

The operator split approach separates the ALE conservation equations into a source equation, typically called the Lagrangian step, and convective equations, typically called the advection or remap step. Figure 2.1 provides a graphical representation of the operator split solution process. In ALE codes that make use of an Eulerian mesh description, as will be used in this work, the mesh is returned to its original orientation during the remap step while material is allowed to pass across element boundaries. Other ALE implementations also allow flux across element boundaries, but the mesh can be restored to an arbitrary orientation using user supplied relaxation parameters. The two steps are solved independently and sequentially, with the remap step typically being solved in one-dimensional sweeps in which the order of advection directions is alternated with each timestep to alleviate directional bias.

The general form of an ALE conservation equation is

$$\frac{\partial}{\partial t} J\phi + J\nabla \cdot \Phi = JS \quad (2.13)$$

where  $\phi$  is the solution variable,  $\Phi$  is a flux function,  $S$  is the source term, and  $J$  is the Jacobian. Operator splitting divides the solution variable term in Equation 2.8 into a Lagrangian and an Eulerian part as:

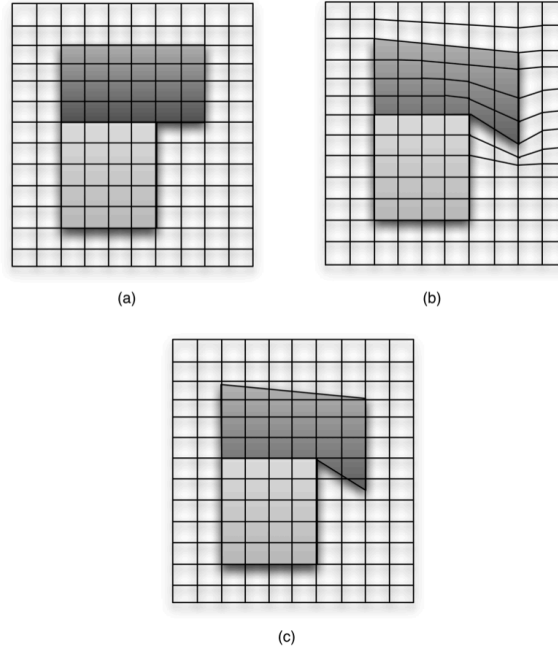


**Figure 2.1:** Geometric interpretation of operator splitting in an Eulerian framework, with (a) the initial condition, (b) the Lagrangian step, and (c) the advection step

$$\frac{\partial}{\partial t} J\phi = \frac{\partial}{\partial t} J\phi^{Lag} + \frac{\partial}{\partial t} J\phi^{Eul} \quad (2.14)$$

These parts are then divided to solve the source and convective terms separately as follows. For the source step, or Lagrangian step as it is typically called, the flux terms are excluded. During this step the mesh deforms and time is advanced. The Lagrangian step used in most ALE and Eulerian codes uses the same algorithms used in a Lagrangian hydrocode. The Lagrangian step is given by:

$$\frac{\partial}{\partial t} J\phi^{Lag} = JS \quad (2.15)$$

For the convective step, or remap step, the flux terms are solved. During this step the mesh is either restored to its original location, as would be the case for an Eulerian

method, or to some other configuration determined by a mesh relaxation algorithm.

During this step material is transported between adjacent cells. The transport of mass, momentum, energy, stress, and other quantities is handled by advection algorithms during this step. The remap step is given by:

$$\frac{\partial}{\partial t} J \phi^{Eul} + J \nabla \cdot \Phi = 0 \quad (2.16)$$

### The Donor Cell Advection Algorithm

During the remap step the distorted Lagrangian mesh must be returned to its original location and material flux must take place across element boundaries. It is important that this process be stable, accurate, conservative, and monotonic. The stability requirement comes from the Courant condition, i.e.  $v\Delta t/\Delta x \leq 1$ , which states transport can only occur between neighboring cells, meaning that material cannot flow more than one element width during a single time step. The conservation requirement ensures that the original and remapped meshes have the same mass, momentum, and energy, and the monotonicity requirement ensures that the range of solution variables does not increase after the remap. This is important, for example, in ensuring that negative masses and energies are not obtained after the remap step. The donor cell algorithm used in this work is very simple to implement, and, with the exception of being first order accurate, meets all of the requirements for advection.

The donor cell algorithm is given by

$$\varphi_{i+\frac{1}{2}}^{n+1} = \varphi_{i+\frac{1}{2}}^n + \frac{\Delta t}{\Delta x} (f_i^\varphi - f_{i+1}^\varphi) \quad (2.17)$$



where  $\varphi$  is the solution variable and  $f^\varphi$  is the transport volume between adjacent elements, which is given by

$$f_i^\varphi = \frac{a_i}{2} \left( \varphi_{i-\frac{1}{2}}^n + \varphi_{i+\frac{1}{2}}^n \right) + \frac{|a_i|}{2} \left( \varphi_{i-\frac{1}{2}}^n - \varphi_{i+\frac{1}{2}}^n \right) \quad (2.18)$$

where  $a_i$  is the velocity of the contact discontinuity at node  $i$ .

Higher order methods, including the van Leer monotonic upwind scheme for convection laws (MUSCL) exist, but have not currently been implemented in ALEAS. Implementation of a higher order advection scheme is an area of future work.

#### The Half-Index Shift (HIS) Momentum Advection Algorithm

Unlike advection of element centered quantities such as mass, density, and energy which is straightforward and done by the donor cell approach in this work, the velocity is a node centered quantity and determining how it is advected requires considerably more care to be taken. In most codes, including the one developed for this work, momentum is advected instead of velocity to ensure momentum conservation. The element centered advection algorithms must be modified in some way to advect node centered momentum. The method used in this work was initially developed by Benson [12] and was based on an analysis of other element centered advection algorithms. The Half-Index Shift (HIS) algorithm eliminates dispersion errors associated with other element centered advection algorithms while also maintaining the monotonicity of the velocity field.

A monotonic element-centered momentum advection algorithm is obtained by choosing the identity matrix for the transformation and by using mass weighting for the inverse relationship.

$$\begin{Bmatrix} \Psi_{(1,i+\frac{1}{2})} \\ \Psi_{(2,i+\frac{1}{2})} \end{Bmatrix} = \begin{bmatrix} 1 & 0 \\ 0 & 1 \end{bmatrix} \begin{Bmatrix} v_i \\ v_{i+1} \end{Bmatrix} \quad (2.19)$$

To conserve momentum, variable  $\Psi$  is advected with the transport masses. The updated value for  $\Psi$  is given by

$$\Psi_{m,i+\frac{1}{2}}^+ = \frac{M_{i+\frac{1}{2}}^- \Psi_{(m,i+\frac{1}{2})}^- + \Psi_{(m,j-1)} \bar{f}_{i-1} - \Psi_{(m,i+1)} \bar{f}_{i+1}}{M_{i+\frac{1}{2}}^+} \quad (2.20)$$

where the '+' and '-' denote the variable value before and after advection,  $M$  is the lumped mass at the node, and  $\bar{f}$  is the transported nodal mass. From this we can now obtain the velocity update using the following equation:

$$v_i = \frac{1}{2M_i} \begin{bmatrix} M_{i+\frac{1}{2}} & M_{i-\frac{1}{2}} \end{bmatrix} \begin{Bmatrix} \Psi_{(1,i+\frac{1}{2})} \\ \Psi_{(2,i-\frac{1}{2})} \end{Bmatrix} \quad (2.21)$$

More details about the derivation of this algorithm can be found in [12] for structured meshes and [20] for unstructured quadrilateral meshes.

## CHAPTER 3

### FORMULATIONS

This work represents a significant departure from traditional treatment of sliding contact with Eulerian and ALE methods. It essentially represents a generalization of a technique used in Lagrangian formulations and implements it in an ALE reference frame in order to avoid the mesh distortion drawbacks of Lagrangian methods while also removing contact problems associated with Eulerian and ALE methods. In this work, mixed cell thermodynamic and constitutive models traditionally used in Eulerian and ALE methods are not used. Rather, the governing equations are solved for each material separately and then specific contact constraints are imposed. After these constraints are enforced the traction, which is traditionally treated implicitly through stress and pressure increases that occur as a result of the conservation of volume, is treated explicitly. This results in a set of coupled equations which can be approximated using an uncoupled system.

#### Development of the Conservation Equations and Finite Element Formulation

The conservation of mass, momentum, and energy equations presented in Chapter 2 must be rewritten in a manner suitable to carry out the calculations that will be considered in this work. The formulation presented here is the Arbitrary Lagrangian-

Eulerian (ALE) form of the conservation equations. In this section we will develop the conservation equations in the form necessary to arrive at the finite element approximation of each equation using two operator splits. The first operator split is traditionally performed in the ALE formulation and is solved without accounting for the traction. The second operator split enforces contact by determining the traction and enforcing the Signorini contact constraints. This second operator split is valid everywhere, but since the traction has a value of zero everywhere except in elements where contact occurs it is only performed when the contact constraints are not identically satisfied.

Let  $\mathbf{X}$  denote the Lagrangian, or current, coordinate system of a given volume,  $V$ . We must also define two additional coordinate systems: the Eulerian coordinates, where  $\mathbf{x} = \mathbf{x}(\mathbf{X}, t)$ , and the ALE coordinates, where  $\mathbf{y} = \mathbf{y}(\mathbf{X}, t)$ . The ALE coordinates describe the deformation of the volume  $V$ , while the Eulerian coordinates describe the deformation of a body of interest  $\Omega$ , as shown in Figure 3.1.

Initially, the Lagrangian, Eulerian, and ALE coordinate systems are equivalent, however, at later times all three can become distinct assuming deformation and advection. Note that it is possible to convert between reference frames. The Lagrangian description is recovered from the ALE equations by setting the advection velocity  $\mathbf{c}$  to zero. The Eulerian description is given by setting the material velocity  $\mathbf{v}$  equal to  $\mathbf{c}$  and the Jacobian,  $J$ , equal to one.

#### *Conservation of Momentum in ALE Coordinates*

From this description of motion, it is desirable to express the conservation of momentum in terms of the deforming ALE coordinate system. The conservation of

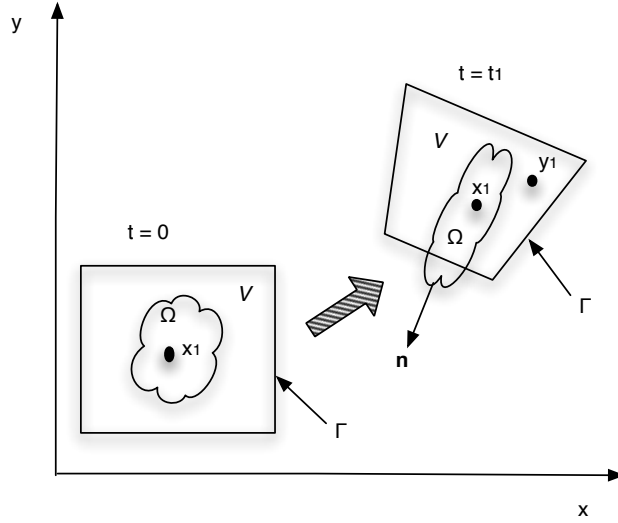


**Figure 3.1:** Lagrangian, Eulerian, and ALE coordinate systems. Initially, the Lagrangian, Eulerian, and ALE coordinate systems are identical, however, as time progresses each system can become distinct.

momentum equation is solved by performing one dimensional sweeps in each direction, so for three dimensions it would be solved a total of three times to find the three components of the velocity vector. The initial momentum,  $\mathbf{M}_0$ , of the body  $\Omega$  at  $t = 0$  is given by:

$$\mathbf{M}_0 = \int_{\Omega \cap V} \rho_0 \mathbf{v}_0 dX \tag{3.1}$$

Likewise, at some later time  $t = t_1$ , the momentum of the body,  $\mathbf{M}_1$ , is given by:

$$\mathbf{M}_1 = \int_{\Omega \cap V} \rho \mathbf{v} dy + \int_0^t \int_{\Gamma} \rho \mathbf{v} (\mathbf{c} \cdot \mathbf{n}) ds \tag{3.2}$$

where  $\mathbf{n}$  is the outward unit normal vector to  $V$  along its boundary  $\Gamma$  and  $\mathbf{c}$  is the advection velocity, given by:

$$\mathbf{c} = \mathbf{v} - \frac{d\mathbf{y}}{dt} = \mathbf{v} - \dot{\mathbf{y}} \quad (3.3)$$

where  $\dot{\mathbf{y}}$  is the ALE reference frame velocity. The change in momentum is given by  $\mathbf{M}_1 - \mathbf{M}_0$ , and the rate of change is the time derivative, which can be written as:

$$\frac{\partial \mathbf{M}}{\partial t} = \frac{\partial \mathbf{M}_1}{\partial t} = \frac{\partial}{\partial t} \int_{\Omega \cap V} \rho \mathbf{v} dy + \int_{\Gamma} \rho \mathbf{v} (\mathbf{c} \cdot \mathbf{n}) ds \quad (3.4)$$

Now, let

$$\mathbf{F}_y = \frac{d\mathbf{y}}{d\mathbf{X}} \quad \text{or} \quad F_{y,ij} = \frac{dy_i}{dX_j} \quad (3.5)$$

be the second-order tensor describing the deformation of the ALE coordinate system.

Using this we can transform the first term on the right-hand side of Equation 3.4 into the original coordinate system as follows:

$$\frac{\partial}{\partial t} \int_{\Omega \cap V} \rho \mathbf{v} dy = \frac{\partial}{\partial t} \int_{\Omega \cap V} \rho \mathbf{v} \det(\mathbf{F}_y) dX = \frac{\partial}{\partial t} \int_{\Omega \cap V} (\rho J \mathbf{v}) dX \quad (3.6)$$

where  $J = \det(\mathbf{F}_y)$ , and is the Jacobian of the reference frame. Then applying Gauss' theorem to the second integral gives:

$$\int_{\Gamma} \rho \mathbf{v} (\mathbf{c} \cdot \mathbf{n}) ds = \int_{\Omega \cap V} \nabla \cdot (\rho \mathbf{v} \mathbf{c}) dy = \int_{\Omega \cap V} J \nabla \cdot (\rho \mathbf{v} \mathbf{c}) dX \quad (3.7)$$

Using Cauchy's law the forces acting on the body are given by:

$$\mathbf{F} = \int_{\Gamma} \mathbf{n} \cdot \boldsymbol{\sigma} ds + \int_{\Omega \cap V} \mathbf{f} dy \quad (3.8)$$

where  $\mathbf{f}$  is an externally applied force per unit volume and  $\boldsymbol{\sigma}$  is the Cauchy stress tensor previously denoted in Chapter 2 with indicial notation as  $\sigma_{ij}$ .

Using Gauss' Theorem on the first integral in Equation 3.8 gives:

$$\mathbf{F} = \int_{\Gamma} \mathbf{n} \cdot \boldsymbol{\sigma} ds + \int_{\Omega \cap V} \mathbf{f} dy = \int_{\Omega \cap V} [\nabla \cdot \boldsymbol{\sigma} + \mathbf{f}] dy \quad (3.9)$$

Changing the reference frame of Equation 3.9 gives:

$$\int_{\Omega \cap V} [\nabla \cdot \boldsymbol{\sigma} + \mathbf{f}] dy = \int_{\Omega \cap V} J[\nabla \cdot \boldsymbol{\sigma} + \mathbf{f}] dX \quad (3.10)$$

So, the conservation of momentum equation now becomes:

$$\int_{\Omega \cap V} \left[ \frac{\partial}{\partial t} (\rho J \mathbf{v}) + J \nabla \cdot (\rho \mathbf{v} \mathbf{c}) \right] dX = \int_{\Omega \cap V} J[\nabla \cdot \boldsymbol{\sigma} + \mathbf{f}] dX \quad (3.11)$$

This must be valid for any choice of control volume  $V$ , so therefore the integrand must be zero. Using this and dividing through by  $J$  gives:

$$\frac{1}{J} \frac{\partial}{\partial t} (\rho J \mathbf{v}) + \nabla \cdot (\rho \mathbf{v} \mathbf{c}) = \nabla \cdot \boldsymbol{\sigma} + \mathbf{f} \quad (3.12)$$

Using the product rule on the first term on the left-hand side gives:

$$\frac{1}{J} \frac{\partial}{\partial t} (\rho J \mathbf{v}) = \frac{1}{J} \left[ J \frac{\partial}{\partial t} (\rho \mathbf{v}) + \rho \mathbf{v} \frac{\partial J}{\partial t} \right] = \frac{\partial}{\partial t} (\rho \mathbf{v}) + \frac{\rho \mathbf{v}}{J} \frac{\partial J}{\partial t} \quad (3.13)$$

It can be shown [105] that the time derivative of the Jacobian is given by:

$$\frac{\partial J}{\partial t} = \frac{dJ}{dt} = J \nabla \cdot \dot{\mathbf{y}} \quad (3.14)$$

Substituting Equations 3.13 and 3.14 into Equation 3.12 gives:

$$\frac{\partial}{\partial t} (\rho \mathbf{v}) + \rho \mathbf{v} \nabla \cdot \dot{\mathbf{y}} + \nabla \cdot (\rho \mathbf{v} \mathbf{c}) = \nabla \cdot \boldsymbol{\sigma} + \mathbf{f} \quad (3.15)$$

The first term on the left-hand side can be rewritten as:

$$\frac{\partial}{\partial t} (\rho \mathbf{v}) = \rho \frac{\partial \mathbf{v}}{\partial t} + \mathbf{v} \frac{\partial \rho}{\partial t} \quad (3.16)$$

The third term on the left-hand side of Equation 3.15 can be rewritten as:

$$\begin{aligned} \nabla \cdot (\rho \mathbf{v} \mathbf{c}) &= \rho \mathbf{v} \nabla \cdot \mathbf{c} + \mathbf{c} \cdot \nabla (\rho \mathbf{v}) = \rho \mathbf{v} \nabla \cdot (\mathbf{v} - \dot{\mathbf{y}}) + \mathbf{c} \cdot \nabla (\rho \mathbf{v}) \\ &= \rho \mathbf{v} \nabla \cdot (\mathbf{v} - \dot{\mathbf{y}}) + \rho \mathbf{c} \nabla \cdot \mathbf{v} + \mathbf{c} \mathbf{v} \cdot \nabla \rho \end{aligned} \quad (3.17)$$

Using Equations 3.16 and 3.17 and canceling terms, Equation 3.15 becomes:

$$\rho \frac{\partial \mathbf{v}}{\partial t} + \mathbf{v} \frac{\partial \rho}{\partial t} + \rho \mathbf{v} \nabla \cdot \mathbf{v} + \rho \mathbf{c} \nabla \cdot \mathbf{v} + \mathbf{c} \mathbf{v} \cdot \nabla \rho = \nabla \cdot \boldsymbol{\sigma} + \mathbf{f} \quad (3.18)$$

From the conservation of mass equation shown later in this chapter in Equation 3.58 we know  $\partial \rho / \partial t + \rho \nabla \cdot \mathbf{v} + \mathbf{c} \cdot \nabla \rho = 0$ , so we are left with:

$$\rho \frac{\partial \mathbf{v}}{\partial t} + \rho \mathbf{c} \nabla \cdot \mathbf{v} = \nabla \cdot \boldsymbol{\sigma} + \mathbf{f} \quad (3.19)$$



This is the conservation of momentum expressed in the ALE coordinate system. Note that the divergence operator  $\nabla$  is the divergence in the Eulerian system.

In order to develop the finite element approximation we must express the momentum equation in the weak form. This is done by multiplying by a test function  $w$  and integrating over the volume  $V$  to give:

$$\int_V w \left[ \rho \frac{\partial \mathbf{v}}{\partial t} + \rho \mathbf{c} \nabla \cdot \mathbf{v} \right] dy = \int_V w [\nabla \cdot \boldsymbol{\sigma} + \mathbf{f}] dy \quad (3.20)$$

Using Gauss's theorem, the second term on the left-hand side can be integrated by parts to obtain:

$$\int_V w \rho \mathbf{c} \nabla \cdot \mathbf{v} dy = - \int_V \nabla w \cdot (\rho \mathbf{v} \mathbf{c}) dy + \int_{\Gamma} w \rho \mathbf{v} \cdot \mathbf{n} ds \quad (3.21)$$

Likewise, the stress term on the right-hand side can be integrated using Gauss' theorem and Cauchy's Law to give:

$$\int_V w \nabla \cdot \boldsymbol{\sigma} dy = - \int_V \nabla w \cdot \boldsymbol{\sigma} dy + \int_{\Gamma} w \mathbf{t} ds \quad (3.22)$$

where  $\mathbf{t}$  is the traction.

So, the weak form of the conservation of momentum equation can be written in ALE form as:

$$\begin{aligned}
& \int_V \left[ w\rho \frac{\partial \mathbf{v}}{\partial t} - \nabla w \cdot (\rho \mathbf{v} \mathbf{c}) \right] dy + \int_{\Gamma} w \mathbf{c} \rho \mathbf{v} \cdot \mathbf{n} ds \\
& = \int_V [w \mathbf{f} - \nabla w \cdot \boldsymbol{\sigma}] dy + \int_{\Gamma} w \mathbf{t} ds
\end{aligned} \tag{3.23}$$

In traditional Eulerian and ALE formulations that use mixture theory the traction term is implied as part of the conservation of volume since the Cauchy stress will increase or decrease as material moves into and out of elements. However, in the formulation developed in this work the traction is included explicitly by performing a second operator split which enforces contact in elements where the contact constraints are not identically satisfied. For the first operator split this leaves us with:

$$\begin{aligned}
& \int_V \left[ w\rho \frac{\partial \mathbf{v}}{\partial t} - \nabla w \cdot (\rho \mathbf{v} \mathbf{c}) \right] dy + \int_{\Gamma} w \mathbf{c} \rho \mathbf{v} \cdot \mathbf{n} ds \\
& = \int_V [w \mathbf{f} - \nabla w \cdot \boldsymbol{\sigma}] dy
\end{aligned} \tag{3.24}$$

Performing the first operator split gives:

*Lagrangian step*

$$\int_V w\rho \frac{\partial}{\partial t} (\mathbf{v}^{lag}) dy = \int_V [w \mathbf{f} - \nabla w \cdot \boldsymbol{\sigma}] dy \tag{3.25}$$

*Remap step*

$$\int_V \left[ w\rho \frac{\partial}{\partial t} (\mathbf{v}^{remap}) - \nabla w \cdot (\rho \mathbf{v}^{lag} \mathbf{c}) \right] dy + \int_{\Gamma} w \mathbf{c} \rho \mathbf{v}^{lag} \cdot \mathbf{n} ds = 0 \tag{3.26}$$

And the second operator split gives:

*Contact enforcement step*

$$\int_V w \rho \frac{\partial}{\partial t} (\mathbf{v}^{ce}) dy = \int_{\Gamma} w t ds \quad (3.27)$$

*Contact remap step*

$$\int_V \left[ w \rho \frac{\partial}{\partial t} (\mathbf{v}^{ce \text{ remap}}) - \nabla w \cdot (\rho \mathbf{v}^{ce} \mathbf{c}^{ce}) \right] dy + \int_{\Gamma} w \mathbf{c}^{ce} \rho \mathbf{v}^{ce} \cdot \mathbf{n} ds = 0 \quad (3.28)$$

where here the superscripts *lag*, *remap*, *ce*, and *ce remap* indicate values obtained in the Lagrangian step, remap step, contact enforcement step, and contact remap step respectively, and  $\mathbf{c}^{ce}$  is the advection velocity for the contact remap step, which is given by  $\mathbf{c}^{ce} = \mathbf{v}^{ce} - \mathbf{v}^{remap}$ .

*Finite element approximation of the conservation of momentum equation*

The finite element approximation can be developed by replacing the test function  $w$  with the shape function  $N_l$  in the Lagrangian step and using a piecewise constant function  $N_k^\alpha$ , which has a value of one for element  $k$  and zero otherwise, in the remap step. It should be noted that Equations 3.25 to 3.28 are solved separately for each material, so we will now introduce the subscript  $m$  to indicate the material of interest. The material velocity vector,  $\mathbf{v}$ , and the advection velocity,  $\mathbf{c}$ , are replaced with the following approximations:

$$\mathbf{v}_m = \sum_{j=1}^{n_n} N_j \mathbf{v}_{m,j} \quad (3.29)$$

$$\mathbf{c}_m = \sum_{j=1}^{n_n} N_j \mathbf{c}_{m,j} \quad (3.30)$$

where  $n_n$  is the total number of nodes and the subscript  $m$  indicates the material of interest. Using indicial notation the Cauchy stress,  $\sigma$ , can be decomposed into its components as:

$$\sigma_{ij} = -p^* \delta_{ij} + s_{ij} \quad (3.31)$$

where  $p^*$  is the pressure,  $\delta_{ij}$  is the Kronecker delta function, and  $s_{ij}$  is the deviatoric stress, and the indices  $i$  and  $j$  have values  $1, \dots, n$  where  $n$  is the number of dimensions of the problem. The pressure term,  $p^*$ , is the sum of the pressure,  $p$ , determined by the equation of state, and the artificial viscosity,  $q$ , while the six deviatoric stress terms that arise in three-dimensions are found through the constitutive laws. Each of these must be written in a form suitable for the finite element method and are given by:

$$\sigma_m = \sum_{k=1}^{n_e} N_k^\alpha \sigma_{m,k} \quad (3.32)$$

$$p_m = \sum_{k=1}^{n_e} N_k^\alpha p_{m,k} \quad (3.33)$$

$$q_m = \sum_{k=1}^{n_e} N_k^\alpha q_{m,k} \quad (3.34)$$

$$s_m = \sum_{k=1}^{n_e} N_k^\alpha s_{m,k} \quad (3.35)$$

where  $n_e$  is the number of elements. Furthermore, the density term,  $\rho$ , can be approximated by:

$$\rho_m = \sum_{k=1}^{n_e} N_k^\alpha \rho_{m,k} \quad (3.36)$$

So for the Lagrangian step the finite element approximation for the conservation of momentum equation is given by:

$$\begin{aligned} & \sum_{k=1}^{n_e} \int_{\Omega_k} N_l N_k^\alpha \rho_{m,k} \left( \sum_{j=1}^{n_n} N_j \frac{\partial}{\partial t} \mathbf{v}_{m,j}^{lag} \right) \phi_{m,k} dy \\ &= \sum_{k=1}^{n_e} \int_{\Omega_k} (N_l \mathbf{f} - \nabla N_l \cdot N_k^\alpha \sigma_{m,k}) \phi_{m,k} dy \end{aligned} \quad (3.37)$$

$$l = 1, 2, \dots, n_n$$

where we have made use of the fact that  $N_k^\alpha$  is a piecewise constant function to eliminate the sums for  $\sigma$  and  $\rho$  in Equations 3.32 and 3.36. The left-hand side term

$\sum_{k=1}^{n_e} \int_{\Omega_k} N_l N_j \rho_{m,k} \phi_{m,k} dy$  is known as the consistent mass matrix. It is not diagonalized

and results in a high computational cost. Therefore, to simplify the solution we can

diagonalize Equation 3.37 by using the lumped mass,  $M_{m,l}^{lag}$ , at node  $l$ , which is defined

as:

$$M_{m,l}^{lag} = \frac{1}{n_e^l} \sum_{j=1}^{n_n} \sum_{k=1}^{n_e} \int_{\Omega_k} N_l N_j \rho_{m,k} \phi_{m,k} dy \quad (3.38)$$

where  $n_e^l$  is the number of elements connected to node  $l$ . Equation 3.38 is usually referred

to as the nodal mass. Furthermore, the  $N_k^\alpha$  term is equal to one for element  $k$ . Thus,

Equation 3.37 simplifies to:

$$M_{m,l}^{lag} \frac{\partial}{\partial t} (\mathbf{v}_{m,l}^{lag}) = \sum_{k=1}^{n_e} \int_{\Omega_k} (N_l \mathbf{f} - \nabla N_l \cdot \boldsymbol{\sigma}_{m,k}) \phi_{m,k} dy$$

$$l = 1, 2, \dots, n_n \quad (3.39)$$

In the remap step, the test function  $w$  is replaced by the weight function  $N_k^\alpha$ . Likewise the velocity, advection velocity, and density are replaced by their approximations given in Equations 3.29, 3.30, and 3.36 respectively. This gives:

$$\int_{\Omega_k} N_k^\alpha N_k^\alpha \rho_{m,k} \left( \sum_{j=1}^{n_n} N_j \frac{\partial}{\partial t} \mathbf{v}_{m,j}^{remap} \right) \phi_{m,k} dy$$

$$- \int_{\Omega_k} \nabla N_k^\alpha \cdot \left( N_k^\alpha \rho_{m,k} \left( \sum_{j=1}^{n_n} N_j \mathbf{v}_{m,j}^{lag} \right) \left( \sum_{i=1}^{n_n} N_i \mathbf{c}_{m,i} \right) \right) \phi_{m,k} dy$$

$$+ \int_{\Gamma_k} N_k^\alpha \left( \sum_{j=1}^{n_n} N_j \mathbf{v}_{m,j}^{lag} \right) N_k^\alpha \rho_{m,k} \left( \sum_{i=1}^{n_n} N_i \mathbf{c}_{m,i} \right) \cdot \mathbf{n} \phi_{m,k} ds = 0$$

$$k = 1, 2, \dots, n_e \quad (3.40)$$

Again, we have made use of the fact that  $N_k^\alpha$  is piecewise constant to eliminate the sum for  $\rho$  in Equation 3.36. The choice of the piecewise constant function  $N_k^\alpha$  limits the accuracy of the solution but also results in a significant simplification because  $\nabla N_k^\alpha = 0$ . Therefore, the second term in the left-hand side disappears. So we are left with:

$$\int_{\Omega_k} \rho_{m,k} \left( \sum_{j=1}^{n_n} N_j \frac{\partial}{\partial t} \mathbf{v}_{m,j}^{remap} \right) \phi_{m,k} dy$$

$$+ \int_{\Gamma_k} \left( \sum_{j=1}^{n_n} N_j \mathbf{v}_{m,j}^{lag} \right) \rho_{m,k} \left( \sum_{i=1}^{n_n} N_i \mathbf{c}_{m,i} \right) \cdot \mathbf{n} \phi_{m,k} ds = 0$$

$$k = 1, 2, \dots, n_e \quad (3.41)$$

The first term contains the integral  $\int_{\Omega_k} \rho_{m,k} \phi_{m,k} dy$  which is the mass of element  $k$  denoted as  $m_{m,k}^{remap}$ . So Equation 3.41 becomes:

$$m_{m,k}^{remap} \left( \sum_{j=1}^{n_n} N_j \frac{\partial}{\partial t} \mathbf{v}_{m,j}^{remap} \right) + \int_{\Gamma_k} \left( \sum_{j=1}^{n_n} N_j \mathbf{v}_{m,j}^{lag} \right) \rho_{m,k} \left( \sum_{i=1}^{n_n} N_i \mathbf{c}_{m,i} \right) \cdot \mathbf{n} \phi_{m,k} ds = 0$$

$$k = 1, 2, \dots, n_e \quad (3.42)$$

Note that Equation 3.42 contains multiple velocity unknowns and is therefore not diagonalized, much like Equation 3.37 was before the lumped mass approximation was used. There are many methods to reduce Equation 3.42 to a diagonal system. One approach is to use the Half-Index Shift (HIS) algorithm presented in Chapter 2, which was used in this work.

At this point for the contact formulation developed for this work the materials have been permitted to move independently without interaction or deformation due to contact. The equations developed to this point could also be used with the standard mixture theory formulation, where they are no longer solved independently for each material, but rather mixture theory is applied. For the mixture theory formulation the  $\mathbf{v}_{m,j}$  and  $\mathbf{c}_{m,j}$  terms would no longer be determined for each material, but rather for all materials due to the use of a single velocity field. The  $\phi_{m,k}$  term in the Lagrangian step would become  $1 - \phi_{void}$ , and the components of the Cauchy stress tensor would be determined through mixture theory. There are numerous methods for determining the mixed element quantities, but the method implemented in the ALEAS mixture theory formulation shown in Chapter 6 is:

$$p_{0,k} = \frac{\sum_{m=1}^{n_m} (p_{m,k} \phi_{m,k})}{\sum_{m=1}^{n_m} \phi_{m,k}} \quad (3.43)$$

$$q_{0,k} = \frac{\sum_{m=1}^{n_m} (q_{m,k} \phi_{m,k})}{\sum_{m=1}^{n_m} \phi_{m,k}} \quad (3.44)$$

$$s_{0,k} = \frac{\sum_{m=1}^{n_m} (s_{m,k} \phi_{m,k})}{\sum_{m=1}^{n_m} \phi_{m,k}} \quad (3.45)$$

where the  $0$  subscript indicates the value determined through mixture theory and  $n_m$  is the total number of materials in the problem.

At this point the mixture theory formulation would be complete, because forces exchanged between interacting materials are taken into account by replacing them with what is essentially an equivalent single material since only one velocity field and stress state is present in the element. All remaining surfaces are free surfaces, so the traction is always zero in mixture theory formulations. However, when mixture theory is not used surfaces are permitted to interact and accumulate surface forces so that a second operator split is necessary to conserve momentum. The momentum equation for the contact enforcement step is similar to the one derived for the Lagrangian step, so the procedure is not shown here. The contact enforcement step is given by:

$$M_{m,l}^{ce} \frac{\partial}{\partial t} (\mathbf{v}_{m,l}^{ce}) = \sum_{k=1}^{n_e} \int_{\Gamma_k} N_l \mathbf{t} \, ds$$

$$l = 1, 2, \dots, n_n \quad (3.46)$$



where  $M_{m,l}^{ce}$  is the nodal lumped mass associated the contact enforcement step. The right-hand side of this equation can be solved in a number of different ways and in this work is handled by the Eulerian contact enforcement method presented later in this chapter.

The last step of the second operator split is the contact enforcement remap step, which is derived in a similar fashion to the first remap step and is given by:

$$m_{m,k}^{ce\ remap} \left( \sum_{j=1}^{n_n} N_j \frac{\partial}{\partial t} \mathbf{v}_{m,j}^{ce\ remap} \right) + \int_{\Gamma_k} \left( \sum_{j=1}^{n_n} N_j \mathbf{v}_{m,j}^{ce} \right) \rho_{m,k} \left( \sum_{j=1}^{n_n} N_j \mathbf{c}_{m,j}^{ce} \right) \cdot \mathbf{n} \phi_{m,k} ds = 0$$

$$k = 1, 2, \dots, n_e \quad (3.47)$$

where  $m_{m,l}^{ce\ remap}$  is the element mass.

#### *Conservation of Mass in ALE Coordinates*

Using the same description as the conservation of momentum, we also need to express the conservation of mass in the ALE coordinate system. The conservation of mass equation solves for the mass and, by extension, the density,  $\rho$ . At  $t = 0$ , the mass of the body is given by:

$$m_0 = \int_{\Omega \cap V} \rho_0 dX \quad (3.48)$$

Likewise, the mass at some later time,  $t = t_1$ , can be written as:

$$m_1 = \int_{\Omega \cap V} \rho dy + \int_0^t \int_{\Gamma} \rho \mathbf{c} \cdot \mathbf{n} ds dt \quad (3.49)$$

where  $\mathbf{n}$  is the outward unit normal vector to  $V$  along the boundary  $\Gamma$  and  $\mathbf{c}$  is the advection velocity.

Since we know that mass is conserved over all time we can now express the conservation of mass as:

$$\int_V \rho_0 dX = \int_V \rho dy + \int_0^t \int_{\Gamma} \rho \mathbf{c} \cdot \mathbf{n} ds dt \quad (3.50)$$

Here we have replaced  $\Omega \cap V$  with  $V$  by setting  $\rho = 0$  in  $V - \Omega \cap V$ . Substituting this, changing reference frames, and differentiating with respect to time, we get:

$$\int_V \frac{\partial}{\partial t} (\rho J) dX + \int_{\Gamma} \rho \mathbf{c} \cdot \mathbf{n} ds = 0 \quad (3.51)$$

Now using Gauss's theorem, we find the second integral to be:

$$\int_{\Gamma} \rho \mathbf{c} \cdot \mathbf{n} ds = \int_V \nabla \cdot (\rho \mathbf{c}) dy = \int_V J \nabla \cdot (\rho \mathbf{c}) dX \quad (3.52)$$

So, by substituting this, the conservation of mass equation can now be rewritten as:

$$\int_V \left[ \frac{\partial}{\partial t} (\rho J) + J \nabla \cdot (\rho \mathbf{c}) \right] dX = 0 \quad (3.53)$$

Since this must apply for any choice of control volume  $V$ , we can conclude that the integrand must be zero, so using this and dividing through by  $J$  gives:

$$\frac{1}{J} \frac{\partial}{\partial t} (\rho J) + \nabla \cdot (\rho \mathbf{c}) = 0 \quad (3.54)$$

Using the product rule, the first term on the left-hand side gives:

$$\frac{1}{J} \frac{\partial}{\partial t} (\rho J) = \frac{1}{J} \left[ J \frac{\partial \rho}{\partial t} + \rho \frac{\partial J}{\partial t} \right] = \frac{\partial \rho}{\partial t} + \frac{\rho}{J} \frac{\partial J}{\partial t} \quad (3.55)$$

Using Equation 3.14, Equation 3.55 can be rewritten:

$$\frac{\partial \rho}{\partial t} + \frac{\rho}{J} \frac{\partial J}{\partial t} = \frac{\partial \rho}{\partial t} + \rho \nabla \cdot \dot{\mathbf{y}} \quad (3.56)$$

The second term on the left-hand side of Equation 3.54 can be rewritten as:

$$\nabla \cdot (\rho \mathbf{c}) = \rho \nabla \cdot \mathbf{c} + \mathbf{c} \cdot \nabla \rho = \rho \nabla \cdot (\mathbf{v} - \dot{\mathbf{y}}) + \mathbf{c} \cdot \nabla \rho \quad (3.57)$$

Substituting Equations 3.56 and 3.57 into Equation 3.54 and canceling terms gives:

$$\frac{\partial \rho}{\partial t} + \rho \nabla \cdot \mathbf{v} + \mathbf{c} \cdot \nabla \rho = 0 \quad (3.58)$$

This is mass conservation expressed in the ALE coordinate system.

In order for this formulation to be implemented using the finite element method we must now express the conservation of mass equation in a weak form. This is accomplished by multiplying the governing differential equation by a test function,  $w$ , and integrating over the volume,  $V$ , to get:

$$\int_V w \left[ \frac{\partial \rho}{\partial t} + \rho \nabla \cdot \mathbf{v} + \mathbf{c} \cdot \nabla \rho \right] dy = 0 \quad (3.59)$$

Using the Reynolds transport theorem on the first term on the left-hand side gives:

$$\int_{\mathcal{V}} w \frac{\partial \rho}{\partial t} dy = \frac{\partial}{\partial t} \int_{\mathcal{V}} w \rho dy - \int_{\Gamma} w \rho \dot{\mathbf{y}} \cdot \mathbf{n} ds \quad (3.60)$$

The second term can be integrated by parts to obtain:

$$\begin{aligned} \int_{\mathcal{V}} w \rho \nabla \cdot \mathbf{v} dy &= - \int_{\mathcal{V}} \nabla w \cdot (\rho \mathbf{v}) dy + \int_{\mathcal{V}} \rho \nabla \cdot (w \mathbf{v}) dy \\ &= - \int_{\mathcal{V}} \nabla w \cdot (\rho \mathbf{v}) dy + \int_{\Gamma} w \rho \mathbf{v} \cdot \mathbf{n} ds \\ &= - \int_{\mathcal{V}} \nabla w \cdot (\rho \mathbf{v}) dy + \int_{\Gamma} w \rho (\mathbf{c} + \dot{\mathbf{y}}) \cdot \mathbf{n} ds \end{aligned} \quad (3.61)$$

So, after canceling terms the statement of the weak form of the conservation of mass equation in the ALE coordinate system becomes:

$$\frac{\partial}{\partial t} \int_{\mathcal{V}} w \rho dy + \int_{\mathcal{V}} [w \mathbf{c} \cdot \nabla \rho - \nabla w \cdot (\rho \mathbf{v})] dy + \int_{\Gamma} w \rho \mathbf{c} \cdot \mathbf{n} ds = 0 \quad (3.62)$$

Performing the first operator split we arrive at the following:

*Lagrangian step*

$$\frac{\partial}{\partial t} \int_{\mathcal{V}} w \rho^{lag} dy = 0 \quad (3.63)$$

*Remap step*

$$\frac{\partial}{\partial t} \int_V w \rho^{remap} dy + \int_V [w \mathbf{c} \cdot \nabla \rho^{lag} - \nabla w \cdot (\rho^{lag} \mathbf{v})] dy + \int_{\Gamma} w \rho^{lag} \mathbf{c} \cdot \mathbf{n} ds = 0 \quad (3.64)$$

Performing the second operator split we have:

*Contact enforcement step*

$$\frac{\partial}{\partial t} \int_V w \rho^{ce} dy = 0 \quad (3.65)$$

*Contact remap step*

$$\frac{\partial}{\partial t} \int_V w \rho^{ce remap} dy + \int_V [w \mathbf{c}^{ce} \cdot \nabla \rho^{ce} - \nabla w \cdot (\rho^{ce} \mathbf{v}^{ce})] dy + \int_{\Gamma} w \rho^{ce} \mathbf{c}^{ce} \cdot \mathbf{n} ds = 0 \quad (3.66)$$

*Finite element approximation of the conservation of mass equation*

In order to develop the finite element approximation of the conservation of mass equation we replace the test function  $w$  with a piecewise constant  $N_k^\alpha$  which is equal to one for element  $k$ . Likewise, the density, velocity, and advection velocity are approximated using Equations 3.36, 3.29, and 3.30, respectively.

For the Lagrangian step, the finite element formulation for the conservation of mass equation is given by:

$$\frac{\partial}{\partial t} \int_{\Omega_k} N_k^\alpha (N_k^\alpha \rho_{m,k}^{lag}) \phi_{m,k} dy = 0 \quad (3.67)$$

$$k = 1, 2, \dots, n_e$$

Since  $N_k^\alpha = 1$  for element  $k$  Equation 3.67 becomes:

$$\frac{\partial}{\partial t} \int_{\Omega_k} \rho_{m,k}^{lag} \phi_{m,k} dy = 0$$

$$k = 1, 2, \dots, n_e \quad (3.68)$$

The integral  $\int_{\Omega_k} \rho_{m,k}^{lag} \phi_{m,k} dy$  is equal to the element mass  $m_{m,k}^{lag}$ , and can be written as:

$$\frac{\partial}{\partial t} m_{m,k}^{lag} = 0$$

$$k = 1, 2, \dots, n_e \quad (3.69)$$

This shows that the mass is constant in element  $k$  during the Lagrangian step, therefore it is not necessary to carry out the finite element approximation for conservation of mass in the Lagrangian step.

For the remap step, the finite element approximation is again obtained by replacing the test function  $w$  with a piecewise constant function  $N_k^\alpha$  which is equal to one for element  $k$  and zero otherwise. The use of  $N_k^\alpha$  limits the accuracy of the solution, however it leads to a significant simplification by eliminating the  $\nabla w$  term in the remap step of the conservation of mass equation. Using this we can write the remap step of the conservation of mass equation as:

$$\begin{aligned}
& \frac{\partial}{\partial t} \int_{\Omega_k} [N_k^\alpha N_k^\alpha \rho_{m,k}^{remap}] \phi_{m,k} dy - \int_{\Omega_k} \left[ \nabla N_k^\alpha \cdot \left( N_k^\alpha \rho_{m,k}^{lag} \left( \sum_{j=1}^{n_n} N_j \mathbf{v}_{m,j}^{lag} \right) \right) \right] \phi_{m,k} dy \\
& + \int_{\Omega_k} \left[ N_k^\alpha \left( \sum_{j=1}^{n_n} N_j \mathbf{c}_{m,j} \right) \cdot \nabla (N_k^\alpha \rho_{m,k}^{remap}) \right] \phi_{m,k} dy \\
& + \int_{\Gamma_k} N_k^\alpha N_k^\alpha \rho_{m,k}^{lag} \left( \sum_{j=1}^{n_n} N_j \mathbf{c}_{m,j} \right) \cdot \mathbf{n} \phi_{m,k} ds = 0 \\
& k = 1, 2, \dots, n_e
\end{aligned} \tag{3.70}$$

Again we have made use of the fact that  $N_k^\alpha$  is piecewise constant to eliminate the sum for  $\rho$ . At the element level  $\rho_{m,k}^{remap}$  is a piecewise constant, so  $\nabla(N_k^\alpha \rho_{m,k}^{remap}) = 0$ . Since  $\nabla N_k^\alpha = 0$  and  $N_k^\alpha = 1$  for element  $k$  we are left with:

$$\begin{aligned}
& \frac{\partial}{\partial t} \int_{\Omega_k} \rho_{m,k}^{remap} \phi_{m,k} dy + \int_{\Gamma_k} \rho_{m,k}^{lag} \left( \sum_{j=1}^{n_n} N_j \mathbf{c}_{m,j} \right) \cdot \mathbf{n} \phi_{m,k} ds = 0 \\
& k = 1, 2, \dots, n_e
\end{aligned} \tag{3.71}$$

The first term contains the volume integral  $\int_{\Omega_k} \rho_{m,k}^{remap} \phi_{m,k} dy$  which is the element mass for material  $m$  given by  $m_{m,k}^{remap}$ , so Equation 3.71 becomes:

$$\begin{aligned}
& \frac{\partial}{\partial t} m_{m,k}^{remap} + \int_{\Gamma_k} \rho_{m,k}^{lag} \left( \sum_{j=1}^{n_n} N_j \mathbf{c}_{m,j} \right) \cdot \mathbf{n} \phi_{m,k} ds = 0 \\
& k = 1, 2, \dots, n_e
\end{aligned} \tag{3.72}$$

The conservation of mass is also performed for each material in traditional Eulerian and ALE formulations that use mixture theory, so the only difference between the traditional formulation and the contact formulation developed for this work is the use of individual velocity fields for the velocity,  $\mathbf{c}_{m,j}$ . In the traditional formulation with

mixture theory the velocity is the same for all materials in the problem space, however in the contact formulation developed in this work each material has its own advection velocity. This requires a second operator split to conserve mass. The conservation of mass for the contact enforcement step is similar in form to the Lagrangian step and again remains constant. The conservation of mass for the contact enforcement step is given by:

$$\begin{aligned} \frac{\partial}{\partial t} m_{m,k}^{ce} &= 0 \\ k &= 1, 2, \dots, n_e \end{aligned} \quad (3.73)$$

where  $m_{m,k}^{ce}$  is the mass for the contact enforcement step.

The last step of the second operator split is the contact enforcement remap step, which is derived in a similar fashion to the first remap step and is given by:

$$\begin{aligned} \frac{\partial}{\partial t} m_{m,k}^{ce \text{ remap}} + \int_{\Gamma_k} \rho_{m,k}^{ce} \left( \sum_{j=1}^{n_n} N_j \mathbf{c}_{m,j}^{ce} \right) \cdot \mathbf{n} \phi_{m,k} ds &= 0 \\ k &= 1, 2, \dots, n_e \end{aligned} \quad (3.74)$$

where  $m_{m,k}^{ce \text{ remap}}$  is the element mass for the contact remap step.

### *Conservation of Energy in ALE Coordinates*

The initial total energy,  $E_0$ , of a body  $\Omega$  at  $t = 0$  is given by:

$$E_0 = \int_{\Omega \cap V} \rho_0 E_0 dX \quad (3.75)$$

Likewise, at some later time  $t = t_1$ , the total energy of the body,  $E_1$ , is given by:



$$E_1 = \int_{\Omega \cap V} \rho E dy + \int_0^t \int_{\Gamma} \rho E(\mathbf{c} \cdot \mathbf{n}) ds \quad (3.76)$$

The change in total energy is given by  $E_1 - E_0$ , and the rate of change is the time derivative, which can be written as:

$$\frac{\partial E}{\partial t} = \frac{\partial E_1}{\partial t} = \frac{\partial}{\partial t} \int_{\Omega \cap V} \rho E dy + \int_{\Gamma} \rho E(\mathbf{c} \cdot \mathbf{n}) ds \quad (3.77)$$

Using Equation 3.5 we can convert the first term on the left-hand side of Equation 3.77 to the original coordinate system as:

$$\frac{\partial}{\partial t} \int_{\Omega \cap V} \rho E dy = \frac{\partial}{\partial t} \int_{\Omega \cap V} (\rho J E) dX = \int_{\Omega \cap V} \frac{\partial}{\partial t} (\rho J E) dX \quad (3.78)$$

Applying Gauss' theorem to the second term in Equation 3.77 gives:

$$\int_{\Gamma} \rho E(\mathbf{c} \cdot \mathbf{n}) ds = \int_{\Omega \cap V} \nabla \cdot (\rho E \mathbf{c}) dy = \int_{\Omega \cap V} J \nabla \cdot (\rho E \mathbf{c}) dX \quad (3.79)$$

The total energy is the sum of the work done by the body, where  $\dot{W}$  is the rate of mechanical work and  $\dot{Q}$  is the rate of energy supplied by heat transfer or energy sources.

In this work we do not consider the rate of energy supplied by heat transfer or energy sources, so  $\dot{Q}$  is assumed to be zero.

The rate of mechanical work is the sum of the work done by external forces and body forces given by:

$$\dot{W} = \int_{\Gamma} \mathbf{t} \cdot \mathbf{v} ds + \int_{\Omega \cap V} \mathbf{f} \cdot \mathbf{v} dy \quad (3.80)$$

Using Cauchy's Law on the first integral in Equation 3.80 becomes:

$$\int_{\Gamma} \mathbf{t} \cdot \mathbf{v} ds + \int_{\Omega \cap V} \mathbf{f} \cdot \mathbf{v} dy = \int_{\Gamma} (\boldsymbol{\sigma} \cdot \mathbf{n}) \cdot \mathbf{v} ds + \int_{\Omega \cap V} \mathbf{f} \cdot \mathbf{v} dy \quad (3.81)$$

Applying Gauss' theorem to the first integral on the right-hand side of Equation 3.81 gives:

$$\int_{\Gamma} \boldsymbol{\sigma} \cdot \mathbf{n} \cdot \mathbf{v} ds + \int_{\Omega \cap V} \mathbf{f} \cdot \mathbf{v} dy = \int_{\Omega \cap V} \nabla \cdot (\mathbf{v} \cdot \boldsymbol{\sigma}) dy + \int_{\Omega \cap V} \mathbf{f} \cdot \mathbf{v} dy \quad (3.82)$$

So, the conservation of total energy equation now becomes:

$$\int_{\Omega \cap V} \left[ \frac{\partial}{\partial t} (\rho J E) + J \nabla \cdot (\rho \mathbf{E} \mathbf{c}) \right] dX = \int_{\Omega \cap V} J [\nabla \cdot (\mathbf{v} \cdot \boldsymbol{\sigma}) + \mathbf{f} \cdot \mathbf{v}] dX \quad (3.83)$$

This must be valid for any choice of control volume  $V$ , so therefore the integrand must be zero. Using this and dividing through by  $J$  gives:

$$\frac{1}{J} \frac{\partial}{\partial t} (\rho J E) + \nabla \cdot (\rho \mathbf{E} \mathbf{c}) = \nabla \cdot (\mathbf{v} \cdot \boldsymbol{\sigma}) + \mathbf{f} \cdot \mathbf{v} \quad (3.84)$$

Using the product rule on the first term on the left-hand side gives:

$$\frac{1}{J} \frac{\partial}{\partial t} (\rho J E) = \frac{1}{J} \left[ J \frac{\partial}{\partial t} (\rho E) + \rho E \frac{\partial J}{\partial t} \right] = \frac{\partial}{\partial t} (\rho E) + \rho E \mathbf{v} \cdot \dot{\mathbf{y}} \quad (3.85)$$

Substituting Equations 3.85 into Equation 3.84 gives:

$$\frac{\partial}{\partial t}(\rho E) + \rho E \nabla \cdot \dot{\mathbf{y}} + \nabla \cdot (\rho E \mathbf{c}) = \nabla \cdot (\mathbf{v} \cdot \boldsymbol{\sigma}) + \mathbf{f} \cdot \mathbf{v} \quad (3.86)$$

The first term on the left-hand side can be rewritten as:

$$\frac{\partial}{\partial t}(\rho E) = \rho \frac{\partial E}{\partial t} + E \frac{\partial \rho}{\partial t} \quad (3.87)$$

The third term on the left-hand side of Equation 3.86 can be rewritten as:

$$\begin{aligned} \nabla \cdot (\rho E \mathbf{c}) &= \rho E \nabla \cdot \mathbf{c} + \mathbf{c} \cdot \nabla(\rho E) \\ &= \rho E \nabla \cdot (\mathbf{v} - \dot{\mathbf{y}}) + \rho \mathbf{c} \nabla \cdot E + \mathbf{c} E \cdot \nabla \rho \end{aligned} \quad (3.88)$$

Using Equations 3.87 and 3.88 and canceling terms, Equation 3.86 becomes:

$$\rho \frac{\partial E}{\partial t} + E \frac{\partial \rho}{\partial t} + \rho E \nabla \cdot \mathbf{v} + \rho \mathbf{c} \nabla \cdot E + \mathbf{c} E \cdot \nabla \rho = \nabla \cdot (\mathbf{v} \cdot \boldsymbol{\sigma}) + \mathbf{f} \cdot \mathbf{v} \quad (3.89)$$

Using the conservation of mass equation shown in Equation 3.58 we can simplify

Equation 3.89 as:

$$\rho \frac{\partial E}{\partial t} + \rho \mathbf{c} \nabla \cdot E = \nabla \cdot (\mathbf{v} \cdot \boldsymbol{\sigma}) + \mathbf{f} \cdot \mathbf{v} \quad (3.90)$$

This is one form of the conservation of energy in the ALE coordinate system expressed in terms of total energy  $E$ . But the total energy  $E$  is the sum of the internal energy  $e$  and the kinetic energy  $k$ , where the kinetic energy is given by:

$$k = \frac{\mathbf{v} \cdot \mathbf{v}}{2} \quad (3.91)$$

So the total energy is given by:

$$E = e + \frac{\mathbf{v} \cdot \mathbf{v}}{2} \quad (3.92)$$

Substituting this into Equation 3.90 gives:

$$\rho \frac{\partial}{\partial t} \left( e + \frac{\mathbf{v} \cdot \mathbf{v}}{2} \right) + \rho \mathbf{c} \nabla \cdot \left( e + \frac{\mathbf{v} \cdot \mathbf{v}}{2} \right) = \nabla \cdot (\mathbf{v} \cdot \sigma) + \mathbf{f} \cdot \mathbf{v} \quad (3.93)$$

The right-hand side can be rewritten as:

$$\nabla \cdot (\mathbf{v} \cdot \sigma) + \mathbf{f} \cdot \mathbf{v} = \sigma : (\nabla \mathbf{v}) + \mathbf{v} \cdot (\nabla \cdot \sigma) + \mathbf{f} \cdot \mathbf{v} \quad (3.94)$$

Substituting this and using the product rule on the kinetic energy terms gives:

$$\rho \frac{\partial e}{\partial t} + \rho \mathbf{c} \nabla \cdot e + \rho \mathbf{v} \frac{\partial \mathbf{v}}{\partial t} + \rho \mathbf{c} \mathbf{v} \nabla \cdot \mathbf{v} = \sigma : (\nabla \mathbf{v}) + \mathbf{v} \cdot (\nabla \cdot \sigma) + \mathbf{f} \cdot \mathbf{v} \quad (3.95)$$

Using the conservation of momentum equation given in Equation 3.19, this equation simplifies to:

$$\rho \frac{\partial e}{\partial t} + \rho \mathbf{c} \nabla \cdot e = \sigma : (\nabla \mathbf{v}) \quad (3.96)$$

This is another form of the conservation on energy equation, expressed in terms of internal energy.

Taking the weak form of Equation 3.96 gives:

$$\int_{\mathcal{V}} w \left[ \rho \frac{\partial e}{\partial t} + \rho \mathbf{c} \nabla \cdot e \right] dy = \int_{\mathcal{V}} w [\sigma : (\nabla \mathbf{v})] dy \quad (3.97)$$

Using Gauss's theorem, the second term on the left-hand side can be integrated by parts to obtain:

$$\int_V w \rho \mathbf{c} \nabla \cdot \mathbf{e} dy = - \int_V \nabla w \cdot (\rho \mathbf{e}) dy + \int_{\Gamma} w \rho \mathbf{c} \cdot \mathbf{n} ds \quad (3.98)$$

So, the weak form of the conservation of energy equation can be written in ALE form as:

$$\int_V \left[ w \rho \frac{\partial e}{\partial t} - \nabla w \cdot (\rho \mathbf{e}) \right] dy + \int_{\Gamma} w \rho \mathbf{c} \cdot \mathbf{n} ds = \int_V w [\sigma : (\nabla \mathbf{v})] dy \quad (3.99)$$

This is the form of the energy equation used in ALEAS and many other hydrocodes. It should be noted that the traction is implied in the rate of work, and thus does not appear in this equation. Other forms of the energy equation are possible in which the traction is explicitly included, but such forms have not been examined in this work. While the effects of using this form of the energy equation have not been quantified, it is likely that using a different form for which a traction is included explicitly would result in a negligible difference in accuracy. This will be examined in more detail in future work.

Performing the first operator split we arrive at the following:

*Lagrangian step*

$$\int_V w \rho \frac{\partial}{\partial t} (e^{lag}) dy = \int_V w [\sigma : (\nabla \mathbf{v})] dy \quad (3.100)$$

*Remap step*

$$\int_V \left[ w \rho \frac{\partial}{\partial t} (e^{remap}) - \nabla w \cdot \rho \mathbf{c} e^{lag} \right] dy + \int_{\Gamma} w \rho e^{lag} \mathbf{c} \cdot \mathbf{n} ds = 0 \quad (3.101)$$

The second operator split for contact enforcement gives:

*Contact enforcement step*

$$\int_V w \rho \frac{\partial}{\partial t} (e^{ce}) dy = 0 \quad (3.102)$$

*Contact remap step*

$$\int_V \left[ w \rho \frac{\partial}{\partial t} (e^{ce \text{ remap}}) - \nabla w \cdot \rho \mathbf{c}^{ce} e^{ce} \right] dy + \int_{\Gamma} w \rho e^{ce} \mathbf{c}^{ce} \cdot \mathbf{n} ds = 0 \quad (3.103)$$

*Finite element approximation of the conservation of energy equation*

As was described for the mass and momentum equations, the test function  $w$  is replaced by the shape function a piecewise constant function  $N_k^\alpha$ , which has a value of one for element  $k$  and zero otherwise. The approximations for  $\mathbf{v}$ ,  $\mathbf{c}$ ,  $\rho$ , and  $\sigma$  are the same as those given in the derivation of the mass and momentum equations. The specific internal energy term is given by:

$$e_m = \sum_{k=1}^{n_e} N_k^\alpha e_{m,k} \quad (3.104)$$

Using this in the Lagrangian step of the conservation of energy equation we have:

$$\begin{aligned} & \sum_{k=1}^{n_e} \left[ \int_{\Omega_m} N_k^\alpha \rho_{m,k} \frac{\partial}{\partial t} (e_{m,k}^{lag}) \phi_{m,k} dy \right] \\ &= \sum_{k=1}^{n_e} \left[ \int_{\Omega_m} N_k^\alpha \left[ \sigma_{m,k} : \nabla \left( \sum_{j=1}^{n_n} N_j \mathbf{v}_{m,j} \right) \right] \phi_{m,k} dy \right] \end{aligned} \quad (3.105)$$

where we have made use of the fact that  $N_k^\alpha$  is a piecewise constant function to eliminate the sums for  $e$ ,  $\rho$ , and  $\sigma$ . Since  $N_k^\alpha = 1$  and  $\nabla \mathbf{v} = \partial v_i / \partial x_j = D_{ij} + W_{ij}$  and also  $\sigma_{ij} W_{ij} = 0$ . Therefore, we can rewrite Equation 3.105 as:

$$\sum_{k=1}^{n_e} \left[ \int_{\Omega_k} \rho_{m,k} \frac{\partial}{\partial t} (e_{m,k}^{lag}) \phi_{m,k} dy \right] = \sum_{k=1}^{n_e} \left[ \int_{\Omega_k} [\sigma_{m,k} : \dot{\epsilon}_{m,k}] \phi_{m,k} dy \right] \quad (3.106)$$

where  $\dot{\epsilon}_{m,k} = D_{m,k}$  is the strain rate for element  $k$ . The volume integral on the left-hand side,  $\sum_{k=1}^{n_e} \int_{\Omega_k} \rho_{m,k} \phi_{m,k} dy$ , is the element mass  $m_{m,k}^{lag}$ , so we can rewrite the Lagrangian step of the conservation of energy equation as:

$$m_{m,k}^{lag} \frac{\partial}{\partial t} e_{m,k}^{lag} = \int_{\Omega_k} [\sigma_{m,k} : \dot{\epsilon}_{m,k}] \phi_{m,k} dy$$

$$k = 1, 2, \dots, n_e \quad (3.107)$$

For the remap step, the finite element approximation is again obtained by replacing the advection velocity,  $\mathbf{c}$ , with the approximation given in Equation 3.30 and the test function  $w$  with the piecewise constant function  $N_k^\alpha$ , which is equal to one for element  $k$  and is zero otherwise. The finite element approximation of the remap step of the energy equation is given by:

$$\int_{\Omega_k} \left[ N_k^\alpha \rho_{m,k} \frac{\partial}{\partial t} (e_{m,k}^{remap}) - \nabla N_k^\alpha \cdot \rho_{m,k} \left( \sum_{j=1}^{n_n} N_j \mathbf{c}_{m,j} \right) e_{m,k}^{lag} \right] \phi_{m,k} dy$$

$$+ \int_{\Gamma_k} N_k^\alpha \rho_{m,k} e_{m,k}^{lag} \left( \sum_{j=1}^{n_n} N_j \mathbf{c}_{m,j} \right) \cdot \mathbf{n} \phi_{m,k} ds = 0$$

$$k = 1, 2, \dots, n_e \quad (3.108)$$

Again we have made use of the fact that  $N_k^\alpha$  is piecewise constant to eliminate the sums for  $\rho$  and  $e$ . Since  $\nabla N_k^\alpha = 0$  and  $N_k^\alpha = 1$  for element  $k$  we are left with:

$$\int_{\Omega_k} \rho_{m,k} \frac{\partial}{\partial t} (e_{m,k}^{remap}) \phi_{m,k} dy + \int_{\Gamma_k} \rho_{m,k} e_{m,k}^{lag} \left( \sum_{j=1}^{n_n} N_j \mathbf{c}_{m,j} \right) \cdot \mathbf{n} \phi_{m,k} ds = 0$$

$k = 1, 2, \dots, n_e$

(3.109)

The first term contains the volume integral  $\int_{\Omega_k} \rho_{m,k} \phi_{m,k} dy$  which is the element mass  $m_{m,k}^{remap}$ , so we can rewrite the remap step of the energy equation as:

$$m_{m,k}^{remap} \frac{\partial}{\partial t} (e_{m,k}^{remap}) + \int_{\Gamma_k} \rho_{m,k} e_{m,k}^{lag} \left( \sum_{j=1}^{n_n} N_j \mathbf{c}_{m,j} \right) \cdot \mathbf{n} \phi_{m,k} ds = 0$$

$k = 1, 2, \dots, n_e$

(3.110)

As with the conservation of mass, the conservation of energy is solved for each material separately, but for the traditional formulation with mixture theory the Cauchy stress term,  $\sigma_{m,k}$ , will be the mixture theory result described in the conservation of momentum section. The material and advection velocity terms  $\mathbf{v}_{m,j}$  and  $\mathbf{c}_{m,j}$  as well as the strain rate  $\dot{\epsilon}_{m,k}$  are for all materials as a result of the single velocity field. The traditional ALE formulation with mixture theory stops here, however, since materials do not interact during the first operator split in the method developed here we must perform a second operator split in order to satisfy the no-penetration constraint and conserve energy. The contact enforcement step has similar form to the Lagrangian step and is given by:



$$m_{m,k}^{ce} \frac{\partial}{\partial t} e_{m,k}^{ce} = 0$$

$$k = 1, 2, \dots, n_e \quad (3.111)$$

The last step of the second operator split is the contact enforcement remap step, which is derived in a similar fashion to the first remap step and is given by:

$$m_{m,k}^{ce \text{ remap}} \frac{\partial}{\partial t} (e_{m,k}^{ce \text{ remap}}) + \int_{\Gamma_k} \rho_{m,k} e_{m,k}^{ce} \left( \sum_{j=1}^{n_n} N_j \mathbf{c}_{m,j}^{ce} \right) \cdot \mathbf{n} \phi_{m,k} ds = 0$$

$$k = 1, 2, \dots, n_e \quad (3.112)$$

### *Summary of the ALE Finite Element Contact Formulation*

In the preceding sections we have developed the ALE finite element approximation of the mass, momentum, and energy equations using a four step operator split approach. The equations solved for each step are summarized below. Figure 3.2 shows a graphical interpretation corresponding to each of the steps outlined in this section.

### *Lagrangian Step:*

#### *Conservation of Momentum*

$$M_{m,l}^{lag} \frac{\partial}{\partial t} (\mathbf{v}_{m,l}^{lag}) = \sum_{k=1}^{n_e} \int_{\Omega_k} (N_l \mathbf{f} - \nabla N_l \cdot \sigma_{m,k}) \phi_{m,k} dy$$

$$l = 1, 2, \dots, n_n \quad (3.113)$$

*Conservation of Energy*

$$m_{m,k}^{lag} \frac{\partial}{\partial t} e_{m,k}^{lag} = \int_{\Omega_k} [\sigma_{m,k} : \dot{\epsilon}_{m,k}] \phi_{m,k} dy$$

$$k = 1, 2, \dots, n_e \quad (3.114)$$

*Remap Step:*

*Conservation of Mass*

$$\frac{\partial}{\partial t} m_{m,k}^{remap} + \int_{\Gamma_k} \rho_{m,k}^{lag} \left( \sum_{j=1}^{n_n} N_j \mathbf{c}_{m,j} \right) \cdot \mathbf{n} \phi_{m,k} ds = 0$$

$$k = 1, 2, \dots, n_e \quad (3.115)$$

*Conservation of Momentum*

$$m_{m,k}^{remap} \frac{\partial}{\partial t} \left( \sum_{j=1}^{n_n} N_j \mathbf{v}_{m,j}^{remap} \right) + \int_{\Gamma_k} \left( \sum_{j=1}^{n_n} N_j \mathbf{v}_{m,j}^{lag} \right) \rho_{m,k} \left( \sum_{i=1}^{n_n} N_i \mathbf{c}_{m,i} \right) \cdot \mathbf{n} \phi_{m,k} ds = 0$$

$$k = 1, 2, \dots, n_e \quad (3.116)$$

*Conservation of Energy*

$$m_{m,k}^{remap} \frac{\partial}{\partial t} (e_{m,k}^{remap}) + \int_{\Gamma_k} \rho_{m,k} e_{m,k}^{lag} \left( \sum_{j=1}^{n_n} N_j \mathbf{c}_{m,j} \right) \cdot \mathbf{n} \phi_{m,k} ds = 0$$

$$k = 1, 2, \dots, n_e \quad (3.117)$$

*Contact Enforcement Step:*

*Conservation of Momentum*

$$M_{m,l}^{ce} \frac{\partial}{\partial t} (\mathbf{v}_{m,l}^{ce}) = \sum_{k=1}^{n_e} \int_{\Gamma_k} N_l \mathbf{t} ds$$

$$l = 1, 2, \dots, n_n \quad (3.118)$$

*Conservation of Energy*

$$m_{m,k}^{ce} \frac{\partial}{\partial t} e_{m,k}^{ce} = 0$$

$$k = 1, 2, \dots, n_e \quad (3.119)$$

*Contact Remap Step:*

*Conservation of Mass*

$$\frac{\partial}{\partial t} m_{m,k}^{ce \text{ remap}} + \int_{\Gamma_k} \rho_{m,k}^{ce} \left( \sum_{j=1}^{n_n} N_j \mathbf{c}_{m,j}^{ce} \right) \cdot \mathbf{n} \phi_{m,k} ds = 0$$

$$k = 1, 2, \dots, n_e \quad (3.120)$$

*Conservation of Momentum*

$$m_{m,k}^{ce \text{ remap}} \frac{\partial}{\partial t} \left( \sum_{j=1}^{n_n} N_j \mathbf{v}_{m,j}^{ce \text{ remap}} \right) + \int_{\Gamma_k} \left( \sum_{j=1}^{n_n} N_j \mathbf{v}_{m,j}^{ce} \right) \rho_{m,k} \left( \sum_{j=1}^{n_n} N_j \mathbf{c}_{m,j}^{ce} \right) \cdot \mathbf{n} \phi_{m,k} ds = 0$$

$$k = 1, 2, \dots, n_e \quad (3.121)$$

*Conservation of Energy*

$$m_{m,k}^{ce\ remap} \frac{\partial}{\partial t} (e_{m,k}^{ce\ remap}) + \int_{\Gamma_k} \rho_{m,k} e_{m,k}^{ce} \left( \sum_{j=1}^{n_n} N_j \mathbf{c}_{m,j}^{ce} \right) \cdot \mathbf{n} \phi_{m,k} ds = 0$$

$$k = 1, 2, \dots, n_e \quad (3.122)$$

These equations can be used along with the problem specific equations of state and constitutive laws, which give the pressure and deviatoric stress terms, to solve for the density  $\rho$ , components of the velocity  $\mathbf{v}$ , and specific internal energy  $e$  for each body  $\Omega_m$ .

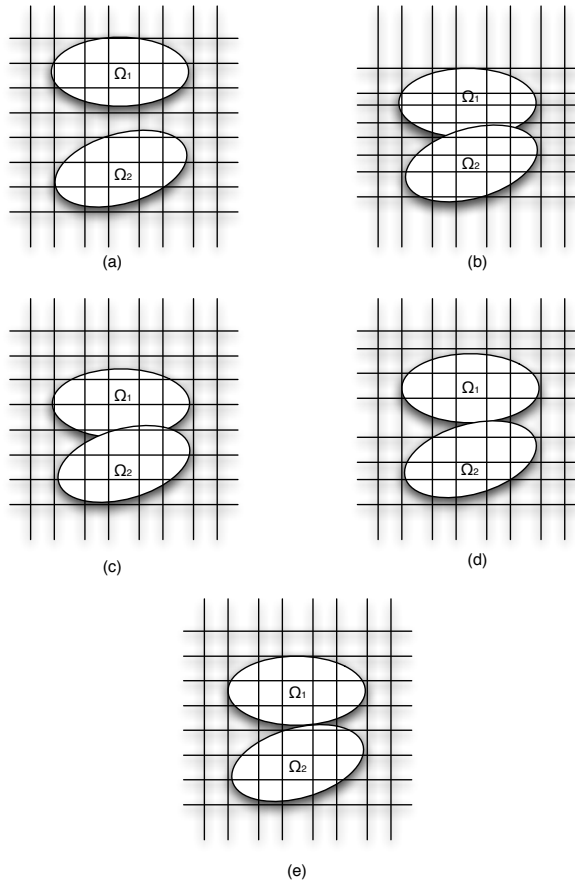


**Figure 3.2:** The multi-material contact process implemented in this work: This consists of four steps comprised of two operator splits. Following the initial condition (a) the materials move along with the mesh and the solution is advanced in time, this is the Lagrangian step (b). This is followed by the advection or remap step (c) in which the mesh is restored to its original configuration. The contact constraints are then imposed in (d) followed by a second remap step (e). Steps (d) and (e) are unique to this work.

### The Contact Enforcement Model

When contact between two bodies  $\Omega_a$  and  $\Omega_b$  occurs a traction must be imposed along the interface boundary  $\Gamma_c$ . In order for the tractions to be implemented correctly several contact constraints must be enforced. In the Signorini form, these constraints are:

*The No-Penetration Constraint*

$$(\mathbf{x}_a - \mathbf{x}_b) \cdot \mathbf{n}_j \geq 0 \quad (3.123)$$

*The traction must be compressive or zero*

$$\mathbf{t} \cdot \mathbf{n}_a \leq 0 \quad (3.124)$$

*And the product of the first two conditions must be zero*

$$(\mathbf{t} \cdot \mathbf{n}_a) (\mathbf{x}_a - \mathbf{x}_b) \cdot \mathbf{n}_b = 0 \quad (3.125)$$

In these constraints,  $\mathbf{x}_a$  and  $\mathbf{x}_b$  are the points along the interface boundary for each body  $\Omega_a$  and  $\Omega_b$ , and  $\mathbf{n}_a$  and  $\mathbf{n}_b$  are the unit normal vectors on the boundaries of each domain. The first constraint specifies that two materials cannot occupy the same place at the same time. The second condition requires a compressive traction force to be present along the boundary region of interest in order for the traction to be applied. The final condition dictates that the product of the first two conditions is always zero, or in other words,  $\Omega_a$  and  $\Omega_b$  do not have the same unit normal vectors.

These inequality constraints must be satisfied everywhere along the material interface boundary  $\Gamma_c$ . Since Eulerian and ALE formulations implicitly prescribe the relative locality of materials, a check for satisfaction of Equation 3.123 is

straightforward. A volume-based interpretation of Equation 3.123 can be inferred at a node  $l$  by the relation:

$$\sum_{k=1}^{n_e^l} \max \left[ \left( \sum_{m=1}^{n_m} \phi_{m,k} \right) - 1, 0 \right] = 0 \quad (3.126)$$

where  $n_e^l$  is the number of attached elements,  $n_m$  is the number of materials, and  $\phi_{m,k}$  is the volume fraction of material  $m$  in element  $k$ . For this constraint to hold the sum of the volume fractions in all elements attached to node  $l$  must be less than or equal to one.

Arbitrarily, one material can be selected as the master and one as the slave corresponding to the subscripts  $a$  and  $b$  in Equation 3.123. Due to the discrete approximation of the relative locality of these materials, the outward normals on the slave and master surfaces may not be equal and opposite. Likewise, the tractions on these surfaces may not be compressive. Enforcement of the contact constraints leads to velocity updates as governed by the contact enforcement steps in Equations 3.118 to 3.122.

The formulation presented in this work allows for forces to accumulate along surfaces which were originally free and then come into contact during the problem evolution. The numerical approximation that incorporates the accumulation of these surface forces is the second operator split which is needed to preserve conservation of mass, momentum, and energy. For example, the momentum equation for the second operator split is given by:

$$\int_V \left[ w\rho \frac{\partial \mathbf{v}}{\partial t} - \nabla w \cdot (\rho \mathbf{v} \mathbf{c}) \right] dy + \int_{\Gamma} w \mathbf{c} \rho \mathbf{v} \cdot \mathbf{n} ds = \int_{\Gamma} w \mathbf{t} ds \quad (3.127)$$

The traction  $\mathbf{t}$  is zero except when contact occurs.

Performing a second operator split on Equation 3.127, as described previously, results in the finite element formulation developed in the previous section where the contact enforcement step is:

$$M_{m,l}^{ce} \frac{\partial}{\partial t} (\mathbf{v}_{m,l}^{ce}) = \sum_{k=1}^{n_e} \int_{\Gamma_k} N_l \mathbf{t} ds$$

$$l = 1, 2, \dots, n_n \quad (3.128)$$

The finite element formulation for the contact remap step is given by:

$$m_{m,k}^{ce \text{ remap}} \left( \sum_{j=1}^{n_n} N_j \frac{\partial}{\partial t} \mathbf{v}_{m,j}^{ce \text{ remap}} \right) + \int_{\Gamma_k} \left( \sum_{j=1}^{n_n} N_j \mathbf{v}_{m,j}^{ce} \right) \rho_{m,k} \left( \sum_{j=1}^{n_n} N_j \mathbf{c}_{m,j}^{ce} \right) \cdot \mathbf{n} \phi_{m,k} ds = 0$$

$$k = 1, 2, \dots, n_e \quad (3.129)$$

In the first Lagrangian step we solved for each material separately without allowing them to interact, i.e.  $\mathbf{t} = 0$ . A geometric interpretation of this interaction is two distorted elements which are remapped and then might contain overlapping volumes. If the contact is frictionless, then tractions accumulate only in a direction normal to the contacting surfaces. Thus, Equation 3.128 only needs to be cast in a direction normal to the contacting surface. This requires:

$$M_{a,l}^{ce} \Delta v_{a,l}^n = -\Delta t \sum_{k=1}^{n_e} \int_{A_{a,k}} \sum_{j=1}^{n_n} N_j t_{a,k}^n ds$$

$$l = 1, 2, \dots, n_n \quad (3.130a)$$

$$M_{b,l}^{ce} \Delta v_{b,l}^n = \Delta t \sum_{k=1}^{n_e^l} \int_{A_{b,k}} \sum_{j=1}^{n_n} N_j t_{b,k}^n ds$$

$$l = 1, 2, \dots, n_n \quad (3.130b)$$

where the subscripts  $a$  and  $b$  are now being used to denote the master and slave materials respectively, the superscript  $n$  refers to the normal direction,  $t_{(a,b),k}^n$  are the tractions resulting from contact, and  $N_j$  is the shape function at node  $j$  attached to element  $k$  which is attached to the node of interest  $l$ . The  $\Delta t$  term is the timestep and the  $\Delta v_{a,l}^n$  and  $\Delta v_{b,l}^n$  terms are the velocity change due to contact defined by:

$$\Delta v_{(a,b),l}^n = v_{(a,b),l}^{n,ce} - v_{(a,b),l}^{n,remap} \quad (3.131)$$

where  $v_{(a,b),l}^{n,remap}$  is the material specific nodal velocity from the first operator split and  $v_{(a,b),l}^{n,ce}$  is the material specific nodal velocity at the end of the contact enforcement step. The negative sign in Equation 3.130a results from the normal being assigned to the direction associated with the master surface.

Newton's third law requires the tractions applied at the contacting interface to be equal and opposite, so the right-hand sides of Equations 3.130 (a) and (b) must be equal and opposite as well. This results in a momentum balance given by:

$$M_{a,l}^{ce} \Delta v_{a,l}^n + M_{b,l}^{ce} \Delta v_{b,l}^n = 0 \quad (3.132)$$

Equations 3.126, 3.130, and 3.132 must now be satisfied to conserve momentum while at the same time satisfying the constraints in Equations 3.123 to 3.125. A volume-based interpretation of Equation 3.123 yields an expression for the volume that must be removed from an element given by:



$$V_{e,k} = \max \left[ \left( \left( \sum_{m=1}^{n_m} \phi_{m,k} \right) - 1 \right) \cdot V_{0,k}, 0 \right] \quad (3.133)$$

where  $V_{0,k}$  is the remapped volume of element  $k$ . It is important to note here that  $V_{e,k}$  only has a non-zero value when an overlap exists, resulting in the element being overfilled.

For a given node  $l$  the total volume that must be removed from elements attached to node  $l$  is thus:

$$V_e^t = \sum_{k=1}^{n_e^l} V_{e,k} \quad (3.134)$$

where  $V_e^t$  is the total excess volume for all elements attached to node  $l$ .

To satisfy Equation 3.123, the excess volume given in Equation 3.134 needs to be moved to the surrounding elements. This comes from determining the distance that the interface surface, which has an area denoted as  $A_{(a,b),jk}^w$ , must be moved in order to align with other material interface during the timestep. The volume fraction of each material that needs to be moved is given by:

$$V_{e,a}^t = \sum_{k=1}^{n_e^l} \int_{A_{a,k}} \Delta v^n \Delta t ds = \Delta t \sum_{k=1}^{n_e^l} \int \sum_{j=1}^{n_n^k} N_j \Delta v_{a,j}^n ds \quad (3.135a)$$

$$V_{e,b}^t = \sum_{k=1}^{n_e^l} \int_{A_{b,k}} \Delta v^n \Delta t ds = \Delta t \sum_{k=1}^{n_e^l} \int \sum_{j=1}^{n_n^k} N_j \Delta v_{b,j}^n ds \quad (3.135b)$$

where  $n_n^k$  is the number of nodes attached to element  $k$ . The term  $\Delta v_{(a,b),j}^n$  is specific to node  $j$ , but as a simplification we can diagonalize the right-hand side of Equations 3.135

(a) and (b) by setting  $\Delta v_{(a,b),j}^n = \Delta v_{(a,b),l}^n$ . It should be noted that this diagonalization is potentially a significant source of approximation error because in the double sum we are replacing  $\Delta v^n$  for all nodes on all elements attached to a node  $l$  by a single value.

Applying this approximation allows us to remove  $\Delta v_{(a,b),l}^n$  from the integral and we are left with the weighted area  $A_{(a,b),jk}^w$  after taking the surface integral of the shape function  $N_j$ . After these simplifications the volume of each material that needs to be moved is given by:

$$V_{e,a}^t = -\Delta v_{a,l}^n \Delta t \left( \sum_{k=1}^{n_e^l} \sum_{j=1}^{n_n^k} A_{a,jk}^w \right) \quad (3.136a)$$

$$V_{e,b}^t = \Delta v_{b,l}^n \Delta t \left( \sum_{k=1}^{n_e^l} \sum_{j=1}^{n_n^k} A_{b,jk}^w \right) \quad (3.136b)$$

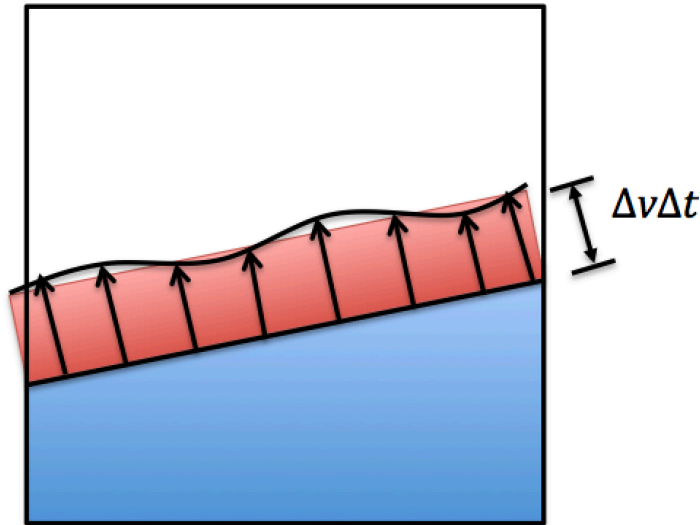


**Figure 3.3:** Representation of excess volume determination

$A_{a,jk}^w$  and  $A_{b,jk}^w$  are defined as:

$$\sum_{k=1}^{n_e^l} \sum_{j=1}^{n_n^k} A_{a,jk}^w = \sum_{k=1}^{n_e^l} \sum_{j=1}^{n_n^k} \int_{A_{a,k}} N_j ds \quad (3.137a)$$

$$\sum_{k=1}^{n_e^l} \sum_{j=1}^{n_n^k} A_{b,jk}^w = \sum_{k=1}^{n_e^l} \sum_{j=1}^{n_n^k} \int_{A_{b,k}} N_j ds \quad (3.137b)$$

where  $N_j$  is the nodal shape function for node  $j$  in element  $k$  attached to node  $l$ . The total excess volume is the sum of the material specific excess volumes, so we can rewrite  $V_e^t$  as:

$$V_e^t = \Delta t \left[ \Delta v_{b,l}^n \sum_{k=1}^{n_e^l} \sum_{j=1}^{n_n^k} A_{b,jk}^w - \Delta v_{a,l}^n \sum_{k=1}^{n_e^l} \sum_{j=1}^{n_n^k} A_{a,jk}^w \right] \quad (3.138)$$

We now have two equations for the two unknowns,  $\Delta v_{a,l}^n$  and  $\Delta v_{b,l}^n$ . From Equation 3.132 we have:

$$\Delta v_{a,l}^n = -\frac{M_{b,l}^{ce} \Delta v_{b,l}^n}{M_{a,l}^{ce}} \quad (3.139a)$$

or

$$\Delta v_{b,l}^n = -\frac{M_{a,l}^{ce} \Delta v_{a,l}^n}{M_{b,l}^{ce}} \quad (3.139b)$$

Substituting Equation 3.139a into Equation 3.138 and solving for  $\Delta v_{b,l}^n$  gives:

$$\Delta v_{b,l}^n = \frac{1}{\Delta t} \sum_{k=1}^{n_e^l} \frac{V_e^t}{\sum_{j=1}^{n_n^k} \left( A_{b,jk}^w + \frac{M_{b,l}^{ce}}{M_{a,l}^{ce}} A_{a,jk}^w \right)} \quad (3.140a)$$

Likewise, substituting Equation 3.139b into Equation 3.138 and solving for  $\Delta v_{a,l}^n$  gives:

$$\Delta v_{a,l}^n = -\frac{1}{\Delta t} \sum_{k=1}^{n_e^l} \frac{V_e^t}{\sum_{j=1}^{n_n^k} \left( \frac{M_{a,l}^{ce}}{M_{b,l}^{ce}} A_{a,jk}^w + A_{a,jk}^w \right)} \quad (3.140b)$$

The values of  $A_{a,jk}^w$  and  $A_{b,jk}^w$  are interface areas weighted by  $N_j$  for element  $k$ , and the method for determining these quantities is a geometric problem developed later in this section. At this point we have completed the contact enforcement step, so we can now proceed to the contact remap step that was developed in the previous section to conserve mass, momentum, and energy.

There are many assumptions that can be made in order to simplify Equations 3.140 (a) and (b). One method that was used in this work was assuming that the interface areas  $A_{a,jk}^w$  and  $A_{b,jk}^w$  are equal. This is done by first determining the interface area for each material, then taking the average of the two values. While this is a source of error in all cases except where the interfaces are parallel and aligned to the mesh, it results in a significant simplification. Doing so allows us to move the lumped mass terms out of the summations, resulting in Equations 3.141 (a) and (b).

$$\Delta v_{b,l}^n = \frac{M_{a,l}^{ce}}{\Delta t (M_{a,l}^{ce} + M_{b,l}^{ce})} \sum_{k=1}^{n_e^l} \frac{V_e^t}{\sum_{j=1}^{n_n^k} A_{jk}^w} \quad (3.141a)$$

$$\Delta v_{a,l}^n = -\frac{M_{b,l}^{ce}}{\Delta t(M_{a,l}^{ce} + M_{b,l}^{ce})} \sum_{k=1}^{n_e^l} \frac{V_e^t}{\sum_{j=1}^{n_n^k} A_{jk}^w} \quad (3.141b)$$

where we have set  $A_{a,jk}^w = A_{b,jk}^w = A_{jk}^w$ . Equation 3.141 can be further simplified given the definition of  $A_{jk}^w$ .

$$\sum_{k=1}^{n_e^l} \sum_{j=1}^{n_n^k} A_{jk}^w = \sum_{k=1}^{n_e^l} \int_{A_k} \left( \sum_{j=1}^{n_n^k} N_j \right) ds \quad (3.142)$$

where  $N_j$  is the shape function for a node  $j$  in element  $k$ , which is attached to the node of interest  $l$ . This can be further simplified because the sum of the shape functions for a given element are equal to one. Therefore, the right-hand side of Equation 3.142 becomes:

$$\sum_{k=1}^{n_e^l} \int_{A_k} \left( \sum_{j=1}^{n_n^k} N_j \right) ds = \sum_{k=1}^{n_e^l} A_k \quad (3.143)$$

where  $A_k$  is the average interface area for element  $k$ . The final master and slave velocities and can now be written as:

$$v_{a,l}^{n,ce} = v_{a,l}^{n,remap} - \frac{M_{b,l}^{ce} V_e^t}{\Delta t(M_{a,l}^{ce} + M_{b,l}^{ce})} \sum_{k=1}^{n_e^l} \frac{1}{A_k} \quad (3.144a)$$

$$v_{b,l}^{n,ce} = v_{b,l}^{n,remap} + \frac{M_{a,l}^{ce} V_e^t}{\Delta t(M_{a,l}^{ce} + M_{b,l}^{ce})} \sum_{k=1}^{n_e^l} \frac{1}{A_k} \quad (3.144b)$$

### Determining Interface Areas

The interface areas are determined using an approach similar to that which was used for determining the advection volume explained in the interface tracking section of this chapter. We first need to determine the normal of the contact surface in normalized coordinates as:

$$\mathbf{n} = -\frac{\nabla\phi}{|\nabla\phi|} \quad (3.145)$$

where  $\phi$  is the volume fraction of the material of interest and  $\nabla\phi$  is given by:

$$\nabla\phi = \sum_{i=1}^n \frac{\partial\phi}{\partial x_i} \hat{e}_i \quad (3.146)$$

Once the components of the normal vector are known we can then determine the shape of the plane intersecting the unit cube. To do this we need to determine the corner distance,  $d$ , using the method described in the interface tracking section of this chapter and we can then determine the  $h_i$  values from:

$$\mathcal{H}_i = \frac{d}{n_i} \quad (3.147)$$

where here  $i$  is the direction of the component of the normal vector. Once the  $\mathcal{H}_i$  values have been determined, we can then convert back to the local coordinate system and

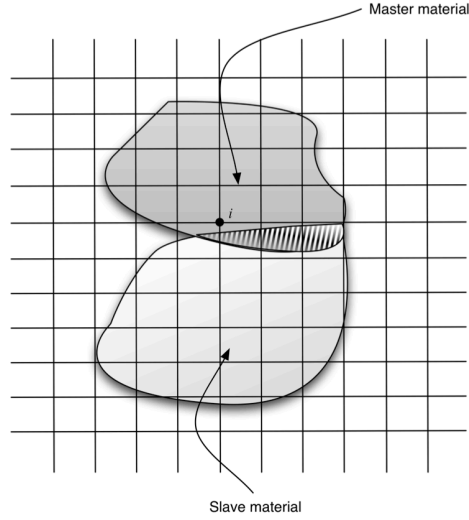


**Figure 3.4:** Schematic of choice for master and slave materials

determine values of  $h_i$  in the global coordinate space. We can then determine the area of the large blue triangles in Figure 3.5 defined by points  $H_1 = (h_1, 0, 0)$ ,  $H_2 = (0, h_2, 0)$ , and  $H_3 = (0, 0, h_3)$ , by taking the cross product of two vectors making up two sides of the triangle. All area calculations are performed on a unit cube. The normalized interface area,  $\check{A}$ , is given by:

$$\check{A} = \frac{|\overline{H_2 H_1} \times \overline{H_3 H_1}|}{2} \quad (3.148)$$

Solving this gives:

$$\check{A} = \frac{\sqrt{(h_2 h_3)^2 + (h_1 h_3)^2 + (h_1 h_2)^2}}{2} \quad (3.149)$$

where the  $\check{\sim}$  symbol denotes a normalized quantity determined for the unit cube.

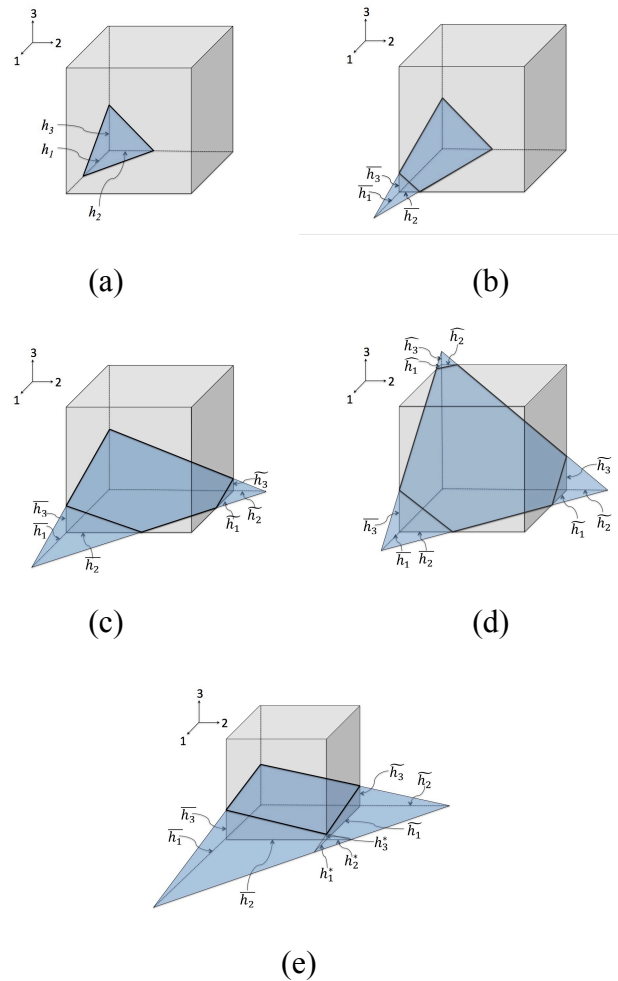


**Figure 3.5:** Five possible intersection conditions for the unit cube. (a) Triangular Intersection, (b) Quadrilateral Intersection A, (c) Pentagonal Intersection, (d) Hexagonal Intersection, and (e) Quadrilateral Intersection B

This gives the area for the triangular section of the plane intersecting the element. If all of the values of  $h_i$  fall within the element then we have the equation for area of the triangular intersection condition. If the  $h_i$  values are greater than the length of the side of the element in any direction then we have one of the four remaining intersection conditions shown in Figure 3.5. The number of possible intersection conditions is reduced to the five shown in Figure 3.5 by applying three restrictions. First, all calculations are performed on a unit cube. Second, if the total volume fraction is greater



than  $\frac{1}{2}$  then the area is calculated based on the values of  $1-\phi$  (i.e. the other material).

Finally, the interface is determined with respect to a specific corner of the unit cube and at a specific orientation with the components of the normal vector,  $\mathbf{n}$ , being ordered from smallest to largest and then appropriate axis sign changes are applied.

The areas for each of these intersection conditions can be found by finding the total area of the intersecting triangle and subtracting the areas of the triangles that fall outside the element. Following this procedure for each intersection condition we get:

*Triangular Intersection Condition*

$$\check{A} = \frac{\sqrt{(h_2 h_3)^2 + (h_1 h_3)^2 + (h_1 h_2)^2}}{2} \quad (3.150)$$

which occurs when

$$n_1^3 > 6\phi n_1 n_2 n_3 \quad (3.151)$$

*Quadrilateral Intersection Condition A*

$$\check{A} = \frac{\sqrt{(h_2 h_3)^2 + (h_1 h_3)^2 + (h_1 h_2)^2}}{2} - \frac{\sqrt{(\bar{h}_2 \bar{h}_3)^2 + (\bar{h}_1 \bar{h}_3)^2 + (\bar{h}_1 \bar{h}_2)^2}}{2} \quad (3.152)$$

which occurs when

$$n_1^3 \leq 6\phi n_1 n_2 n_3 < 3n_1 n_2^2 - 3n_1^2 n_2 + n_1^3 = n_2^3 - (n_2 - n_1)^3 \quad (3.153)$$

*Pentagonal Intersection Condition*

$$\check{A} = \frac{\sqrt{(h_2 h_3)^2 + (h_1 h_3)^2 + (h_1 h_2)^2}}{2} - \frac{\sqrt{(\bar{h}_2 \bar{h}_3)^2 + (\bar{h}_1 \bar{h}_3)^2 + (\bar{h}_1 \bar{h}_2)^2}}{2} - \frac{\sqrt{(\tilde{h}_2 \tilde{h}_3)^2 + (\tilde{h}_1 \tilde{h}_3)^2 + (\tilde{h}_1 \tilde{h}_2)^2}}{2} \quad (3.154)$$

which occurs when either

$$n_2^3 - (n_2 - n_1)^3 \leq 6\phi n_1 n_2 n_3 < n_3^3 - (n_3 - n_1)^3 - (n_3 - n_2)^3 \quad (3.155)$$

$$\text{and } n_1 + n_2 > n_3$$

or

$$n_2^3 - (n_2 - n_1)^3 \leq 6\phi n_1 n_2 n_3 < (n_1 + n_2)^3 - n_2^3 - n_1^3 \text{ and } n_1 + n_2 \leq n_3 \quad (3.156)$$

*Hexagonal Intersection Condition*

$$\check{A} = \frac{\sqrt{(h_2 h_3)^2 + (h_1 h_3)^2 + (h_1 h_2)^2}}{2} - \frac{\sqrt{(\bar{h}_2 \bar{h}_3)^2 + (\bar{h}_1 \bar{h}_3)^2 + (\bar{h}_1 \bar{h}_2)^2}}{2} - \frac{\sqrt{(\tilde{h}_2 \tilde{h}_3)^2 + (\tilde{h}_1 \tilde{h}_3)^2 + (\tilde{h}_1 \tilde{h}_2)^2}}{2} - \frac{\sqrt{(\hat{h}_2 \hat{h}_3)^2 + (\hat{h}_1 \hat{h}_3)^2 + (\hat{h}_1 \hat{h}_2)^2}}{2} \quad (3.157)$$

which occurs when

$$n_3^3 - (n_3 - n_1)^3 - (n_3 - n_2)^3 \leq 6\phi n_1 n_2 n_3 \text{ for } n_1 + n_2 > n_3 \quad (3.158)$$

*Quadrilateral Intersection Condition B*

$$\check{A} = \frac{\sqrt{(h_2 h_3)^2 + (h_1 h_3)^2 + (h_1 h_2)^2}}{2} - \frac{\sqrt{(\bar{h}_2 \bar{h}_3)^2 + (\bar{h}_1 \bar{h}_3)^2 + (\bar{h}_1 \bar{h}_2)^2}}{2} - \frac{\sqrt{(\tilde{h}_2 \tilde{h}_3)^2 + (\tilde{h}_1 \tilde{h}_3)^2 + (\tilde{h}_1 \tilde{h}_2)^2}}{2} + \frac{\sqrt{(h_2^* h_3^*)^2 + (h_1^* h_3^*)^2 + (h_1^* h_2^*)^2}}{2} \quad (3.159)$$

which occurs when

$$(n_2 + n_1)^3 - n_2^3 - n_1^3 \leq 6\phi n_1 n_2 n_3 \text{ for } n_1 + n_2 \leq n_3 \quad (3.160)$$

For uniform meshes the physical area  $A$  is then determined from the normalized area as

$A = (\Delta x)^2 \check{A}$ , where  $\Delta x$  is the element edge length.

Since the method for determining the contact velocities only requires the interface areas, and not the volume weighted components of the area the  $\check{A}^w$  values are not necessary, however, they are required for other derivations of the contact method that do not assume equal interface areas for both materials. While this work has not explored these methods for determining the contact velocity updates, the  $\check{A}^w$  equations are presented in the remainder of this section for completeness.

The weighted area,  $\check{A}^w$ , is given by:

$$\check{A}^w = \sum_{k=1}^{n_e^l} \sum_{j=1}^{n_n^k} \int_{A_k} N_{jk} ds \quad (3.161)$$

where  $N_{jk}$  is the nodal shape function at node  $j$  for element  $k$  attached the node of interest, which is given in three dimensional natural coordinates as

$$N_{jk} = \frac{1}{8}(1 + \xi\xi_i)(1 + \eta\eta_i)(1 + \mu\mu_i) \quad (3.162)$$

Writing the equation for the surface we get

$$f(\xi, \eta) = \mu = \frac{1}{n_z}(d - n_x\xi - n_y\eta) \quad (3.163)$$

We can then solve the equation for  $\check{A}^w$  by evaluating the surface integral

$$\check{A}^w = \iint_{\xi, \eta} N_{jk}(\xi, \eta, f(\xi, \eta)) \cdot \left[ 1 + \left( \frac{\partial f}{\partial \xi} \right)^2 + \left( \frac{\partial f}{\partial \eta} \right)^2 \right]^{\frac{1}{2}} d\xi d\eta \quad (3.164)$$

But,

$$1 + \left( \frac{\partial f}{\partial \xi} \right)^2 + \left( \frac{\partial f}{\partial \eta} \right)^2 = 1 + \left( \frac{n_x}{n_z} \right)^2 + \left( \frac{n_y}{n_z} \right)^2 \quad (3.165)$$

Since  $d$ ,  $n_x$ ,  $n_y$ , and  $n_z$  are all expressed in terms of the normalized coordinate system, in other words the limits the cell of interest are  $(0, 0, 0)$  to  $(1, 1, 1)$ , we must move the origin and convert the shape functions from the natural coordinate system. Converting the shape function to the normalized coordinate system gives:

$$N_{jk} = (1 - \xi_i - (1 - 2\xi_i)\xi)(1 - \eta_i - (1 - 2\eta_i)\eta)(1 - \mu_i - (1 - 2\mu_i)\mu) \quad (3.166)$$

Replacing  $\mu$  with  $f(\xi, \eta)$  from above, the equation for  $N_{jk}$  becomes

$$N_{jk} = (1 - \xi_i - (1 - 2\xi_i)\xi)(1 - \eta_i - (1 - 2\eta_i)\eta) \cdot \left( 1 - \mu_i - \frac{(1 - 2\mu_i)}{n_z}(d - n_x\xi - n_y\eta) \right) \quad (3.167)$$

So the surface integral we need to solve becomes

$$\begin{aligned} \check{A}^w &= (1 - \xi_i - (1 - 2\xi_i)\xi)(1 - \eta_i - (1 - 2\eta_i)\eta) \cdot \\ &\iint_{\xi, \eta} \left( 1 - \mu_i - \frac{(1 - 2\mu_i)}{n_z} (d - n_x \xi - n_y \eta) \right) \cdot \left[ 1 + \left( \frac{n_x}{n_z} \right)^2 + \left( \frac{n_y}{n_z} \right)^2 \right]^{\frac{1}{2}} d\eta d\xi \end{aligned} \quad (3.168)$$

where here  $\xi_i$ ,  $\eta_i$ , and  $\mu_i$  are the natural coordinates and the domain of the surface integral depends of the shape of the intersection projected into the  $\xi$ - $\eta$  plane as shown in Figure 3.6.

The domains for each of the five intersection conditions are given by:

*Triangular Intersection Condition*

$$\check{A}^w = \int_0^{\xi_b} \int_0^{\eta_a \left(1 - \frac{\xi}{\xi_b}\right)} F d\eta d\xi \quad (3.169)$$

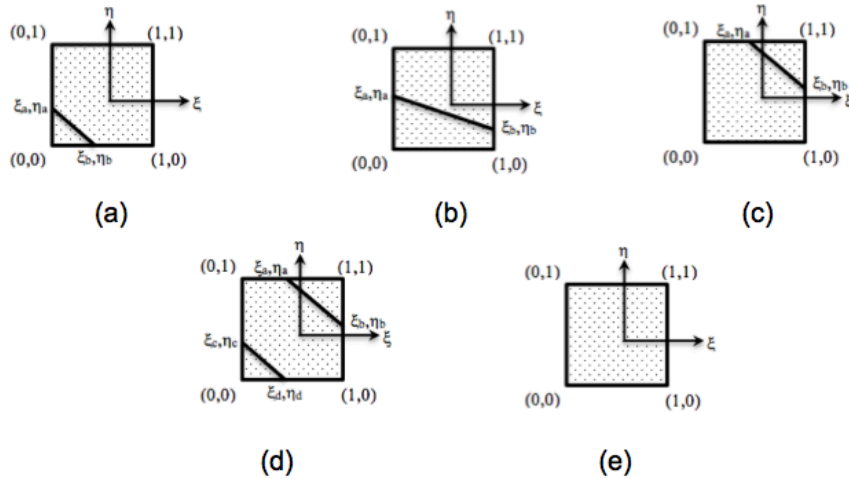


**Figure 3.6:** Projections of the five intersection conditions into the  $\xi$ - $\eta$  plane. (a) Triangular Intersection, (b) Quadrilateral Intersection A, (c) Pentagonal Intersection, (d) Hexagonal Intersection, and (e) Quadrilateral Intersection B

*Quadrilateral Intersection Condition A*

$$\check{A}^w = \int_0^1 \int_0^{\eta_a + \xi(\eta_b - \eta_a)} F d\eta d\xi \quad (3.170)$$

*Pentagonal Intersection Condition*

$$\check{A}^w = \int_0^{\xi_a} \int_0^1 F d\eta d\xi + \int_{\xi_a}^1 \int_0^{1 + \frac{(\eta_b - 1)(\xi - \xi_a)}{1 - \xi_a}} F d\eta d\xi \quad (3.171)$$

*Hexagonal Intersection Condition*

$$\check{A}^w = \int_0^{\xi_a} \int_0^1 F d\eta d\xi + \int_{\xi_a}^1 \int_0^{1 + \frac{(\eta_b - 1)(\xi - \xi_a)}{1 - \xi_a}} F d\eta d\xi - \int_0^{\xi_b} \int_0^{\eta_a \left(1 - \frac{\xi}{\xi_b}\right)} F d\eta d\xi \quad (3.172)$$

*Quadrilateral Intersection Condition B*

$$\check{A}^w = \int_0^1 \int_0^1 F d\eta d\xi \quad (3.173)$$

where  $F$  is given by

$$F = (1 - \xi_i - (1 - 2\xi_i)\xi)(1 - \eta_i - (1 - 2\eta_i)\eta) \cdot \left(1 - \mu_i - \frac{(1 - 2\mu_i)}{n_z}(d - n_x\xi - n_y\eta)\right) \cdot \left[1 + \left(\frac{n_x}{n_z}\right)^2 + \left(\frac{n_y}{n_z}\right)^2\right]^{\frac{1}{2}} \quad (3.174)$$

For uniform meshes the physical weighted area  $A^w$  is then determined from the normalized weighted area as  $A^w = (\Delta x)^2 \check{A}^w$ , where  $\Delta x$  is the length of an element edge.

## Interface Tracking Formulations

The interface tracking algorithm is an important part of the advection step in Eulerian and ALE hydrocodes. This algorithm defines the contents of the advection volume and is used to ensure that the correct material volumes are exchanged between adjacent cells during the advection step. The material contents of each element must be found for the solution to the conservation equations, and thus interface tracking is useful for determining the amounts of each material within an element.

There are several algorithms that can be used for interface tracking. One such algorithm is the SLIC algorithm. The SLIC algorithm assumes that interfaces are aligned parallel to the mesh contours, as is shown in Figure 3.7 (c). In multi-dimensional problems in which the material is moving in an off-grid direction, or in problems with material geometries that are not aligned with the grid, this algorithm often results in advection errors that distort the material interface artificially. This is because it is possible for the incorrect material volumes to get transported between cells. Therefore, the SLIC algorithm is only correct in cases with one-dimensional velocity fields and geometries with interfaces aligned with the mesh and should be used with caution.

Youngs' algorithm [100] provides a much better representation of interface planes than the SLIC algorithm because it assumes that interface planes are inclined at an arbitrary angle with respect to the mesh contours, as can be seen in Figure 3.7 (d). Because it represents interface boundaries much more accurately, Youngs' method results in significantly reduced artificial distortion. However, since Youngs' algorithm is piecewise linear or planar in nature it is unable to accurately resolve sharp features within an element such as corners. Furthermore, no enforcement takes place to ensure that

interfaces align at mesh boundaries, resulting in discontinuities at the faces of the elements. These limitations affect the accuracy of the interface reconstruction, but are a significant improvement over SLIC.

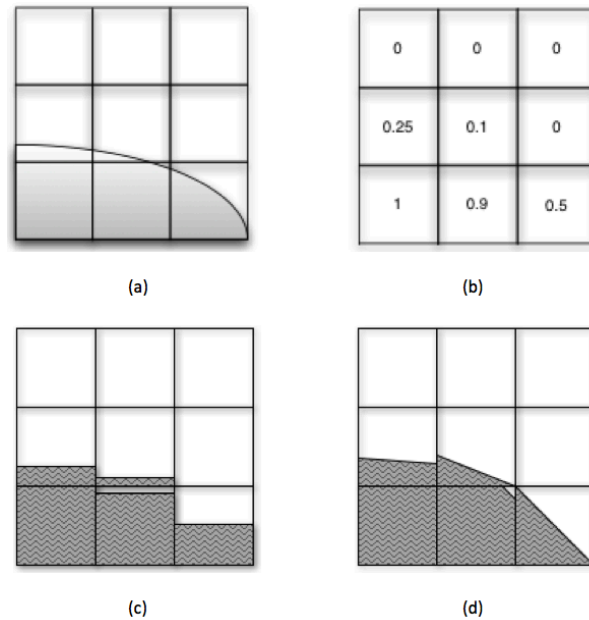


**Figure 3.7:** Interface tracking methods. Interface tracking represent a material interface shown in (a) by storing appropriate volume fractions as seen in (b). An approximation to the interface can be constructed using the SLIC algorithm (c), or Youngs' method (d).

The interface tracking method implemented in ALEAS is a modified version of Youngs' method. In the approach taken here no material ordering algorithm is required, as would be the case with a traditional Eulerian or ALE formulation that makes use of mixture theory and is described in [7] and [65]. Instead, the interface tracking routine is run for each material separately and the interface is determined between the volume fraction of the material of interest and the volume fraction of the cell not occupied by that material. Since the interface tracking routine used for the contact formulation does not account for interaction of materials it is possible that multiple materials will overlap and



result in an element being overfilled. This is corrected through the use of the contact formulation developed in the previous section, which moves the material and aligns the interfaces. The form of the interface tracking algorithm implemented here allows the advected quantities to be determined directly once the advection volumes exchanged between adjacent elements are determined. However, one complication that arises from this is that the advection volumes can have an arbitrary shape or even become disjoint since each material has its own velocity field. In this work the shape of the advection volume is determined through interface tracking, whereas in single velocity field formulations interface tracking is used to determine the contents of an advection volume whose shape is known. In the following sections the interface tracking algorithms have been developed in two- and three-dimensions. It is worth noting that the two-dimensional equations are used in three-dimensions when the minimum component of the reoriented normal vector, denoted as  $n_l$  in the three-dimensional equations, is equal to zero.

### Interface Tracking in Two Dimensions

The interface tracking scheme implemented in ALEAS is a modified version of Young's method [100]. The basic strategy is to first determine the outward unit normal vector  $\mathbf{n}$  separating the material of interest from other materials, and the distance  $d$  from the interface plane to a reference corner, measured along the direction parallel to  $\mathbf{n}$ . If there are only two materials in the cell and the interface plane is assumed to be planar, these two quantities uniquely define the location of the interface plane. Based on these values, the volume fraction of material-specific volumes in the advection volume can then be determined.

The first step in this method is to determine the direction of  $\mathbf{n}$ . This is done by normalizing the direction for the maximum rate of change of the volume fraction as described in the equation below:

$$\mathbf{n} = -\frac{\nabla\phi}{|\nabla\phi|} \quad (3.175)$$

where  $\phi$  is the volume fraction of the material of interest and  $\nabla\phi$  is given by:

$$\nabla\phi = \sum_{i=1}^n \frac{\partial\phi}{\partial x_i} \hat{e}_i \quad (3.176)$$

where  $\hat{e}_i$  is the unit vector. In order to find  $\nabla\phi$  we must use a symmetric difference approach, where we can define  $\phi_e$  and  $\phi_w$  in terms of their Taylor series approximations:

$$\phi_e = \phi(x + \Delta x) = \phi(x) + \phi'(x)\Delta x + \frac{\phi''(x)(\Delta x)^2}{2!} + \dots \quad (3.177a)$$

$$\phi_w = \phi(x - \Delta x) = \phi(x) - \phi'(x)\Delta x + \frac{\phi''(x)(\Delta x)^2}{2!} - \dots \quad (3.177b)$$

The symmetric difference for  $\partial\phi/\partial x$  can then be expressed as:

$$\phi'(x) = \frac{\partial\phi}{\partial x} = \frac{\phi_e - \phi_w}{2\Delta x} \quad (3.178)$$

The approximations for  $\phi_e$  and  $\phi_w$  are formed from the unit cell linear interpolation of values for the total material volume, that is the cell volume multiplied by the volume fraction, for each edge of the cell of interest parallel to the defined axis, and evaluated at the center of the cell. To further illustrate this in two-dimensions consider a cell and its eight neighboring cells shown Figure 3.8.

The symmetric difference approximation for  $\partial\phi/\partial x$  in cell 5 can be expressed as is shown in the equation above, where  $\phi_e$  can be calculated as follows:

$$\Delta x_2(\Delta y_2\phi_9 + 2\Delta y\phi_6 + \Delta y_1\phi_3) = \Delta x_2(\Delta y_2 + 2\Delta y + \Delta y_1)\phi_e \quad (3.179)$$

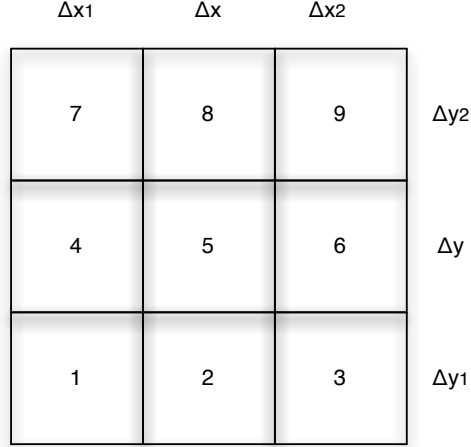


**Figure 3.8:** Schematic of a central cell (cell 5) and its 8 surrounding cells.

Normalizing with respect to  $\Delta y$  gives:

$$\frac{\Delta y_2}{\Delta y}\phi_9 + 2\phi_6 + \frac{\Delta y_1}{\Delta y}\phi_3 = \left(\frac{\Delta y_2}{\Delta y} + 2 + \frac{\Delta y_1}{\Delta y}\right)\phi_e \quad (3.180)$$

This equation can be simplified by introducing the dimensionless parameter  $\xi_i$  which is defined as:

$$\xi_i = \frac{\Delta y_i}{\Delta y} \quad (3.181)$$

Therefore, for two-dimensional problems,  $\phi_e$  can be expressed as:

$$\phi_e = \frac{\xi_2\phi_9 + 2\phi_6 + \xi_1\phi_3}{(2 + \xi_1 + \xi_2)} \quad (3.182)$$

Following the same procedure  $\phi_w$  can also be represented as:

$$\phi_w = \frac{\xi_2\phi_7 + 2\phi_4 + \xi_1\phi_1}{(2 + \xi_1 + \xi_2)} \quad (3.183)$$

Likewise,  $\partial\phi/\partial y$  can be found using  $\phi_n$  and  $\phi_s$ , where  $\partial\phi/\partial y$  is defined as:

$$\frac{\partial\phi}{\partial y} = \frac{\phi_n - \phi_s}{2\Delta y} \quad (3.184)$$

And  $\phi_n$  and  $\phi_s$  are defined as:

$$\phi_n = \frac{\eta_1\phi_7 + 2\phi_8 + \eta_2\phi_9}{(2 + \eta_1 + \eta_2)} \quad (3.185a)$$

$$\phi_s = \frac{\eta_1\phi_1 + 2\phi_2 + \eta_2\phi_3}{(2 + \eta_1 + \eta_2)} \quad (3.185b)$$

where  $\eta_i$  is given by:

$$\eta_i = \frac{\Delta x_i}{\Delta x} \quad (3.186)$$

Once the normal vector has been defined, the interface plane can be located and the value for  $d$  can be found. In order to minimize the number of intersections that must be considered, it is useful to apply restrictions to the calculation. First, all calculations must be made with respect to the unit square. Second, for volume fractions greater than 1/2, the interface is located based on the values of  $1-\phi$ , which is the volume fraction of the other material, for the cell of interest and each of its 8 neighboring cells. Finally, the interface reconstruction is made with respect to a specific corner and orientation of the unit square. This corner and orientation is determined as follows. The absolute values of

the components of  $\mathbf{n}$  are ordered from smallest to largest. Let these values be designated as  $n_1$  and  $n_2$ . Then, the interface determination is made in the 1-2 coordinate system having directions corresponding to the direction of  $n_1$  and  $n_2$ . A series of axis sign changes and/or axis swaps will also transform the x-y coordinate system to the 1-2 coordinate system. Having applied these restrictions, we must now consider two possible intersection conditions, including the triangle and quadrilateral sections, as shown in Figure 3.9.

Depending on the relative values for  $n_1$  and  $n_2$ , only one of these two intersection conditions can be produced. From this comes the interface geometry as well as the value for  $d$ . The development of each intersection condition is described below.

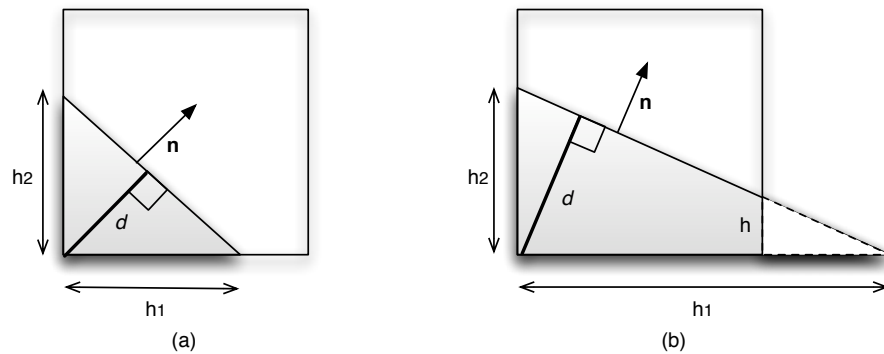


**Figure 3.9:** Possible two-dimensional intersection conditions include the triangle intersection (a) and the quadrilateral intersection (b).

### *Triangle Intersection Condition*

The volume fraction  $\phi$  is the area of the triangle, and is defined as:

$$\phi = \frac{1}{2} h_1 h_2 \quad (3.187)$$

We can then define  $h_1$  and  $h_2$  as:

$$h_i = \frac{d}{n_i} \quad (3.188)$$

where  $i=1,2$ .

This can then be solved for  $d$  as:

$$d = (2\phi n_1 n_2)^{\frac{1}{2}} \quad (3.189)$$

Since we require that  $n_1 \geq n_2$ , the triangle condition is true for  $h_1 < 1$ . At  $h_1 = 1$  we have the transition to the quadrilateral section, therefore at  $h_1 = 1$  we can solve to find the situations at which each section occurs. At  $h_1 = 1$ , we see that  $d = n_1$ , so:

$$n_1 = 2\phi n_2 \quad (3.190)$$

Therefore, the triangle intersection condition occurs for:

$$n_1 > 2\phi n_2 \quad (3.191)$$

#### *Quadrilateral Intersection Condition*

The quadrilateral intersection condition occurs when  $h_1 \geq 1$ , and therefore occurs when:

$$n_1 \leq 2\phi n_2 \quad (3.192)$$

The volume fraction of the section  $\phi$ , is defined as:

$$\phi = \frac{1}{2}(h_1 + h_2) \quad (3.193)$$

where  $h_1$  and  $h_2$  are defined as:

$$h_i = \frac{d}{n_i} \quad (3.194)$$

where  $i=1,2$ . The height  $h$ , can be found using the property of similar triangles, which yields:

$$h = \frac{h_2}{h_1}(h_1 - 1) = \frac{n_1}{n_2} \left( \frac{d}{n_1} - 1 \right) \quad (3.195)$$

Using this value for  $h$ , we can then solve for  $d$  by plugging  $h$  and  $h_1$  into the above equation for  $\phi$ . This yields:

$$d = \phi n_2 + \frac{n_1}{2} \quad (3.196)$$

### Determining Material Specific Advection Volumes in Two-Dimensions

After the components of the unit normal  $n_1$  and  $n_2$  and the perpendicular corner distance  $d$  are determined, the material-specific volume in the advection volume can be determined. In Youngs' original work, these volumes were determined directly by deriving formulas for possible intersection conditions between the material volume and advection volume. An alternative to this procedure is to recast the advection volume into a unit square using normalized coordinates. This procedure has been used in this work.

For advection in the +1 direction, the components of the normal and corner distance in the advection volume are given by:

$$\tilde{n}_1 = \frac{\varepsilon n_1}{\left[ (\varepsilon n_1)^2 + n_2^2 \right]^{\frac{1}{2}}} \quad (3.197a)$$

$$\tilde{n}_2 = \frac{n_2}{\left[ (\varepsilon n_1)^2 + n_2^2 \right]^{\frac{1}{2}}} \quad (3.197b)$$

where,

$$n_i = \frac{\bar{d}}{\bar{h}_i} \quad (3.198)$$

for  $i=1,2$ , and

$$\bar{h}_i = h_i - (1 - \varepsilon) \quad (3.199)$$

where  $\varepsilon$  is the advection dimension used to normalize the coordinate system.

It is important to note that since we require  $n_1 < n_2$ , then  $\tilde{n}_1 < \tilde{n}_2$  as well. Also, if  $\tilde{h}_1 < 0$ , then there is no intersection condition present. We can find determine the normalized advection distance  $\tilde{h}_1$  with the following relations:

$$\tilde{h}_1 = \frac{\bar{h}_1}{\varepsilon} = \frac{1}{\varepsilon} (h_1 + \varepsilon - 1) = \frac{1}{\varepsilon} \left( \frac{d}{n_1} + \varepsilon - 1 \right) \quad (3.200)$$

we can also find the value  $\tilde{h}_2$  by finding the value  $\bar{h}_2$ , which can be found using similar triangles as follows:

$$\bar{h}_2 = \frac{h_2}{h_1} \bar{h}_1 \quad (3.201)$$



Using this value we can now find  $\tilde{h}_2$ :

$$\tilde{h}_2 = \bar{h}_1 \frac{d/n_2}{d/n_1} = \bar{h}_1 \frac{n_1}{n_2} = \frac{n_1}{n_2} (h_1 + \varepsilon - 1) = \bar{h}_2 \quad (3.202)$$

Therefore,  $\tilde{h}_2 = \bar{h}_2$ , which is readily apparent from the figure above because we are only normalizing in the +1 direction, so there is no transformation taking place in the 2 direction.

Using the values for  $\tilde{h}_1$  and  $\tilde{h}_2$ , we can now find  $\tilde{d}$ , which can be written as:

$$\tilde{d} = \tilde{n}_1 \tilde{h}_1 = \tilde{n}_2 \tilde{h}_2 \quad (3.203)$$

and can be further simplified as:

$$\tilde{d} = \frac{\tilde{n}_1}{\varepsilon} (h_1 + \varepsilon - 1) \quad (3.204)$$

We can also write  $\tilde{d}$  in terms of  $d$  as:

$$\tilde{d} = n_1 \frac{\left( \frac{d}{n_1} + \varepsilon - 1 \right)}{\left[ (\varepsilon n_1)^2 + n_2^2 \right]^{\frac{1}{2}}} \quad (3.205)$$

Since we know  $\tilde{d}$ ,  $\tilde{n}_1$ , and  $\tilde{n}_2$ , we can now find the normalized volume fraction,  $\tilde{\phi}$ . For the triangular section, the normalized volume fraction can be written as:

$$\tilde{\phi} = \frac{1}{2} \tilde{h}_1 \tilde{h}_2 = \frac{1}{2} \frac{\tilde{d}^2}{\tilde{n}_1 \tilde{n}_2} \quad (3.206)$$

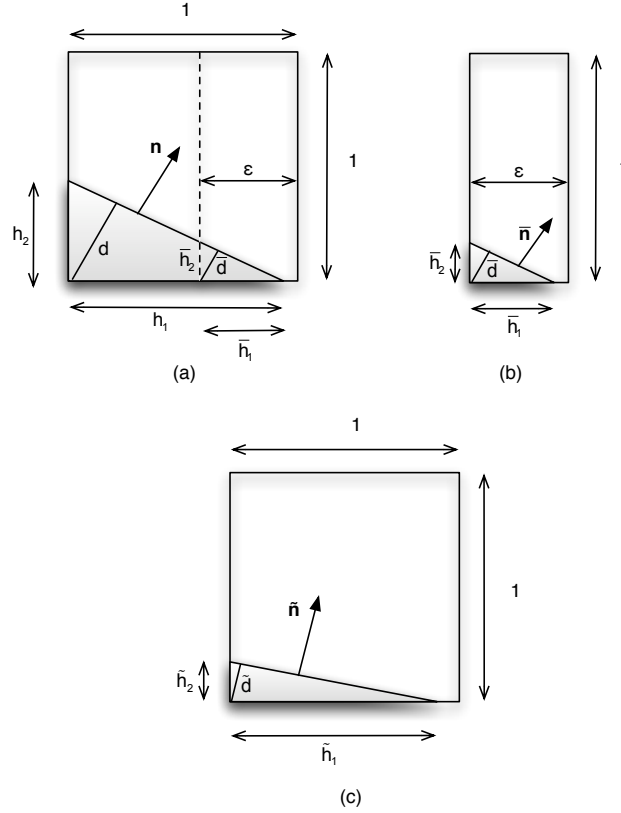


**Figure 3.10:** Illustration of the normalization process for determining the material-specific advection volume. The original unit cell containing the advection volume is shown in (a), the un-normalized advection volume is depicted in (b), and the normalized advection volume is shown in (c).

which occurs when  $\tilde{n}_1 > \tilde{d}$ . For the quadrilateral section, the normalized volume fraction is given by:

$$\tilde{\phi} = \frac{1}{2}(\tilde{h} + \tilde{h}_2) = \frac{\tilde{d}}{\tilde{n}_2} - \frac{1}{2} \frac{\tilde{n}_1}{\tilde{n}_2} \quad (3.207)$$

which occurs when  $\tilde{n}_1 \leq \tilde{d}$ . So, we can now write  $\tilde{d}$  in terms of  $\tilde{\phi}$ ,  $\tilde{n}_1$ , and  $\tilde{n}_2$ :

$$\tilde{d} = \tilde{\phi}\tilde{n}_2 + \frac{\tilde{n}_1}{2} \quad (3.208)$$

Finally, we need to transform the volume fraction from the normalized system back to the unit square. Since  $\tilde{\phi}$  is in terms of  $\tilde{n}$ , this can be done by:

$$\phi = \varepsilon \tilde{\phi} \quad (3.209)$$

### Extensions to Interface Tracking in Three-Dimensions

All of the above mentioned interface tracking equations can be extended to three-dimensions in a straightforward manner. In like manner to the two-dimensional case, the direction of the normal vector  $\mathbf{n}$  must be determined. This is done by normalizing the direction for the maximum rate of change of the volume fraction as described previously and repeated in the equation below:

$$\mathbf{n} = -\frac{\nabla\phi}{|\nabla\phi|} \quad (3.210)$$

Where  $\phi$  is the volume fraction of the material of interest and  $\nabla\phi$  is given by:

$$\nabla\phi = \sum_{i=1}^n \frac{\partial\phi}{\partial x_i} \hat{e}_i \quad (3.211)$$

Following the method presented for the two-dimensional case, the symmetric difference approximations for  $\partial\phi/\partial x$ ,  $\partial\phi/\partial y$ , and  $\partial\phi/\partial z$  can then be expressed as:

$$\frac{\partial\phi}{\partial x} = \frac{\phi_e - \phi_w}{2\Delta x} \quad (3.212a)$$

$$\frac{\partial\phi}{\partial y} = \frac{\phi_b - \phi_f}{2\Delta y} \quad (3.212b)$$

$$\frac{\partial \phi}{\partial z} = \frac{\phi_n - \phi_s}{2\Delta z} \quad (3.212c)$$

The approximations for  $\phi_e$ ,  $\phi_w$ ,  $\phi_f$ ,  $\phi_b$ ,  $\phi_n$ , and  $\phi_s$  are formed from the unit cell linear interpolation of values for the total material volume, that is the cell volume multiplied by the volume fraction, for each edge of the cell of interest parallel to the defined axis, and evaluated at the center of the cell. To further illustrate this in three-dimensions consider a cell and its 26 neighboring cells shown Figure 3.11.

Using a symmetric difference approach similar to that used in the two-dimensional case, it is possible to determine appropriate representations for  $\phi_e$ ,  $\phi_w$ ,  $\phi_f$ ,  $\phi_b$ ,  $\phi_n$ , and  $\phi_s$ . For example, it is possible to determine  $\phi_e$  by using the unit cell linear interpolation of values for the total material volume for each of the edges of cell 15 parallel to the  $x$ -axis, evaluated at the center of cell 15. Likewise, the values for the total material volume at each of these edges is determined from unit cell linear interpolation for each of the cells sharing that edge. For example, as can be seen in Figure 3.12, one of these edges is formed by cells 12, 15, 21, and 24, as denoted by A.

In order to determine  $\phi_e$ , values for  $\phi_A$ ,  $\phi_B$ ,  $\phi_C$ , and  $\phi_D$  must first be determined. The relationship between  $\phi_e$  and  $\phi_A$ ,  $\phi_B$ ,  $\phi_C$ , and  $\phi_D$  is given by:

$$\phi_e = \phi_A + \phi_B + \phi_C + \phi_D \quad (3.213)$$

The difference approximation of  $\phi_A$  can be given by

$$\begin{aligned} & (\Delta y_1 \Delta z_2 \phi_{21} + \Delta y \Delta z_2 \phi_{24} + \Delta y_1 \Delta z \phi_{12} + \Delta y \Delta z \phi_{15}) \\ & = (\Delta y_1 \Delta z_2 + \Delta y \Delta z_2 + \Delta y_1 \Delta z + \Delta y \Delta z) \phi_A \end{aligned} \quad (3.214)$$

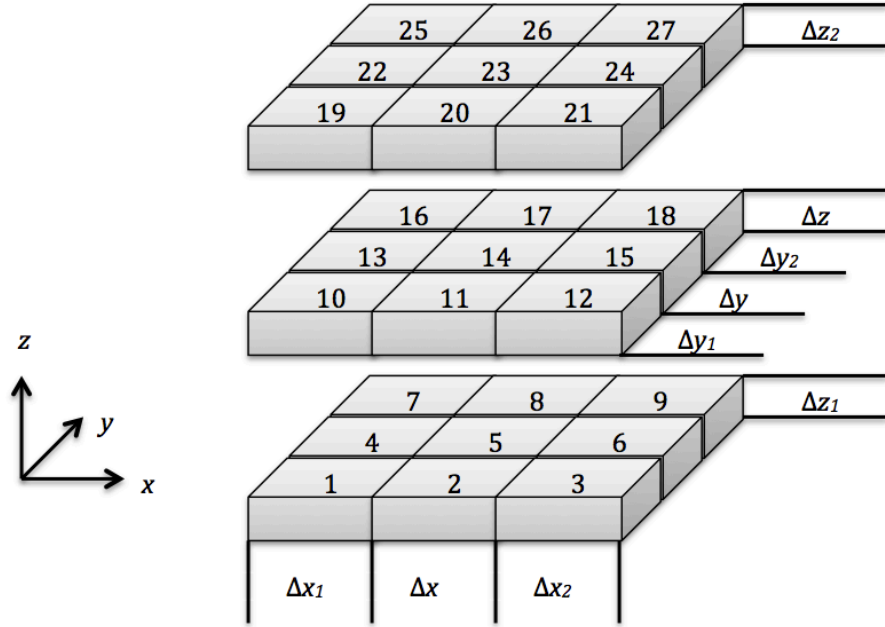


Figure 3.11: Schematic of central cell (cell 14) and its 26 neighboring cells

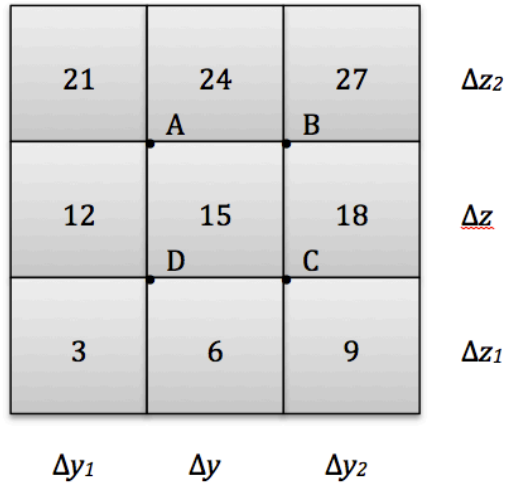


Figure 3.12: Schematic of neighboring cells used for determining  $\phi_e$  for cell 14

This approximation can be simplified by introducing the dimensionless normalization parameters  $\eta_i$ ,  $\xi_i$ , and  $\zeta_i$  which are defined as:

$$\eta_i = \frac{\Delta x_i}{\Delta x} \quad (3.215a)$$

$$\xi_i = \frac{\Delta y_i}{\Delta y} \quad (3.215b)$$

$$\zeta_i = \frac{\Delta z_i}{\Delta z} \quad (3.215c)$$

Introducing these dimensionless parameters into the difference approximation for  $\phi_A$  gives

$$(1 + \xi_1)(1 + \zeta_2)\phi_A = \xi_1\zeta_2\phi_{21} + \zeta_2\phi_{24} + \xi_1\phi_{12} + \phi_{15} \quad (3.216)$$

Likewise, for  $\phi_B$ ,  $\phi_C$ , and  $\phi_D$  the difference approximations can be given as

$$\begin{aligned} &(\Delta y\Delta z_2\phi_{24} + \Delta y_2\Delta z_2\phi_{27} + \Delta y_2\Delta z\phi_{18} + \Delta y\Delta z\phi_{15}) \\ &= (\Delta y\Delta z_2 + \Delta y_2\Delta z_2 + \Delta y_2\Delta z + \Delta y\Delta z)\phi_B \end{aligned} \quad (3.217a)$$

$$\begin{aligned} &(\Delta y\Delta z\phi_{15} + \Delta y_2\Delta z\phi_{18} + \Delta y_2\Delta z_1\phi_9 + \Delta y\Delta z_1\phi_6) \\ &= (\Delta y\Delta z + \Delta y_2\Delta z + \Delta y_2\Delta z_1 + \Delta y\Delta z_1)\phi_C \end{aligned} \quad (3.217b)$$

$$\begin{aligned} &(\Delta y_1\Delta z\phi_{12} + \Delta y\Delta z\phi_{15} + \Delta y\Delta z_1\phi_6 + \Delta y_1\Delta z_1\phi_3) \\ &= (\Delta y_1\Delta z + \Delta y\Delta z + \Delta y\Delta z_1 + \Delta y_1\Delta z_1)\phi_D \end{aligned} \quad (3.217c)$$

which can be normalized to give

$$(1 + \xi_2)(1 + \zeta_2)\phi_B = \zeta_2\phi_{24} + \xi_2\zeta_2\phi_{27} + \xi_2\phi_{18} + \phi_{15} \quad (3.218a)$$

$$(1 + \xi_2)(1 + \zeta_1)\phi_C = \phi_{15} + \xi_2\phi_{18} + \xi_2\zeta_1\phi_9 + \zeta_1\phi_6 \quad (3.218b)$$

$$(1 + \xi_1)(1 + \zeta_1)\phi_D = \xi_1\phi_{12} + \phi_{15} + \zeta_1\phi_6 + \xi_1\zeta_1\phi_3 \quad (3.218c)$$

The difference equation for  $\phi_e$  can now be written as

$$\begin{aligned} & (1 + \xi_1)(1 + \zeta_2)\phi_A + (1 + \xi_2)(1 + \zeta_2)\phi_B \\ & + (1 + \xi_2)(1 + \zeta_1)\phi_C + (1 + \xi_1)(1 + \zeta_1)\phi_D \\ & = \left[ \begin{array}{l} (1 + \xi_1)(1 + \zeta_2) + (1 + \xi_2)(1 + \zeta_2) \\ + (1 + \xi_2)(1 + \zeta_1) + (1 + \xi_1)(1 + \zeta_1) \end{array} \right] \phi_e \end{aligned} \quad (3.219)$$

Which, after gathering terms and substituting the right-hand-sides of the relations for  $\phi_A$ ,  $\phi_B$ ,  $\phi_C$ , and  $\phi_D$ , the equation for  $\phi_e$  can be written as

$$\phi_e = \frac{\zeta_1(\xi_1\phi_3 + \xi_2\phi_9) + \zeta_2(\xi_1\phi_{21} + \xi_2\phi_{27}) + 2(\xi_1\phi_{12} + \xi_2\phi_{18} + \zeta_1\phi_6 + \zeta_2\phi_{24}) + 4\phi_{15}}{(2 + \xi_1 + \xi_2)(2 + \zeta_1 + \zeta_2)} \quad (3.220)$$

The steps for determining the difference approximations for  $\phi_w$ ,  $\phi_f$ ,  $\phi_b$ ,  $\phi_n$ , and  $\phi_s$  can be easily determined following the procedure outlined above and thus are not presented here. The difference approximations for  $\phi_w$ ,  $\phi_f$ ,  $\phi_b$ ,  $\phi_n$ , and  $\phi_s$  are given by

$$\phi_w = \frac{\zeta_1(\xi_1\phi_1 + \xi_2\phi_7) + \zeta_2(\xi_1\phi_{19} + \xi_2\phi_{25}) + 2(\xi_1\phi_{10} + \xi_2\phi_{16} + \zeta_1\phi_4 + \zeta_2\phi_{22}) + 4\phi_{13}}{(2 + \xi_1 + \xi_2)(2 + \zeta_1 + \zeta_2)} \quad (3.221a)$$

$$\phi_f = \frac{\zeta_1(\eta_1\phi_1 + \eta_2\phi_3) + \zeta_2(\eta_1\phi_{19} + \eta_2\phi_{21}) + 2(\eta_1\phi_{10} + \eta_2\phi_{12} + \zeta_1\phi_2 + \zeta_2\phi_{20}) + 4\phi_{11}}{(2 + \eta_1 + \eta_2)(2 + \zeta_1 + \zeta_2)} \quad (3.221b)$$

$$\phi_b = \frac{\zeta_1(\eta_1\phi_7 + \eta_2\phi_9) + \zeta_2(\eta_1\phi_{25} + \eta_2\phi_{27}) + 2(\eta_1\phi_{16} + \eta_2\phi_{18} + \zeta_1\phi_8 + \zeta_2\phi_{26}) + 4\phi_{17}}{(2 + \eta_1 + \eta_2)(2 + \zeta_1 + \zeta_2)} \quad (3.221c)$$

$$\phi_n = \frac{\xi_1(\eta_1\phi_{19} + \eta_2\phi_{21}) + \xi_2(\eta_1\phi_{25} + \eta_2\phi_{27}) + 2(\eta_1\phi_{22} + \eta_2\phi_{24} + \xi_1\phi_{20} + \xi_2\phi_{26}) + 4\phi_{23}}{(2 + \eta_1 + \eta_2)(2 + \xi_1 + \xi_2)}$$

**(3.221d)**

$$\phi_s = \frac{\xi_1(\eta_1\phi_1 + \eta_2\phi_3) + \xi_2(\eta_1\phi_7 + \eta_2\phi_9) + 2(\eta_1\phi_4 + \eta_2\phi_6 + \xi_1\phi_2 + \xi_2\phi_8) + 4\phi_5}{(2 + \eta_1 + \eta_2)(2 + \xi_1 + \xi_2)}$$

**(3.221e)**

Once the normal vector has been defined, the interface plane can be located and the value for  $d$  can be found. In order to minimize the number of intersections that must be considered, it is useful to apply restrictions to the calculation. First, all calculations must be made with respect to the unit cube. Second, for volume fractions greater than  $\frac{1}{2}$ , the interface is located based on the values of  $1-\phi$ , which is the volume fraction of the other material, for the cell of interest and each of its 26 neighboring cells. Finally, the interface determination is made with respect to a specific corner and orientation of the unit cube. This corner and orientation is determined as follows. The absolute values of the components of  $\mathbf{n}$  are ordered from smallest to largest. Let these values be designated as  $n_1$ ,  $n_2$ , and  $n_3$ . Then, the interface determination is made in the 1-2-3 coordinate system having directions corresponding to the direction of  $n_1$ ,  $n_2$ , and  $n_3$ . A series of axis sign changes and/or axis swaps will also transform the x-y-z coordinate system to the 1-2-3 coordinate system. Having applied these restrictions, we must now consider five possible intersection conditions, including the triangle section, quadrilateral section A, pentagonal section, hexagonal section, and the quadrilateral section B.

Depending on the relative values for  $n_1$ ,  $n_2$ ,  $n_3$ , and  $\phi$  only one of these five intersection conditions can be produced. From this comes the interface geometry as well



as the value for  $d$ . The applicable ranges and development for each intersection condition is described below.

*Triangular Pyramid Intersection Condition*

The volume fraction  $\phi$  is the volume of a right triangular pyramid, shown in Figure 3.13, and is defined as:

$$\phi = \frac{1}{6}(h_1 h_2 h_3) \quad (3.222)$$

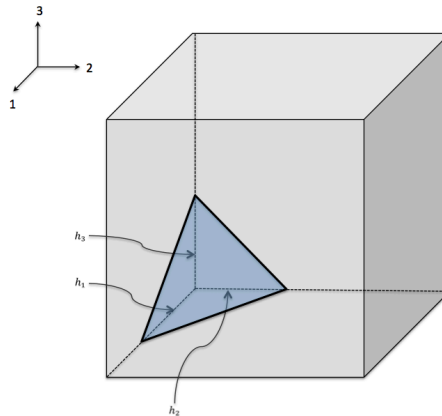


**Figure 3.13:** Triangular pyramid intersection condition

We can then define  $h_1$ ,  $h_2$ , and  $h_3$  as:

$$h_i = \frac{d}{n_i} \quad (3.223)$$

where  $i=1,2,3$ .

Substituting the expression for  $h_i$  into the expression for  $\phi$  results in the following expression:

$$\phi = \frac{1}{6} \frac{d^3}{n_1 n_2 n_3} \quad (3.224)$$

This can then be solved for  $d$  as:

$$d = (6\phi n_1 n_2 n_3)^{\frac{1}{3}} \quad (3.225)$$

Since we require that  $n_1 \geq n_2 \geq n_3$ , the triangle condition is true for  $h_1 < 1$ . At  $h_1 = 1$  we have the transition to the quadrilateral section condition A, therefore at  $h_1 = 1$  we can solve to find the situations at which each section occurs. At  $h_1 = 1$ , we see that  $d = n_1$ , so:

$$n_1^3 = 6\phi n_1 n_2 n_3 \quad (3.226)$$

Therefore, the triangle intersection condition occurs for:

$$n_1^3 > 6\phi n_1 n_2 n_3 \quad (3.227)$$

#### *Quadrilateral Intersection Condition A*

The quadrilateral intersection condition, shown in Figure 3.14, occurs when  $h_1 \geq 1 > h_2 > h_3$ . To find the advection volume it is necessary to first determine the total volume of the intersecting triangular pyramid section and subtract the volume that lies outside the unit cube. This can be expressed as

$$\phi = \phi_{Total} - \phi_{Outside} \quad (3.228)$$

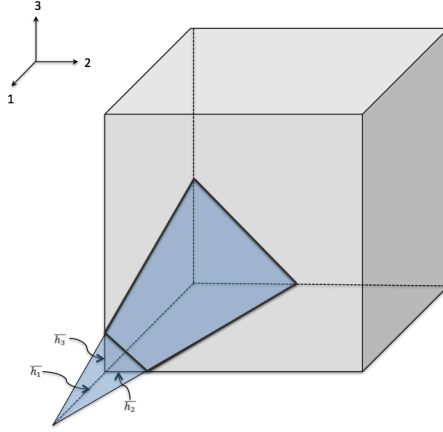


**Figure 3.14:** Quadrilateral intersection condition A

The total volume of the intersecting triangular pyramid is given by:

$$\phi_{Total} = \frac{1}{6}(h_1 h_2 h_3) \quad (3.229)$$

The volume outside the unit cube can be written as

$$\phi_{Outside} = \frac{1}{6}(\bar{h}_1 \bar{h}_2 \bar{h}_3) \quad (3.230)$$

where,

$$\bar{h}_1 = h_1 - 1 \quad (3.231a)$$

$$\bar{h}_2 = \frac{h_2}{h_1} \bar{h}_1 = \frac{h_2}{h_1} (h_1 - 1) \quad (3.231b)$$

$$\bar{h}_3 = \frac{h_3}{h_1} \bar{h}_1 = \frac{h_3}{h_1} (h_1 - 1) \quad (3.231c)$$

So,  $\phi_{\text{Outside}}$  can be rewritten as,

$$\phi_{\text{Outside}} = \frac{1}{6} (h_1 - 1)^3 \frac{h_2 h_3}{h_1 h_1} \quad (3.232)$$

Given this relation, a value for the advection volume,  $\phi$ , inside the unit cube can now be determined and is expressed as

$$\phi = \frac{1}{6} (h_1 h_2 h_3) - \frac{1}{6} (h_1 - 1)^3 \frac{h_2 h_3}{h_1^2} \quad (3.233)$$

$h_1$ ,  $h_2$ , and  $h_3$  can then be defined as:

$$h_i = \frac{d}{n_i} \quad (3.234)$$

where  $i=1,2,3$ . So in terms of  $d$  and  $n_i$  the expression for  $\phi$  becomes,

$$\phi = \frac{1}{6} \left( \frac{3d^2}{n_2 n_3} - \frac{3dn_1}{n_2 n_3} + \frac{n_1^2}{n_2 n_3} \right) \quad (3.235)$$

This intersection condition is applicable for cases in which  $h_2 < 1$ , or as it can also be written,  $n_2 > d$ , and also requires  $h_1 \geq 1$ , so  $n_1 \leq d$ . Therefore, the quadrilateral intersection condition A occurs when

$$n_1^3 \leq 6\phi n_1 n_2 n_3 < 3n_1 n_2^2 - 3n_1^2 n_2 + n_1^3 = n_2^3 - (n_2 - n_1)^3 \quad (3.236)$$

To find  $d$ , the expression for  $\phi$  must be rearranged as

$$6\phi n_1 n_2 n_3 = 3n_1 d^2 - 3dn_1^2 + n_1^3 \quad (3.237)$$

This equation can be rewritten and set equal to zero to give

$$d^3 - (d - n_1)^3 - 6\phi n_1 n_2 n_3 = 0 \tag{3.238}$$

This equation can then be solved for  $d$  resulting in the expression

$$d = \frac{n_1}{2} + \left[ 2n_2 n_3 \phi - \frac{n_1^2}{12} \right]^{\frac{1}{2}} \tag{3.239}$$

*Pentagonal Intersection Condition*

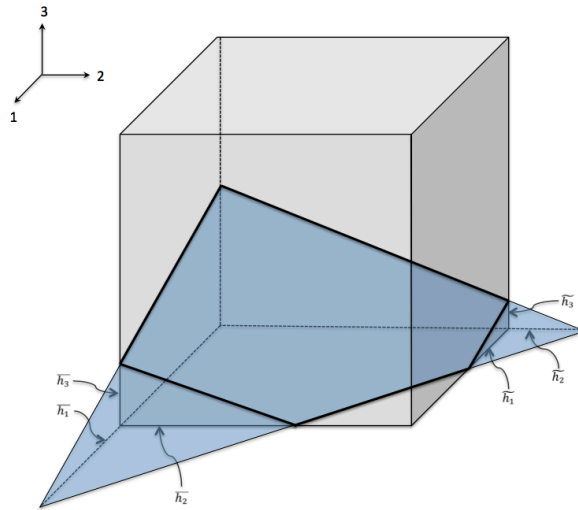


**Figure 3.15:** Pentagonal intersection condition

The pentagonal intersection condition, shown in Figure 3.15, occurs when  $h_1 > h_2 \geq 1 > h_3$  and for values of  $\tilde{h}_1, \tilde{h}_2 \leq 1$ . In a similar manner to the quadrilateral intersection A, to find the advection volume it is necessary to first determine the total volume of the intersecting triangular pyramid section and subtract the volume that lies outside the unit cube. This can be expressed as

$$\phi = \phi_{Total} - \phi_{Outside} \quad (3.240)$$

The total volume of the intersecting triangular pyramid is given by:

$$\phi_{Total} = \frac{1}{6} (h_1 h_2 h_3) \quad (3.241)$$

The volume outside the unit cube can be written as

$$\phi_{Outside} = \frac{1}{6} (\bar{h}_1 \bar{h}_2 \bar{h}_3) + \frac{1}{6} (\tilde{h}_1 \tilde{h}_2 \tilde{h}_3) \quad (3.242)$$

where,

$$\bar{h}_1 = h_1 - 1 \quad (3.243a)$$

$$\bar{h}_2 = \frac{h_2}{h_1} \bar{h}_1 = \frac{h_2}{h_1} (h_1 - 1) \quad (3.243b)$$

$$\bar{h}_3 = \frac{h_3}{h_1} \bar{h}_1 = \frac{h_3}{h_1} (h_1 - 1) \quad (3.243c)$$

$$\tilde{h}_1 = \frac{h_1}{h_2} \tilde{h}_2 = \frac{h_1}{h_2} (h_2 - 1) \quad (3.243d)$$

$$\tilde{h}_2 = (h_2 - 1) \quad (3.243e)$$

$$\tilde{h}_3 = \frac{h_3}{h_2} \tilde{h}_2 = \frac{h_3}{h_2} (h_2 - 1) \quad (3.243f)$$

So,  $\phi_{Outside}$  can be rewritten as,

$$\phi_{Outside} = \frac{1}{6} (h_1 - 1)^3 \frac{h_2 h_3}{h_1 h_1} + \frac{1}{6} (h_2 - 1)^3 \frac{h_1 h_3}{h_2^2} \quad (3.244)$$

Given this relation, a value for the advection volume,  $\phi$ , inside the unit cube can now be determined and is expressed as

$$\phi = \frac{1}{6}(h_1 h_2 h_3) - \frac{1}{6}(h_1 - 1)^3 \frac{h_2 h_3}{h_1^2} - \frac{1}{6}(h_2 - 1)^3 \frac{h_1 h_3}{h_2^2} \quad (3.245)$$

$h_1$ ,  $h_2$ , and  $h_3$  can then be defined as:

$$h_i = \frac{d}{n_i} \quad (3.246)$$

where  $i=1,2,3$ . So in terms of  $d$  and  $n_i$  the expression for  $\phi$  becomes,

$$\phi = \frac{1}{6} \left( \frac{3d^2}{n_2 n_3} - \frac{3dn_1}{n_2 n_3} + \frac{n_1^2}{n_2 n_3} - \frac{d^3}{n_1 n_2 n_3} + \frac{3d^2}{n_1 n_3} - \frac{3dn_2}{n_1 n_3} + \frac{n_2^2}{n_1 n_3} \right) \quad (3.247)$$

There are two possible conditions for which this intersection condition is applicable. The first condition requires  $h_3 < 1$  and  $\tilde{h}_1, \bar{h}_2 < 1$ , or as it can also be written,  $n_3 > d$  and  $n_1 + n_2 > n_3$ , and also requires  $h_1 \geq 1$ , so  $n_1 \leq d$ . Therefore, for this condition, the pentagonal intersection condition occurs when

$$n_2^3 - (n_2 - n_1)^3 \leq 6\phi n_1 n_2 n_3 < n_3^3 - (n_3 - n_1)^3 - (n_3 - n_2)^3 \text{ and } n_1 + n_2 > n_3 \quad (3.248)$$

The second condition occurs when  $h_3 < 1$  and  $\tilde{h}_1, \bar{h}_2 = 1$ , or when  $n_1 + n_2 \leq n_3$ . For this condition it is necessary to include the following

$$\tilde{h}_1 = \frac{h_1}{h_2}(h_2 - 1) = 1 \quad (3.249a)$$

$$h_2 = h_1(h_2 - 1) \quad (3.249b)$$

$$\bar{h}_2 = \frac{h_2}{h_1}(h_1 - 1) = 1 \quad (3.249c)$$

$$0 = h_1 h_2 - h_1 - h_2 \quad (3.249d)$$

In terms of  $n_i$  and  $d$  these equations can be expressed as

$$\frac{d}{n_1} = \frac{d}{n_2} \left( \frac{d}{n_1} - 1 \right) \quad (3.250a)$$

$$0 = \frac{d^2}{n_1 n_2} - \frac{d}{n_1} - \frac{d}{n_2} \quad (3.250b)$$

$$0 = d^2 - d n_1 - d n_2 \quad (3.250c)$$

From this we can apply the condition  $n_1 + n_2 > d$ , which gives

$$6\phi n_1 n_2 n_3 < 3(n_1 + n_2)^2 n_1 - 3(n_1 + n_2)n_1^2 + n_1^3 - (n_1 + n_2)^3 + 3(n_1 + n_2)^2 n_2 - 3(n_1 + n_2)n_2^2 + n_2^3 \quad (3.251)$$

Which can be simplified to give

$$6\phi n_1 n_2 n_3 < (n_1 + n_2)^3 - n_2^3 - n_1^3 \quad (3.252)$$

Therefore, for the second condition, the pentagonal intersection condition occurs when

$$n_2^3 - (n_2 - n_1)^3 \leq 6\phi n_1 n_2 n_3 < (n_1 + n_2)^3 - n_2^3 - n_1^3 \text{ and } n_1 + n_2 \leq n_3 \quad (3.253)$$

To find  $d$ , the expression for  $\phi$  must be rearranged as

$$6\phi n_1 n_2 n_3 = 3n_1 d^2 - 3d n_1^2 + n_1^3 - d^3 + 3n_2 d^2 - 3d n_2^2 + n_2^3 \quad (3.254)$$



This equation can be rewritten and set equal to zero to give

$$d^3 - (d - n_1)^3 - (d - n_2)^3 - 6\phi n_1 n_2 n_3 = 0 \quad (3.255)$$

which can then be solved for  $d$ .

### *Hexagonal Intersection Condition*

The hexagonal intersection condition, shown in Figure 3.16, occurs when  $h_1 > h_2 > h_3 \geq 1$ . In a similar manner to the previously described intersection conditions, to find the advection volume it is necessary to first determine the total volume of the intersecting triangular pyramid section and subtract the volume that lies outside the unit cube. This can be expressed as

$$\phi = \phi_{Total} - \phi_{Outside} \quad (3.256)$$

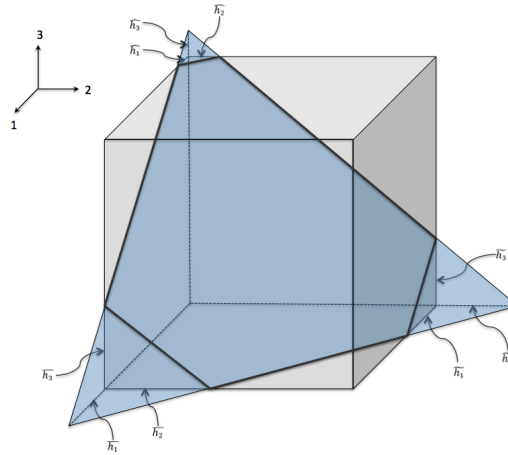


**Figure 3.16:** Hexagonal intersection condition

The total volume of the intersecting triangular pyramid is given by:

$$\phi_{Total} = \frac{1}{6} (h_1 h_2 h_3) \quad (3.257)$$

The volume outside the unit cube can be written as

$$\phi_{Outside} = \frac{1}{6}(\bar{h}_1\bar{h}_2\bar{h}_3) + \frac{1}{6}(\tilde{h}_1\tilde{h}_2\tilde{h}_3) + \frac{1}{6}(\hat{h}_1\hat{h}_2\hat{h}_3) \quad (3.258)$$

where,

$$\bar{h}_1 = h_1 - 1 \quad (3.259a)$$

$$\bar{h}_2 = \frac{h_2}{h_1}\bar{h}_1 = \frac{h_2}{h_1}(h_1 - 1) \quad (3.259b)$$

$$\bar{h}_3 = \frac{h_3}{h_1}\bar{h}_1 = \frac{h_3}{h_1}(h_1 - 1) \quad (3.259c)$$

$$\tilde{h}_1 = \frac{h_1}{h_2}\tilde{h}_2 = \frac{h_1}{h_2}(h_2 - 1) \quad (3.259d)$$

$$\tilde{h}_2 = (h_2 - 1) \quad (3.259e)$$

$$\tilde{h}_3 = \frac{h_3}{h_2}\tilde{h}_2 = \frac{h_3}{h_2}(h_2 - 1) \quad (3.259f)$$

$$\hat{h}_1 = \frac{h_1}{h_3}\hat{h}_3 = \frac{h_1}{h_3}(h_3 - 1) \quad (3.259g)$$

$$\hat{h}_2 = \frac{h_2}{h_3}\hat{h}_3 = \frac{h_2}{h_3}(h_3 - 1) \quad (3.259h)$$

$$\hat{h}_3 = (h_3 - 1) \quad (3.259i)$$

So,  $\phi_{Outside}$  can be rewritten as,

$$\phi_{Outside} = \frac{1}{6}(h_1 - 1)^3 \frac{h_2 h_3}{h_1^2} + \frac{1}{6}(h_2 - 1)^3 \frac{h_1 h_3}{h_2^2} + \frac{1}{6}(h_3 - 1)^3 \frac{h_1 h_2}{h_3^2} \quad (3.260)$$

Given this relation, a value for the advection volume,  $\phi$ , inside the unit cube can now be determined and is expressed as

$$\phi = \frac{1}{6}(h_1 h_2 h_3) - \frac{1}{6}(h_1 - 1)^3 \frac{h_2 h_3}{h_1^2} - \frac{1}{6}(h_2 - 1)^3 \frac{h_1 h_3}{h_2^2} - \frac{1}{6}(h_3 - 1)^3 \frac{h_1 h_2}{h_3^2} \quad (3.261)$$

$h_1$ ,  $h_2$ , and  $h_3$  can then be defined as:

$$h_i = \frac{d}{n_i} \quad (3.262)$$

where  $i=1,2,3$ . So in terms of  $d$  and  $n_i$  the expression for  $\phi$  becomes,

$$\begin{aligned} & \phi \\ &= \frac{1}{6} \left( \frac{3d^2}{n_2 n_3} - \frac{3dn_1}{n_2 n_3} + \frac{n_1^2}{n_2 n_3} - \frac{2d^3}{n_1 n_2 n_3} + \frac{3d^2}{n_1 n_3} - \frac{3dn_2}{n_1 n_3} + \frac{n_2^2}{n_1 n_3} + \frac{3d^2}{n_1 n_2} - \frac{3dn_3}{n_1 n_2} + \frac{n_3^2}{n_1 n_2} \right) \end{aligned} \quad (3.263)$$

This intersection condition is applicable when  $h_3 \geq 1$  so  $n_3 \geq d$ . Therefore, the hexagonal intersection condition occurs when

$$n_3^3 - (n_3 - n_1)^3 - (n_3 - n_2)^3 \leq 6\phi n_1 n_2 n_3 \text{ for } n_1 + n_2 > n_3 \quad (3.264)$$

To find  $d$ , the expression for  $\phi$  must be rearranged as

$$6\phi n_1 n_2 n_3 = 3n_1 d^2 - 3dn_1^2 + n_1^3 - 2d^3 + 3n_2 d^2 - 3dn_2^2 + n_2^3 + 3n_3 d^2 - 3dn_3^2 + n_3^3 \quad (3.265)$$

This equation can be rewritten and set equal to zero to give

$$d^3 - (d - n_1)^3 - (d - n_2)^3 - (d - n_3)^3 - 6\phi n_1 n_2 n_3 = 0 \quad (3.266)$$

which can then be solved for  $d$ .

### *Quadrilateral Intersection Condition B*

Quadrilateral intersection condition B, shown in Figure 3.17, occurs when  $\tilde{h}_1 \geq \bar{h}_2 \geq 1 > h_3$  or when  $n_1 + n_2 = n_3$ . In a similar manner to the previously described intersection conditions, to find the advection volume it is necessary to first determine the total volume of the intersecting triangular pyramid section and subtract the volume that lies outside the unit cube. This can be expressed as

$$\phi = \phi_{Total} - \phi_{Outside} \quad (3.267)$$

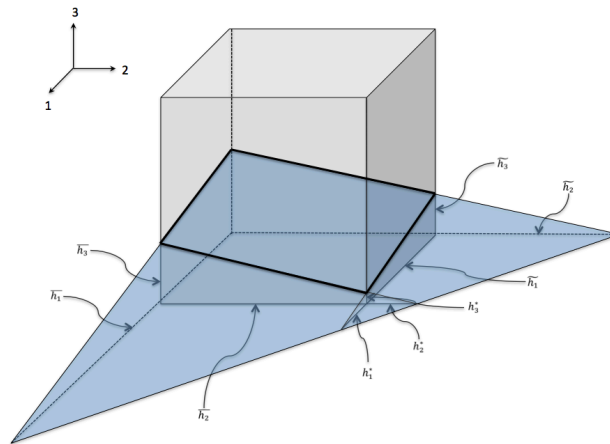


**Figure 3.17:** Quadrilateral intersection condition B

The total volume of the intersecting triangular pyramid is given by:

$$\phi_{Total} = \frac{1}{6} (h_1 h_2 h_3) \quad (3.268)$$

The volume outside the unit cube can be written as

$$\phi_{Outside} = \frac{1}{6}(\bar{h}_1\bar{h}_2\bar{h}_3) + \frac{1}{6}(\tilde{h}_1\tilde{h}_2\tilde{h}_3) - \frac{1}{6}(h_1^*h_2^*h_3^*) \quad (3.269)$$

where,

$$\bar{h}_1 = h_1 - 1 \quad (3.270a)$$

$$\bar{h}_2 = \frac{h_2}{h_1}\bar{h}_1 = \frac{h_2}{h_1}(h_1 - 1) \quad (3.270b)$$

$$\bar{h}_3 = \frac{h_3}{h_1}\bar{h}_1 = \frac{h_3}{h_1}(h_1 - 1) \quad (3.270c)$$

$$\tilde{h}_1 = \frac{h_1}{h_2}\tilde{h}_2 = \frac{h_1}{h_2}(h_2 - 1) \quad (3.270d)$$

$$\tilde{h}_2 = (h_2 - 1) \quad (3.270e)$$

$$\tilde{h}_3 = \frac{h_3}{h_2}\tilde{h}_2 = \frac{h_3}{h_2}(h_2 - 1) \quad (3.270f)$$

$$h_1^* = \tilde{h}_1 - 1 = h_1 - \frac{h_1}{h_2} - 1 \quad (3.270g)$$

$$h_2^* = \frac{\tilde{h}_2}{\tilde{h}_1}(\tilde{h}_1 - 1) = h_2 - \frac{h_2}{h_1} - 1 \quad (3.270h)$$

$$h_3^* = \frac{\tilde{h}_3}{\tilde{h}_1}(\tilde{h}_1 - 1) = h_3 - \frac{h_3}{h_2} - \frac{h_3}{h_1} \quad (3.270i)$$

So,  $\phi_{Outside}$  can be rewritten after some algebraic manipulation as,

$$\phi_{Outside} = \frac{1}{6} \left( h_1 h_2 h_3 - 6h_3 + \frac{3h_3}{h_1} + \frac{3h_3}{h_2} \right) \quad (3.271)$$

Given this relation, a value for the advection volume,  $\phi$ , inside the unit cube can now be determined and is expressed as

$$\phi = \frac{1}{6} (h_1 h_2 h_3) - \frac{1}{6} \left( h_1 h_2 h_3 - 6h_3 + \frac{3h_3}{h_1} + \frac{3h_3}{h_2} \right) = h_3 + \frac{h_3}{2h_1} + \frac{h_3}{2h_2} \quad (3.272)$$

$h_1$ ,  $h_2$ , and  $h_3$  can then be defined as:

$$h_i = \frac{d}{n_i} \quad (3.273)$$

where  $i=1,2,3$ . So in terms of  $d$  and  $n_i$  the expression for  $\phi$  becomes,

$$\phi = \frac{d}{n_3} - \frac{n_1}{2n_3} - \frac{n_2}{2n_3} \quad (3.274)$$

This intersection condition is applicable when

$$(n_2 + n_1)^3 - n_2^3 - n_1^3 \leq 6\phi n_1 n_2 n_3 \text{ for } n_1 + n_2 \leq n_3 \quad (3.275)$$

To find  $d$ , the expression for  $\phi$  was found to be

$$\phi = \frac{d}{n_3} - \frac{n_1}{2n_3} - \frac{n_2}{2n_3} \quad (3.276)$$

This equation can be rewritten to solve for  $d$  as

$$d = \phi n_3 + \frac{n_1 + n_2}{2} \quad (3.277)$$

### Determining Material Specific Advection Volumes in Three-Dimensions

Having determined the value for  $d$  it is now possible to determine the volume intersection with the advection volume. For advection in the +1-direction, as was shown previously for the two-dimensional case, the unit normals in the normalized system are

$$\tilde{n}_1 = \frac{\varepsilon n_1}{\sqrt{(\varepsilon n_1)^2 + n_2^2 + n_3^2}} \quad (3.278a)$$

$$\tilde{n}_2 = \frac{n_2}{\sqrt{(\varepsilon n_1)^2 + n_2^2 + n_3^2}} \quad (3.278b)$$

$$\tilde{n}_3 = \frac{n_3}{\sqrt{(\varepsilon n_1)^2 + n_2^2 + n_3^2}} \quad (3.278c)$$

Similar to the two-dimensional case, the values for  $\tilde{h}_i$  are found to be

$$\tilde{h}_1 = \frac{h_1 + \varepsilon - 1}{\varepsilon} = \frac{1}{\varepsilon} \left( \frac{d}{n_1} + \varepsilon - 1 \right) \quad (3.279a)$$

$$\tilde{h}_2 = \frac{h_2}{h_1} (h_1 + \varepsilon - 1) = \frac{n_1}{n_2} \left( \frac{d}{n_1} + \varepsilon - 1 \right) \quad (3.279b)$$

$$\tilde{h}_3 = \frac{h_3}{h_1} (h_1 + \varepsilon - 1) = \frac{n_1}{n_3} \left( \frac{d}{n_1} + \varepsilon - 1 \right) \quad (3.279c)$$

but, it may not be necessary to determine  $\tilde{h}_2$  and  $\tilde{h}_3$  since advection is in the +1-direction in this case, and therefore there is no transformation taking place in the 2 or 3 directions.

Also, if  $\tilde{h}_1 < 0$ , then there is no intersection condition present.

Using the value for  $\tilde{h}_1$ , we can now find  $\tilde{d}$ , which can be written as:

$$\tilde{d} = \tilde{n}_1 \tilde{h}_1 \quad (3.280)$$

and can be further simplified as:

$$\tilde{d} = \tilde{n}_1 \left( \frac{h_1 + \varepsilon - 1}{\varepsilon} \right) \quad (3.281)$$

We can also write  $\tilde{d}$  in terms of  $d$  as:

$$\tilde{d} = \frac{n_1 \left( \frac{d}{n_1} + \varepsilon - 1 \right)}{\sqrt{(\varepsilon n_1)^2 + n_2^2 + n_3^2}} \quad (3.282)$$

Since we know  $\tilde{d}$ ,  $\tilde{n}_1$ ,  $\tilde{n}_2$ , and  $\tilde{n}_3$ , we can now find the normalized volume fraction,  $\tilde{\phi}$ , in the normalized system. For the triangular pyramid intersection condition, the normalized volume fraction can be written as:

$$\tilde{\phi} = \frac{1}{6} \tilde{h}_1 \tilde{h}_2 \tilde{h}_3 = \frac{1}{6} \left( \frac{\tilde{d}^3}{\tilde{n}_1 \tilde{n}_2 \tilde{n}_3} \right) \quad (3.283)$$

which occurs when  $\tilde{n}_1 > \tilde{d}$ .

For the quadrilateral intersection condition A, the normalized volume fraction is given by:

$$\tilde{\phi} = \frac{1}{6} \tilde{h}_1 \tilde{h}_2 \tilde{h}_3 - \frac{1}{6} (\tilde{h}_1^3 - 3\tilde{h}_1^2 + 3\tilde{h}_1 - 1) \frac{\tilde{h}_2 \tilde{h}_3}{\tilde{h}_1^2} \quad (3.284)$$

which can be written in terms of  $\tilde{d}$ ,  $\tilde{n}_1$ ,  $\tilde{n}_2$ , and  $\tilde{n}_3$  as

$$\tilde{\phi} = \frac{\tilde{d}^3 - (\tilde{d} - \tilde{n}_1)^3}{6\tilde{n}_1 \tilde{n}_2 \tilde{n}_3} \quad (3.285)$$

which occurs when  $\tilde{n}_2 \geq \tilde{d}$ .



For the pentagonal intersection condition, the normalized volume fraction is given by:

$$\tilde{\phi} = \frac{1}{6}\tilde{h}_1\tilde{h}_2\tilde{h}_3 - \frac{1}{6}(\tilde{h}_1 - 1)^3 \frac{\tilde{h}_2\tilde{h}_3}{\tilde{h}_1^2} - \frac{1}{6}(\tilde{h}_2 - 1)^3 \frac{\tilde{h}_1\tilde{h}_3}{\tilde{h}_2^2} \quad (3.286)$$

which can be written in terms of  $\tilde{d}$ ,  $\tilde{n}_1$ ,  $\tilde{n}_2$ , and  $\tilde{n}_3$  as

$$\tilde{\phi} = \frac{\tilde{d}^3 - (\tilde{d} - \tilde{n}_1)^3 - (\tilde{d} - \tilde{n}_2)^3}{6\tilde{n}_1\tilde{n}_2\tilde{n}_3} \quad (3.287)$$

which occurs when  $\tilde{n}_3 \geq \tilde{d}$  and  $\tilde{n}_1 + \tilde{n}_2 \leq \tilde{d}$ .

For the hexagonal intersection condition, the normalized volume fraction is given by:

$$\tilde{\phi} = \frac{1}{6}\tilde{h}_1\tilde{h}_2\tilde{h}_3 - \frac{1}{6}(\tilde{h}_1 - 1)^3 \frac{\tilde{h}_2\tilde{h}_3}{\tilde{h}_1^2} - \frac{1}{6}(\tilde{h}_2 - 1)^3 \frac{\tilde{h}_1\tilde{h}_3}{\tilde{h}_2^2} - \frac{1}{6}(\tilde{h}_3 - 1)^3 \frac{\tilde{h}_1\tilde{h}_2}{\tilde{h}_3^2} \quad (3.288)$$

which can be written in terms of  $\tilde{d}$ ,  $\tilde{n}_1$ ,  $\tilde{n}_2$ , and  $\tilde{n}_3$  as

$$\tilde{\phi} = \frac{\tilde{d}^3 - (\tilde{d} - \tilde{n}_1)^3 - (\tilde{d} - \tilde{n}_2)^3 - (\tilde{d} - \tilde{n}_3)^3}{6\tilde{n}_1\tilde{n}_2\tilde{n}_3} \quad (3.289)$$

which occurs when  $\tilde{n}_3 < \tilde{d}$  and  $\tilde{n}_1 + \tilde{n}_2 \leq \tilde{d}$ .

For the quadrilateral intersection condition B, the normalized volume fraction is given by:

$$\tilde{\phi} = \tilde{h}_3 - \frac{\tilde{h}_3}{2\tilde{h}_1} - \frac{\tilde{h}_3}{2\tilde{h}_2} \quad (3.290)$$

which can be written in terms of  $\tilde{d}$ ,  $\tilde{n}_1$ ,  $\tilde{n}_2$ , and  $\tilde{n}_3$  as

$$\tilde{\phi} = \frac{1}{\tilde{n}_3} \left( \tilde{d} - \frac{\tilde{n}_1 + \tilde{n}_2}{2} \right) \quad (3.291)$$

which occurs when  $\tilde{n}_3 > \tilde{d}$  and  $\tilde{n}_1 + \tilde{n}_2 > \tilde{d}$ .

Finally, we need to transform the volume fraction from the normalized system back to the unit square. Since  $\tilde{\phi}$  is in terms of  $\tilde{n}$ , this can be done by solving

$$\phi = \varepsilon \tilde{\phi} \quad (3.292)$$

#### Advection in Directions other than the +1-Direction

In two-dimensions we also need to consider advection in the -1, +2, and -2 directions. For the -1 direction, all the equations presented above are still valid, however, we must find the volume of the  $1-\varepsilon$  of the unit square instead of the  $\varepsilon$  side. The volume we get will not be the advection volume, but rather it will be the total volume minus the advection volume. To get the advection volume, we simply subtract:

$$\phi_A = \phi_T - \phi \quad (3.293)$$

where  $\phi_A$  is the advection volume fraction,  $\phi_T$  is the total volume fraction, and  $\phi$  is the volume fraction determined based on the  $1-\varepsilon$  side of the unit square.

For advection in the +2-direction we need to normalize the 2-direction based on  $\varepsilon$ , which can be accomplished using the following equations:

$$\tilde{n}_1 = \frac{n_1}{\left[n_1^2 + (\varepsilon n_2)^2\right]^{\frac{1}{2}}} \quad (3.294a)$$

$$\tilde{n}_2 = \frac{\varepsilon n_2}{\left[n_1^2 + (\varepsilon n_2)^2\right]^{\frac{1}{2}}} \quad (3.294b)$$

It is important to note that  $\tilde{n}_2$  may now be less than  $\tilde{n}_1$ . If this is the case,  $\tilde{n}_1$  and  $\tilde{n}_2$  must be interchanged before the volume fraction calculation can be performed. After this interchange is made, the formulas for  $\tilde{\phi}$  given previously are the correct ones, except that  $\tilde{d}$  is now given by:

$$\tilde{d} = \frac{\tilde{n}_2}{\varepsilon} \left[ \frac{d}{n_2} + \varepsilon - 1 \right] = n_2 \frac{\left( \frac{d}{n_2} + \varepsilon - 1 \right)}{\left[ n_1^2 + (\varepsilon n_2)^2 \right]^{\frac{1}{2}}} \quad (3.295)$$

In the -2-direction, the process is the same as the process described above for the -1-direction.

In three-dimensions, we need to consider advection in the -1, +2, -2, +3, and -3 directions as well. The methodology described for the two-dimensional cases can be extended to three-dimensions in a straightforward fashion. Advection in the -1, -2, and -3 directions are done in the same manner described in two-dimensions. For advection in the +2 direction, we determine  $\tilde{d}$ ,  $\tilde{n}_1$ ,  $\tilde{n}_2$ , and  $\tilde{n}_3$  as

$$\tilde{d} = \frac{n_2 \left( \frac{d}{n_2} + \varepsilon - 1 \right)}{\sqrt{n_1^2 + (\varepsilon n_2)^2 + n_3^2}} \quad (3.296a)$$

$$\tilde{n}_1 = \frac{n_1}{\sqrt{n_1^2 + (\varepsilon n_2)^2 + n_3^2}} \quad (3.296b)$$

$$\tilde{n}_2 = \frac{\varepsilon n_2}{\sqrt{n_1^2 + (\varepsilon n_2)^2 + n_3^2}} \quad (3.296c)$$

$$\tilde{n}_3 = \frac{n_3}{\sqrt{n_1^2 + (\varepsilon n_2)^2 + n_3^2}} \quad (3.296d)$$

The order of  $\tilde{n}_1$ ,  $\tilde{n}_2$ , and  $\tilde{n}_3$  may have to be changed at this point to insure that  $\tilde{n}_1 \leq \tilde{n}_2 \leq \tilde{n}_3$ . The advection calculation can then proceed as described previously.

Advection in the +3 direction proceeds in a manner similar to that described above for advection in the +2 direction.

### Limits on the Advection Volume Calculation

If the advection volume is too large, we should instead find the advection volume based on  $1-\phi$  instead of  $\phi$ . In two-dimensions, the limit is reached when  $\tilde{h}_2 = 1$ . This gives:

$$\tilde{h}_2 = \frac{\tilde{d}}{\tilde{n}_2} \leq 1 \quad (3.297a)$$

or

$$\tilde{n}_2 \geq \tilde{d} \quad (3.297b)$$

If this limit is reached, we must reverse the advection volume. The normal stays the same, except it changes sign, however, the reference corner also changes, so it keeps the same sign. The corner distance  $\tilde{d}$ , however, must be changed. This new corner distance,  $\hat{d}$ , as seen in Figure 3.18, is given by:

$$\hat{d} = \tilde{n}_1 + \tilde{n}_2 - \tilde{d} \tag{3.298}$$

In three-dimensions, similarly, it is required that for  $\tilde{h}_3 \leq 1$  or  $\tilde{n}_3 \geq \tilde{d}$ , the new corner distance is given by

$$\hat{d} = n_1 + n_2 + n_3 - \tilde{d} \tag{3.299}$$

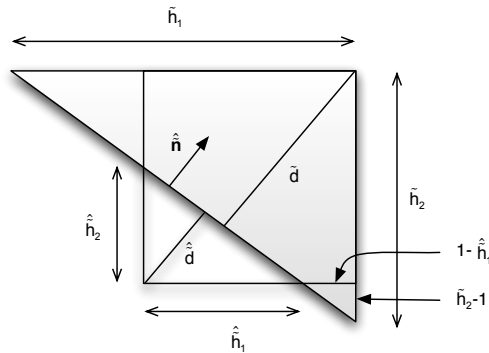


**Figure 3.18:** Limits on the advection calculation

## CHAPTER 4

### SOFTWARE

#### ALEAS

ALEAS (Arbitrary Lagrangian-Eulerian Adaptive Solver) is a finite element research code initially developed in two-dimensions by Littlefield [63] and extended to three-dimensions as part of this work. ALEAS is capable of performing multi-material calculations in Eulerian, Lagrangian, simple ALE, and multi-material ALE frameworks. ALEAS implements the ALE form of the conservation equations presented in Chapter 3, along with the interface tracking algorithms and Eulerian contact algorithm developed in the same chapter. This section will provide a brief description of the ALEAS software package as well as the solution techniques implemented in the package.

ALEAS contains an option to use the contact enforcement approach developed in Chapter 3, or the traditional Eulerian approach which makes use of a single velocity field and mixture theory. Both methods make use of the operator split approach, with the traditional Eulerian formulation using a single operator split, and the contact formulation using the two operator split method developed in Chapter 3. In both approaches, the first operator split consists of a Lagrangian step to advance the solution in time followed by an advection step in which the convection equations are solved in order to move material across interface boundaries. For the contact formulation a second operator split is

performed which enforces contact constraints and calculates changes in the solution variables as a result of the traction. This results in another mesh deformation, so the convection equations must be solved again in a second remap step to calculate the flux across element boundaries. Numerical integration of the Lagrangian and contact enforcement steps follows the usual procedure for linear, constant stress elements. The advection steps are performed differently for node-centered and element-centered variables. Element-centered variables, including density and internal energy, are advected using a simple donor cell algorithm, with fluxes across element boundaries computed using an upwinding scheme. Updates to the velocities, which are node-centered, are determined by advecting momentum, using a lumped mass approximation to define the momentum at each node. The Half-Index Shift (HIS) algorithm for momentum advection implemented in ALEAS was initially developed by Benson [12], [20]. The HIS algorithm was developed to overcome dispersion errors associated with other momentum advection methods while also preserving monotonicity. The HIS algorithm is described in detail in Chapter 2 of this work and more detail can be found in references [12] and [20].

ALEAS contains a multi-material momentum (MMM) option which causes the program to utilize the formulations developed in this work. When this option is turned off the program functions as a traditional Eulerian finite element solver, allowing only a single velocity field to be present in each element and uses mixture theory to handle contact in mixed cells. Applying this option permits multiple velocity fields per element and turns on the contact algorithm described in Chapter 3, and therefore was used in all of the problems labeled as ALEAS MMM in Chapters 5 and 6.

ALEAS outputs results for post-processing in an ASCII VTK file format. The VTK format is widely used and can be read by a number of open-source and commercial post-processing tools, including Paraview and VisIt, which were used to generate images shown in Chapters 5 and 6 of this work.

### CTH

In order to ensure that the traditional Eulerian results in ALEAS were valid and compared well with other hydrocodes a comparison was carried out using CTH, which uses the traditional treatment of multi-material contact through mixture theory. This section provides a general introduction to CTH, for more information about the solution methods used in CTH and the program package as a whole see works by McGlaun and Thompson [71] and Hertel, et al. [42].

CTH is an Eulerian shock physics code under active development at Sandia National Laboratories used to model multi-dimensional, multi-material, large deformation, strong shock wave physics. One-dimensional rectilinear, cylindrical, and spherical meshes; two-dimensional rectangular and cylindrical meshes, and three-dimensional rectangular meshes are available. A two-step Eulerian solution scheme with operator splitting similar to that described in Chapter 2 is used during the solution phase.

The CTH system allows analysts to set up and examine the initial configuration, integrate the problem through time, and examine the results with one integrated software family. CTH uses an Eulerian scheme in which the mesh is fixed in space and the material flows through the mesh. The conservation equations are replaced by finite



volume approximations. The finite volume approximations have been carefully designed to conserve mass, momentum, and energy. In some cases it is impossible to conserve all of these quantities. In these cases, CTH has been designed with several options that the user can use to bound the effects.

CTH is widely used for solving problems across a wide range of spatial scales of varying complexity. It contains a number of advanced equation of state models for gases, fluids, solids, and reactive materials along with strength and fracture models. CTH contains all tools necessary for pre-processing, execution, and post-processing within a single package controlled by a single text input file making for a simplified user experience.

## CHAPTER 5

### VALIDATION AND VERIFICATION PROBLEMS

To demonstrate the advantages of the method developed in this work over traditional treatment of Eulerian contact several validation calculations were performed. Calculations involving the multi-material Eulerian contact algorithm developed in this dissertation were carried out using the multi-material momentum (MMM) option in ALEAS. For comparison, calculations were also performed using the single-material momentum (SMM) option in ALEAS, which treat multi-material contact in the traditional Eulerian sense by using mixture theory. To further verify ALEAS comparisons were made to the production hydrocode CTH, which has undergone extensive validation. While there are several differences between the formulations used in CTH and those used in ALEAS results between the two codes, when run using the traditional Eulerian approach, should have close agreement.

A total of fourteen validation problems and one verification problem have been carried out. The calculations include a mesh aligned normal block sliding problem, an offset normal frictionless block sliding problem, an angled frictionless block sliding problem, both mesh-aligned and offset Taylor impact problems, a long rod penetration of a stationary oblique plate, long rod penetrations of moving oblique plates at  $+10.3^\circ$  and  $-9.3^\circ$  yaw, a normal penetration of a long rod into a 5.08 cm target, a series of tungsten

long rods penetrating a semi-infinite steel target, and a Sod shock tube problem [104].

This section describes the initial conditions of the validation problems as well as some of the theory and experimental background associated with these test cases.

Table 5.1 Mie-Gruneisen equation-of-state parameters used in validation problems

	$\rho_0$ (g/cm <sup>3</sup> )	$C_0$ (cm/s)	$S$ (-)	$\Gamma$ (-)	$C_v$ (erg/g-K)
<i>Steel (RHA)</i>	7.85	4.5e5	1.49	2.17	4.41208e6
<i>Uranium</i>	18.62	2.487e5	1.56	2.32	1.05132e6
<i>Copper</i>	8.93	3.94e5	1.49	1.99	3.92951e6
<i>Tungsten</i>	17.76	4.03e5	1.237	1.67	1.35292e6
<i>Steel (Hardened)</i>	7.85	4.5e5	1.49	2.17	4.41208e6

Table 5.2 Johnson-Cook Strength Parameters used in validation problems

	$\nu$ (-)	$A$ (d/cm <sup>2</sup> )	$B$ (d/cm <sup>2</sup> )	$C$ (-)	$M$ (-)	$N$ (-)	$T_{melt}$ (K)
<i>Steel (RHA)</i>	0.283	1.0e10	0.78e10	0.004	1.0	0.106	1783.0
<i>Uranium</i>	0.3	1.79e10	1.121e10	0.007	1.0	0.25	1497.9
<i>Copper</i>	0.333	8.97e8	2.9187e9	0.025	1.09	0.31	1380.7
<i>Tungsten</i>	0.281	1.365e10	0.1765e10	0.016	1.0	0.12	3695.0
<i>Steel (Hardened)</i>	0.299	0.81e10	0.5095e10	0.014	1.03	0.26	1818.0

### Frictionless Block Sliding

The first three validation problems involve frictionless sliding of two 3cm x 3cm x 3cm steel cubes sliding in opposite directions at 1.0e5 cm/s with friction forces being neglected. In both the normal and angled sliding problems, material was moved through a fixed Eulerian mesh with uniform 0.2cm hexahedral elements. To emphasize the improvements made by the contact algorithm developed for this work three conditions

were examined that sequentially increased the number of mixed elements present in the simulation. First, a normal block sliding problem was run with no mixed material elements. Second, the normal block sliding problem was run with a half element width offset along the material interface. Finally, to further increase the number of elements along the interface boundary the blocks were rotated  $45^\circ$  about the z-axis. The initial configuration of these simulations are shown in Figures 5.1, 5.2, and 5.3 for the mesh aligned normal sliding, half-element offset normal sliding, and angled sliding problems respectively. Both the ALEAS and CTH runs used the Mie-Gruneisen equation of state and the Johnson-Cook strength model for steel. The equation of state and constitutive parameters for these simulations are listed in Tables 5.1 and 5.2 respectively. In the ALEAS with contact enforcement runs the multi-material momentum (MMM) option was turned on. The MMM option implements the contact algorithm created for this work which assigns each material its own velocity field and then performs the contact enforcement described in Chapter 3. For this set of simulations there is no experimental analog. These simulations serve to demonstrate the improvements made by this work and the weakness of Eulerian methods with a single velocity field and mixture theory. The result in this set of simulations is considered accurate if no deformation takes place along the material interface boundary. The results of this set of simulations, along with all other simulations described in this chapter are presented in Chapter 6.

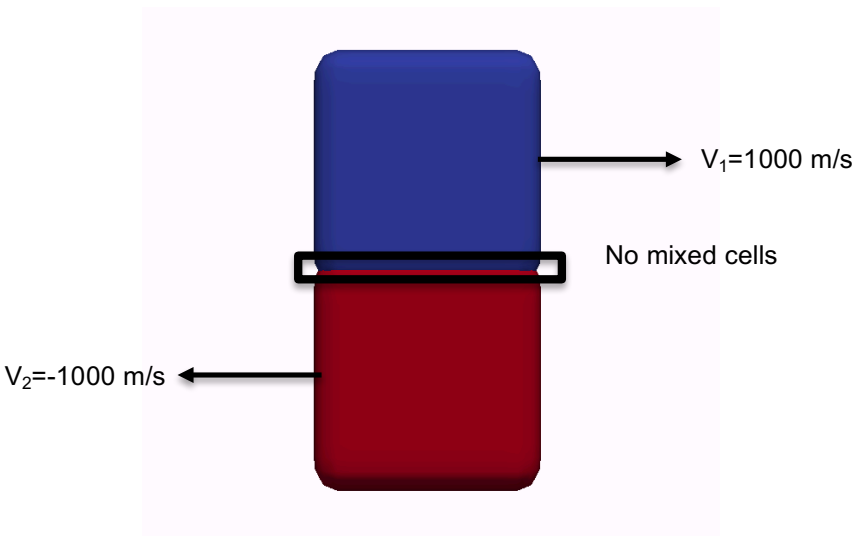


Figure 5.1: Setup for the mesh aligned normal block sliding problem.

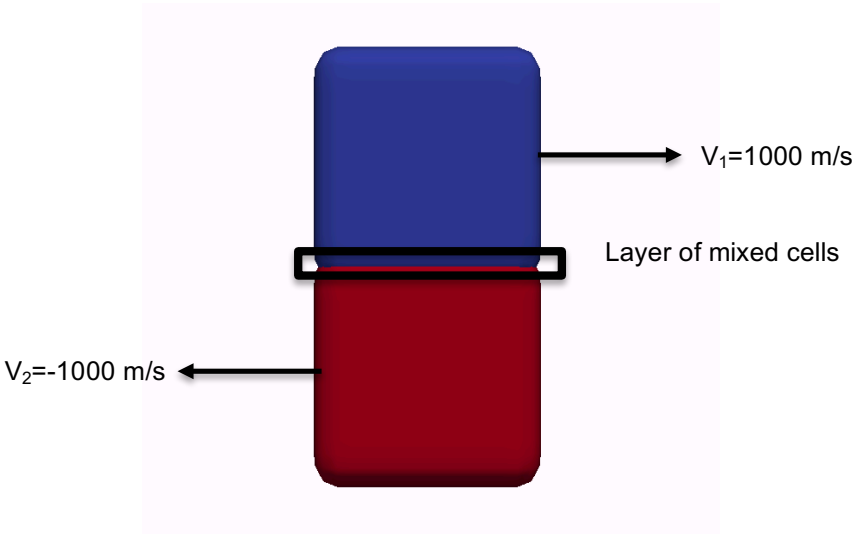
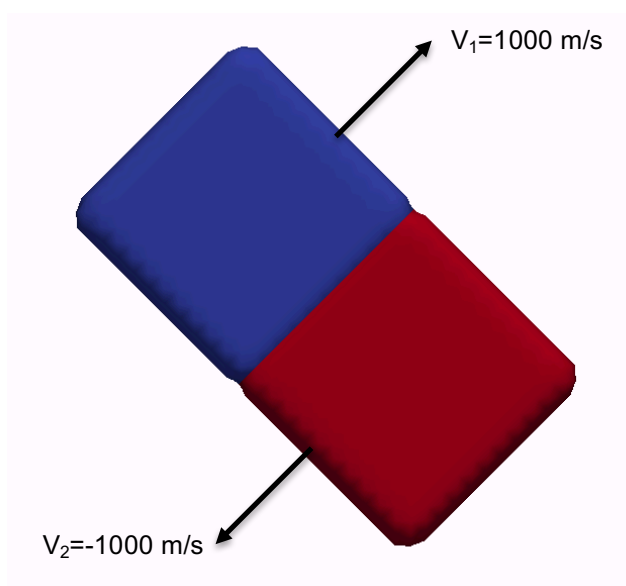


Figure 5.2: Setup for the half-element offset normal block sliding problem.



**Figure 5.3:** Setup for the angled block sliding problem

#### The Taylor Impact Test

The Taylor impact test was developed in 1948 by Taylor [87] to determine the dynamic yield strength of solids. This test involves flat-nosed cylindrical projectiles impacting a rigid target at a nominal incidence. This test is useful because of the fact that it subjects the material to a wide range of strain rates. Strain rates are very high at the impact front, but significantly lower in the undeformed section of the bar. As such, this is a very good test for revealing the strain hardening behavior of materials. Since the test is highly reproducible and relatively inexpensive to perform it has become a standard method for determining material properties in ductile metals, viscoplastic materials, and polymeric materials by measuring the final deformed shape. The test allows the estimation of mean stress, mean strain, and mean strain rate, as well as dynamic yield stress. These results will make up part of the constitutive models used in many numerical simulations [57] [6].

The Taylor impact test is also widely used for the verification of computational codes and the associated material models. Typically, a plot of the deformed configuration of the impactor is superimposed on the experimental data and a visual judgment of the accuracy is made. There are several other methods used to compare Taylor impact tests. These include comparing the final length of the deformed cylinder ( $L_f$ ), the radius of the mushrooming end of the cylinder ( $D_f$ ), the length of the elastic zone ( $X_f$ ), and the bulge at a given distance from the deformed end ( $W_f$ ), as shown in Figure 5.4. While the use of these criteria do not provide a complete comparison of the accuracy of the simulations with experimental results they do allow users to evaluate codes being implemented, as is the case in this work.

Detailed development of the theory and experimental methods of the Taylor impact test is outside the scope of this work and can be found in numerous sources, including [56], [57], [58], [68], and [87] among many others.

As a means of further demonstrating the improvements made in this work and test the validity of ALEAS, the Taylor impact test was performed to model rapidly evolving, dynamic contact. In this case, an annealed OFHC copper cylinder with a diameter of 7.62 mm and a length of 23.47 mm was impacted onto an infinitely rigid plate at 210 m/s as presented by Banerjee in [6]. For this case, a fixed Eulerian mesh with uniform 0.025 cm hexahedral elements was used. The impacting annealed OFHC copper cylinder was represented by a Mie-Gruneisen equation-of-state and a Johnson-Cook elastic plastic data set in both CTH and ALEAS. This problem was allowed to progress for 100 microseconds. Again the multi-material momentum option in ALEAS was turned on. To demonstrate the effect of mixed material elements simulations were performed with no

initial mixed cells as well as a half element offset to create a row of mixed cells along the material interface between the impactor and rigid plate. The setup of this problem is presented in Figures 5.5. A comparison will be made to the results of the experiment presented in [6] to gauge the validity of the numerical results.

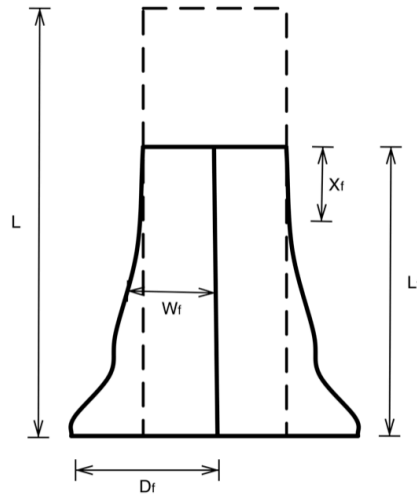


**Figure 5.4:** Schematic of Taylor impact specimen pre-deformation (dotted-line) and post-deformation (solid line), along with common comparison parameters

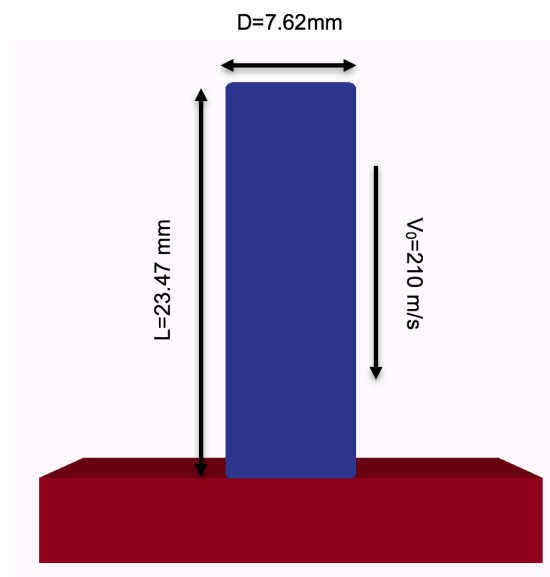


**Figure 5.5:** Setup for Taylor impact problem.



## Long Rod Penetration Problems

Due to their natural ability to form new free surfaces without mesh distortion a primary use of Eulerian hydrocodes is the simulation of penetration problems. However, due to the numerical inaccuracies that arise from mixture theory artificial bonding that takes place in elements with multiple materials leads to a nonphysical reductions in residual penetrator velocities. Therefore, to demonstrate the improvements made by ALEAS a number of simulations have been performed to compare a variety of penetration cases to experimental results to demonstrate that the artificial slowing of the penetrator that results from bonding that takes place in mixture theory is significantly reduced by implementing the method developed in this work.

### *Penetration by Projectiles with Combined Obliquity and Yaw*

Many ballistic penetration and defense applications can result in yawed and oblique impacts. For example, in an oblique impact of an unyawed penetrator into multi-layered spaced armor the first layer deflects and rotates the projectile resulting in a yawed interaction with subsequent layers. Fugelso and Taylor [38] examined the penetration of uranium alloy (U 0.75 wt% Ti) rods into steel targets at a variety of yaws, obliquities, thicknesses, and velocities. As a means of validating the advantages of the method implemented in ALEAS MMM this work will use the three test conditions presented by Cagliostro, et al. [24] which utilized data from Fugelso and Taylor [38] to validate the MESA code.

Figure 5.6 illustrates the orientation of the central axis of the rod and its velocity vector relative to a thin plate at  $+10^\circ$ ,  $0^\circ$ , and  $-10^\circ$  yaw at an obliquity of  $65^\circ$ . In this figure the obliquity,  $\gamma$ , is defined as the angle between the velocity vector of the rod and the

plate normal using a coordinate system fixed to the plate. The angle  $\beta$  is the angle between the central axis of the penetrator and the plate. Therefore, the yaw angle,  $\alpha$ , is defined as  $\gamma - \beta$ , which can be interpreted as the difference between the angle of the central axis of the rod and its velocity vector.

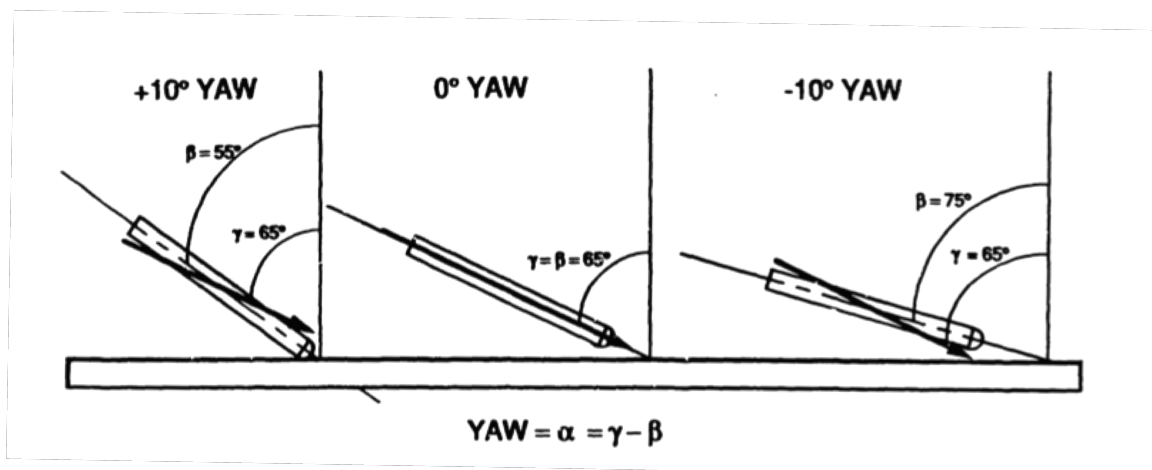


**Figure 5.6:** Rod-plate geometries for oblique impacts at positive, zero, and negative yaws.

These calculations are performed as a means of assessing the effects of positive, negative, and zero yaws on oblique impacts of penetrators into thin plates. Results will be compared to those obtained by Fugelso and Taylor.

In the experiments conducted by Fugelso and Taylor, stable yawed impacts were obtained by moving a target plate with a specified obliquity into the path of a projectile having little or no initial yaw. Positive yaws were obtained by explosively launching a thin plate away from the projectile, while negative yaws were obtained by launching the plate towards the projectile.

The penetrators were cylindrical rods with hemispherical tips composed of uranium alloy (U-0.75 wt% Ti). They had a length of 7.67 cm and an aspect ratio (L/D) of 10. The mass of the projectile was 65 g. The plates had a thickness of 0.64 cm and were composed of rolled homogeneous armor (RHA). The initial velocities and orientations of the rods and plates were designed in such a way that the rod impact velocity relative to the plate was 1.29 km/s at an obliquity of  $65^\circ$  for yaws of  $-9.3^\circ$ ,  $0^\circ$ , and  $+10.3^\circ$ .

Rod and plate materials were modeled using the Mie-Gruneisen equation of state and Johnson-Cook strength model using the characteristics for Uranium and Steel (RHA) in Table 5.1. The mesh consisted of 0.125 cm hexahedral elements. Simulations ran to 100 microseconds. The initial conditions for the  $0^\circ$ ,  $-9.3^\circ$ , and  $+10.3^\circ$  yaw cases are shown in Figures 5.7, 5.8, and 5.9 respectively.

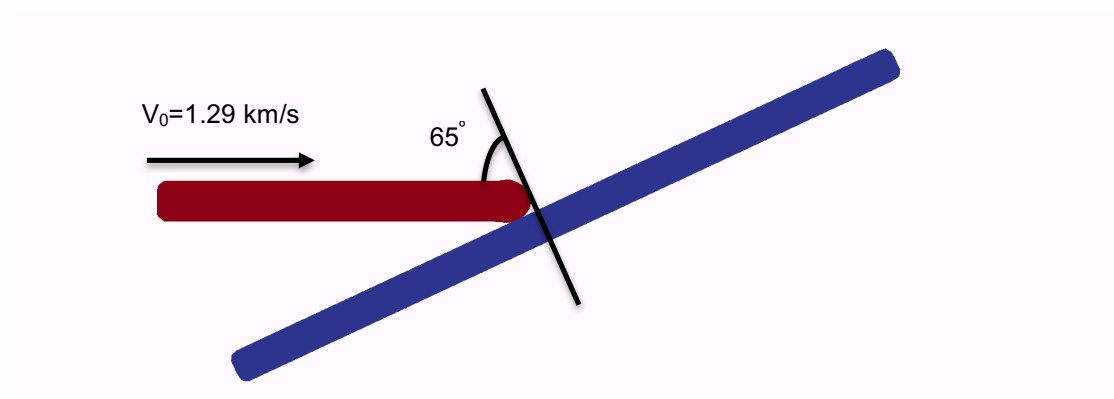


**Figure 5.7:** Initial conditions for  $0^\circ$  yaw case.

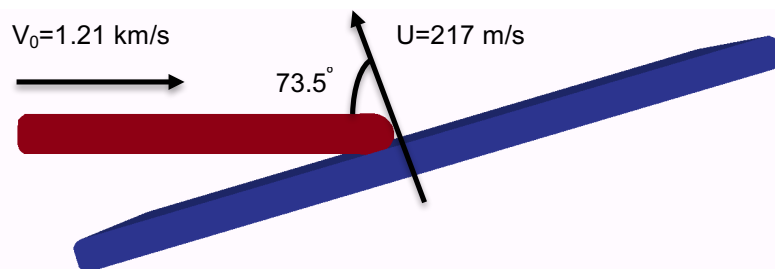


**Figure 5.8:** Initial conditions for  $-9.3^\circ$  yaw case.

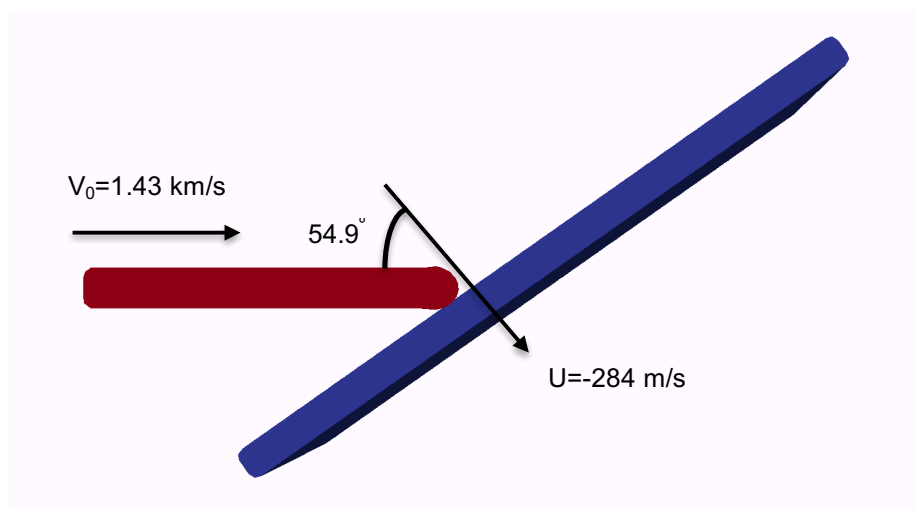


**Figure 5.9:** Initial conditions for  $+10.3^\circ$  yaw case.

### *Normal Impact of Long Rods into Steel Targets*

In addition to oblique impacts with various obliquities and yaws, Fugelso and Taylor also present data for normal ( $0^\circ$  obliquity,  $0^\circ$  yaw) penetration of long uranium rods into a 5.08 cm thick RHA target. As a means of further comparison these experiments will be modeled in ALEAS and CTH and results will be compared to experimental data. The penetrators used in these experiments had the same characteristics as those used for the oblique impacts. The impact velocity of the penetrator was 1.2 km/s. In the experiments the target stopped the penetrator before just before perforating, so

comparisons will be made to PHERMEX radiographs presented in the Fugelso and Taylor report and comparisons will be made to penetration depth and residual length of the penetrator. The mesh consisted of 0.1 cm hexahedral elements. The initial conditions for 5.08 cm plate penetration is shown in Figures 5.10.

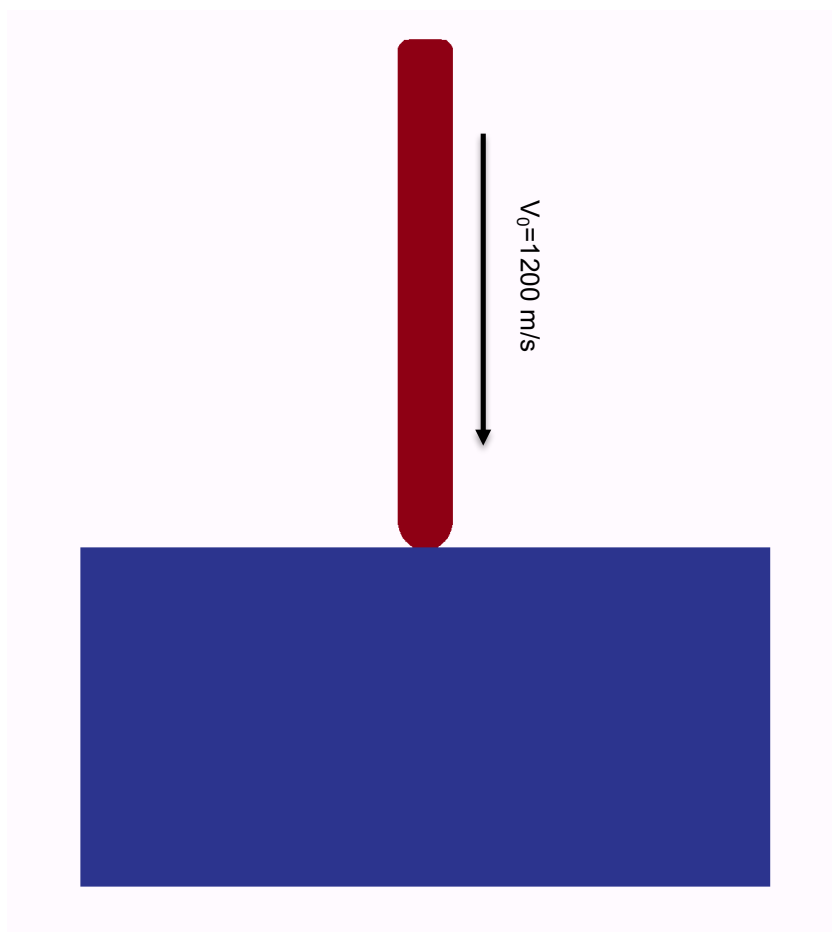


**Figure 5.10:** Initial conditions for 5.08 cm plate penetration.

Another class of impact and penetration events considered for the validation of ALEAS was the penetration of tungsten alloy long rod projectiles into semi-infinite steel targets. This class of problem has been studied extensively by Hohler and Stilp [45], [46]

and reproduced numerically by Anderson, et al. [2]. This class of problems is frequently used as a validation of hydrocodes, including work done by Park, et al. [75] to verify the implementation of the two-dimensional Eulerian X-FEM contact method in the ALEGRA code which serves as the source of data for the validations carried out here. The setup for the simulations, shown in Figure 5.11, consists of a tungsten-heavy-alloy cylindrical penetrator with diameter of 0.5 cm and length of 5 cm impacting a semi-infinite hardened steel target at initial velocities of 500, 1000, 1500, 2000, and 3000 m/s. Results of both CTH and ALEAS runs will be compared to a semi-analytical empirical fit originally devised by Lanz and Odermatt, and modified by Rapacki, et al. as presented in [75]. The semi-analytic fit for normalized penetration depth ( $P/L$ ), a commonly used measure of penetration efficiency, is given by

$$\frac{P}{L} = a \sqrt{\frac{\rho_P}{\rho_T}} e^{-\left(\frac{2S}{\rho_P V_P^2}\right)} \quad (5.1)$$

In this equation, the target material penetration resistance is represented by the quantity

$$S = k(BHN)^M \quad (5.2)$$

which has units of stress. The projectile and target densities are given by  $\rho_P$  and  $\rho_T$ , then striking velocity of the penetrator is given by  $V_P$ , and the Brinnell hardness of the target is given by  $BHN$ . The quantities  $a$ ,  $k$ , and  $M$  are obtained from a least squares fit of the formula to experimental data. For the experiment considered here the fit parameters have values of  $a=1.22817$ ,  $k=1.63084$  GPa, and  $M=0.373287$ .



**Figure 5.11:** Initial conditions for penetration of an  $L/D=10$  tungsten rod into a semi-infinite steel target.

### Sod Shock Tube Problem

The Sod shock tube is a commonly used verification to assess the accuracy of fluid dynamics code which was first introduced by Gary Sod in 1978 [104]. The test consists of a one-dimensional Riemann problem in which an ideal gas at two different pressure and density states is initially separated by a diaphragm as seen in Figure 5.12. At time  $t=0$  the diaphragm is broken resulting in the formation of three regions as the shock progresses through the medium, as seen in Figure 5.13. Regions 1 and 5 contain the undisturbed states of the gases, region 2 contains the rarefaction wave, region 3 contains the contact discontinuity, and region 4 contains the shock discontinuity. An analytical solution to the Sod shock tube problem can be developed to determine how well a code captures and resolves shocks and contact discontinuities. Comparisons will be made for density, pressure, and velocity at 10 ms given the initial conditions in Table 5.3. A Gamma Law equation-of-state was implemented in ALEAS for this validation problem to allow for the simulation of ideal gases. The Gamma Law equation-of-state has the form:

$$p = \rho(\gamma - 1)e \quad (5.3)$$

where  $\gamma = C_p/C_v$ ,  $\rho$  is the gas density, and  $e$  is the specific internal energy. In CTH the Ideal Gas equation-of-state was used with the  $B_v$  parameter set to zero, giving the Gamma Law equation-of-state. The verification case under consideration consisted of a 0.1 cm x 0.1 cm x 1 cm gas filled channel with an initial discontinuity at 0.5 cm. The mesh consisted of 200 elements in the Z-direction and 20 elements in the X- and Y-directions, having a size of 0.005 cm.

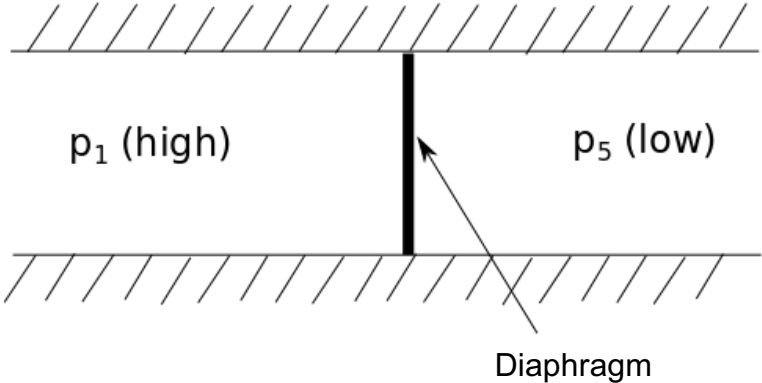


**Figure 5.12:** Initial condition of the Sod shock tube verification.

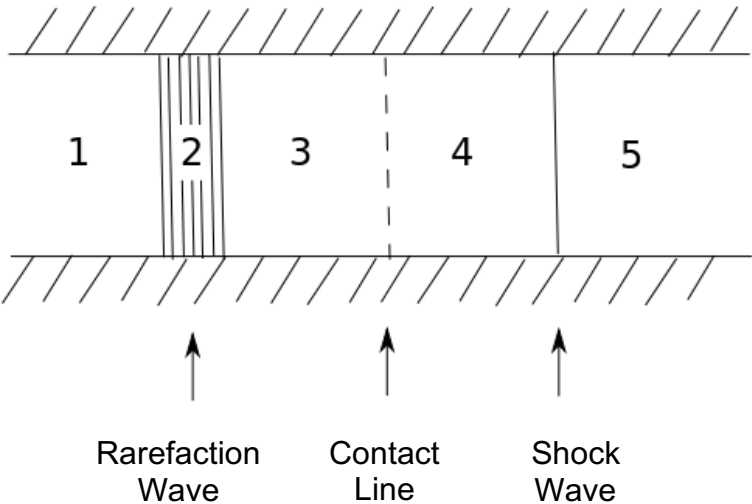


**Figure 5.13:** Sod shock tube at time  $t > 0$ .



Table 5.3: Initial states for the Sod shock tube verification.

	<i>Left</i> $0 \text{ cm} \leq x \leq 0.5 \text{ cm}$	<i>Right</i> $0.5 \text{ cm} \leq x \leq 1 \text{ cm}$
Initial Density ( $\text{g}/\text{cm}^3$ )	1.0	0.125
Initial Pressure ( $\text{d}/\text{cm}^2$ )	100.0	10.0
Initial Specific Energy (erg)	250.0	200.0
Gamma (--)	1.4	1.4

## CHAPTER 6

### DISCUSSION AND RESULTS

#### Results of Numerical Validation and Verification Problems

In this section the results of the numerical validation problems described in Chapter 5 are presented and discussed. These numerical validations will serve to demonstrate the advantages of the Eulerian contact method described in this work as well as a comparison to problems which are handled well by existing Eulerian methods. As discussed in Chapter 4, the Eulerian hydrocode CTH along with the single material momentum (SMM) mixture theory formulation of ALEAS were used to compare to the multi-material momentum (MMM) contact formulation of ALEAS developed for this work. Since CTH uses a finite volume formulation, compared to the finite element formulation in ALEAS, agreement between results is not expected to be exact. Further difference between the two codes include the use of the van Leer MUSCL algorithm for material flux in CTH versus the lower order donor cell approach taken in ALEAS. CTH also uses face centered velocities, whereas ALEAS uses node-centered velocities, and a variety of other factors, including differences in implementation of boundary conditions, treatment of the stress tensor, and handling of multi-material cells will also affect results.

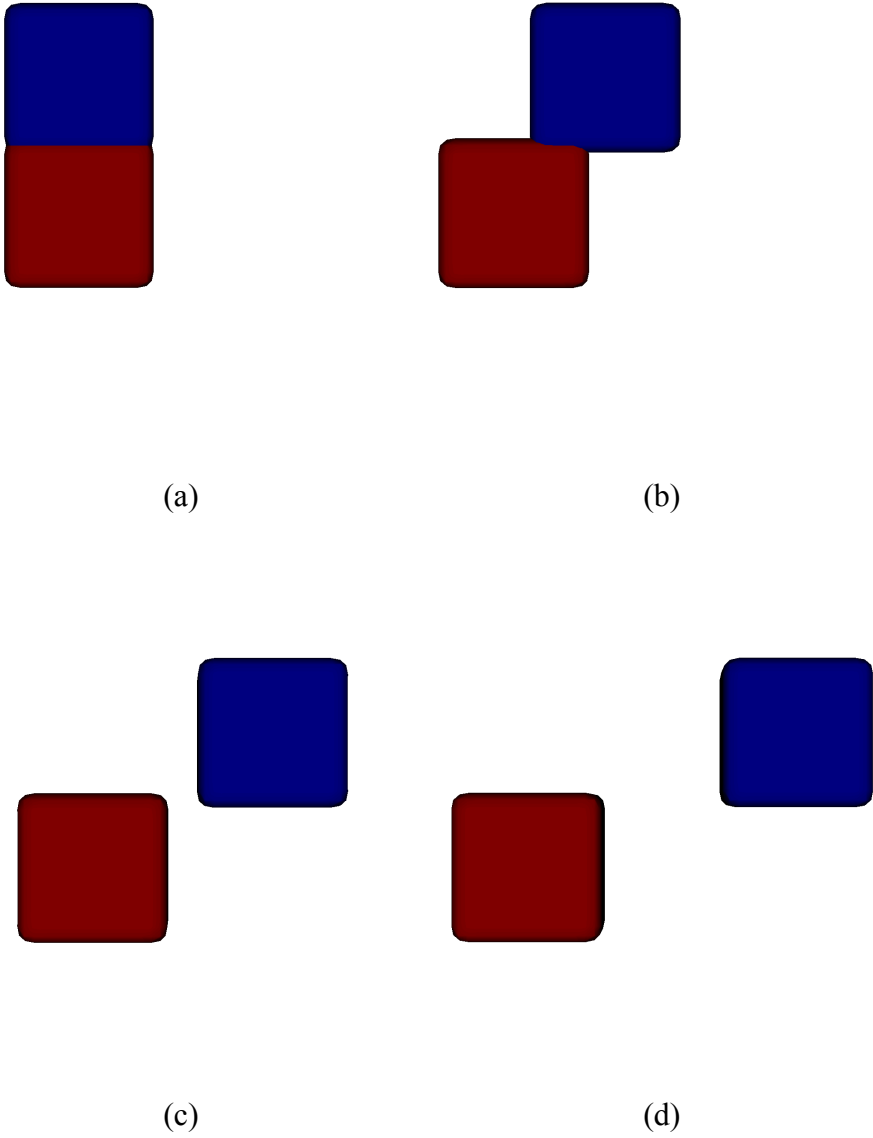
### Frictionless Block Sliding

Three frictionless block sliding problems were conducted to demonstrate the issues associated with a traditional Eulerian formulation which are solved using the approach taken in this work. The normal frictionless block sliding problems indicated that no intra-cell material replacement is taking place in the multi-material contact scheme. The two blocks slid normally to each other at 1000 m/s as discussed previously. In the ALEAS MMM runs there is no deformation of the blocks in the mesh aligned case as can be seen in Figure 6.1 and 6.4. The ALEAS SMM and CTH runs show an erroneous deformation along the material interface in both the mesh aligned and offset mesh cases, as can be seen in Figures 6.2 and 6.5 for ALEAS SMM, and 6.3 and 6.6 for CTH respectively, with the deformation being greater in the offset mesh case due to increased shear stresses being introduced in the mixed elements at the interface. In the mesh aligned case only the four nodes on the face at the interface will have a zero velocity, so the effects are not as pronounced. In each case an erroneous shear strain is added as a result of the material bonding taking place in mixture theory. This results in the presence of the trailing material which is evident as the blocks move away from one another and also imparts a moment on the blocks causing them to rotate as they move away from one another.

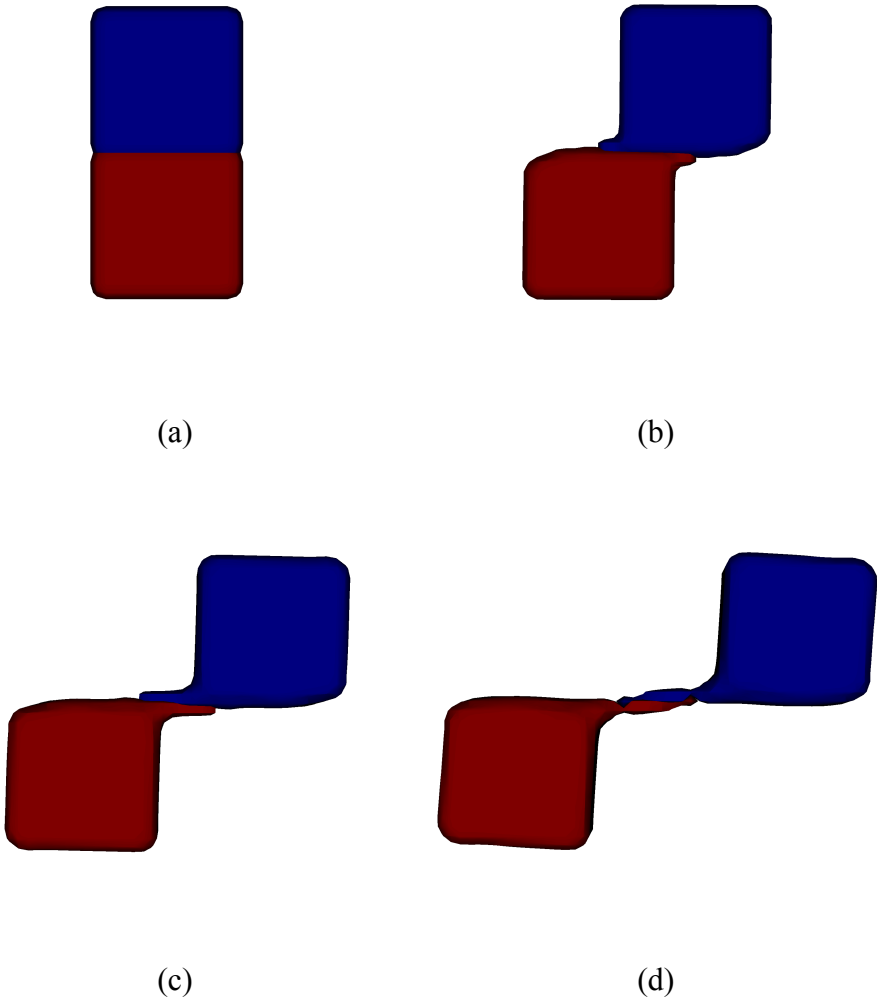
The problems associated with multi-material contact in a traditional Eulerian scheme are further illustrated by the angled frictionless block sliding problem. As discussed in Chapter 5, there was a large amount of deformation along the interface boundary in the ALEAS SMM and CTH calculations, shown in Figures 6.8 and 6.9. This

also resulted in the presence of a large amount of trailing material as the blocks separated from one another. This is indicative of large amounts of material replacement and material bonding taking place along the interface boundary. The increased deformation shown in Figures 6.8 and 6.9 over Figures 6.2, 6.3, 6.5, and 6.6 can be attributed to the increased number of cells in which mixture theory is implemented. By angling the blocks to slide at a 45° angle about the Z-axis the number of cells falling along the material interface is greatly increased and thus causes the problem with mixture theory to be emphasized. When the contact method developed in this work was implemented, however, there was no deformation present along the material interface of the blocks and no material replacement taking place. As such, the pure advection problems have been validated using the multi-material Eulerian scheme with contact described in the formulation section. Figure 6.7 illustrates the ALEAS MMM Eulerian formulation with contact modeling, while Figures 6.8 and 6.9 depict traditional Eulerian methods implemented in ALEAS SMM and CTH for the angle block sliding problem. In CTH the amount of trailing material can be adjusted by changing the  $PFRACn$  parameter in the fracture card. In the cases presented here, a reasonable value of  $-18.0e9$  dynes/cm<sup>2</sup> for RHA was used. Decreasing this value will result in a reduction of trailing material, but it should be noted that this is an ad hoc method for simulating sliding. Since this method involves fracture it does not provide a realistic description of the interface, which are not physically bonded. However, since ALEAS MMM does not use cell mixture theory, the use of a fracture model is unnecessary and, thus, not implemented here. Since no fracture model has currently been implemented in ALEAS the amount of trailing material in the ALEAS SMM cases are slightly greater than those seen in CTH.

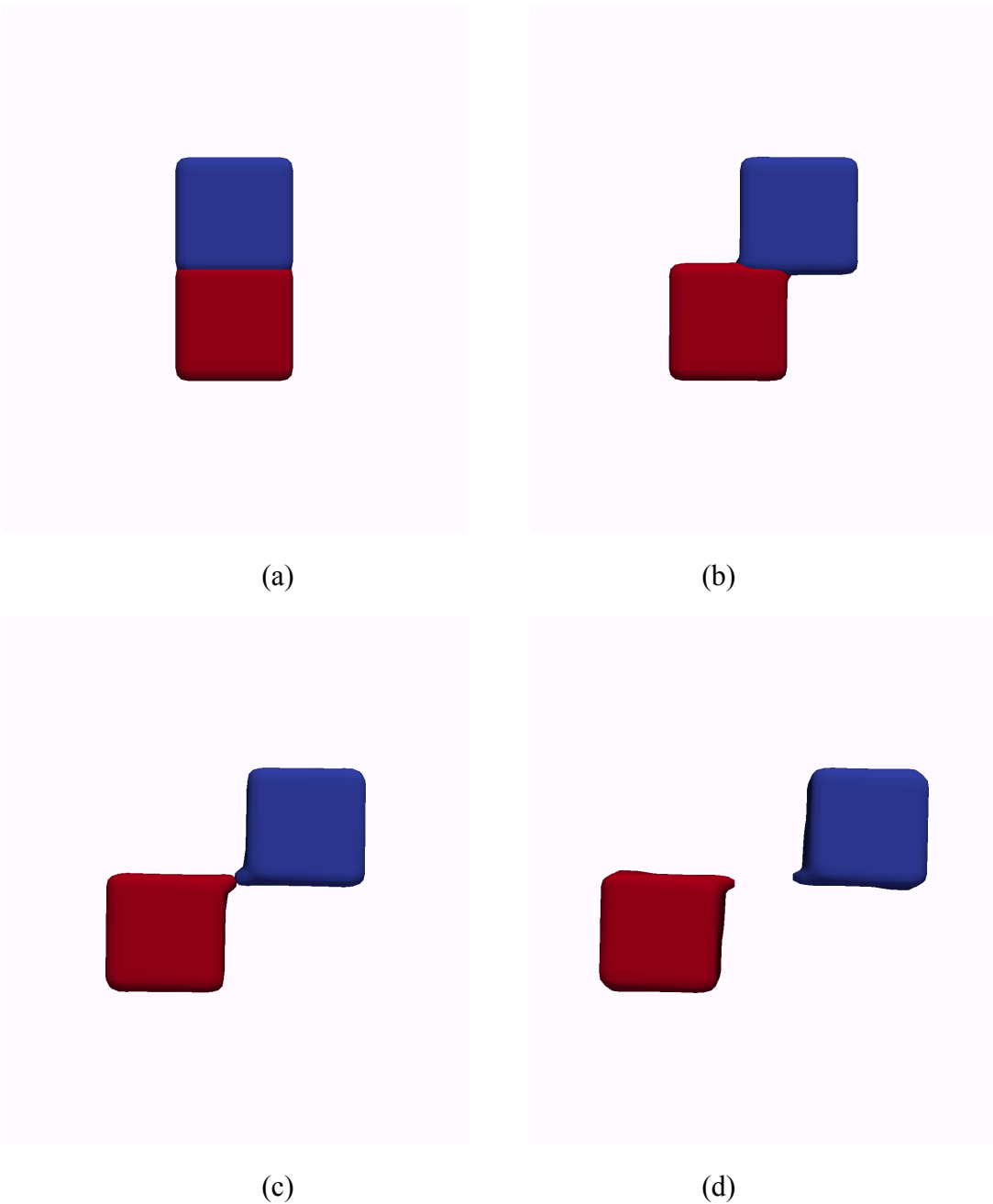
Furthermore, CTH includes a pair of options that attempt to remedy the artificial bonding along material interfaces. The SLIDE option attempts to solve this issue by setting the shearing velocity gradients to zero, approximating the condition that the velocity is discontinuous along the sliding interface. The BLINT option creates a boundary layer between sliding materials. A detailed description of the BLINT algorithm in two-dimensions can be found in [83]. It is important to note that the CTH user's manual [81] indicates that the SLIDE option can produce unexpected results and should be used with care, and that the BLINT option is not fully implemented in three-dimensions. To determine the benefits and limitations of these options, runs were conducted using both options with the mesh aligned and mesh offset normal block sliding cases. As can be seen in Figure 6.10, both the SLIDE and BLINT options perform extremely well in the mesh aligned case where no mixed elements are present, yielding results comparable to those obtained in ALEAS MMM. However, when a layer of mixed elements was introduced both options resulted in larger amounts of trailing material than was seen in the CTH run without the sliding contact options activated. Subsequent tests with the angled sliding problem further illustrated that these options do not perform well for mixed element cases in three dimensions. As a result, it was determined that the applicability of these options was limited in three-dimensions and, as such, they would not be used for comparison of subsequent validation simulations.



**Figure 6.1:** ALEAS MMM normal block sliding problem with no initial mixed elements at 0, 10, 20, and 30  $\mu$ s.

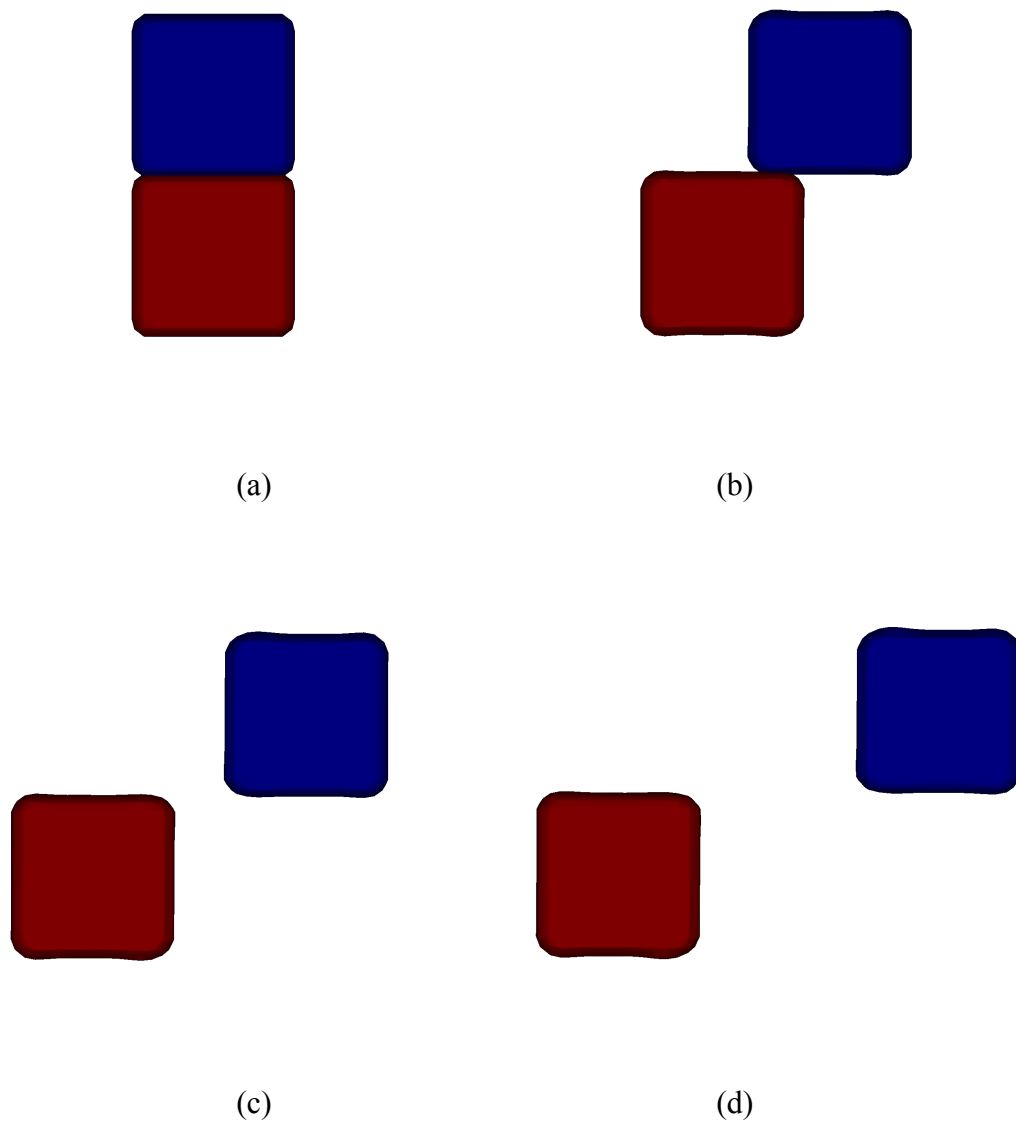


**Figure 6.2:** ALEAS SMM normal block sliding problem with no initial mixed elements at 0, 10, 20, and 30  $\mu$ s.

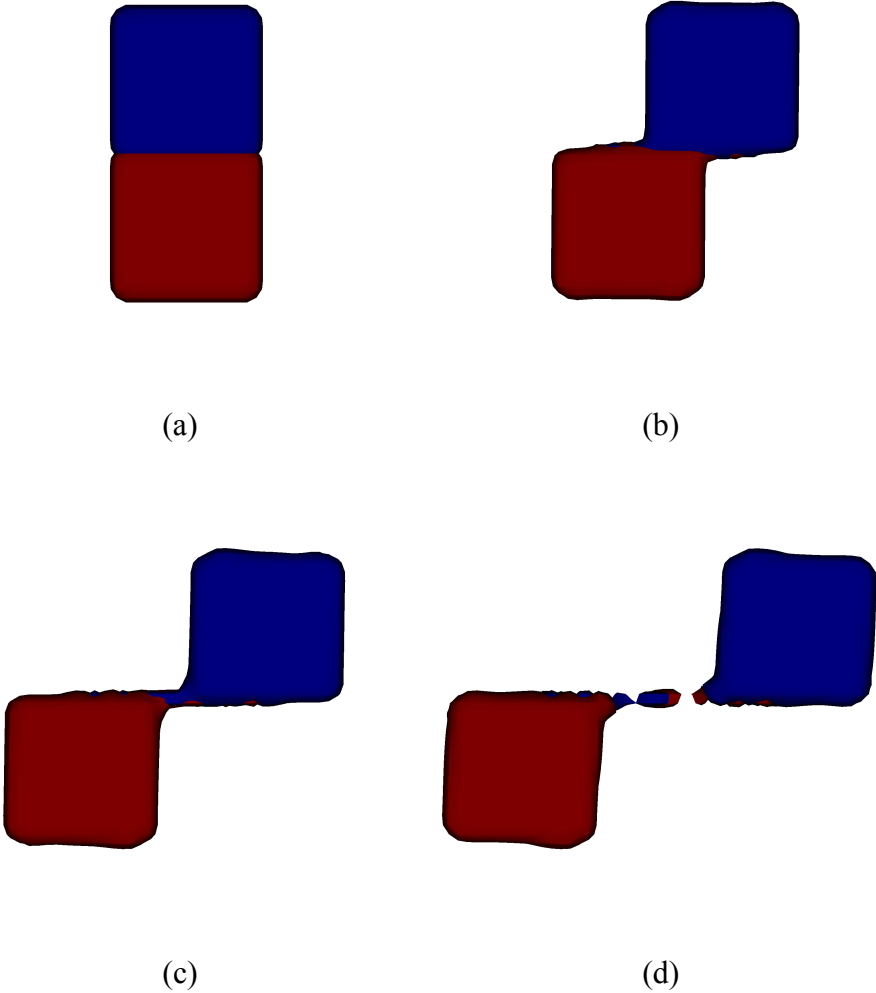


**Figure 6.3:** CTH normal block sliding problem with no initial mixed elements at 0, 10, 20, and 30  $\mu$ s.

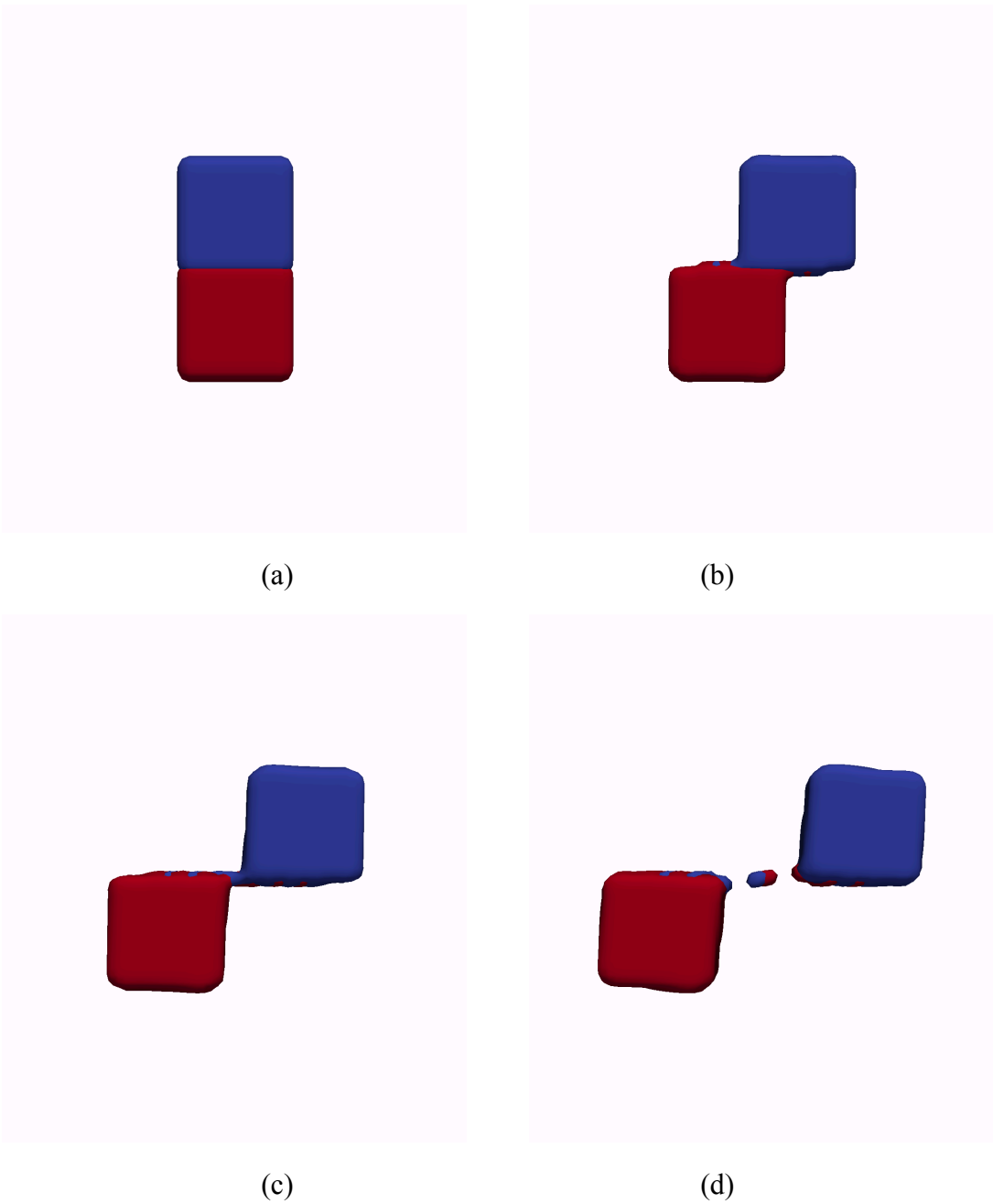




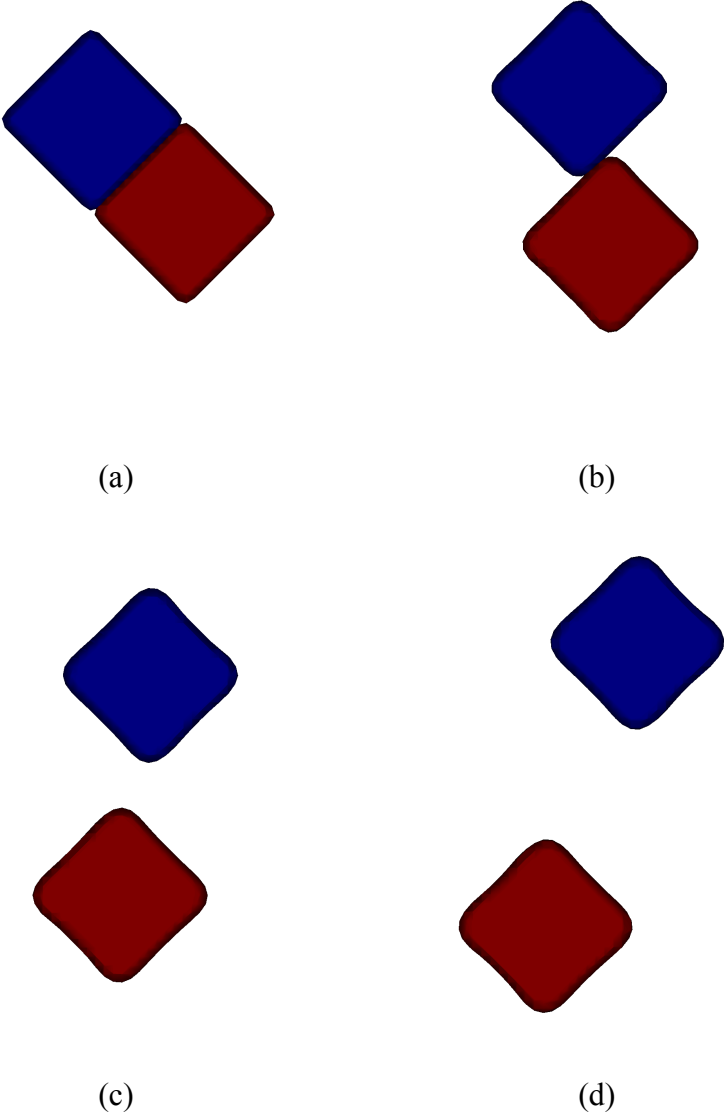
**Figure 6.4:** ALEAS MMM normal block sliding problem with layer of initial mixed elements at 0, 10, 20, and 30  $\mu\text{s}$ .



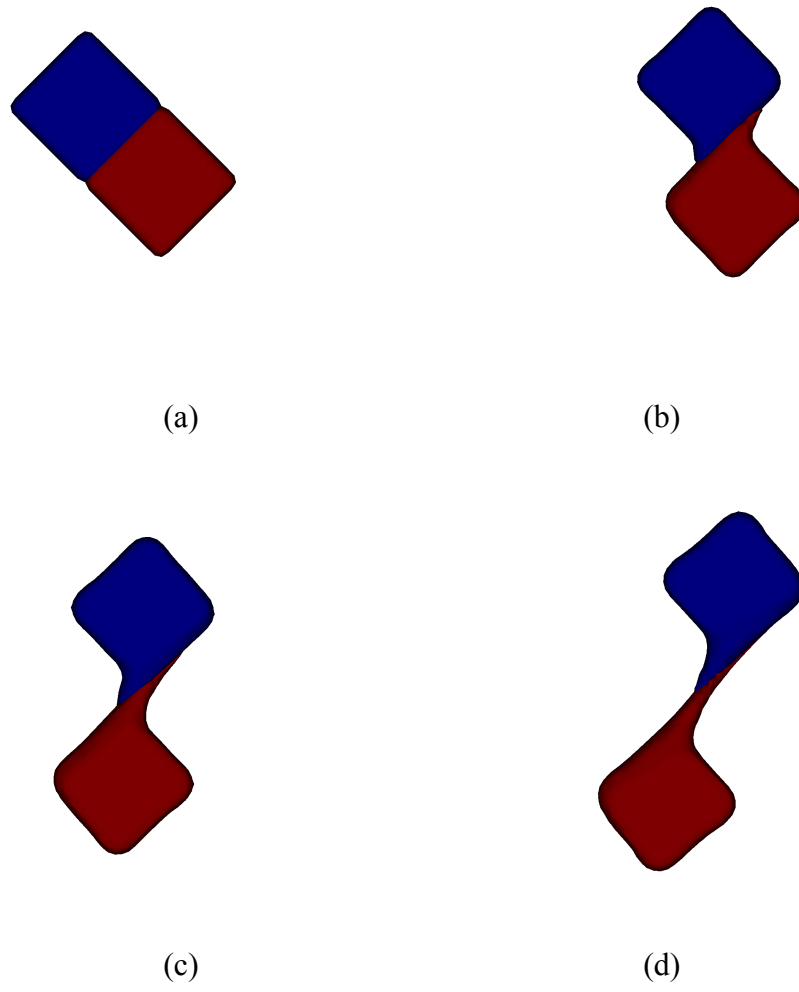
**Figure 6.5:** ALEAS SMM normal block sliding problem with layer of initial mixed elements at 0, 10, 20, and 30  $\mu$ s.



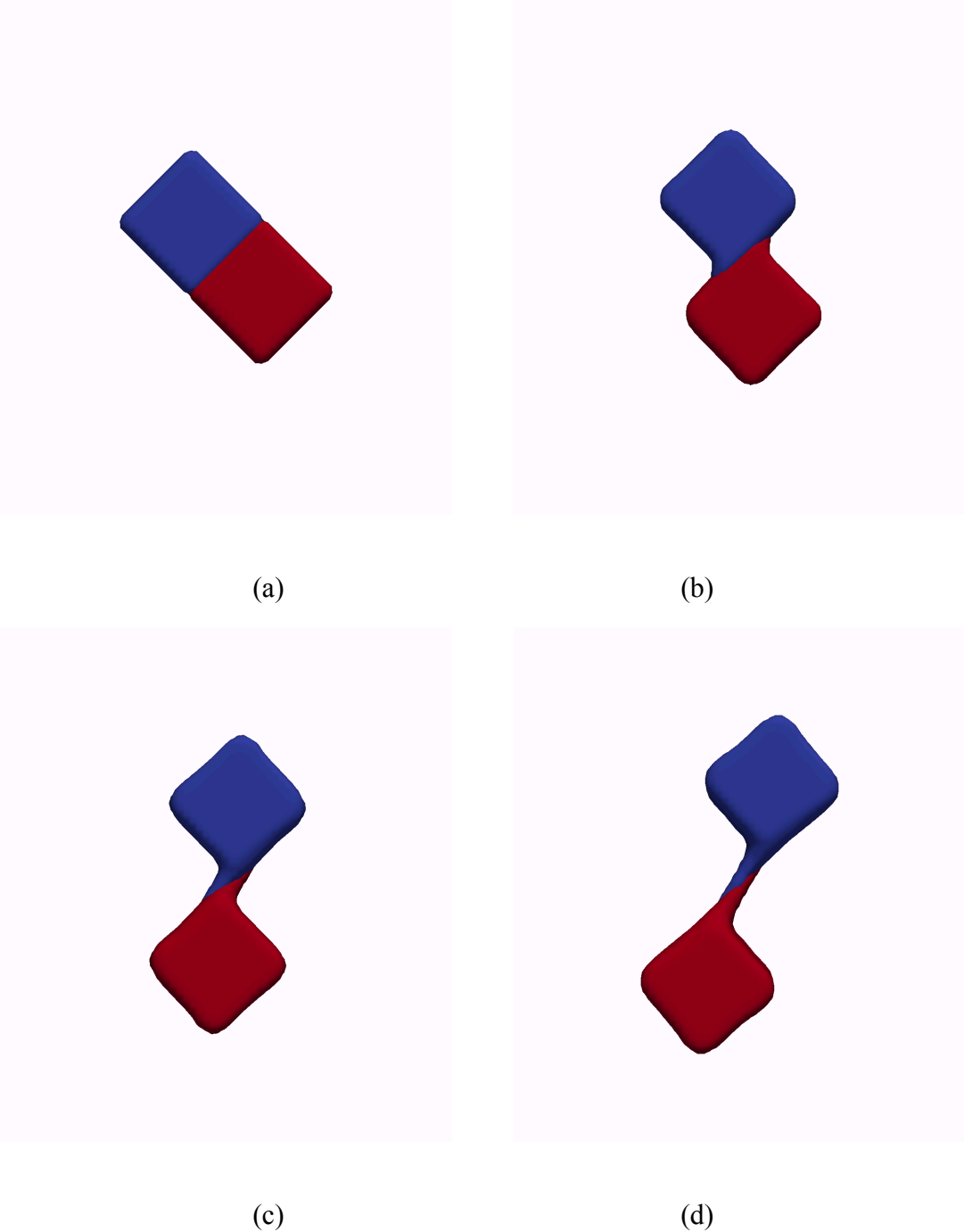
**Figure 6.6:** CTH normal block sliding problem with layer of initial mixed elements at 0, 10, 20, and 30  $\mu$ s.



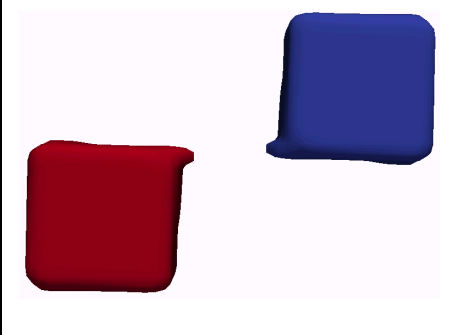
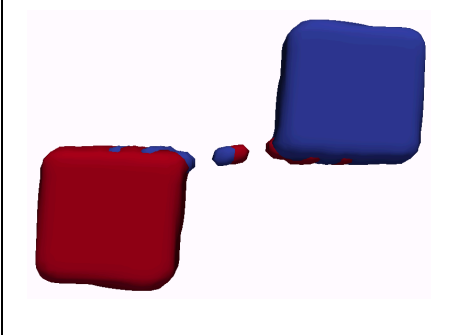
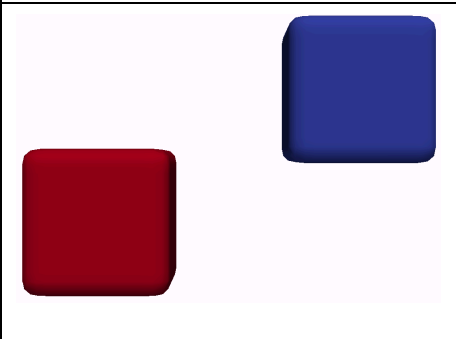
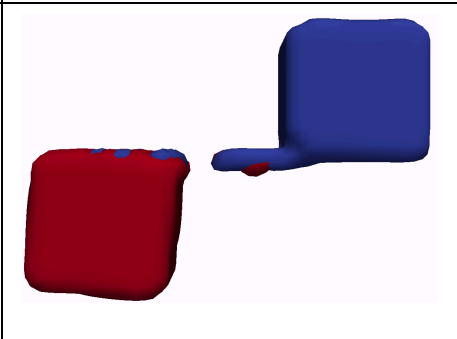
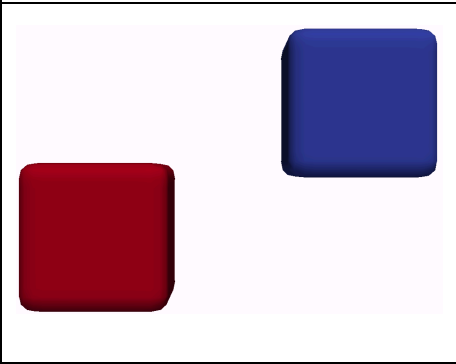
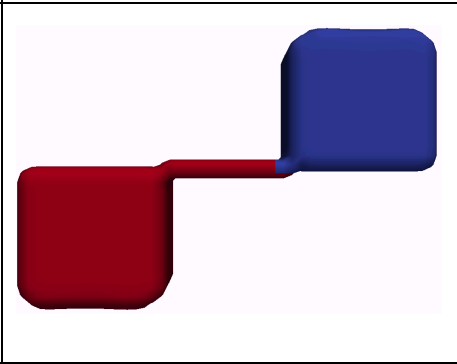
**Figure 6.7:** ALEAS MMM angled block sliding problem at 0, 10, 20, and 30  $\mu$ s.



**Figure 6.8:** ALEAS SMM angled block sliding problem at 0, 10, 20, and 30  $\mu$ s.



**Figure 6.9:** CTH angled block sliding problem at 0, 10, 20, and 30  $\mu$ s.

<i>CTH Option</i>	<i>Mesh Aligned</i>	<i>Offset Mesh</i>
<i>Standard Mixture Theory with Fracture</i>		
<i>BLINT</i>		
<i>SLIDE</i>		

**Figure 6.10:** Comparison of available sliding interface options in CTH

## Taylor Impact Tests

In addition to block sliding and advection problems it was also desired to model contact-impact using the algorithm developed in this work. Since Eulerian hydrocodes are the primary method used for modeling problems that involve large deformations as well as hypervelocity impacts and penetrations, it was desirable to implement the method presented here for that class of problems. This method can thus be used to much more accurately model the physics taking place in the problem. In the Taylor impact test the effects of friction along the interface between the impactor and the rigid target can be neglected, and as such no material replacement along the interaction boundary of the materials should occur.

While it is possible to perform the Taylor test in CTH and ALEAS SMM using a reflective boundary condition, the goal here is to demonstrate contact between a rigid target and a deforming impactor with the target explicitly modeled. CTH does include an option to model a rigid material, which is essentially an internal boundary condition, but in testing of this option parts of the impactor would pass through the rigid boundary rendering the solution invalid. In order to simulate a rigid plate in CTH a plate of uranium alloy with a yield stress of  $1.0E+99$  was placed on a symmetry boundary. While this plate is not truly “rigid” the deformation is negligible and allows for a direct comparison to ALEAS. As can be seen in Figures 6.11 and 6.14 for the mesh aligned and offset mesh cases respectively, the results of the contact algorithm are directly reflected. The ALEAS MMM simulations showed that the lateral velocity of the copper impactor was nonzero at the interface, and as can be seen in Figures 6.17 and 6.18, the deformation profile of the impactor shows significant improvement over the ALEAS SMM and CTH



profiles for both the mesh aligned and offset mesh cases. Furthermore, at late time in the ALEAS MMM cases the impacting bar rebounds off of the rigid target. Material separation is commonly seen in multi-material algorithms that make use of a single-material velocity field; however, in those cases the separation is due to the use of multi-material fracture models. The rebounding occurring in this case, rather, is a direct result of the contact enforcement and has nothing to do with fracture [64]. The traditional Eulerian calculations performed in ALEAS SMM and CTH and displayed in Figures 6.12 and 6.15 and 6.13 and 6.16 demonstrate the advantages of using the contact enforcement method developed in this work. A summary of various measures of the final deformed shape is shown in Table 6.1. In Table 6.1  $L_f$  is the final deformed length of the impactor,  $R_f$  is the maximum radius of spread at the impact interface,  $X_f$  is the length of the undeformed section at the rear of the impactor, and  $W_f$  is the radius of the impactor at 0.4 cm from the impact front. Errors with respect the experimental data for each of these parameters is also reported. First, the spread of material along the interface was significantly reduced in ALEAS SMM and CTH, resulting in poor agreement to the deformation profiles shown in Figures 6.17 and 6.18. This is a direct result of the bonding and material replacement properties of traditional Eulerian methods that utilize mixture theory. In reality, the material should be free to move laterally along the surface of the rigid plate, however, since only a single velocity field is present the velocity of both materials within the element are the same and the shearing velocity gradients are non-zero resulting in the restriction of lateral movement of material. Furthermore, in the ALEAS SMM and CTH runs the bar remains bonded to the target at late time as the deformation reaches its maximum and the sign of the velocity changes. This should result

in rebounding of the bar as was seen in ALEAS MMM, but since no ad hoc fracture method was implemented in these runs the bar remains bonded to the plate, as is typical of mixture theory.

As can be seen in Figure 6.19, it is also interesting to note that at early time, starting around  $2\mu\text{s}$  and lasting until  $\sim 7\mu\text{s}$ , in the ALEAS MMM runs the center of the Taylor bar lifts off the rigid plate. This phenomenon is also noted in Lagrangian simulations of the Taylor impact experiment, but would be impossible to recreate in an Eulerian simulation using mixture theory, such as the ones conducted in this work using ALEAS SMM and CTH.

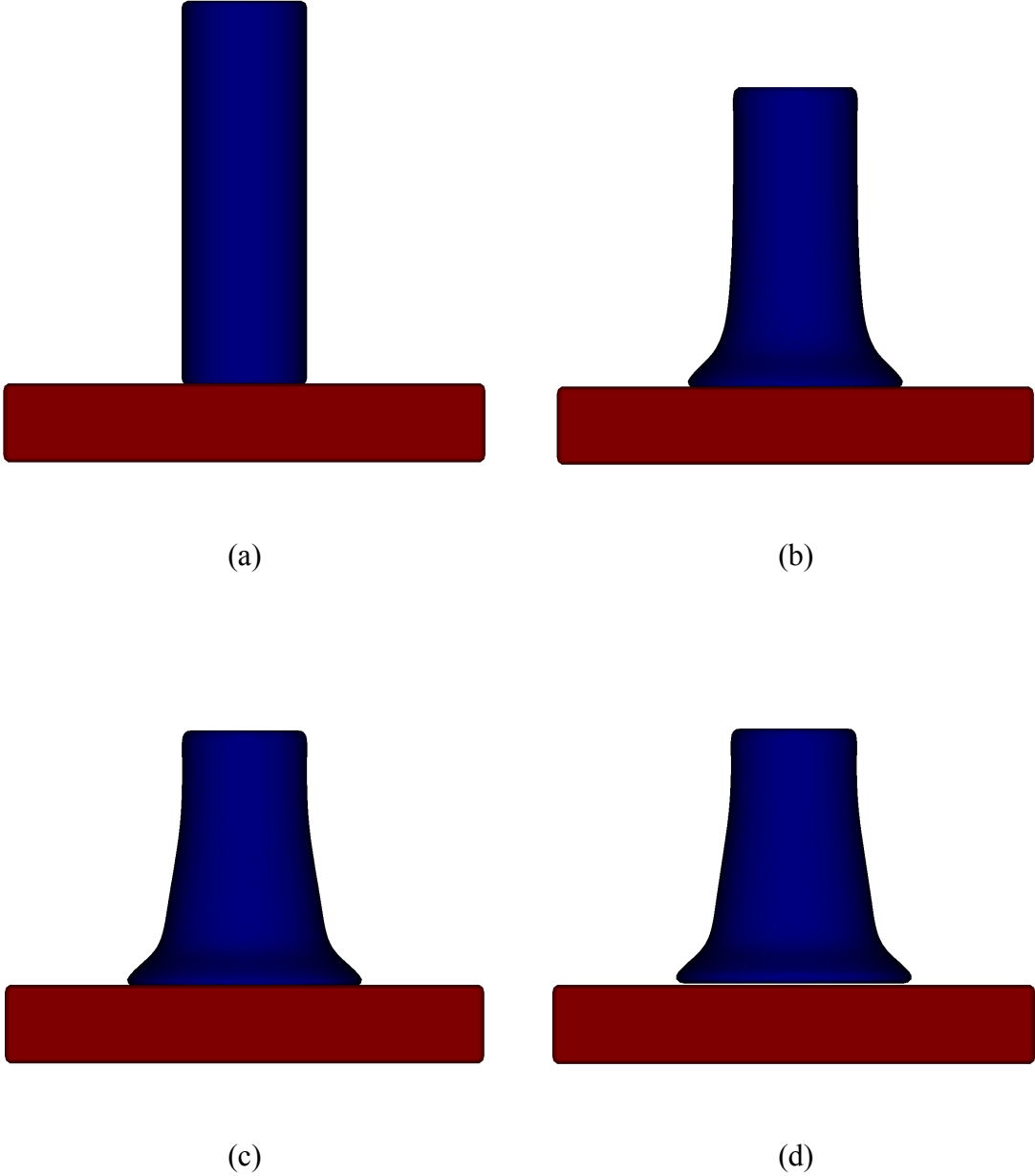


**Figure 6.11:** ALEAS MMM Taylor impact problem with no initial mixed cells at 0, 25, 50, and 100  $\mu$ s.

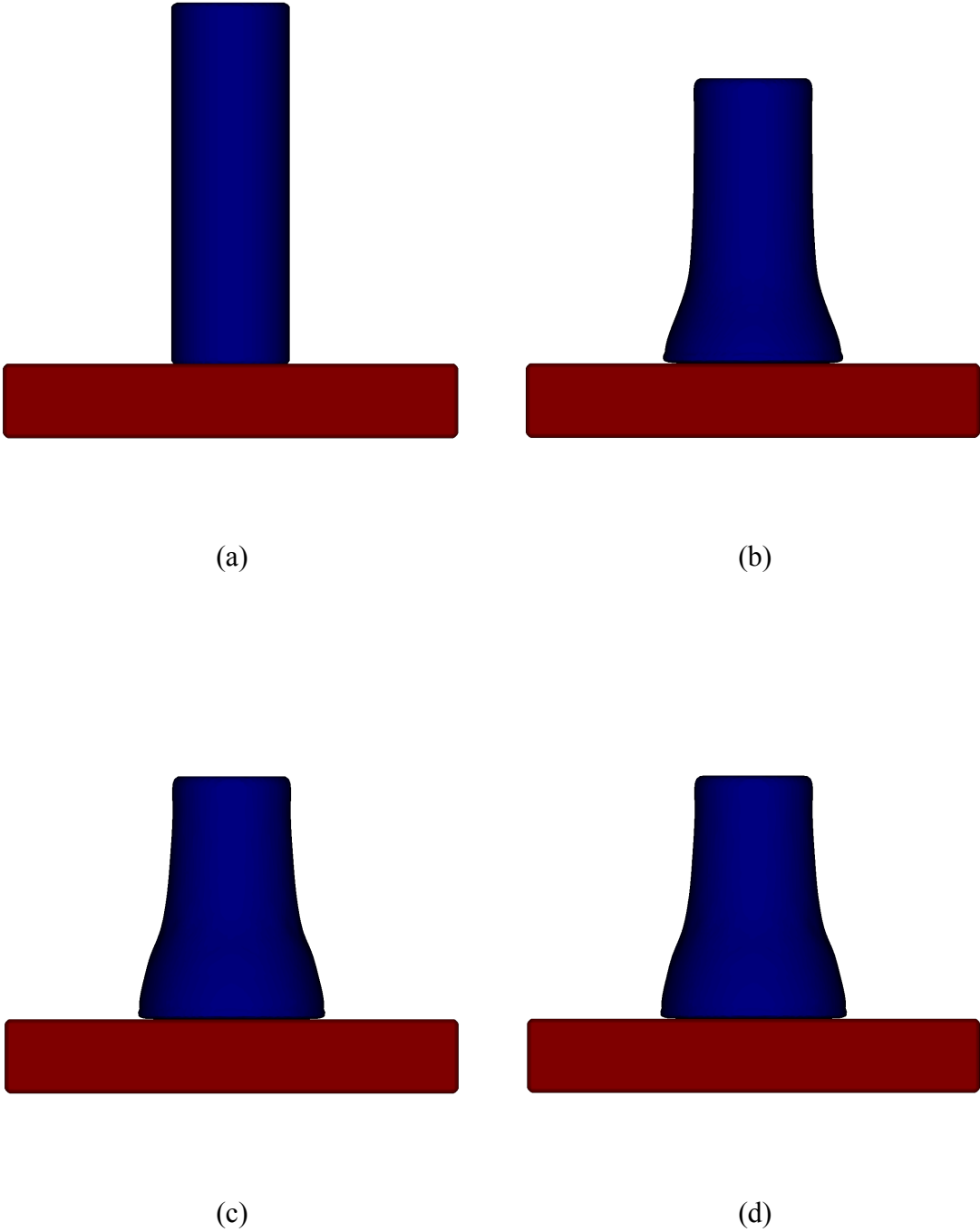


**Figure 6.12:** ALEAS SMM Taylor impact problem with no initial mixed cells at 0, 25, 50, and 100  $\mu$ s.

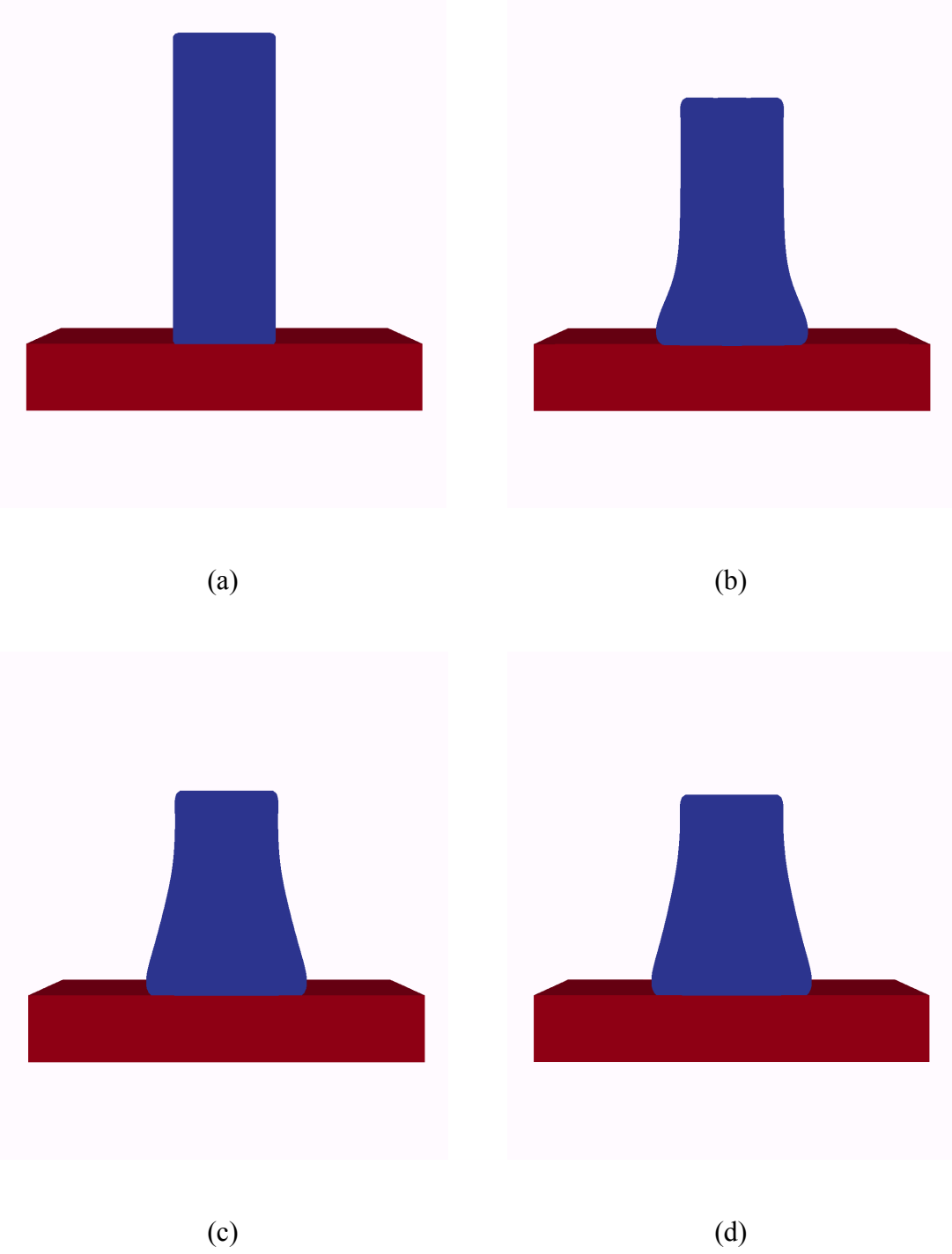


**Figure 6.13:** CTH Taylor impact problem with no initial mixed cells at 0, 25, 50, and 100  $\mu$ s.

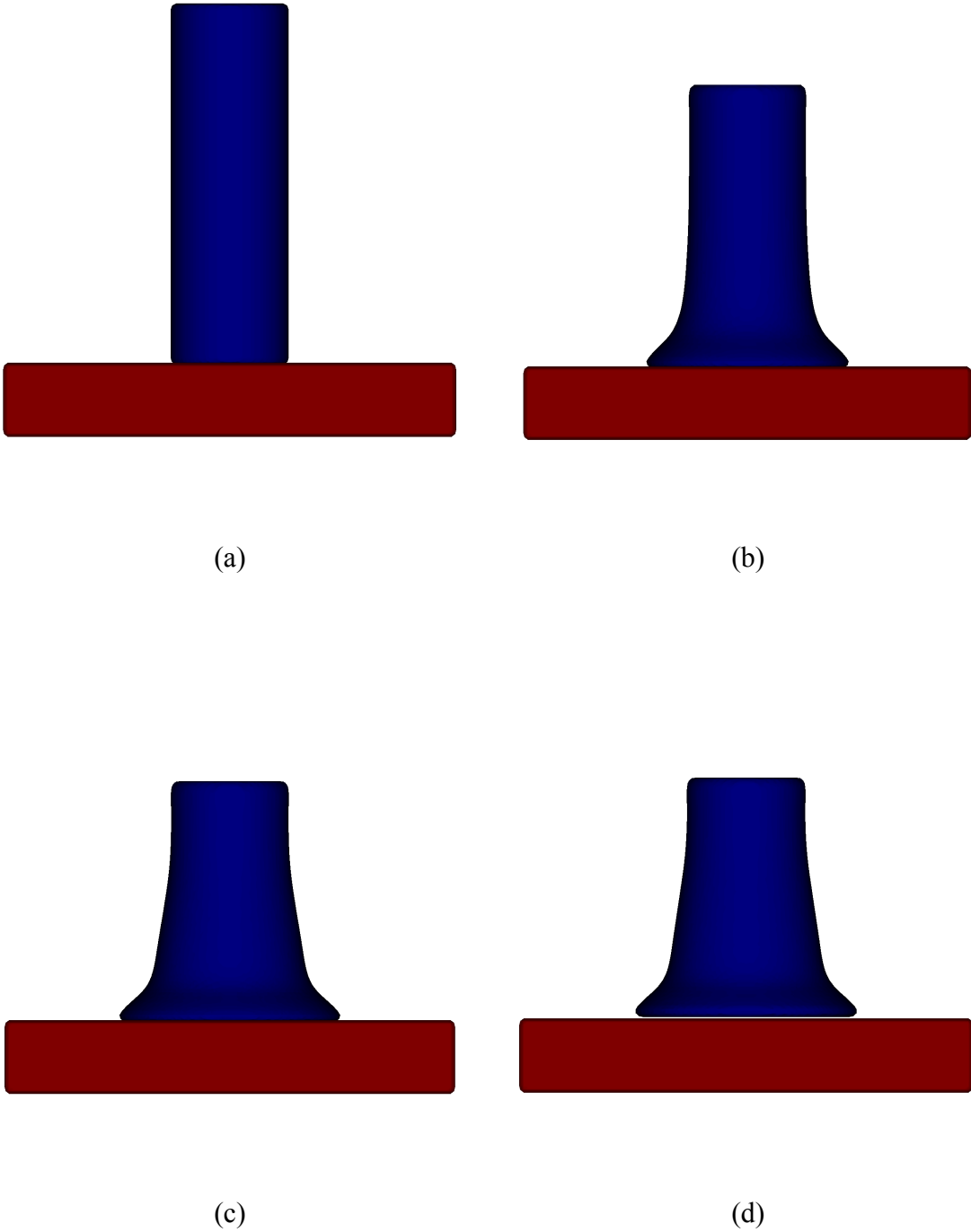


**Figure 6.14:** ALEAS MMM Taylor impact problem with layer of initial mixed cells at 0, 25, 50, and 100  $\mu$ s.

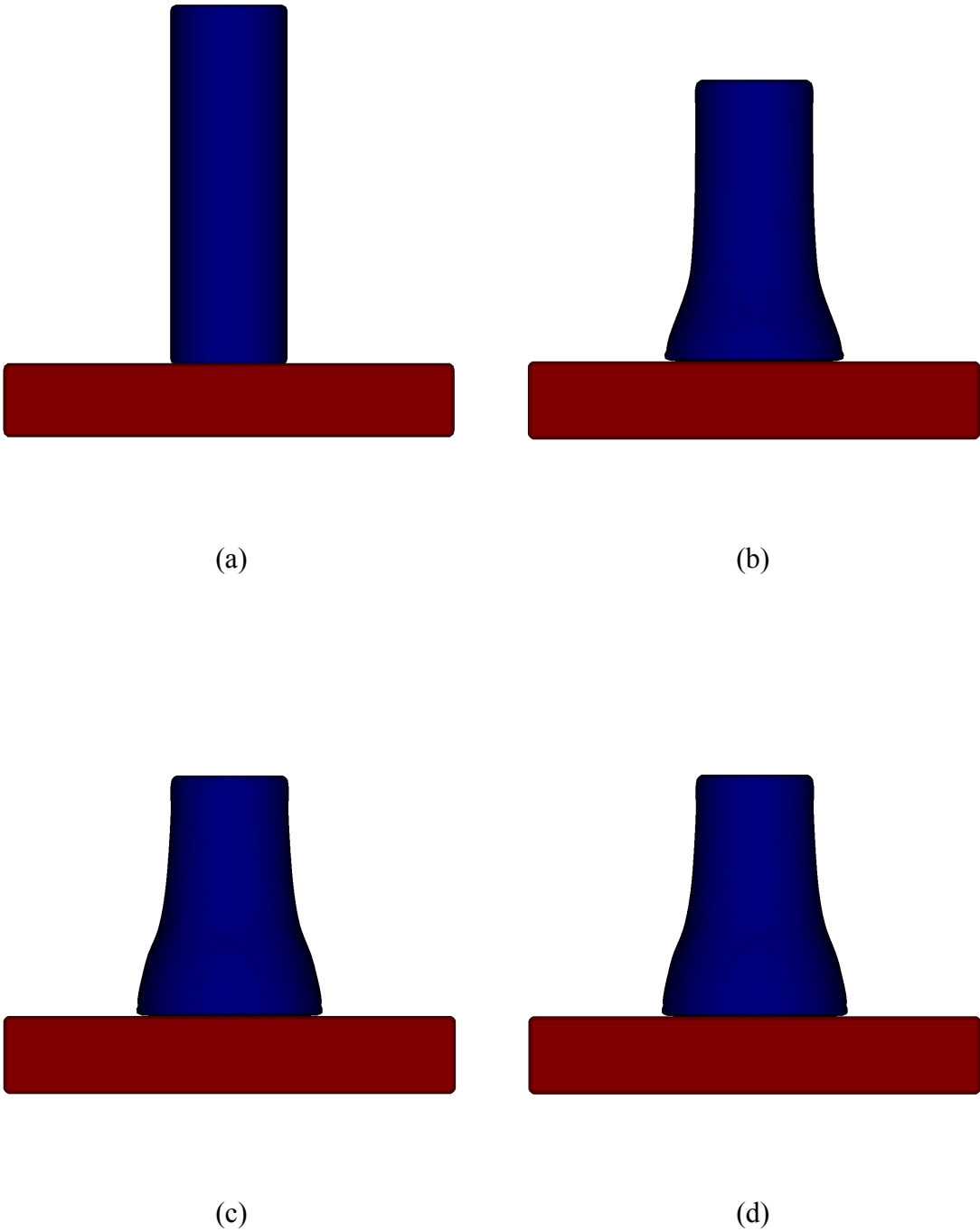


**Figure 6.15:** ALEAS SMM Taylor impact problem with layer of initial mixed cells at 0, 25, 50, and 100  $\mu$ s.

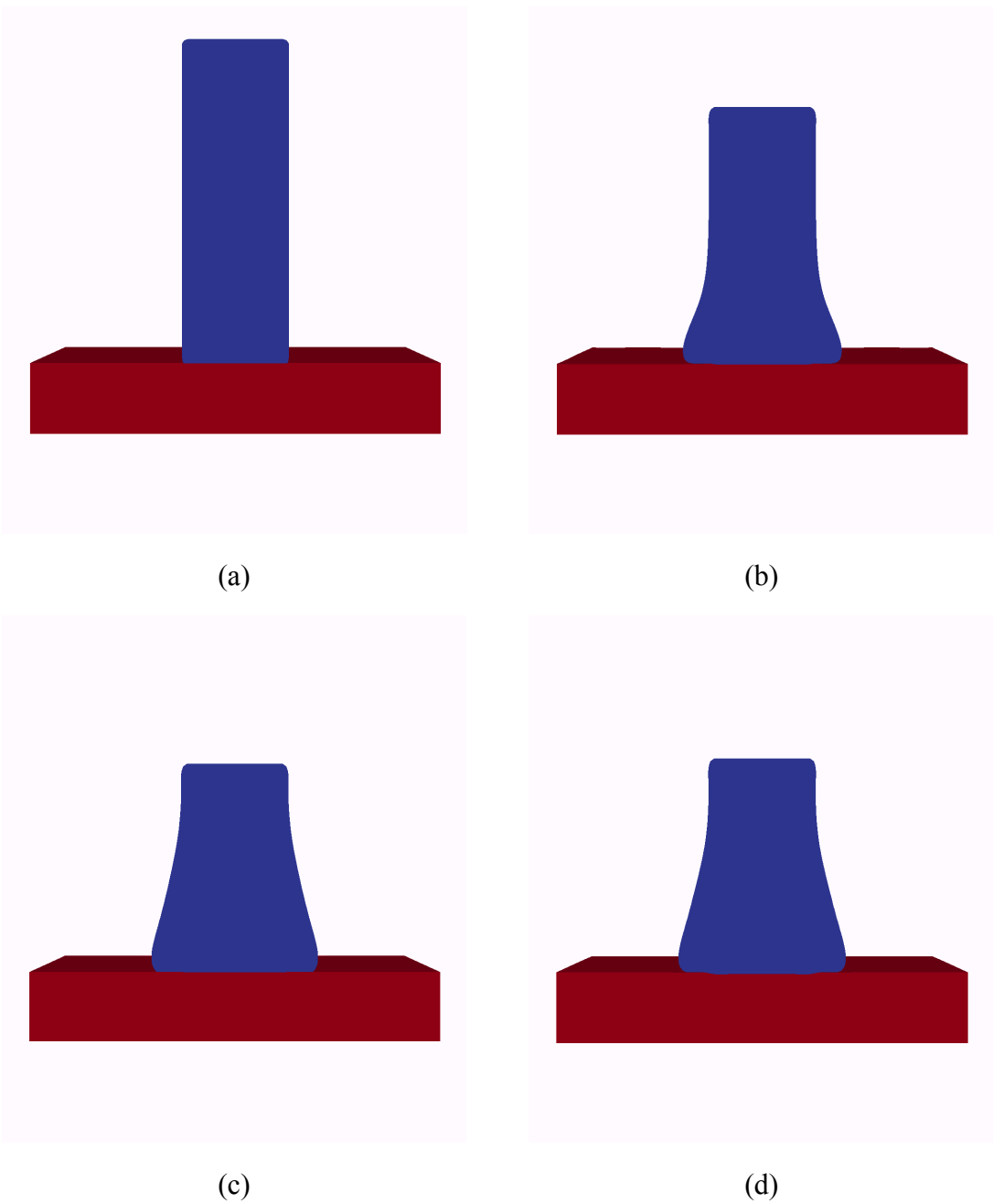


**Figure 6.16:** CTH Taylor impact problem with layer of initial mixed cells at 0, 25, 50, and 100  $\mu$ s.



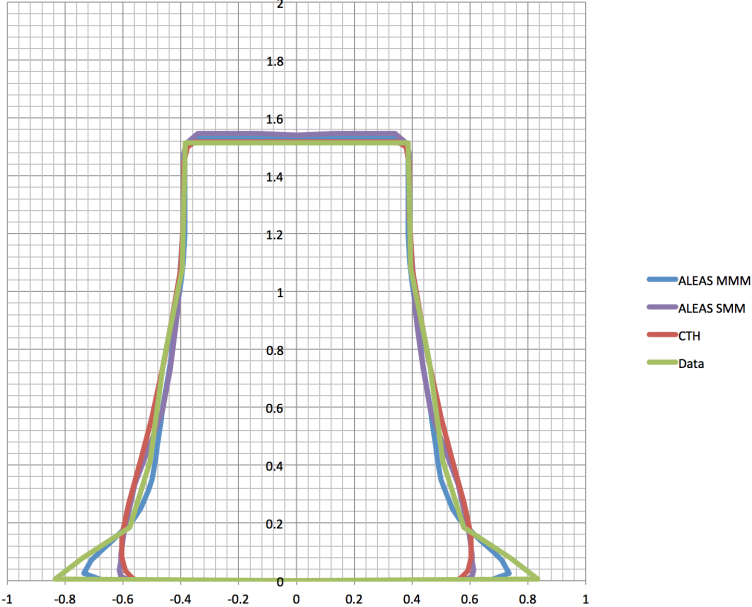


**Figure 6.17:** Comparison of deformation profile for ALEAS MMM, ALEAS SMM, CTH, and experiment for mesh aligned Taylor impact.

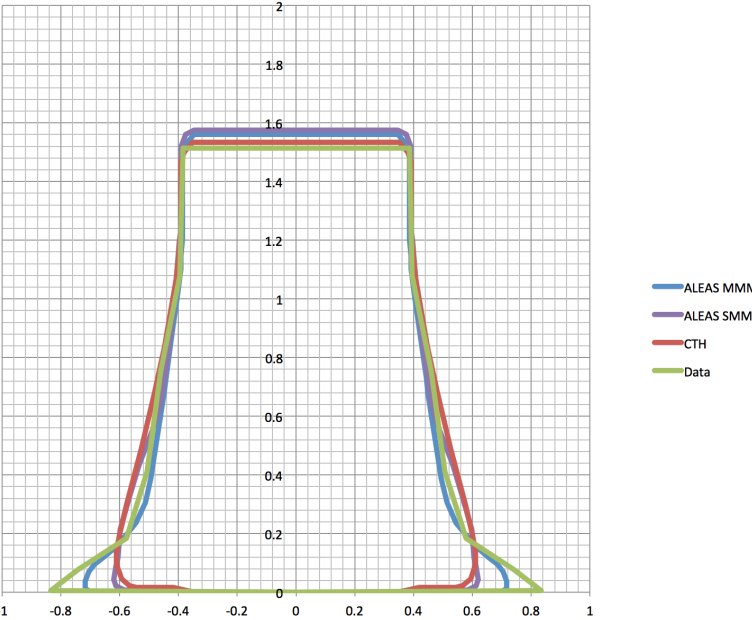


**Figure 6.18:** Comparison of deformation profile for ALEAS MMM, ALEAS SMM, CTH, and experiment for Taylor impact with initial layer of mixed cells.

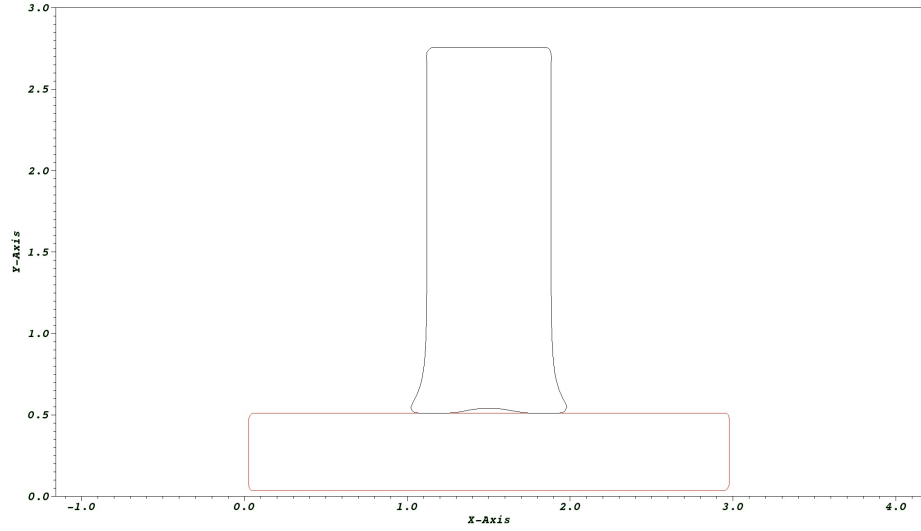


**Figure 6.19:** Profile of ALEAS MMM Taylor impact at 5 $\mu$ s showing separation of the center of the bar from the rigid plate.

Table 6.1: Summary of measures of final deformation for the Taylor impact simulations

	$L_f$ (cm)	$L_f$ Error (%)	$R_f$ (cm)	$R_f$ Error (%)	$X_f$ (cm)	$X_f$ Error (%)	$W_f$ @0.4cm (cm)	$W_f$ Error (%)
<i>Experiment</i>	1.513	-	0.834	-	0.435	-	0.510	-
<i>MMM Aligned</i>	1.530	1.124	0.736	11.75	0.429	1.379	0.491	3.725
<i>SMM Aligned</i>	1.541	1.851	0.613	26.50	0.284	34.71	0.534	4.706
<i>CTH Aligned</i>	1.517	0.026	0.603	27.70	0.248	42.99	0.544	6.667
<i>MMM Offset</i>	1.561	3.173	0.717	14.03	0.414	4.828	0.492	3.529
<i>SMM Offset</i>	1.575	4.098	0.620	25.66	0.323	25.75	0.543	6.471
<i>CTH Offset</i>	1.534	1.388	0.611	26.74	0.303	30.34	0.550	7.843

## Penetration by Projectiles with Combined Obliquity and Yaw

The penetration of oblique plates by projectiles of various yaw serves as a means of demonstrating the shortcomings of traditional Eulerian formulations with mixture theory. Due to the increased interaction between materials as the rod passes through the plate an artificial slowing of the rod compared to experimental data is often seen due to material bonding when mixture theory is employed. This result is not desirable, especially for applications such as multi-layered armor or other events where the ability to accurately model a secondary or further subsequent impact is important. In the simulations presented here a long uranium alloy rod penetrates an oblique RHA plate at various obliquities and yaws. As described previously in Chapter 5, the effective yaws were obtained by launching the plate toward the penetrator in the negative yaw case and away from the penetrator in the positive yaw case. A  $0^\circ$  yaw case was also performed, but no experimental data was available to compare to. This case, shown in Figures 6.20, 6.21, and 6.22 for ALEAS MMM, ALEAS SMM, and CTH respectively, should result in relatively small slowdown of the rod since only the head of the impactor is interacting with the plate. As can be seen in the summary of results in Table 6.2, this was indeed the case for both ALEAS MMM and SMM as well as CTH, which had  $V_f/V_0$  values of 0.9386, 0.8719, and 0.9358, respectively. The ALEAS SMM case resulted in the greatest slowdown due to lack of a fracture model, which was used in the CTH calculations. The true benefit of the contact method employed in ALEAS MMM can be seen in the positive and negative yaw cases. Since the plate is moving relative to the rod the contact will be extended along the body of the rod. Since ALEAS MMM does not employ mixture theory this artificial slowing of the rod is not seen. In the case of the  $+10.3^\circ$  yaw

simulation the top of the rod interacts with the plate for a prolonged period of time. In the ALEAS SMM and CTH simulations this results in a  $V_f/V_0$  value of 0.8350 and 0.8495, compared to the experimental value of 0.9077. The ALEAS MMM simulation resulted in an improved  $V_f/V_0$  of 0.9004. Since the plate obliquity was a fairly steep  $54.9^\circ$  in this case the plate material is displaced fairly quickly, so the interaction with the rod is relatively small compared the  $-9.3^\circ$  yaw case. In that case the bottom of the penetrator is in prolonged contact with the plate due to the relatively flat  $73.5^\circ$  obliquity angle and the upward motion of the plate toward the penetrator. In this case the performance of an Eulerian formulation with mixture theory is severely inhibited. This is apparent in Figures 6.27 and 6.28 in which nearly the entire length of the rod is interacting with the plate at  $50 \mu\text{s}$  and a large fragment sticks to the penetrator and moves away from the plate at late time resulting in a  $V_f/V_0$  values of 0.6802 and 0.7771 for the ALEAS SMM and CTH simulations compared to an experimental value of 0.8835. In the ALEAS MMM simulation of the  $-9.3^\circ$  yaw case no such bonding is present and the  $V_f/V_0$  value is significantly improved to 0.8982.

Table 6.2 also reports the final length of the penetrators at  $100 \mu\text{s}$ . It should be noted that in all cases both the ALEAS and CTH simulations resulted in residual lengths greater than the experimental values, however, as noted by Cagliostro [24], the final rod lengths from the experiments had a fairly high degree of scatter, so the simulations may not be picking up some complex feature that takes place in the experiment due to the relative simplicity and idealized nature of the models.

It should be noted that the ripples along the top of the rod in the  $100 \mu\text{s}$  image of Figure 6.20 and the bulge at the rear of the penetrator at the same time in Figure 6.26 are

a result of self-contact with debris as the rod moves through the plate. Modeling self-contact in an Eulerian hydrocode poses significant difficulty. Since only a single volume fraction is present for each material in an element all material is considered to be in contact and homogeneous. The inability to properly handle self-contact illustrates one limitation that still exists in ALEAS MMM, as well as all current Eulerian hydrocodes. While this problem is not addressed in this dissertation it would be an interesting topic to examine in future work.

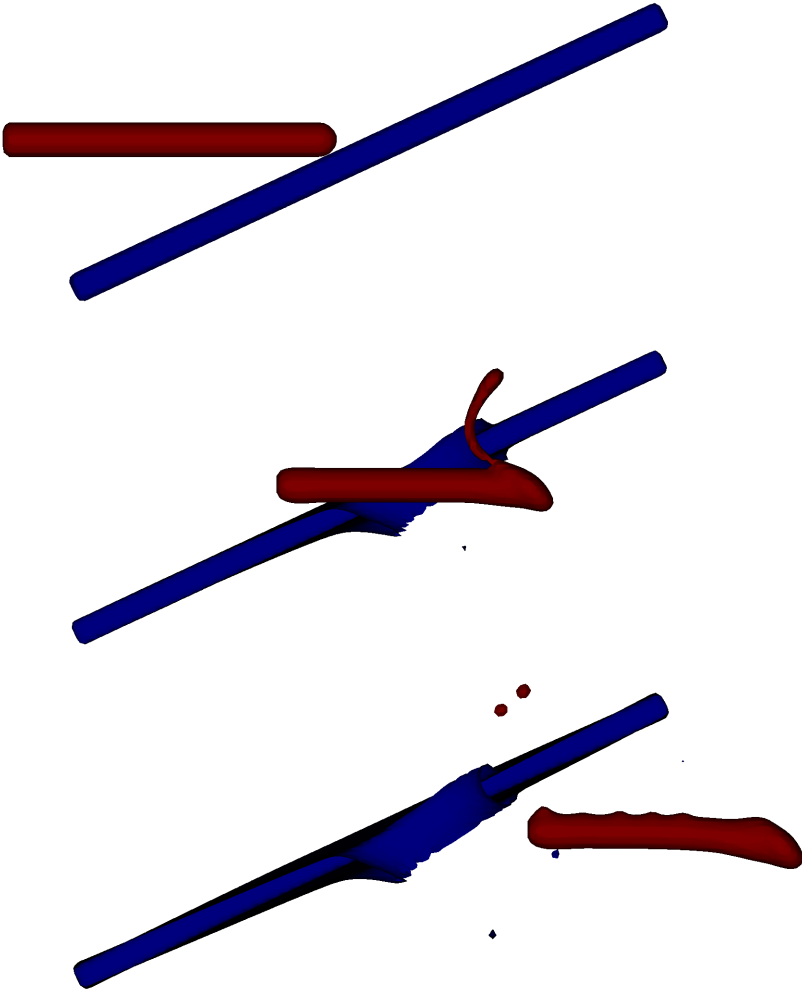


**Figure 6.20:** ALEAS MMM penetration of uranium rod into steel plate with 0° yaw at 0, 50, and 100 μs

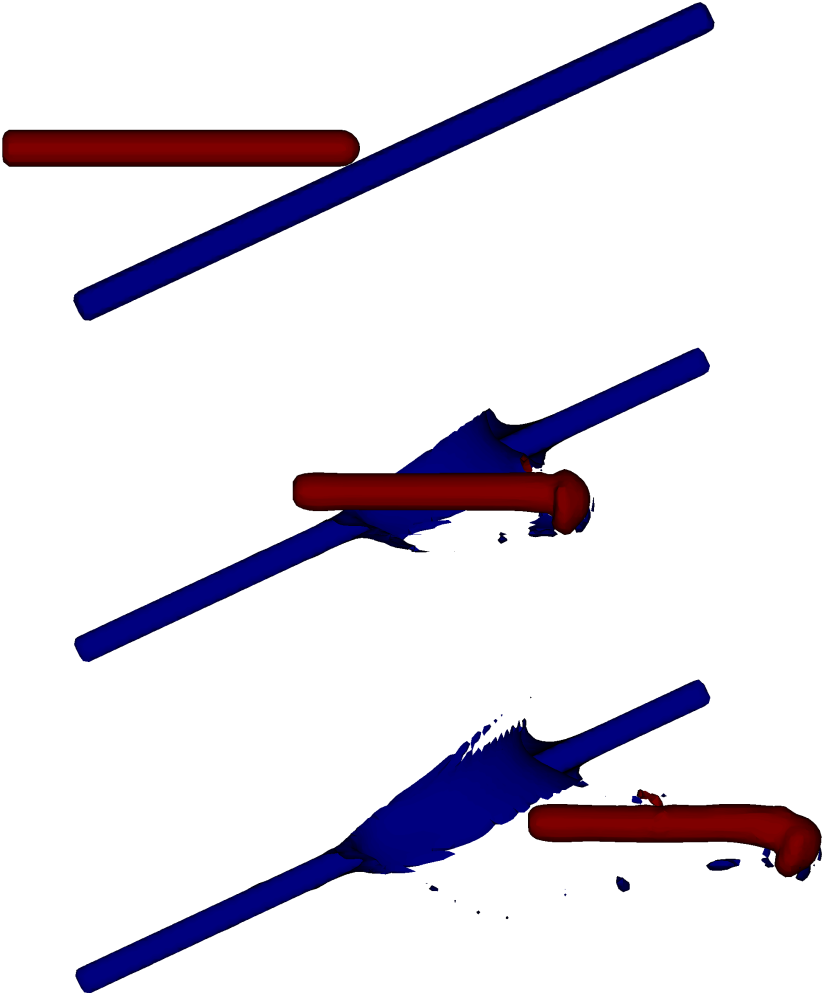


**Figure 6.21:** ALEAS SMM penetration of uranium rod into steel plate with 0° yaw at 0, 50, and 100  $\mu$ s

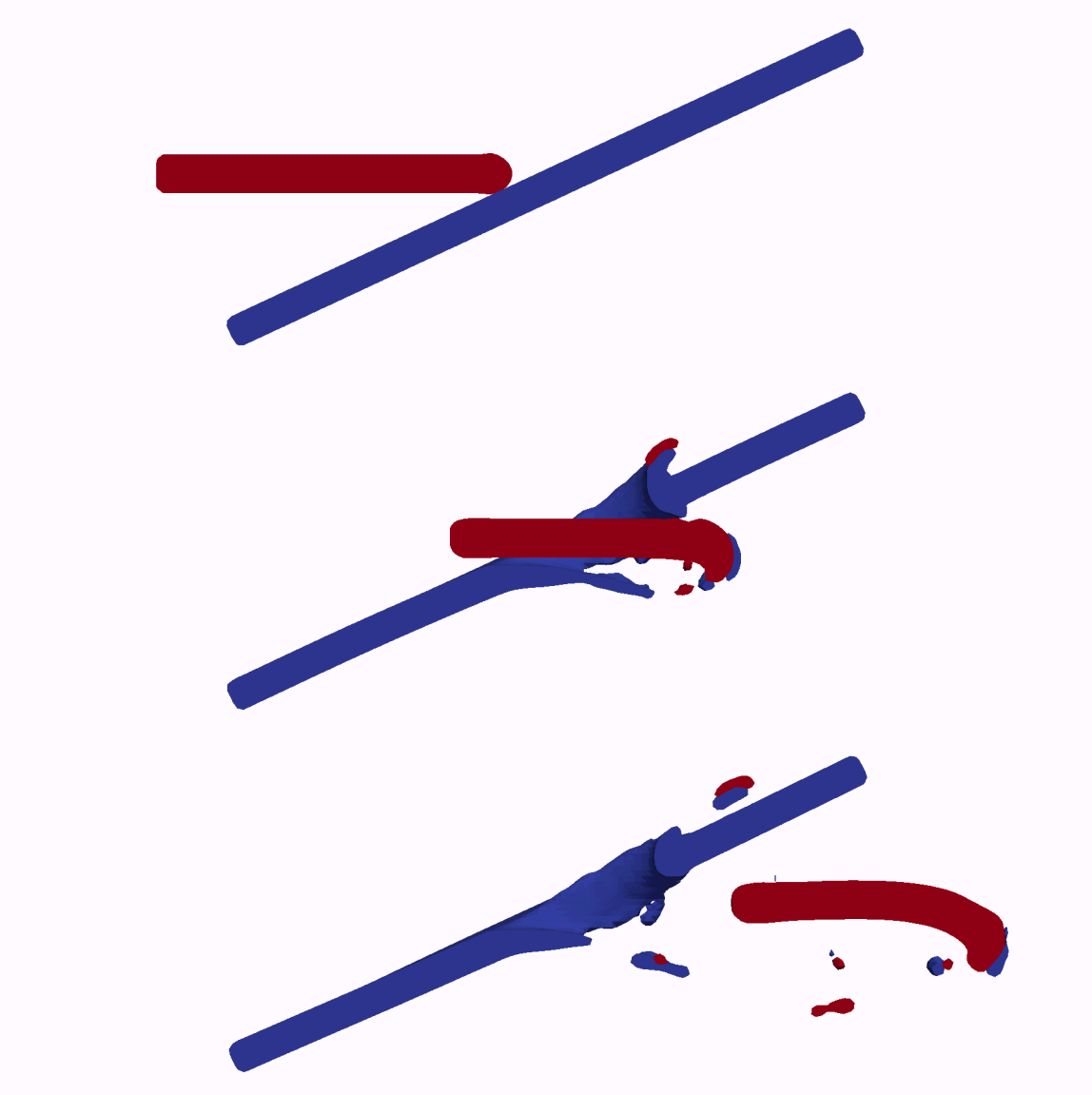


**Figure 6.22:** CTH penetration of uranium rod into steel plate with 0° yaw at 0, 50, and 100  $\mu$ s



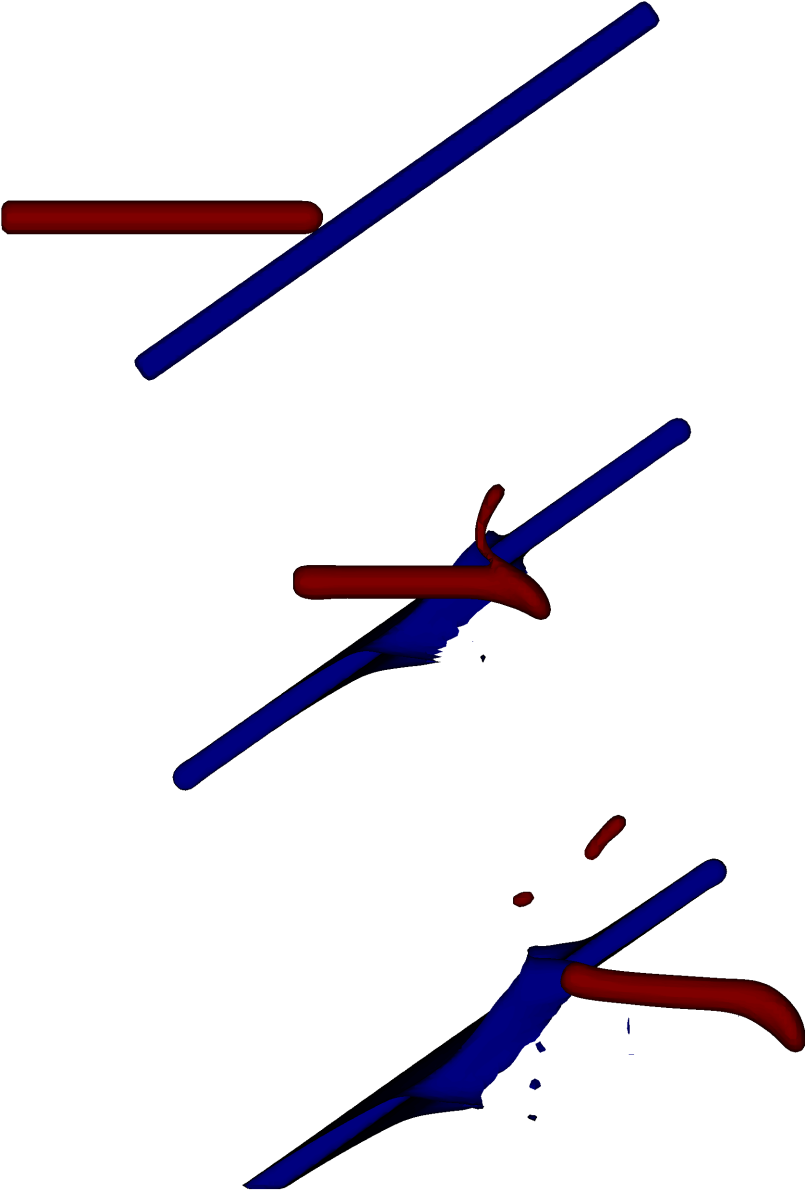


**Figure 6.23:** ALEAS MMM penetration of uranium rod into steel plate with +10.3° yaw at 0, 50, and 100  $\mu$ s

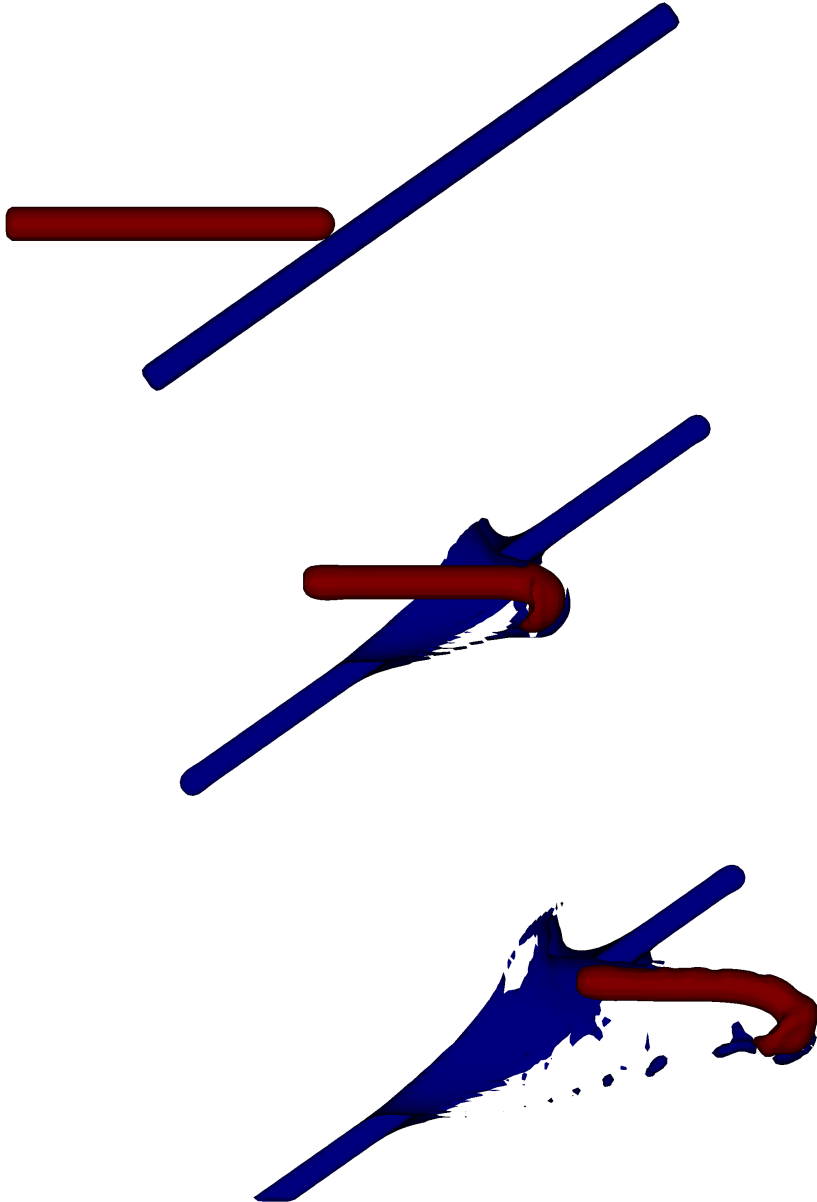


**Figure 6.24:** ALEAS SMM penetration of uranium rod into steel plate with +10.3° yaw at 0, 50, and 100 μs

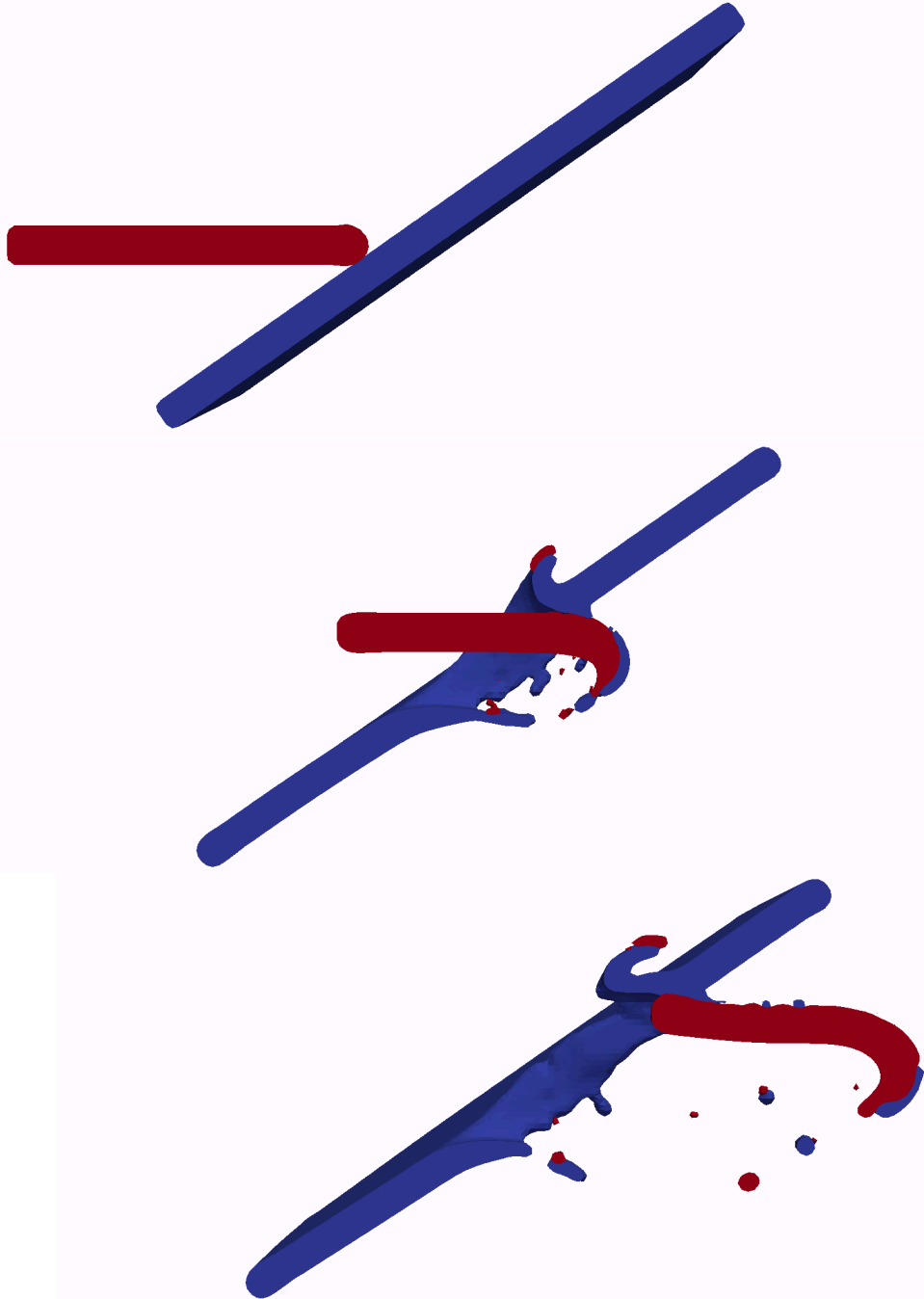


**Figure 6.25:** CTH penetration of uranium rod into steel plate with +10.3° yaw at 0, 50, and 100  $\mu$ s

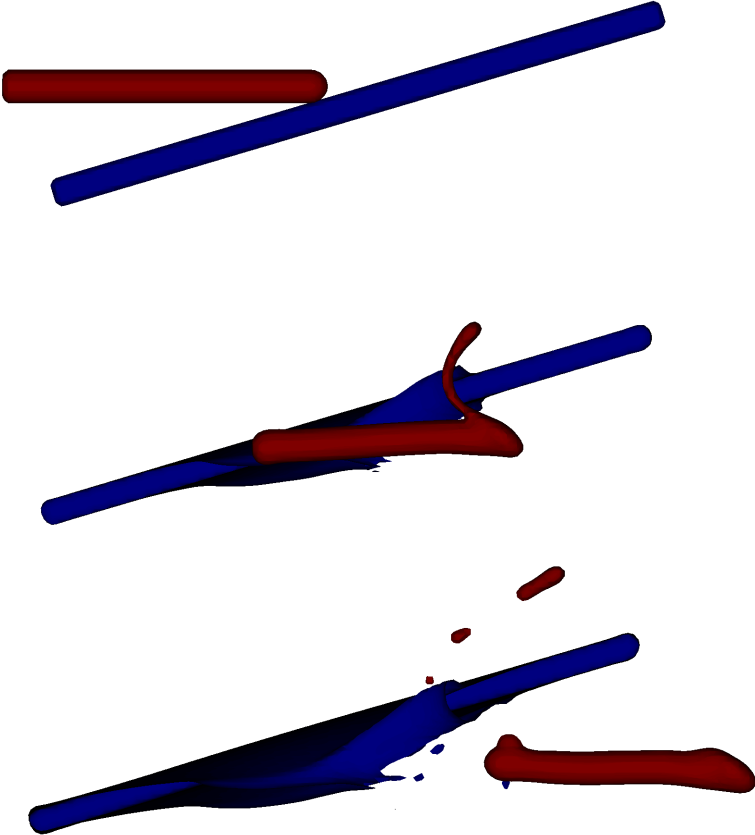


**Figure 6.26:** ALEAS MMM penetration of uranium rod into steel plate with  $-9.3^\circ$  yaw at 0, 50, and 100  $\mu$ s

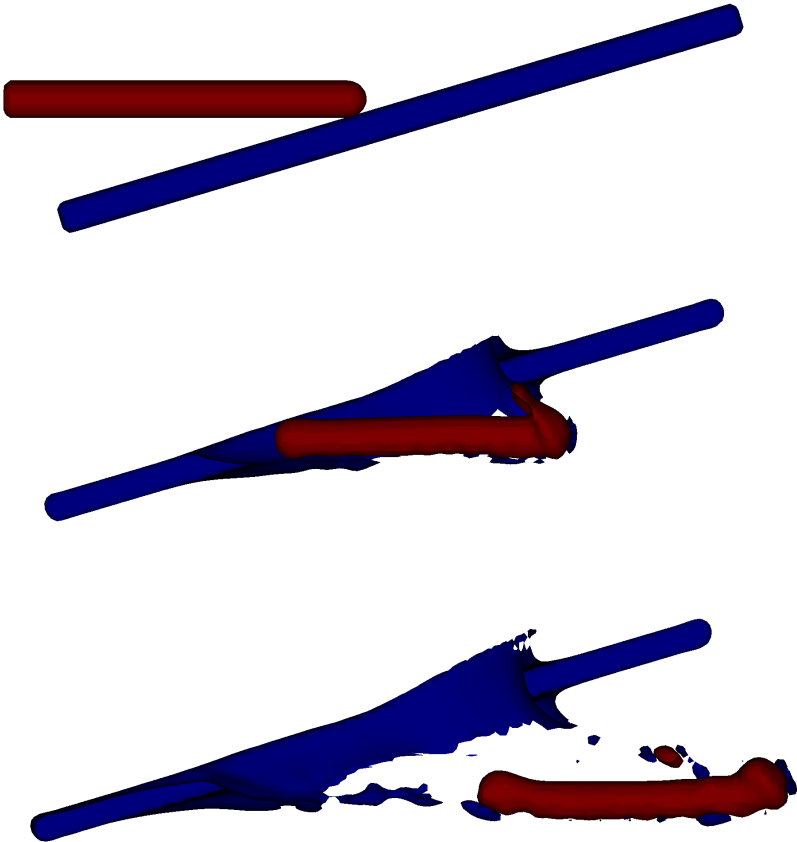


**Figure 6.27:** ALEAS SMM penetration of uranium rod into steel plate with -9.3° yaw at 0, 50, and 100  $\mu$ s

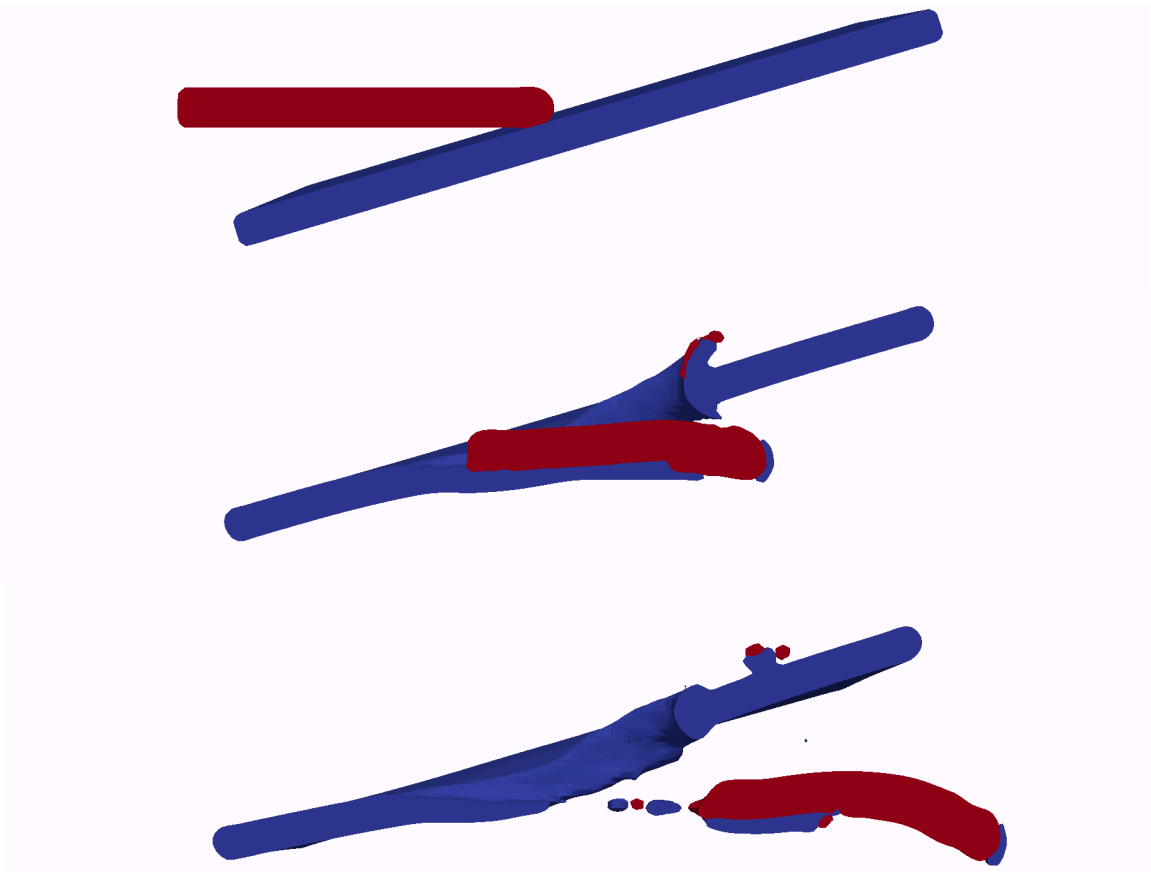


**Figure 6.28:** CTH penetration of uranium rod into steel plate with  $-9.3^\circ$  yaw at 0, 50, and 100  $\mu$ s

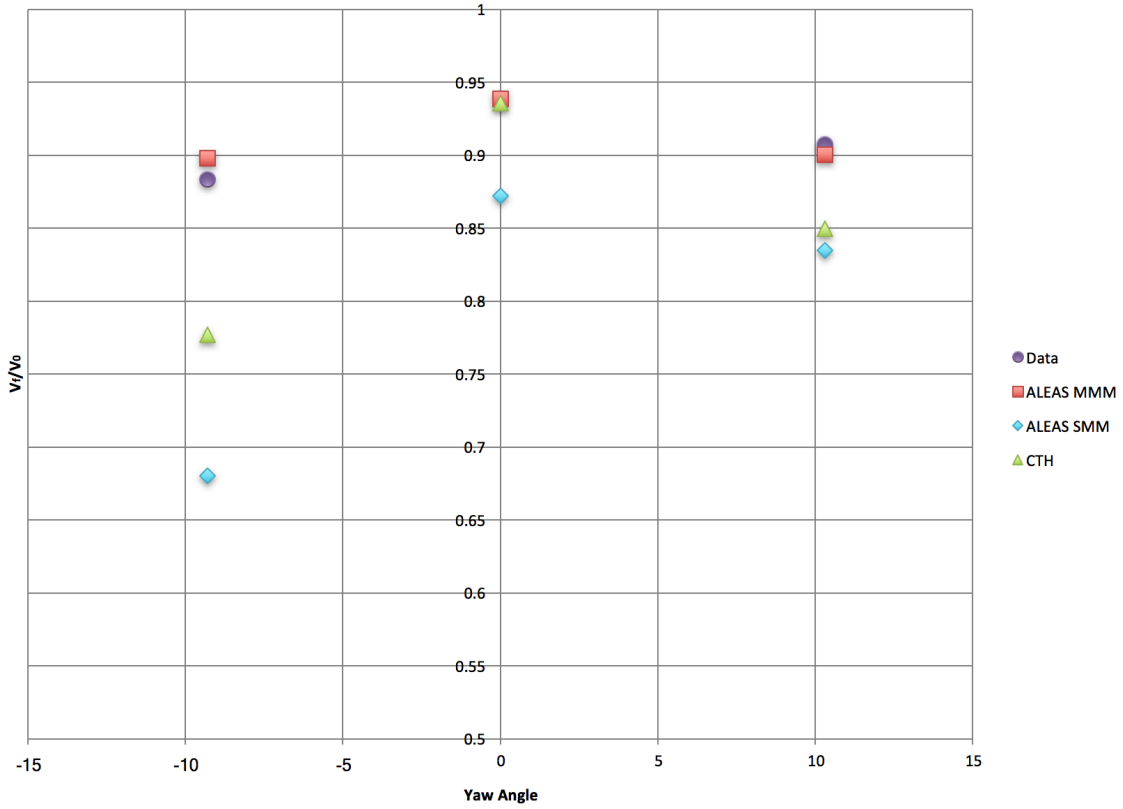


Figure 6.29: Comparison of normalized exit velocity versus yaw angle.

Table 6.2: Summary of results from combined obliquity and yaw simulations and experiments

	$V_{0,rod}$ (km/s)	$V_{0,plate}$ (km/s)	Obliquity (°)	$L_f$ (mm)	$V_{f,rod}$ (km/s)	$V_f/V_{0,rod}$ (-)
ALEAS MMM -9.3° Yaw	1.21	0.217	73.5	64.00	1.087	0.8982
ALEAS SMM -9.3° Yaw	1.21	0.217	73.5	65.48	0.823	0.6802
CTH -9.3° Yaw	1.21	0.217	73.5	61.45	0.940	0.7771
Experiment -9.3° Yaw	1.21	0.217	73.5	55.5	1.069	0.8835
ALEAS MMM +10.3° Yaw	1.43	-0.284	54.9	58.48	1.288	0.9004
ALEAS SMM +10.3° Yaw	1.43	-0.284	54.9	56.51	1.194	0.8350
CTH +10.3° Yaw	1.43	-0.284	54.9	57.32	1.215	0.8495
Experiment +10.3° Yaw	1.43	-0.284	54.9	43.0	1.298	0.9077
ALEAS MMM 0° Yaw	1.29	0	65	63.18	1.211	0.9386
ALEAS SMM 0° Yaw	1.29	0	65	62.83	1.125	0.8719
CTH 0° Yaw	1.29	0	65	58.62	1.207	0.9358
Experiment 0° Yaw	1.29	0	65	-	-	-



### Normal Impact of Long Rods into Steel Targets

The penetration sequence of a uranium long rod impacting a 5.08 cm steel target presented in Figure 5 of Fugelso and Taylor [38] served as another validation of ALEAS. While the role of contact in both this problem and the semi-infinite target problems presented in the next section is less important due to erosion of material at the impact front these problems serve as a good comparison to the traditional Eulerian methods. To ensure that ALEAS is capable of producing reasonable results in problems that standard Eulerian methods tend to handle well the normal penetration of long rods is examined here. In the case presented in Fugelso and Taylor [38] we can examine two measures to determine the validity of the solution, the depth of penetration and the final length of the penetrator,  $L_f$ . The results of the ALEAS MMM, SMM, and CTH simulations are shown in Figures 6.30, 6.31, and 6.32 respectively and are summarized in Table 6.3. As can be seen all three simulations resulted in a reasonable match to depth of penetration. The ALEAS MMM run resulted in an error of 6.58%, compared to the experiment, while ALEAS SMM and CTH had errors of 3.17% and 1.48% respectively. Both CTH and ALEAS underestimated the  $L_f$  of the penetrator. The likely reason for this is an issue with the material strength model. The Cagliostro and Fugelso reports only list a yield stress for the depleted uranium impactor, so parameters from the CTH library Johnson-Cook strength model were used with the  $A$  parameters being adjusted to match the reported yield stress. Figure 6.33 shows a comparison between the PHERMEX radiograph of the test at 98.1  $\mu$ s and the ALEAS MMM, SMM, and CTH results at the same time.

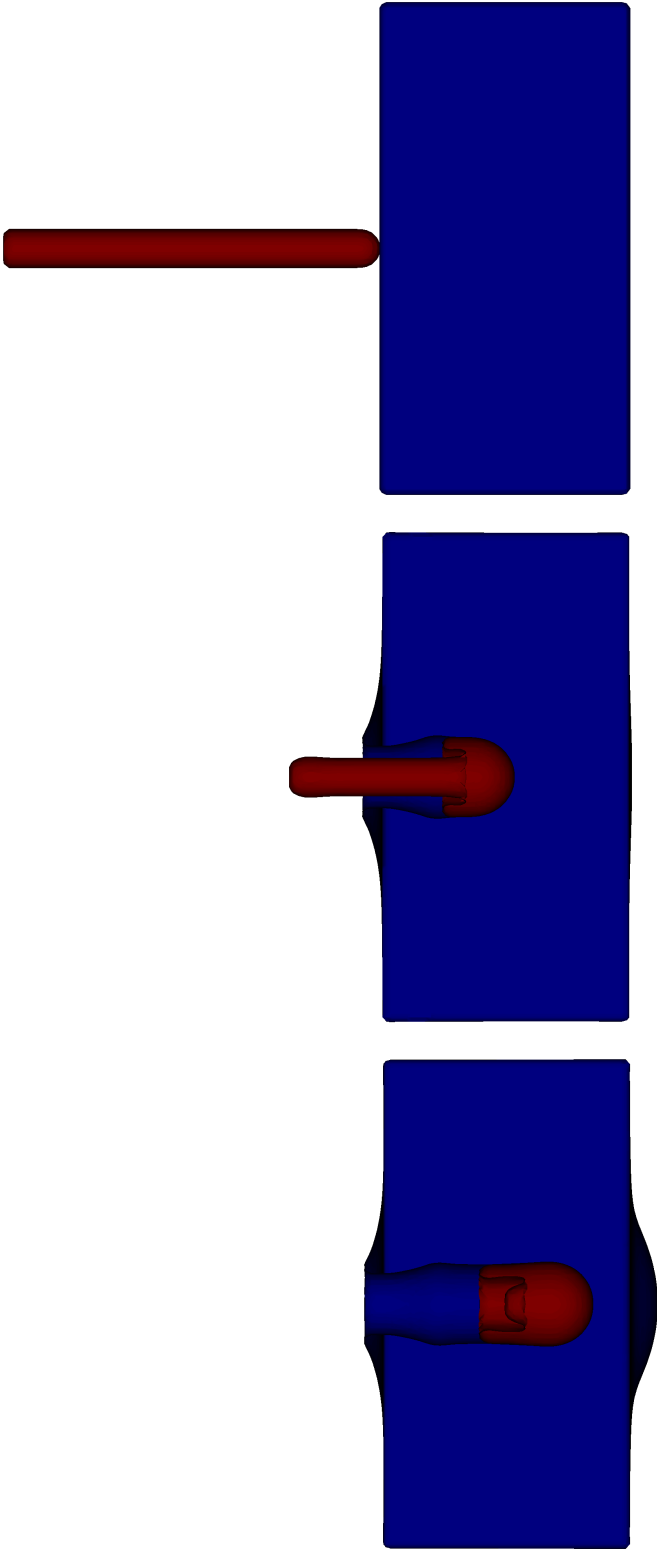


**Figure 6.30:** ALEAS MMM normal penetration of uranium rod into 5.08cm steel plate at 0, 50, and 100  $\mu$ s

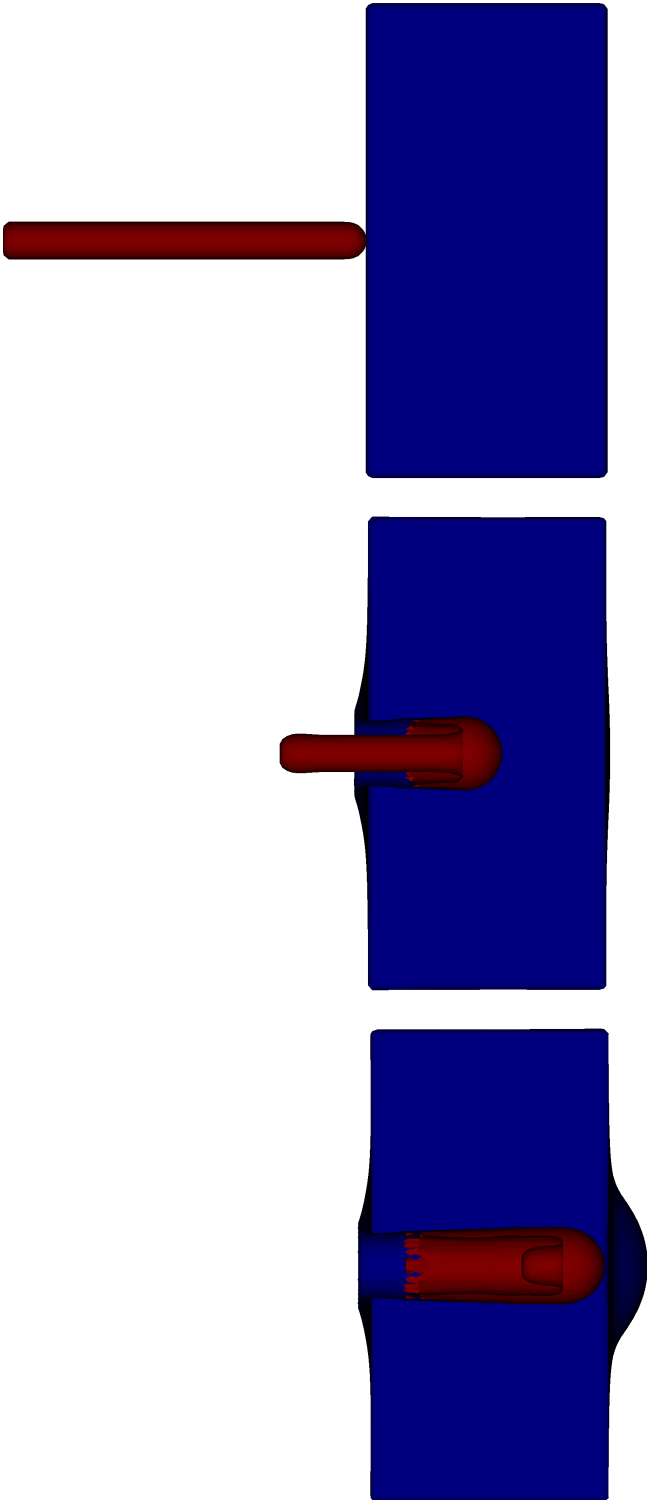


**Figure 6.31:** ALEAS SMM normal penetration of uranium rod into 5.08cm steel plate at 0, 50, and 100  $\mu$ s

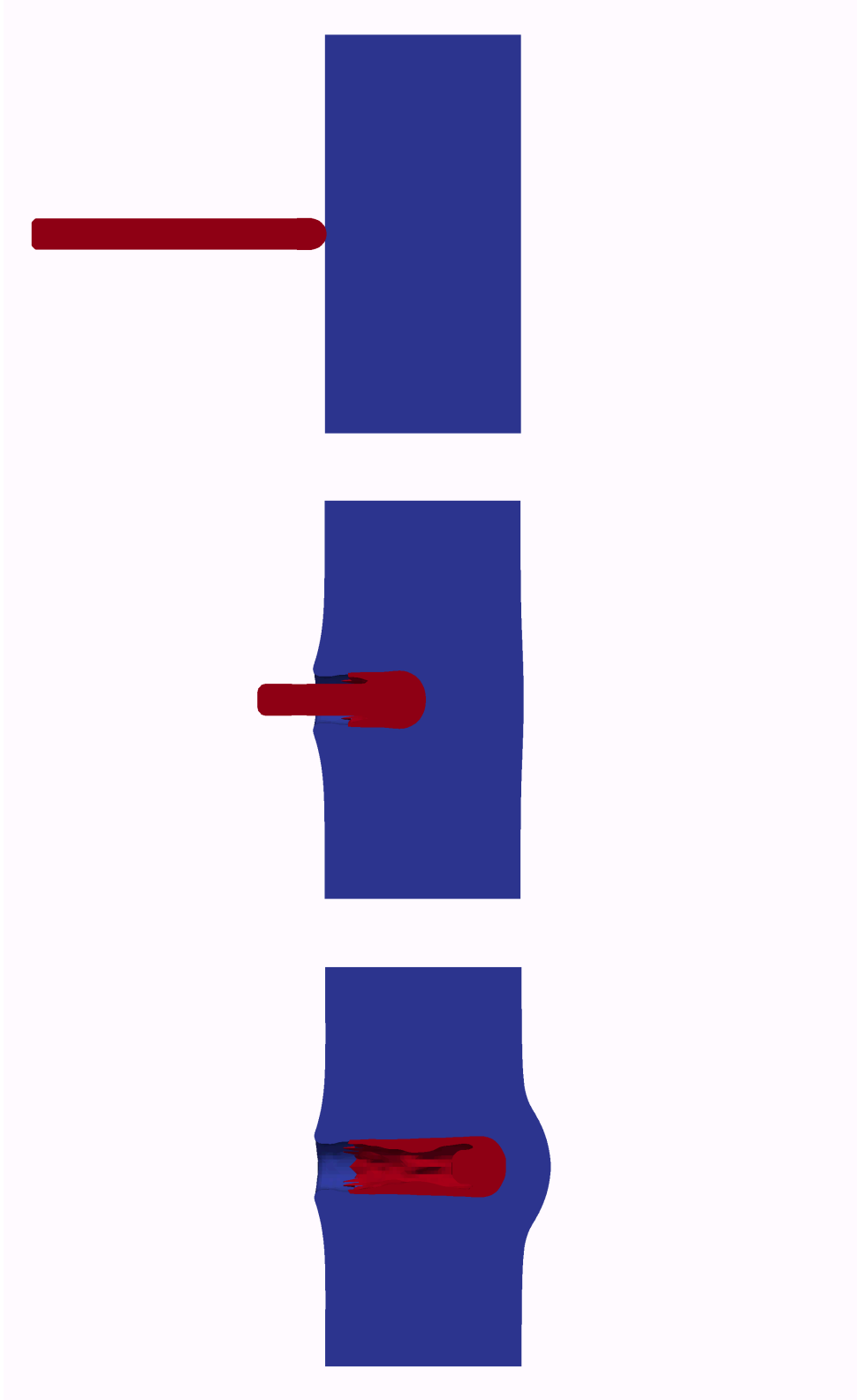


**Figure 6.32:** CTH normal penetration of uranium rod into 5.08cm steel plate at 0, 50, and 100  $\mu$ s

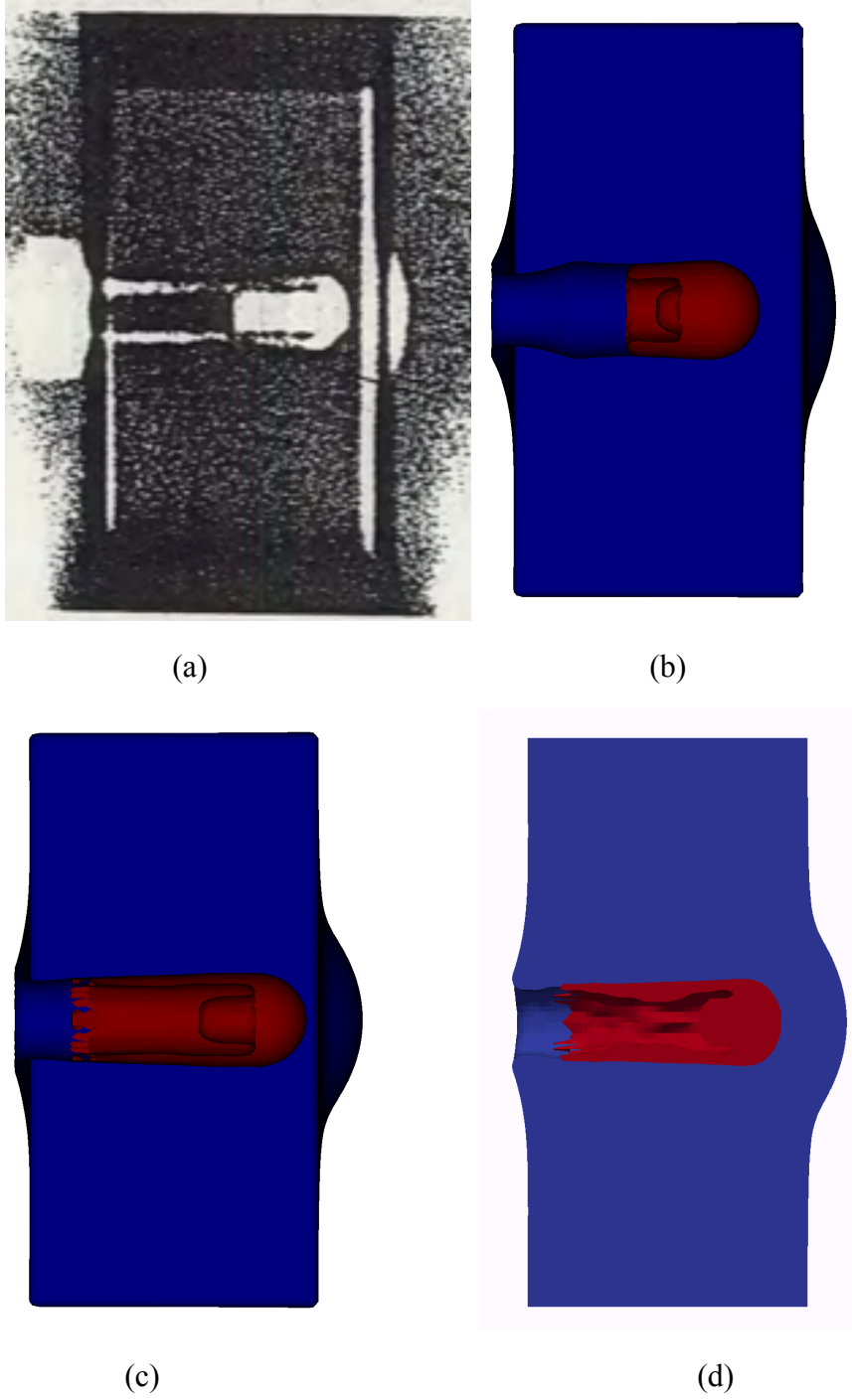


**Figure 6.33:** Comparison of normal penetration of uranium rod into 5.08cm steel plate at 98.1  $\mu$ s, (a) Fugelso and Taylor PHERMEX radiograph [38], (b) ALEAS MMM, (c) ALEAS SMM, and (d) CTH

Table 6.3: Summary of results for 5.08 cm plate penetration

	Depth of Penetration (mm)	$L_f$ (mm)
ALEAS MMM	42.41	17.93
ALEAS SMM	46.84	18.11
CTH	46.07	14.11
Experiment	45.40	21.10

### Long Rod Penetration of Semi-infinite Targets

As mentioned in the previous discussion of the 5.08 cm plate impact, the penetration of long rods is commonly used to validate hydrocodes. This section discusses the results of a series of tungsten long rod penetrations into hardened steel targets as discussed in [75]. As can be seen in Figure 6.42, ALEAS SMM and CTH perform very well when simulating impacts of this type. ALEAS MMM showed very good agreement at high impact velocities, but provided somewhat less accurate results for penetrator velocities of 1500 m/s and lower. Figure 6.42 shows the penetration efficiency (P/L) versus projectile striking velocity. While there are relatively large differences between the simulation results and the fit to experimental data for some cases it should be noted that a mesh convergence study has not been conducted due to the current limitations of ALEAS. As such the most refined mesh possible given ALEAS's current memory limits, as discussed in the next section of this chapter, was used. While this limitation certainly affects the validity of the solution, as can be seen in Figure 6.42, the results obtained for the zoning size used in these ALEAS simulations compare favorably to those reported for the same zoning size at 1500 m/s in the two-dimensional axisymmetric X-FEM contact implementation in the ALEGRA code in [75]. While this could be coincidental, it provides reason to believe that an increased mesh resolution would improve the performance of the contact formulation. In the current implementation of the contact algorithm a fairly refined mesh is required due to averaging that takes place for the determination of the nodal contact normal vector and excess volumes. Furthermore, the contact model implemented in ALEAS MMM relies on averaging of interface areas in order to simplify the algorithm. It is possible that this results in contact velocity changes

that are slightly too high in the direction opposite to the impact direction and leads to decreased penetration depths. Future work will include improvements to the contact algorithm and a mesh resolution study will be conducted once the memory limitation in ALEAS is resolved.

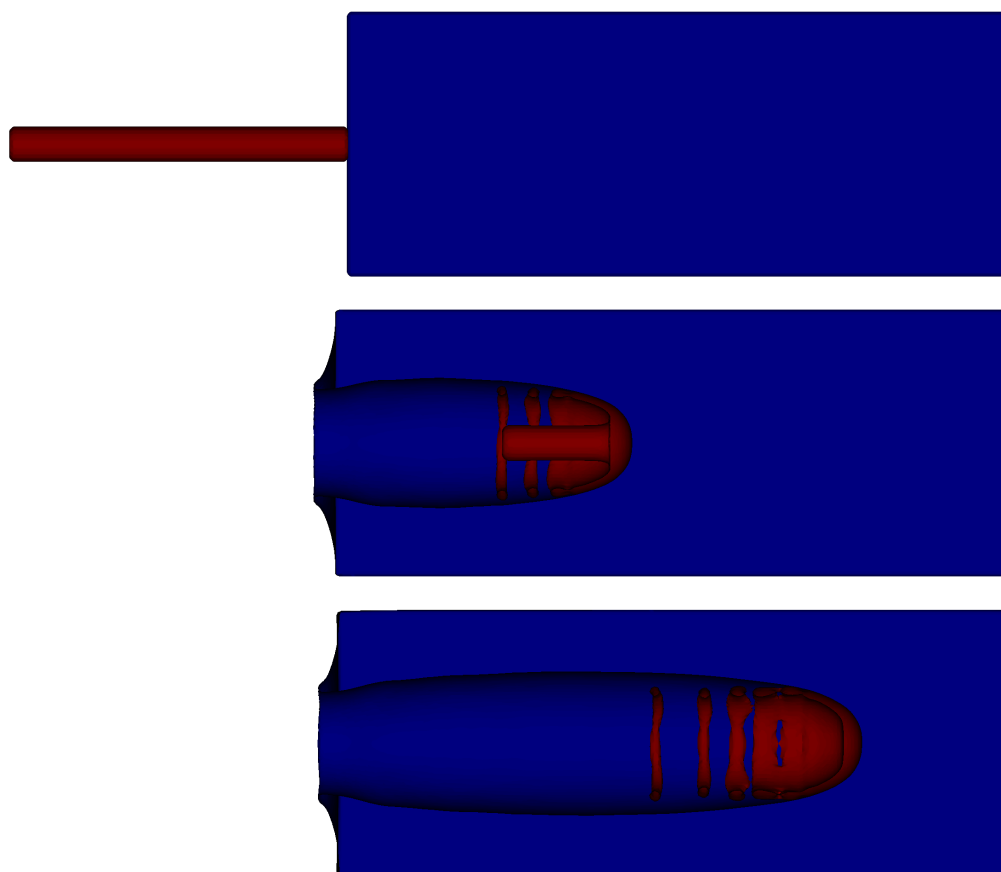


**Figure 6.34:** ALEAS MMM penetration of L/D=10 tungsten alloy rod into steel target with  $V_0=3000\text{m/s}$  at times 0, 25, and 50  $\mu\text{s}$



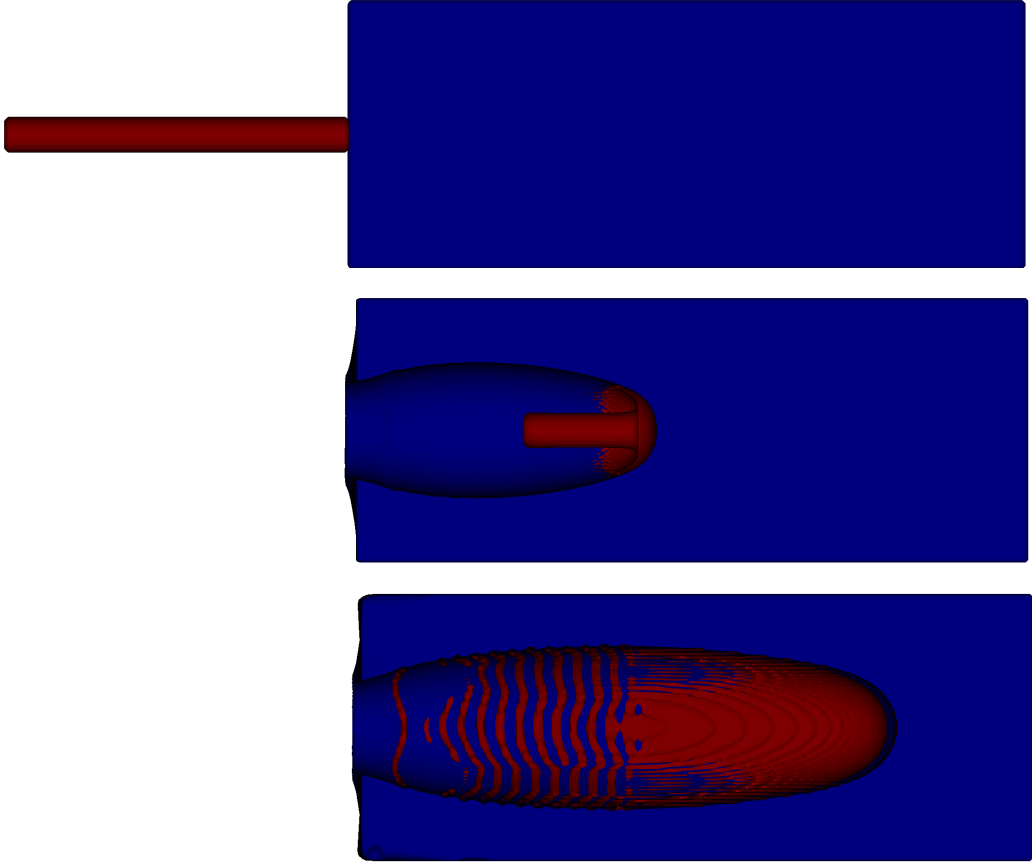


**Figure 6.35:** ALEAS SMM penetration of L/D=10 tungsten alloy rod into steel target with  $V_0=3000\text{m/s}$  at times 0, 25, and 50  $\mu\text{s}$

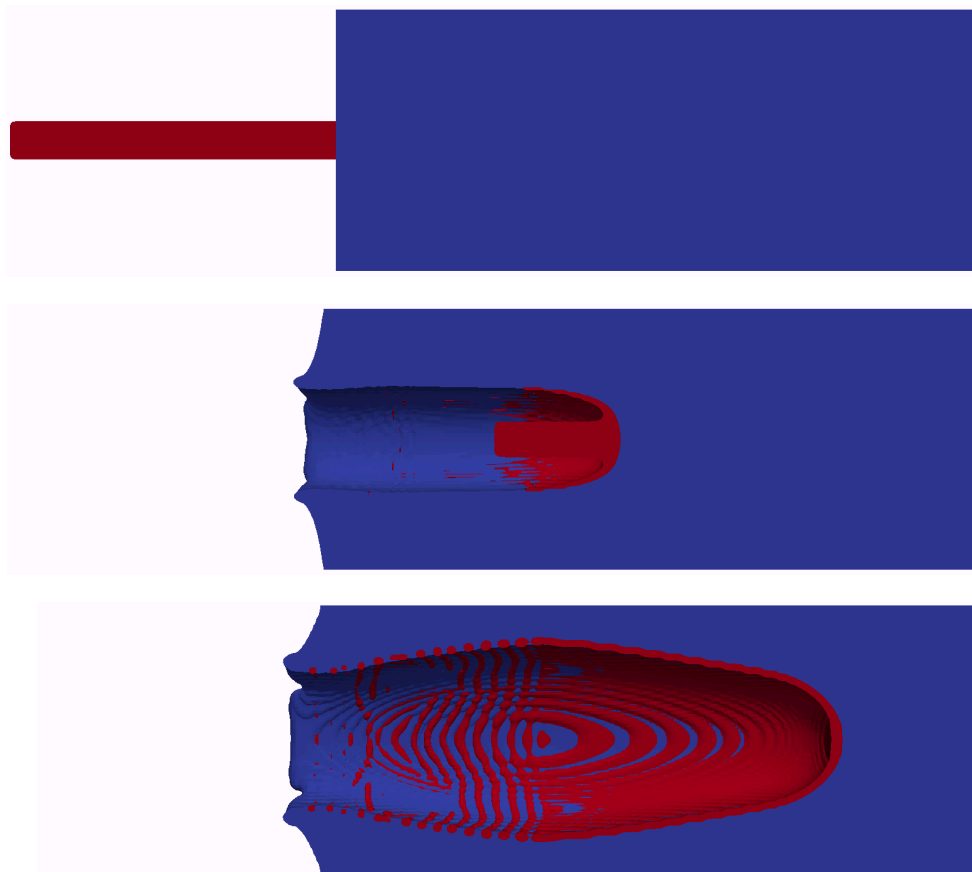


**Figure 6.36:** CTH penetration of L/D=10 tungsten alloy rod into steel target with  $V_0=3000\text{m/s}$  at times 0, 25, and 50  $\mu\text{s}$

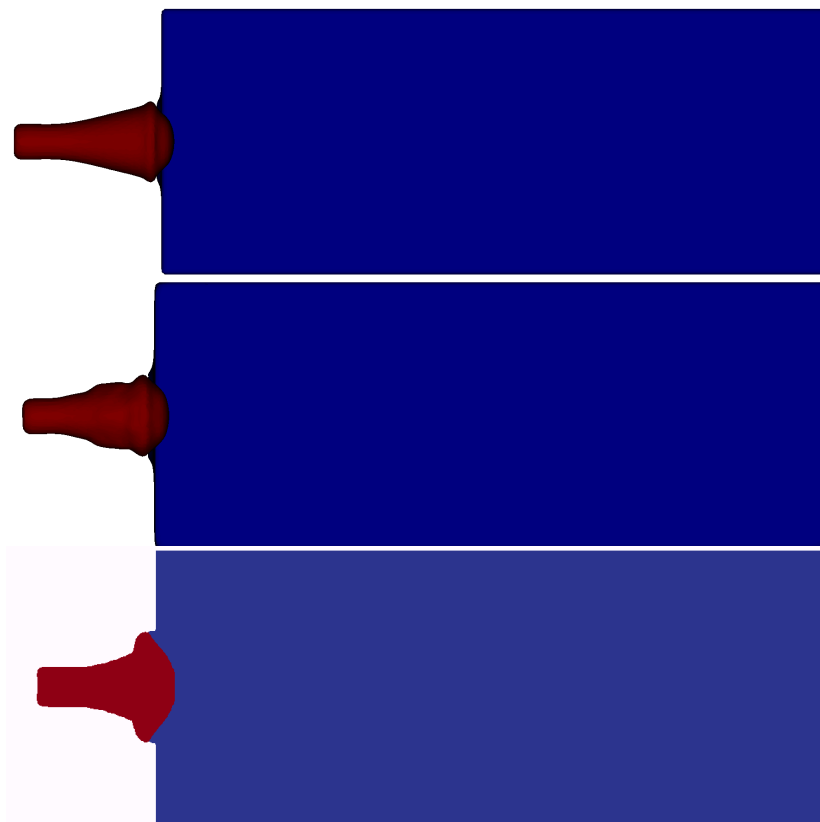


**Figure 6.37:** Comparison of maximum penetration depth for ALEAS MMM (top), ALEAS SMM (center), and CTH (bottom) penetrations of  $L/D=10$  tungsten alloy rods into steel targets with  $V_0$  of 500 m/s

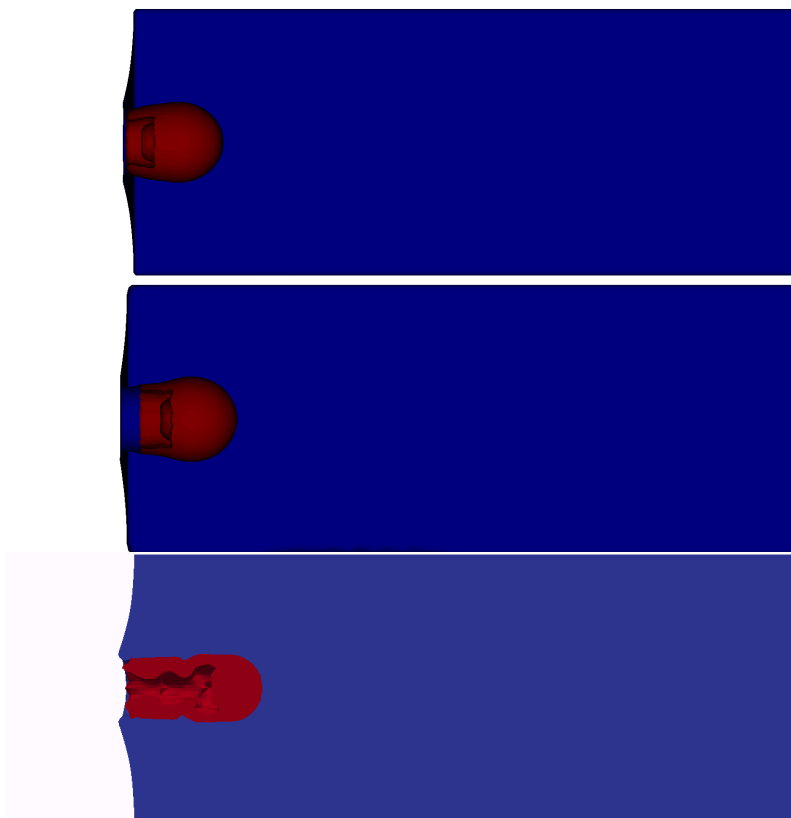


**Figure 6.38:** Comparison of maximum penetration depth for ALEAS MMM (top), ALEAS SMM (center), and CTH (bottom) penetrations of  $L/D=10$  tungsten alloy rods into steel targets with  $V_0$  of 1000 m/s

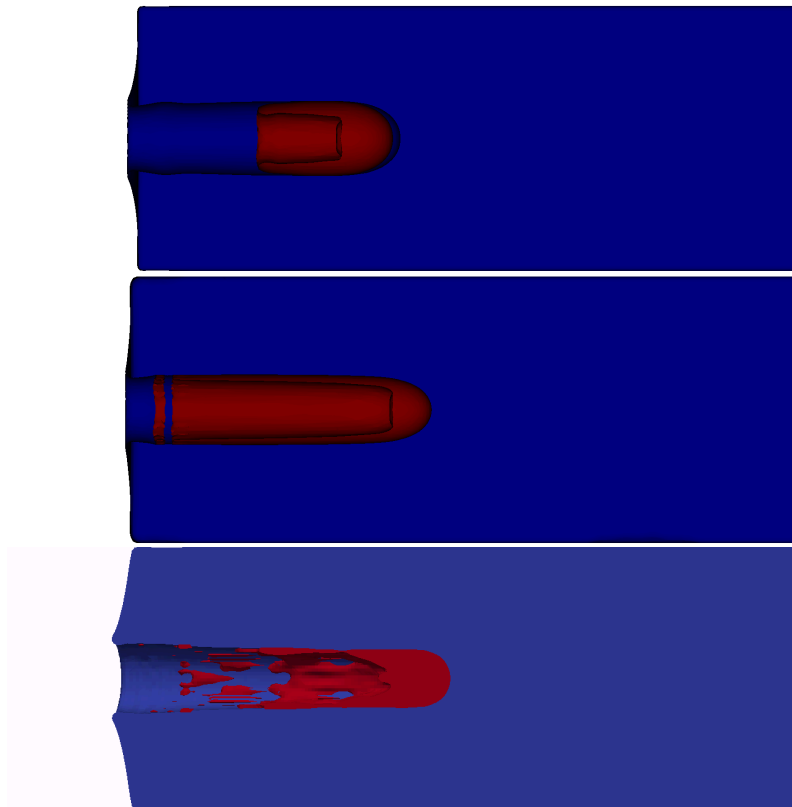


**Figure 6.39:** Comparison of maximum penetration depth for ALEAS MMM (top), ALEAS SMM (center), and CTH (bottom) penetrations of  $L/D=10$  tungsten alloy rods into steel targets with  $V_0$  of 1500 m/s

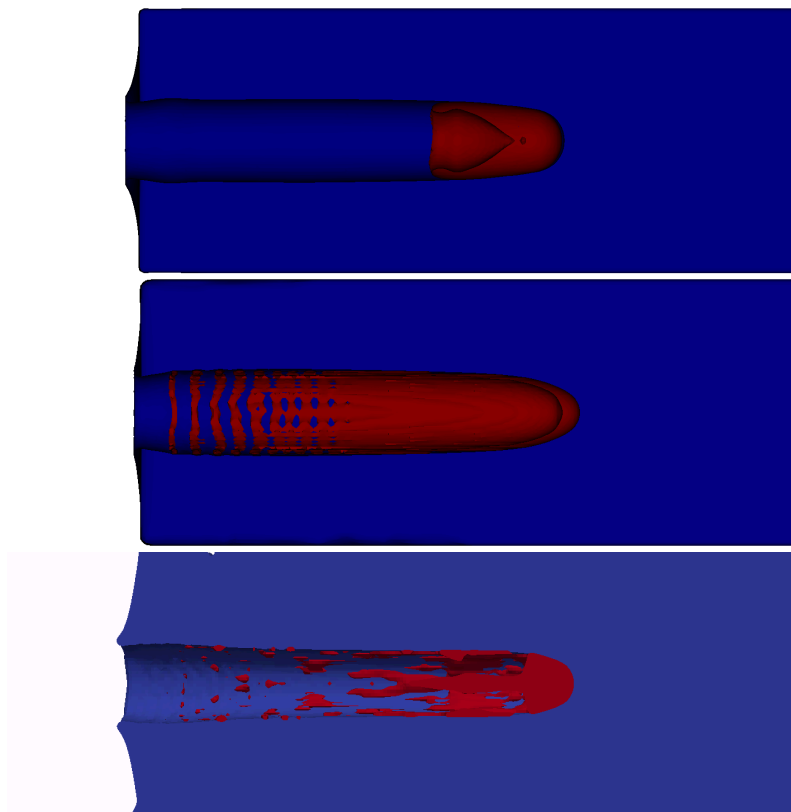


**Figure 6.40:** Comparison of maximum penetration depth for ALEAS MMM (top), ALEAS SMM (center), and CTH (bottom) penetrations of  $L/D=10$  tungsten alloy rods into steel targets with  $V_0$  of 2000 m/s

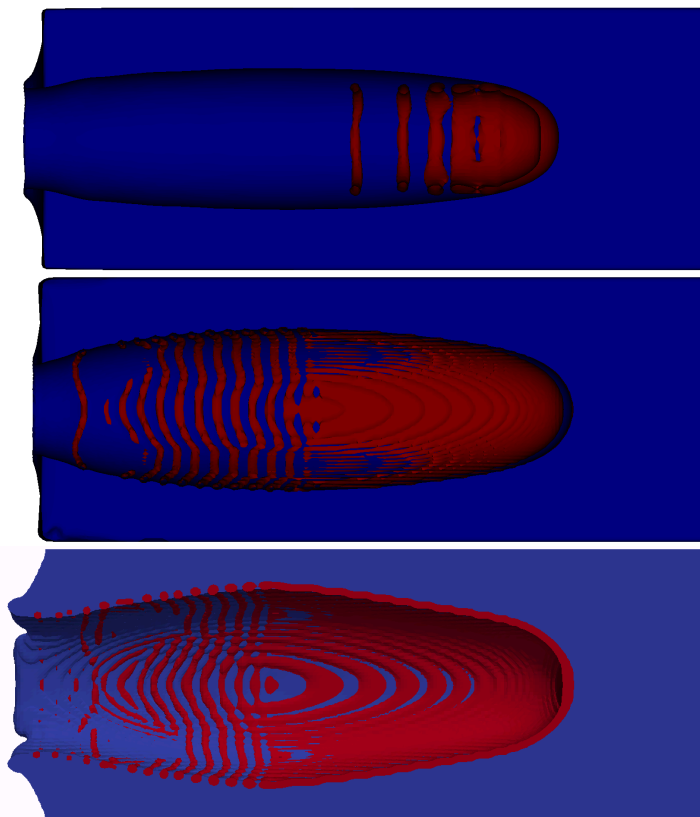


**Figure 6.41:** Comparison of maximum penetration depth for ALEAS MMM (top), ALEAS SMM (center), and CTH (bottom) penetrations of  $L/D=10$  tungsten alloy rods into steel targets with  $V_0$  of 3000 m/s

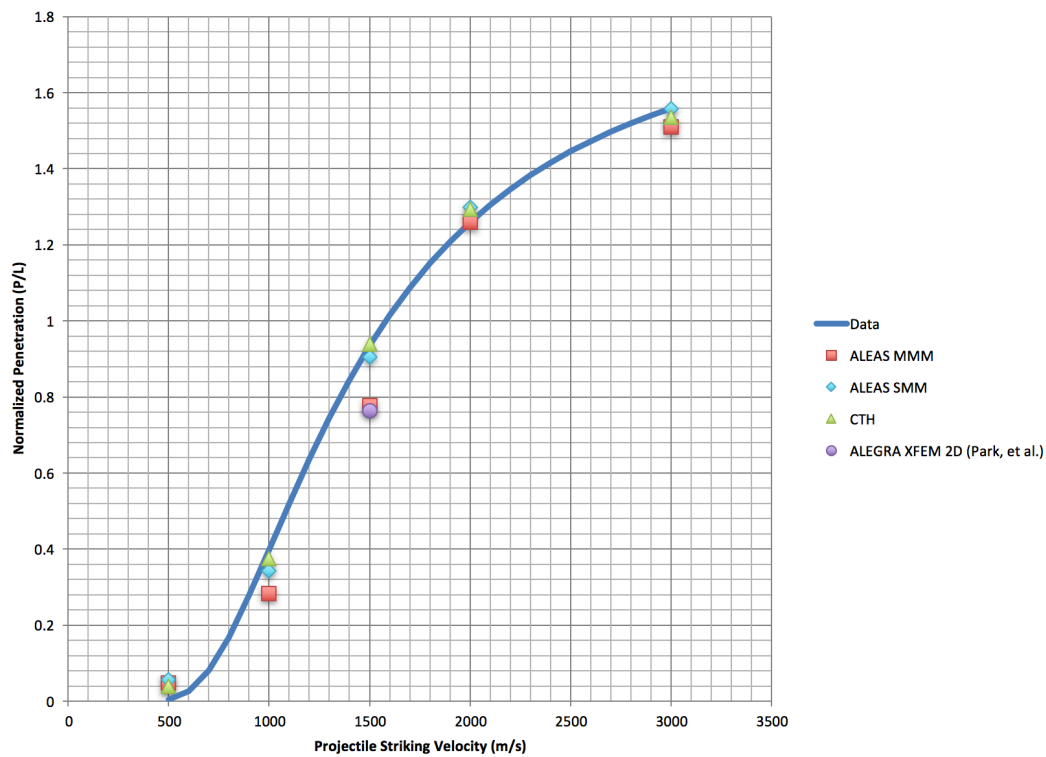


**Figure 6.42:** Comparison of normalized depth of penetration ( $P/L$ ) for ALEAS MMM, ALEAS SMM, CTH, and fit to experimental data [75] for  $L/D=10$  tungsten alloy rods into steel targets



## Sod Shock Tube

The Sod shock tube verification problem presented here is a three-dimensional representation of a one-dimensional problem. The shock moves in a planar fashion as it propagates through the medium in the Z-direction. In these simulations the X- and Y-directions had dimensions of 0.1 cm, while the Z-direction was 1 cm in length. Figures 6.43 to 6.45 show the contour plots of pressure, density, and velocity at 10 ms. These slices were taken at the midplane in the Y-direction. Figures 6.46 to 6.48 show the pressure, density, and velocity values versus position in the Z-direction that correspond to the row of elements along the centerline of Figures 6.43 to 6.45. As can be seen in Figures 6.46 to 6.48, the ALEAS MMM Sod shock tube results, shown in red, show generally good agreement to the analytical solution, shown in black, and agreement could be improved by increasing the mesh refinement. ALEAS MMM also resulted in very close agreement to the ALEAS SMM result, shown as blue dots. The CTH simulation, shown as a green dashed line, tends to more closely approximate the analytical result with the exception of an overshoot in velocity and an undershoot in pressure and velocity at the tail of the rarefaction wave. An oscillation at the contact discontinuity in the ALEAS MMM result can be seen in the velocity plot of Figure 6.43. This is not seen in the ALEAS SMM or CTH results due to the smearing of the interface that takes place as a result of mixture theory. This can be further seen to a small extent in Figure 6.46 and to a greater extent in Figure 6.48 at  $\sim 0.6$  cm, where ALEAS MMM showed a small oscillation due to small amounts of error in the change in velocity due to contact being introduced during the contact enforcement step. The current contact enforcement method implemented in ALEAS MMM tends to over-estimate the  $\Delta v$  values when only one

interface is present in the elements surrounding a node, meaning that the eight elements surrounding the node of interest are completely full of one material and a sliver of another material is present that needs to be moved completely out of the element. Methods for eliminating this are under investigation and will be examined in future work.

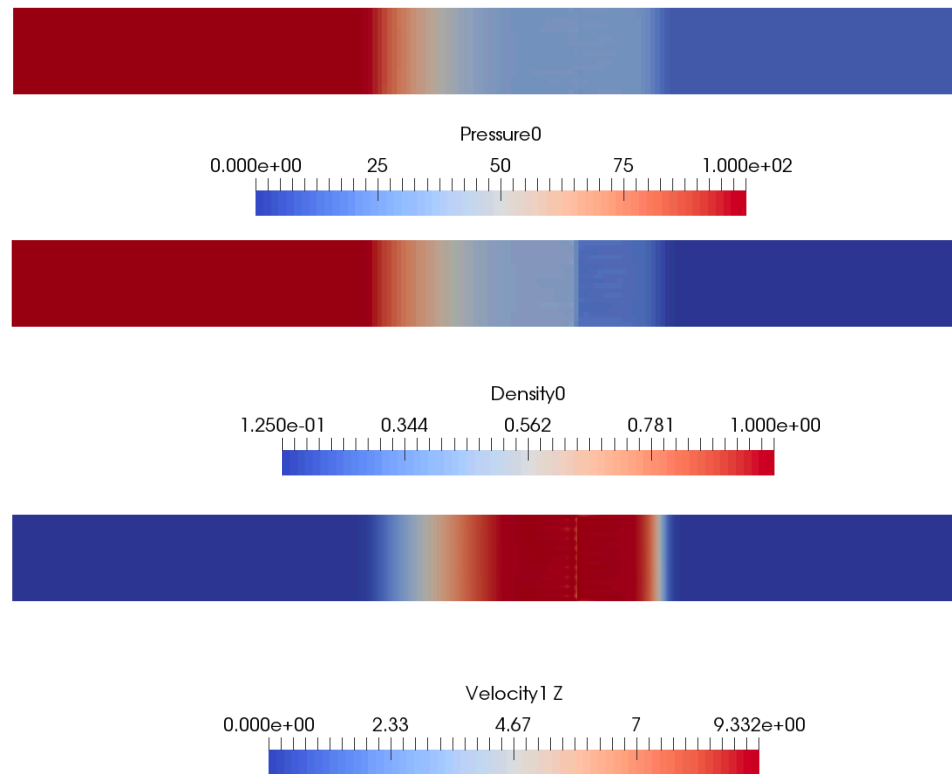


**Figure 6.43:** ALEAS MMM Sod shock tube results for pressure (top), density (center), and velocity (bottom) at 10 ms

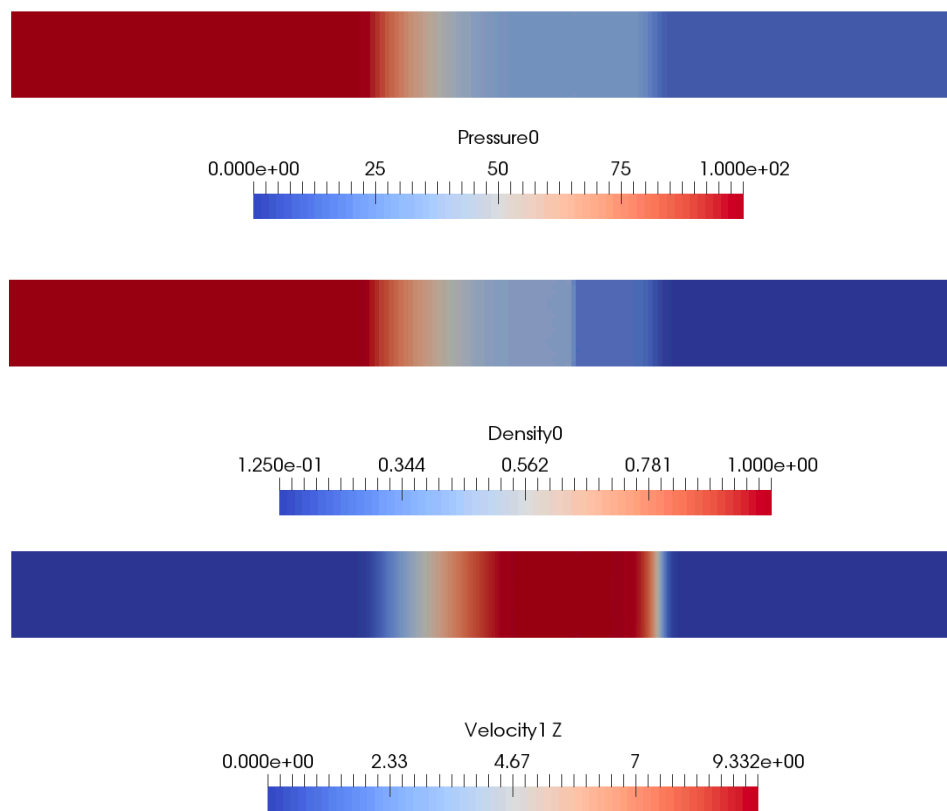


**Figure 6.44:** ALEAS SMM Sod shock tube results for pressure (top), density (center), and velocity (bottom) at 10 ms

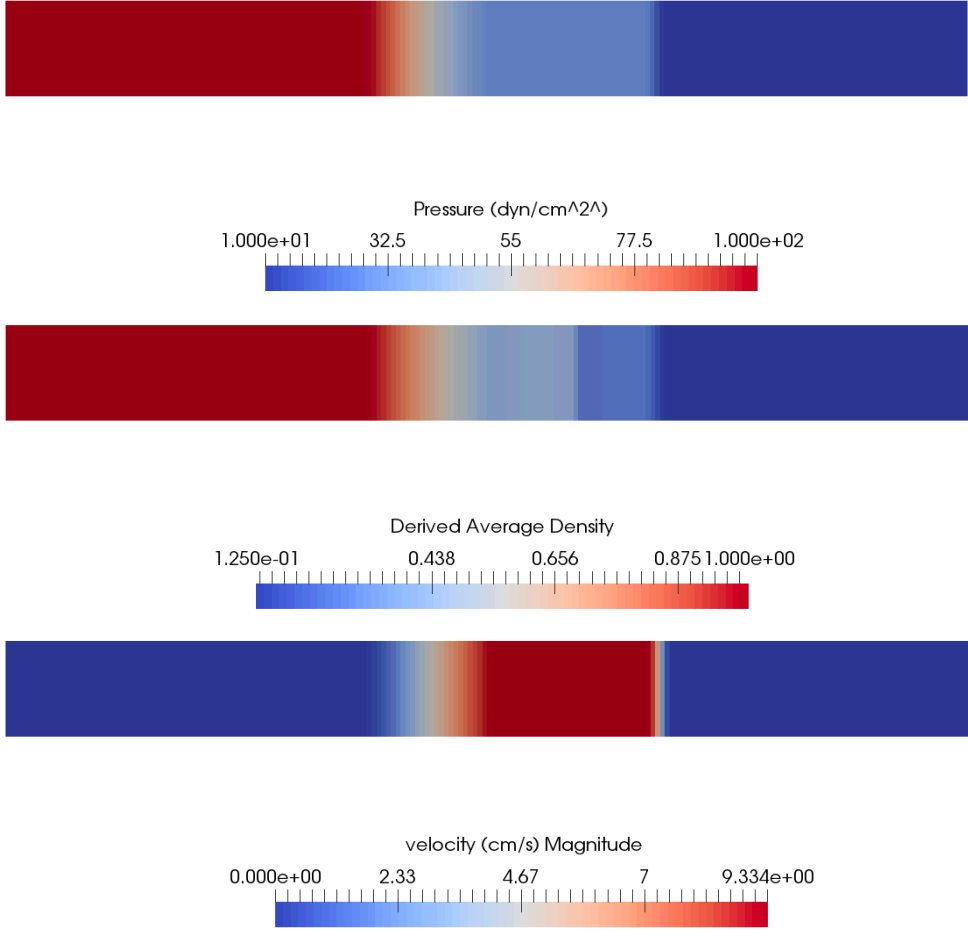


**Figure 6.45:** CTH Sod shock tube results for pressure (top), density (center), and velocity (bottom) at 10 ms

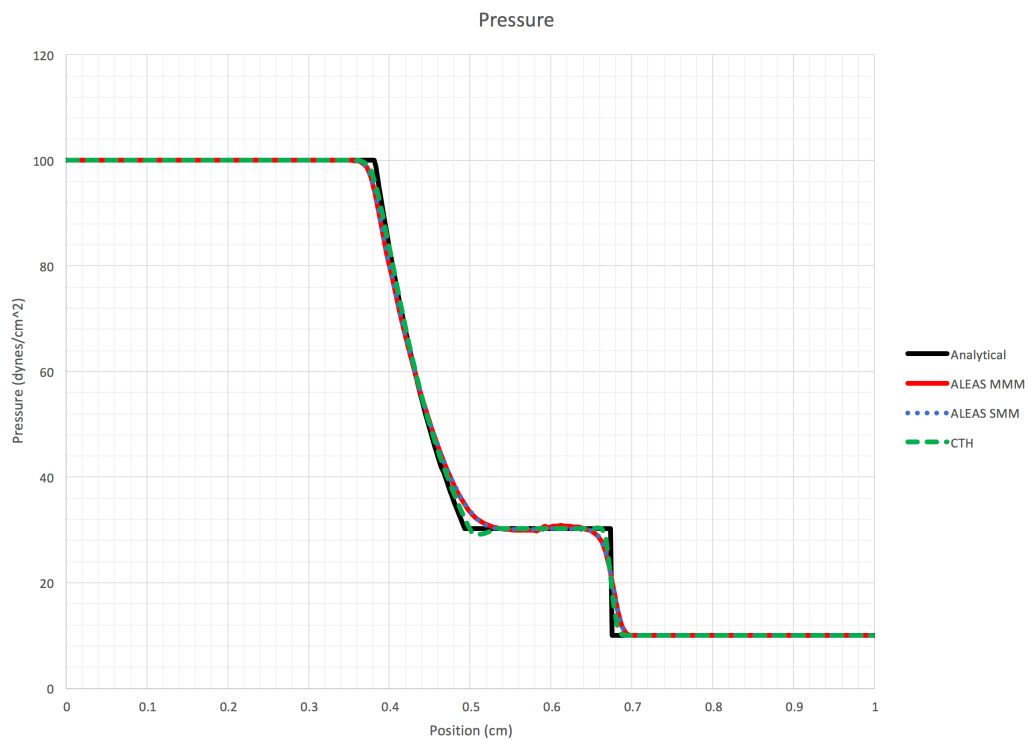


**Figure 6.46:** Comparison of pressure for Sod shock tube validation at 10 ms

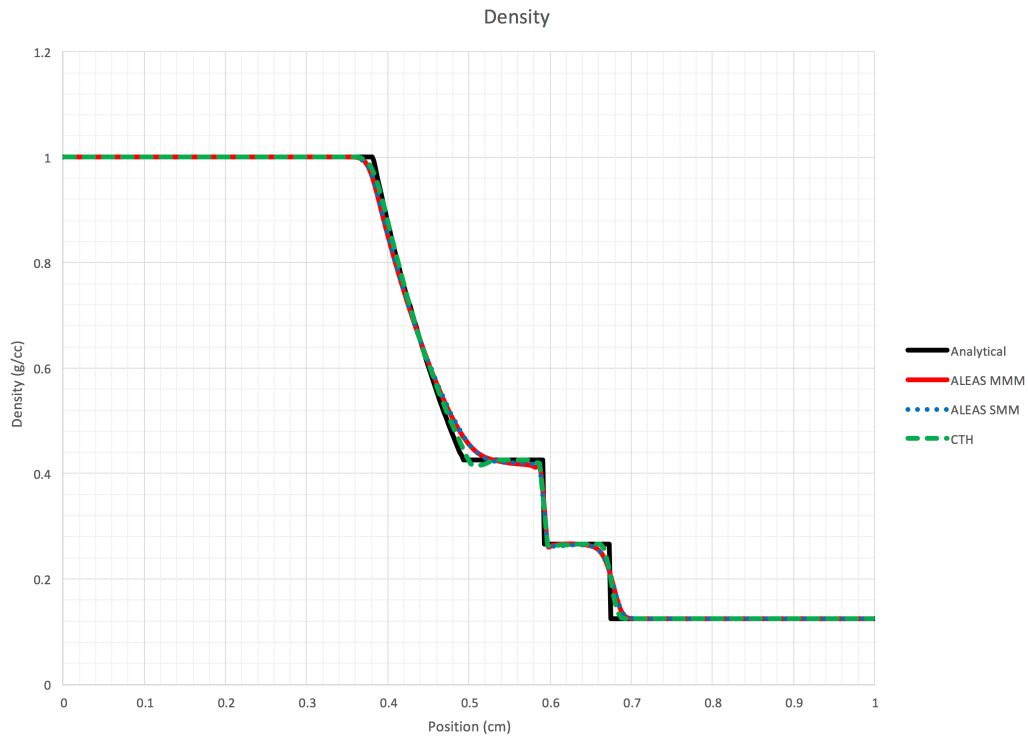


**Figure 6.47:** Comparison of density for Sod shock tube validation at 10 ms

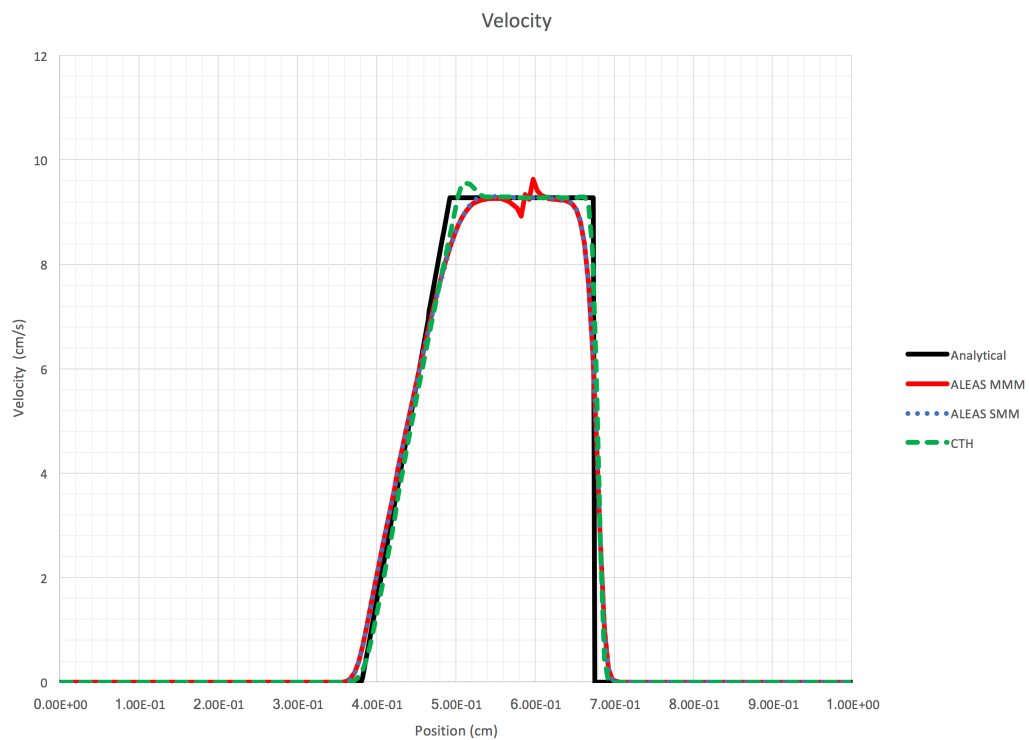


**Figure 6.48:** Comparison of velocity for Sod shock tube validation at 10 ms

## Discussion of Results

There are several advantages to using the contact formulation described in Chapter 3 of this work. Since this formulation treats each material separately, and there are no quantities associated with the whole cell, such as temperature, pressure, or strain rate; there is no need for the use of traditional cell mixture theory involving mixed cell thermodynamic, strength, and fracture algorithms, all of which provide a source of error in the calculations. Additionally, the form of the conservation equations used in these formulations guarantees element-level conservation of mass, momentum, and energy. This allows for the amount of material being transferred between adjacent elements to be determined easily. One other feature that distinguishes the approach used in this work is that each material has its own velocity field and, consequently, separate densities, velocities, energies, and stresses are updated for each material. As a result, contact constraints can be implemented and the physics taking place at the interface can more accurately be modeled.

The main complication of this method is a result of the ability of each material to have its own velocity field. Because of this it is possible for advection volumes to become complicated in shape or even disjoint. This difficulty is accounted for by using interface tracking, however not in the traditional sense. In a typical multi-material Eulerian contact formulation interface tracking is used to determine the contents of an advection volume whose shape is known. However, in this formulation the contents of the advection volume are known, and thus the shape of the advection volume can be determined. The advantages of using the formulation presented in this work are evident and can be seen in the results of the validation problems described shown in this chapter.

This method is most applicable to problems involving large stresses and deformations, but where the role of sliding contact is important. It is best suited to be used when stresses and deformations are too large to be handled by Lagrangian codes, but sliding contact, which cannot be handled properly by traditional Eulerian codes, is also critical to the accuracy of the solution. The normal penetration validation problems, which primarily rely on hydrodynamic deformation, have shown that this method performs admirably in cases where traditional Eulerian formulations perform well, but the added computational cost of the method and slightly reduced accuracy make the choice of the method presented here less appealing for modeling cases where accurately capturing the contact interface is less important.

It should be noted that a finely zoned mesh is important for the problems presented here, however some of these simulations are likely under-refined. For instance, the mesh size used in the semi-infinite rod penetration simulations was 0.05 cm cubes, which [75] notes resulted in relatively poor agreement for the 1500 m/s impact case in the 2D axisymmetric ALEGRA X-FEM code, in that work mesh convergence was reached with zoning of 0.0125 cm in the area of interest. Unfortunately, due to the current limitation of ALEAS only  $\sim 2e6$  elements can be read into memory. Overcoming this limitation would necessitate either an overhaul of the memory allocation structure in ALEAS or a complete changeover from FORTRAN77 to a newer version of FORTRAN to allow for use of quad-precision integers in the memory management routines. Furthermore, ALEAS is currently limited to uniform meshes, so the use of a graded mesh, which would allow for high refinement in the area of interest with coarser



refinement in other areas of the mesh, are not currently available. These issues are currently under investigation and will be addressed in future revisions of the code.

In order to maintain numerical stability a number of steps had to be taken. For instance, elements which contained very small volume fractions, typically less than  $1e-11$ , would sometimes lead to velocities many orders of magnitude greater than expected. To control this materials with element volume fractions less than  $1e-11$  were removed from the calculation and their content replaced with void. While this is a very small source of error it was necessary for stability of the calculation. Furthermore, to avoid issues associated with round-off error a tolerance of  $1e-13$  was implemented throughout the code. In cases where this tolerance was implemented a value less than the tolerance was assumed to be giving a nonzero value because of limitations resulting from the precision of the system and thus was reset to zero.

An artificial viscosity consisting of both a linear and quadratic term was also used to improve the stability of the simulations. This is used to treat discontinuities from shock waves and reduce ringing in the solution. In ALEAS the artificial viscosity calculation has been implemented in the Lagrangian step and included with the Cauchy stress components to solve the momentum and energy equations. This is the method which is commonly implemented in hydrocodes, however, it is unknown how the addition of the contact enforcement step will affect ringing in the simulations and if additional provisions need to be made to improve stability. While this type of stability issue was not noticed in the validation problems presented here more extensive testing is needed. This will be studied as part of future work.

Several approximations were made in order to reduce the complexity of the solution process. For instance, the description of the normal vector in interface tracking by  $\mathbf{n} = -\nabla\phi/|\nabla\phi|$  is one of many possible options. The determination of a surface normal for a non-planar surface contained within an element is inherently difficult. The use of Youngs' interface reconstruction algorithm, while providing a significant improvement over other available methods, does not accurately capture the surface geometry and allows for discontinuities in material interfaces at element boundaries. Despite its drawbacks Youngs' method is relatively simple to implement and more accurate than other existing interface reconstruction methods. Furthermore, determining a normal vector for the contact interface is also difficult. Since the interfaces are not necessarily aligned during contact enforcement it is possible to have normal vectors which are not equal and opposite. A method of determining an average surface and using the normal vector associated with that surface was used in this work, but this may not always be the best choice, especially in cases of contact between hard and soft materials. While the influence of these approximations is small they do contribute a source of error in the calculations, however, this error is expected to be reduced as mesh resolution is increased.

One further drawback of this approach is the added computational cost. A comparison of the computational costs for each class of validation problems when run using ALEAS SMM and ALEAS MMM is shown in Table 6.4. Because each class of validation problems resulted in similar runtimes and memory requirements Table 6.4 lists a typical result for each class of validations. The cost value listed is the runtime or memory required by the ALEAS MMM calculation divided by the value for the ALEAS

SMM calculation. All problems were run to 100  $\mu\text{s}$  with plot dumps performed every 1  $\mu\text{s}$ . The plot format used in ALEAS is a VTK ASCII format, used for its ease of implementation. However, this format is also very inefficient and results in significant slowdowns in runtime. There is also an added cost for ALEAS MMM when generating plot files due to the increased velocity and material specific information. Since the cost of generating plot files can be greatly reduced using a variety of other approaches Table 6.4 also lists runtime costs with the time required to generate plot dumps removed to better demonstrate the cost incurred by the method presented here. It should also be noted that since ALEAS is a research code many of the algorithms and methods used have not undergone optimization to improve code efficiency. Because of this it is likely that the cost of the contact enforcement can be further reduced.

Table 6.4: Computational cost of the contact method

	Runtime Cost Factor (with plots)	Runtime Cost Factor (without plots)	Memory Cost Factor*
Block Sliding	1.209	1.201	1.021
Taylor Impact	1.107	1.065	1.023
Oblique Penetration	1.263	1.074	1.019
Normal Penetration (2" Target)	1.352	1.418	1.017
Normal Penetration (Semi-infinite Target)	1.436	1.529	1.020

As can be seen, the cost of using the method presented here is highly dependent on the number of mixed cells that must be considered during contact enforcement. It should be noted that since ALEAS is a research code several of these runs included job

specific debugging output. In some cases the amount of output was fairly substantial and the output may have changed between MMM and SMM runs. Therefore these runtime cost values may be skewed, but should provide a fairly reasonable approximation of the cost the user might expect for the validation runs presented here. The memory cost appears to be negligible, however, this is likely a result of a bug in the memory allocation routine which initializes arrays based on the expectation for ALEAS MMM, rather than reducing the memory requirement when only a single velocity field is required for ALEAS SMM. The actual memory cost would likely be much more substantial, on the order of 1.5-2.0, if the memory allocation routine was corrected due to the addition of separate velocity fields for each material. However, given the large amounts of memory available on modern computers the added memory cost can often be accommodated fairly easily.

Despite the limitations of ALEAS discussed here, the results show a significant improvement in the accuracy of problems where sliding contact is important and comparable performance to the traditional Eulerian formulation in other situations.

Readers interested in implementing the method presented here should note that the process requires a number of modifications to existing Eulerian and ALE finite element codes. First, the reader must ensure that the form of the conservation equations implemented in the code is the same as that described in Chapter 3 of this work. In terms of data structure, all velocity arrays, as well as those associated with velocity such as momentum arrays, must be made multi-dimensional to accommodate separate velocity fields for each material. Interface tracking routines must be modified to run separately for each material and the velocity used to determine the size of the advection volume in the

contact remap step must be the change of velocity due to contact. Parameters such as deviatoric stress, pressure, temperature, yield stress, shear stress, and artificial viscosity must be material specific values rather than values obtained through the use of mixture theory algorithms. Finally, the two operator split approach to solving the conservation equations must be implemented along with a method similar to what is described in Chapter 3 for enforcing the contact constraints. While this can take many forms, the outline presented in Chapter 3 can serve as a guide.

As with most dissertations, this work builds on prior research so it is important to distinguish the contributions made as a result of this work. The two operator split approach was initially developed by Littlefield as reported in [64] in 2002, and further refined by both Littlefield and this author in [65], [67], [94], and [95]. All prior implementations of the method outlined in Chapter 3 were done in two-dimensions. The major contribution of this work beyond what was reported in the work that this dissertation builds upon was the transition to three-dimensions. This required a significant overhaul of the existing two-dimensional ALEAS code, which was used as a template to transition to three-dimensions. The derivation of the conservation equations and the finite element formulation presented in Chapter 3 are not presented with respect to a specific dimensionality, however, the addition of the third dimension required significant changes to almost every part of the code. Furthermore, the method for determining the contact interface areas during the contact enforcement step had to be derived in three-dimensions. Finally, the method presented here for simplifying the determination of the velocities due to contact enforcement by using an averaged interface area was developed by the author.

## CHAPTER 7

### CONCLUSIONS

This work has presented a new method for the treatment of multi-material contact-impact problems in Eulerian hydrocodes used for computational structural mechanics. The ALE form of the conservation equations have been solved separately for each material in the problem space by using a finite element approximation and contact constraints have been applied so that tractions arising at contact interfaces can be accurately modeled. In this work the traction, which is implied as part of the conservation of volume in traditional approaches, is explicitly included as part of the conservation equations. Since each material is treated separately each contacting body has its own velocity field and contact is handled in a more physically accurate manner. This leads to a significant improvement over traditional Eulerian contact methods that make use of mixture theory for problems which involve large stresses and deformations, but where the ability to accurately model sliding contact is important.

The model presented here provides a much better representation of the physics taking place in the problem. The use of mixed-cell algorithms that replace discontinuities in pressure, stress, and velocity fields at material interfaces with single continuous fields are no longer used and as such are no longer necessary. This work represents a major shift in the implementation of Eulerian hydrocodes. The use of this method is highly

advantageous over Lagrangian methods, which are incapable of handling large deformations and also must account for large mesh distortions, as well as traditional Eulerian methods, which cannot accurately model contact events due to highly inaccurate element mixture algorithms that assume material bonding.

The advantages of using the method presented in this work have been discussed in Chapter 6. The block sliding simulations clearly demonstrate that no material replacement is taking place, whereas the large amount of deformation along the contact boundaries in the traditional Eulerian formulation indicates the weakness of the mixture model used for that method. The Taylor impact test further demonstrates the advantages of the method presented in this work. Since both the rigid plate and the copper impactor have their own unique velocity fields and no mixed element algorithms are used the results are much more physically accurate. The deformation profile of the rod in the ALEAS MMM cases much more closely approximates the experimental profile and rebounding occurs at late times indicating there is no material replacement occurring. Comparing this result to the traditional Eulerian method used in the ALEAS SMM and CTH problems emphasizes the superiority of this formulation in modeling this type of problems. In the traditional approach material bonding is evident along the interface between the copper bar and rigid plate, and as such the spread of material at the interface is much more limited. The practical applications of the method presented in this work were further indicated by simulations of a long rod penetrator into oblique plates at various yaw angles. This class of problems is especially difficult to model accurately using traditional Eulerian methods due to material bonding that takes place as the penetrator passes through the moving plate. This interaction between materials causes an

artificial slowing of the penetrator as it emerges from the plate, which is most clearly evident in the  $-9.3^\circ$  yaw case. In this case nearly the entire length of the penetrator interacts with the moving plate, resulting in a significant reduction in velocity of the penetrator that is not seen experimentally, as well as a large fragment of the plate breaking off and sticking to the penetrator at late time. The ALEAS MMM result much more closely approximates the experimental result, with no artificial slowing of the rod and no plate material being erroneously bonded to the penetrator. Finally, a series of normal long rod penetrations into steel targets showed that the methodology developed here performs admirably in cases where the role of contact is diminished.

### Future Work

While this dissertation has demonstrated a tremendous improvement over traditional Eulerian methods in cases where sliding contact is important, work in this area is far from complete. For the impact types considered the validation calculations have demonstrated the advantages of this method over the traditional approach to Eulerian contact mixture theory, but further improvements can be made. A number of issues were mentioned in previous chapters of this work. For instance, in terms of computational improvements to the ALEAS code, future work will include revisions to the memory structure to allow problems with more than two million computational elements. Furthermore, a significant benefit would be realized by adding the ability to do large scale parallel computations using MPI. Also, much of the code in ALEAS has not been optimized for speed, so improvements to algorithm efficiency will be examined. Since ALEAS is currently limited to uniform meshes, it would be highly beneficial to include



the ability to model non-uniform meshes to cut down on computational cost. Future revisions of ALEAS will also include a number of advanced material models to allow for more accurate modeling of a variety of processes.

The contact algorithm presented in this work is very promising, but its development is still in the early stages and there is considerable room for improvement. Some possible areas of future research include the following list.

- Higher order interface tracking methods that would more accurately define non-planar surfaces, such as corners, and eliminate discontinuities at element boundaries.
- The contact algorithm currently implemented in ALEAS only allows for two materials to be present in the problem domain, so generalizing this to more than two materials would greatly improve its applicability. This will require determining how to model interactions between three or more materials within a single element. This will likely include a method for determining material ordering and multiple contact enforcements to ensure that the contact constraints are satisfied.
- One method for reducing the cost of this method when more than two materials are present is to couple the contact method developed here with mixture theory. This would allow the contact formulation to handle interactions where contact is important, while the less expensive mixture theory algorithms are used elsewhere.
- The method for calculating the contact velocity presented in this work is one of many possibilities. One simplification made in the contact algorithm developed in this work is the use of an averaged interface area for the master and slave

surfaces, which provides a significant simplification to derivation of the algorithm. More advanced contact algorithms are possible that account for individual interface areas, as well as providing better handling of cases where small slivers of material are being moved out of an element.

- The current contact approach only accounts for frictionless sliding, so the addition of a friction model with slip would provide even greater applicability.
- It may be possible to eliminate the need for a second remap step by including the contact enforcement as part of the Lagrangian step. This would result in a significant reduction in the computational cost of the method.
- Finally, the current contact approach does not make provisions for self-contact within a single material. Because each material only has one volume fraction per element, that material is considered to be one unified group. This is a very difficult problem to solve, and not one that will be affected by solving the conservation equations separately for each material as done in this work.

## REFERENCES

- [1] Anderson, C. (1987). An Overview of the Theory of Hydrocodes. *International Journal of Impact Engineering*, 5, 33-59.
- [2] Anderson, C. & Walker, J. (1991). An Examination of Long-rod Penetration. *International Journal of Impact Engineering*, 11 (4), 481-501.
- [3] Anderson, C., Morris, B., & Littlefield, D. (1992). A Penetration Mechanics Database. *Southwest Research Institute Report 3593/001*. San Antonio TX.
- [4] Anitescu, M. & Potra, F. (1996). Formulating Dynamic Multi-rigid-body Contact Problems with Friction as Solvable Linear Complementarity Problems. *Reports on Computational Mathematics*, 93, 1-21.
- [5] Arione, S. & Bjorkman, M. (1986). Scaling Flow Fields from the Impact of Thin Plates. *International Journal of Impact Engineering*, 5.
- [6] Banerjee, B. (2005). An Evaluation of Plastic Flow Stress Models for the Simulation of High-temperature and High-strain-rate Deformation of Metals. *arXiv.org:cong-mat/0512466*.
- [7] Bell, R. & Hertel, E. (1992). An Improved Material Interface Reconstruction Algorithm for Eulerian Codes. *Sandia National Laboratories Report SAND 92-1716*. September 1992.
- [8] Bell, R., et al. (2005). CTH User's Manual and Input Instructions, Version 7.0. CTH Development Project, Sandia National Lab., Albuquerque, New Mexico.
- [9] Ben-Dor, G., Dubinsky, A., & Elperin, T. (2000). Analytical Solutions for Penetration by Rigid Conical Impactors Using Cavity Expansion Models. *Mechanical Research Communications*, 27 (2), 185-189.
- [10] Ben-Dor, G., Dubinsky, A., & Elperin, T. (2005). Ballistic Impact: Recent Advances in Analytical Modeling of Plate Penetration Dynamics—A Review. *Applied Mechanics Reviews*, 58, 355-371.

- [11] Benson, D. (1992). Computational Methods in Lagrangian and Eulerian Hydrocodes. *Computer Methods in Applied Mechanics and Engineering*, 99 (2-3), 235-394.
- [12] Benson, D. (1992). Momentum Advection on a Staggered Mesh. *Journal of Computational Physics*. 100, 143-162.
- [13] Benson, D. (1995). A Multi-material Eulerian Formulation for the Efficient Solution of Impact and Penetration Problems. *Computational Mechanics*, 15, 558-571.
- [14] Benson, D. (1997). A Mixture Theory for Contact in Multi-material Eulerian Formulations. *Computer Methods in Applied Mechanics and Engineering*, 140, 59-86.
- [15] Benson, D. (1998). Eulerian Finite Element Methods for the Micromechanics of Heterogeneous Materials: Dynamic Prioritization of Material Interfaces. *Computer Methods in Applied Mechanics and Engineering*, 151, 343-360.
- [16] Benson, D. (1998). Stable Time Step Estimation for Multi-material Eulerian Hydrocodes. *Computer Methods in Applied Mechanics and Engineering*, 167, 191-205.
- [17] Benson, D. (2000). An Implicit Multi-material Eulerian Formulation. *International Journal for Numerical Methods in Engineering*, 48, 475-499.
- [18] Benson, D. & Hallquist, J. (1986). A Simple Rigid Body Algorithm for Structural Dynamics Programs. *International Journal for Numerical Methods in Engineering*, 22, 723-749.
- [19] Benson, D., & Okazawa, S. (2004). Contact in a Multi-material Eulerian Finite Element Formulation. *Computer Methods in Applied Mechanics and Engineering*, 193, 4277-4298.
- [20] Benson, D. (2008). Momentum Advection on Unstructured Staggered Quadrilateral Meshes. *International Journal for Numerical Methods in Engineering*, 75, 1549-1580.
- [21] Bjork, R. (1986). The Physics of Hypervelocity Lethality. *International Journal of Impact Engineering*, 5.
- [22] Bjorkman, M. & Holsapple (1986). Velocity Scaling Volume of Melted Target Material. *International Journal of Impact Engineering*, 5.

- [23] Brunig, M. & Driemeier, L. (2007). Numerical Simulation of Taylor Impact Tests. *International Journal of Plasticity*, 23, 1979-2003.
- [24] Cagliostro, D., Mandell, D., Schwalbe, L., Adams, T., & Chapyak, E. (1989) MESA 3-D Calculations of Armor Penetration by Projectiles with Combined Obliquity and Yaw. *Proceedings of the Hypervelocity Impact Symposium*. San Antonio, TX, December 12-14, 1989.
- [25] Cengel, Y. & Cimbala, J. (2006). *Fluid Mechanics: Fundamentals and Applications*. New York: McGraw-Hill.
- [26] Cline, M. (2002). Rigid Body Simulation with Contact and Constraints. M.S. Thesis, The University of British Columbia.
- [27] Corley, J. (2001). Characterization and Modeling of the Dynamic Mechanical Properties of a Particulate Composite Material. M.S. Thesis, Universitat der Bundeswehr Munchen, Germany.
- [28] Courant, R. (1943). Variational methods for the solution of problems of equilibrium and vibrations. *Bulletin of the American Mathematical Society*, 49:1-23.
- [29] Clough, R. (1960). The finite element method in plane stress analysis. In *2<sup>nd</sup> Conference in Electronic Computation*, pages 345-378. American Society of Civil Engineers, Pittsburgh, PA.
- [30] Daneshjou, K., Shahravi, & M., Rahimzadeh, M. (2007). Comparative Study of Nose Profile Role in Long-Rod Penetration. *Journal of Solid Mechanics and Materials Engineering*, 1 (5), 635-643.
- [31] Donea, J., Huerta, A., Ponthot, J., & Rodriguez-Ferran, A. (2004). Arbitrary Lagrangian—Eulerian Methods. In E. Stein, R. de Borst, & J. Hughes (Eds.). *Encyclopedia of Computational Mechanics* (pp. 1-25). John Wiley & Sons.
- [32] Drumheller, D. (1987). Hypervelocity Impact of Mixtures. *International Journal of Impact Engineering*, 5, 261-268.
- [33] Eakins, D.E. & Thadhani, N.N. (2006). Instrumented Taylor Anvil-on-Rod Impact Tests for Validating Applicability of Standard Strength Models to Transient Deformation States. *Journal of Applied Physics*, 100, No. 073503.
- [34] Eakins, D.E. & Thadhani, N.N. (2007). Analysis of Dynamic Mechanical Behavior in Reverse Taylor Anvil-on-Rod Impact Tests. *International Journal of Impact Engineering*, 34, 1821-1834.

- [35] Evans, M. & Harlow, F. (1957). The Particle-in-Cell Method for Hydrodynamics Calculations. Los Alamos Scientific Lab. *Report No. LA-2139*, Los Alamos, New Mexico.
- [36] Fleming, M., Chu, Y., Moran, B., and Belytschko, T. (1997). Enriched element-free Galerkin methods for crack tip fields. *International Journal for Numerical Methods in Engineering*, 40:1483-1504.
- [37] Freeman, D., Wriggers, P. (2007). Advection Approaches for Single- and Multi-material Arbitrary Lagrangian-Eulerian Finite Element Procedures. *Journal of Computational Mechanics*, 39, 153-190.
- [38] Fugelso, E., Taylor, J. (1978). Evaluation of Obliquity and Yaw for U 0.75 wt% Ti Penetrators. *Los Alamos National Laboratory Report LA-7402-MS*.
- [39] Galerkin, B. (1915). Series Solution of some problems of elastic equilibrium of rods and plates. *Vestnik Inzhenerov I Tekhnikov*, 19:897-908.
- [40] Gee, D.J. (2003). Plate Perforation by Eroding Rod Projectiles. *International Journal of Impact Engineering*, 28, 377-390.
- [41] Hallquist, J. (2005). LS-Dyna Theory Manual. Livermore Software Technology Corporation. November 2005.
- [42] Hertel, E., et al. (1993). CTH: A Software Family for Multi-Dimensional Shock Physics Analysis. Proceedings of the 19th International Symposium on Shock Waves, Marseille, France, July 1993, 377-382.
- [43] Hertel, E. & Kerley, G. (1998). CTH Reference Manual: The Equation of State Package. Sandia National Lab. Report No. SAND98-0947.
- [44] Heinrich, J. and Pepper, D. (1999). *The intermediate finite element method: fluid flow and heat transfer applications*. Taylor and Francis, 1<sup>st</sup> Ed.
- [45] Hohler, V. & Stilp, A. (1977). Penetration of Steel and High Density Rods in Semi-infinite Steel Targets. *Proceedings of the 3<sup>rd</sup> International Symposium on Ballistics*, Karlsruhe, Germany. March 1977.
- [46] Hohler, V. & Stilp, A. (1987). Hypervelocity Impact of Rod Projectiles with L/D from 1 to 32. *International Journal of Impact Engineering*, 5,323-331.

- [47] Holian, K. & Burkett, M. (1986). Sensitivity of Hypervelocity Impact Simulations to Equation of State. *International Journal of Impact Engineering*, 5.
- [48] Holsapple, K. (1986). On Scaling of Impact Phenomena. *International Journal of Impact Engineering*, 5.
- [49] Hrenikoff, A. (1941). Solution of problems in elasticity by the frame work method. *Journal of Applied Mechanics*, 8(4):169-175.
- [50] Huebner, K., Dewhirst, D., Smith, D., and Byron, T. (2001). *The finite element method for engineers*. Wiley-Interscience, 4<sup>th</sup> Ed.
- [51] Idelsohn, S.R., Onate, E., Nestor, C., & Del Pin, F. (2001). The Meshless Finite Element Method *XII Congress on Numerical Methods and their Applications*. Cordoba, Argentina, October 30-November 11, 2001.
- [52] Jenq, S., et al. (2006). Simulation of a Rigid Plate Hit by a Cylindrical Hemi-spherical Tip-ended Soft Impactor. *Computational Materials Science*, 39, 518-526.
- [53] Johnson, W. (1963). Computer Development to Improve SHELL Code. GA-4673, General Atomic, San Diego, CA.
- [54] Johnson, W. & Anderson, C. (1987). History and Application of Hydrocodes in Hypervelocity Impact. *International Journal of Impact Engineering*, 5, 423-439.
- [55] Johnson, G., Stryk, R., Holmquist, T., & Beissel, S. (1997). Numerical Algorithms in a Lagrangian Hydrocode. *Wright Laboratory, Armament Directorate, WL-TR-1997-7039*. June 1997.
- [56] Jones, S.E., Maudlin, P.J., & Foster, J.C. (1995). Constitutive Modeling Using the Taylor Impact Test. *Symposium on High Strain Rate Effects on Polymers, Metal, and Ceramic Matrix Composites and Other Advanced Materials, ASME Congress and Exposition*, San Francisco, CA, November 14, 1995.
- [57] Jones, S.E., Maudlin, P.J., & Foster, J.C. (1996). An Engineering Analysis of Plastic Wave Propagation in the Taylor Test. *International Journal of Impact Engineering*, 19 (2), 95-106.
- [58] Jones, S.E., Drinkard, J.A., Rule, W.K., & Wilson, L.L. (1997). An Elementary Theory for the Taylor Impact Test. *International Journal of Impact Engineering*, 21, 1-13.

- [59] Jun, B. (2001). A Simple Advection Scheme for Material Interface. *Nuclear Explosives Code Developer's Conference 2000*, Oakland, CA, October 23-27, 2000.
- [61] Lord Rayleigh (John William Strutt). (1877). *Theory of Sound*. Macmillan, London.
- [62] Lim, H. & Taylor, R. (2001). An Explicit-Implicit Method for Flexible-rigid Multibody Systems. *Finite Elements in Analysis and Design*, 37, 881-900.
- [63] Littlefield, D. (2001). The Use of  $r$ -adaptivity with Local, Intermittent Remesh for Modeling Hypervelocity Impact and Penetration. *International Journal of Impact Engineering*, 26 (1), 433-442.
- [64] Littlefield, D. (2002). A Method for Treatment of Dynamic Contact-Impact in Multi-material Frameworks. *Fifth World Congress on Computational Mechanics*, Vienna, Austria, July 7-12, 2002.
- [65] Littlefield, D. (2006). Modeling Contact in Multi-material Frameworks. *Seventh World Congress on Computational Mechanics*. Los Angeles, CA, July 16-22, 2006.
- [66] Littlefield, D. (2007). Improvements to Multi-material Advection Algorithms in MACH. Final report from Air Force Research Laboratory Contract #FA9451-05-M-0225, Submitted August 2007.
- [67] Littlefield, D.L., and Walls, K.C. (2008). An improved contact algorithm for multimaterial continuum codes. *Eighth World Congress on Computational Mechanics*. Venice, Italy, June 30-July 5, 2008.
- [68] Lu, G., Wang, B., & Zhang, T. (2001). Taylor Impact Test for Ductile Porous Materials—Part 1: Theory. *International Journal of Impact Engineering*, 25, 981-991.
- [69] Martin, M., Mishra, A., Meyers, M.A., & Thadhani, N.N. (2007). Instrumented Anvil-on-Rod Tests for Constitutive Model Validation and Determination of Strain-Rate Sensitivity of Ultrafine-grained Copper. *Materials Science and Engineering A*, 464, 202-209.
- [70] Mase, G.T. & Mase, G.E. (1999). *Continuum Mechanics for Engineers* (2<sup>nd</sup> ed.). New York: CRC Press.
- [71] McGlaun, J., Thompson, S., & Elrick, M. (1990). CTH: A Three-dimensional Shock Wave Physics Code. *International Journal of Impact Engineering*, 10, 351-360.



- [72] Mirtich, B. (1998). Rigid Body Contact: Collision Detection to Force Computation. *IEEE International Conference on Robotics and Automation*, May 1998.
- [73] Moes, N., Dolbow, J., and Belytschko, T. (1999). A finite element method for crack growth without remeshing. *International Journal for Numerical Methods in Engineering*. 46:131-150.
- [74] Okazawa, S., Kashiya, K., & Kaneko, Y. (2007). Eulerian Formulation Using Stabilized Finite Element Method for Large Deformation Solid Dynamics. *International Journal for Numerical Methods in Engineering*, 72, 1544-1559.
- [75] Park, B., Leavy, R., & Niederhaus, J. (2013). Penetration of Rod Projectiles in Semi-Infinite Targets: A Validation Test for Eulerian X-FEM in ALEGRA. *Sandia National Laboratories Report SAND2013-1863*. March 12, 2013.
- [76] Perry, J. & Carroll, D. (2000). Multi-material ALE Methods in Unstructured Grids. *Computer Methods in Applied Mechanics and Engineering*, 187 (3), 591-619.
- [77] Piekutowski, A. (1986). Debris Cloud Generated by Hypervelocity Impact of Cylindrical Projectiles with Thin Aluminum Plates. *International Journal of Impact Engineering*, 5.
- [78] Reddy, J. (2006). *An Introduction to the Finite Element Method* (3<sup>rd</sup> ed.). New York: McGraw-Hill.
- [79] Ritz, W. (1909). Uber eine neue method zur losung gewisser variations – problem der mathematischen physic. *Journal fur die Reine und Angewandte Mathematik*, 135:1-61.
- [80] Schmidt, R. & Housen, K. (1986). Some Recent Advances in the Scaling of Impact and Cratering. *International Journal of Impact Engineering*, 5.
- [81] Schmitt, R., *et al.* (2014). CTH User's Manual and Input Instructions. Version 11.0. Sandia National Laboratories.
- [82] Schultz, J., Heimdahl, O., & Finnegan, S. (1986). Computer Characterization of Debris Clouds Resulting from Hypervelocity Impact. *International Journal of Impact Engineering*, 5.

- [83] Silling, S. (1995). CTH Reference Manual: Boundary Layer Algorithm for Sliding Interfaces in Two Dimensions. Sandia National Laboratory. SAND93-2487. September 1995.
- [84] Spillman, G. (1986). A Simple Defense Conservative Model for Mass Requirements of Hypervelocity Projectile Shields for Reentry Vehicles. *International Journal of Impact Engineering*, 5.
- [85] Sukumar, N., Moes, N., Moran, B., and Belytschko, T. (2000). Extended finite element method for three dimensional crack modeling. *International Journal for Numerical Methods in Engineering*, 48(11):1549-1570.
- [86] Sukumar, N. (2003) Meshless Methods and Partition of Unity Finite Elements. *Proceedings of the Sixth International ESAFORM Conference on Material Forming*, 603-606.
- [87] Taylor, G.I. (1948). The Use of Flat-Ended Projectiles for determining Dynamic Yield Stress: I. Theoretical Considerations. *Proceedings of the Royal Society of London. Series A*, 194, 194-289.
- [88] Trucano, T. & Asay, J. (1986). Effects of Vaporization Debris Cloud Dynamics. *International Journal of Impact Engineering*, 5.
- [89] Turner, M., Clough, R., Martin, H., & Topp, L. (1956). Stiffness and deflection analysis of complex structures. *Journal of Aeronautical Sciences*, 23(9):805-824.
- [90] Vitali, E. & Benson, D. (2006). An Extended Finite Element Formulation for Contact in Multi-material Arbitrary Lagrangian-Eulerian Calculations. *International Journal for Numerical Methods in Engineering*, 67, 1420-1444.
- [91] Vitali, E. & Benson, D. (2008). Contact with friction in multi-material arbitrary Lagrangian-Eulerian formulations using X-FEM. *International Journal for Numerical Methods in Engineering*, 76, 893-921.
- [92] Vitali, E. & Benson, D. (2009). Kinetic friction for multi-material arbitrary Lagrangian Eulerian extended finite element formulations. *Journal of Computational Mechanics*, 43, 847-857.
- [93] Walker, J. (2001). Hypervelocity Penetration Modeling: Momentum vs. Energy and Energy Transfer Mechanisms. *International Journal of Impact Engineering*, 26, 809-822.

- [94] Walls, K. C. and Littlefield, D. L. (2013) An Improved Contact Algorithm for Multi-Material Continuum Codes, in *Materials under Extreme Loadings: Application to Penetration and Impact* (eds E. Buzaud, I. R. Ionescu and G. Z. Voyiadjis), John Wiley & Sons, Inc., Hoboken, NJ, USA.
- [95] Walls, K.C. (2008). Multi-material Contact for Computational Structural Mechanics. M.S. Thesis. The University of Alabama at Birmingham.
- [96] Walsh, J. & Johnson, W. (1965). On the Theory of Hypervelocity Impact. *Proceedings of the Seventh Hypervelocity Impact Symposium*, Vol. II, Theory.
- [97] Wang, B., Zhang, J., & Lu, G. (2002). Taylor Impact Test for Ductile Porous Materials—Part 2: Experiments. *International Journal of Impact Engineering*, 28, 499-511.
- [98] White, F. (2006). *Viscous Fluid Flow* (3<sup>rd</sup> Edition). New York: McGraw-Hill.
- [99] Wilkins, M.L. & Guinan, M.W. (1973). Impact of Cylinders on a Rigid Boundary. *Journal of Applied Physics*, 44(3), 1200-1206.
- [100] Youngs, D. (1987). An Interface Tracking Method for a 3D Eulerian Hydrodynamics Code. Atomic Weapons Research Establishment Report No. AWRE/44/92/35.
- [101] Zhong, Z. (1993). *Finite Element Procedures for Contact-Impact Problems*. New York: Oxford University Press.
- [102] Zocher, M.A., Maudlin, P.J., Chen, S.R., & Flower-Maudlin, E.C. (2000). An Evaluation of Several Hardening Models Using Taylor Cylinder Impact Data. *European Congress of Computational Methods in Applied Sciences and Engineering*. Barcelona, Spain, September 11-14, 2000.
- [103] Zukas, J. (1990). *High Velocity Impact Dynamics*. New York: John Wiley & Sons, Inc.
- [104] Sod, G.A. (1978). A Survey of Several Finite Difference Methods for Systems of Nonlinear Hyperbolic Conservation Laws. *Journal of Computational Physics*. 27:1-31.

- [105] Donea, J., Giuliani, S., and Halleux, J. (1982). An Arbitrary Lagrangian-Eulerian Finite Element Method for Transient Dynamic Fluid-Structure Interactions. *Computer Methods in Applied Mechanics and Engineering*. 33:689-723.

## APPENDIX: INPUT FILES

## Example ALEAS Input File

Both ALEAS MMM and ALEAS SMM use the same input file structure. The ALEAS input deck consists of two files, a control file and a mesh file. The control file contains the ‘MMM’ option, which is set to ‘YES’ to implement the contact formulation presented in this work. Setting ‘MMM’ to ‘NO’ causes ALEAS to run with a single velocity field and use mixture theory to handle mixed cells.

### *ALEAS Control File*

```
* input file
jobtitle = 'ALE on mid-sagittal section of brain'
*
* Control Records
*
control
  ttype = explicit      !default is explicit
  mtype = eulerian     !default is lagrangian
  start = yes          !this is the default
  restart = no         !this is the default
  amr = no             !set equal to yes to allow AMR
  nlevel = 4          !number of levels for an AMR
  stest = no           !default is no for seed test
  mtest = no           !default is no for mesh test
  tmin = 0.0          !required input
  tmax = 0.000100     !required input
  timestep = 0.001    !required input for implicit
  cycle_max = 5000    !default is 50000
  gauss = 1           !default is 2
  weight = volume     !default is volume weighting
  file_number = 0     !required input ONLY if restart =
                    !yes or remesh = yes

  coordinate_system = rectangular
  debug=no            !default is no
  verify=no           !default is no
  gmw=no              !default is no
  mmm=yes             !default is no
end_control
*
* Plot and edit dump records
*
plot
  ptime=0.    pdt = 1.0e-6
  etime=0.    edt = 0.5e-1
  pvoid=no    !default is no
  evoid=no    !default is no
end_plot
*
* Region definition records
*
regions
file
eul_2mat.key
*
```

```

end_regions
*
* End of input file
*

```

*Abridged ALEAS Mesh File*

```

*KEYWORD

*NODE
    1          0.0000      0.0000      0.0000
...
 1308125      20.0000      8.0000      15.5000
*
*ELEMENT_SOLID
    1          1          1          2          163          162          10466          10467          10628          10627
...
 1269760      1 1297498 1297499 1297660 1297659 1307963 1307964 1308125 1308124
*
*INITIAL_VOLUME_FRACTION
    21136      0.142857      0.00000000
...
 1248603      0.405896      0.00000000
*
*FECON
    1          1          1
...
 1269760      6          3816352
*
*FACENODES
    1          2          163          10628          10467
    3847296      1307963      1307964      1308125      1308124
*
*INITIAL_VELOCITY_MMM
    1          0.0          0.0
    2 1.290e+5      0.0          0.0
*
*MAT_GRUNEISEN
    1          7.8500      4.500e5      1.49          2.17 4.41208e6      0.283      2.5d10
    1.000E10      0.78e+10      0.106      0.004      1.0e00      1783.0      0.0          0.0
    0.0          0
*
*MAT_GRUNEISEN
    2          18.62      2.487e5      1.56          2.32 1.05132e6      0.3      2.5d10
    1.790E10      1.121e10      0.25      0.007      1.0e00      1497.9      0.0          0.0
    0.0          0
*END

```

## Example CTH Input Files

*CTH Angled Frictionless Block Sliding*

```

*****
*
*   CTH INPUT FOR ANGLED SLIDING BLOCK PROBLEM
*
*****
*
*eor* cthin
*
*****
*
* TITLE RECORD
*
Sliding Blocks XY
*
*****
*
* CONTROL RECORDS
*
control
  mmp
  tstop=100.0e-6
endc
*
*****

* Non-AMR calculation

mesh
  geom=3dr
  x0 0.0
    x1 dx=0.2 dxl=0.2 w=15
  endx
  y0 0.0
    y1 dy=0.2 dyl=0.2 w=15
  endy
  z0 0.0
    z1 dz=0.2 dzl=0.2 w=15
  endz
* active region
  xact= 0, 15.0
  yact= 0, 15.0
  zact= 0, 15.0
endmesh

* Spymaster input

spy

PlotTime(0,1e-6);
Save("VOLM,M,P,VX,VY,VZ,CS,VOID,DENS,DENSM,VMAG");
SaveTime(0,1e-6);

%ImageFormat(1024,1024); % uncomment for 1024x1024 image size
% default is 800x800

define main() {
  pprintf(" PLOT: Cycle=%d, Time=%e\n",CYCLE,TIME);
  XLimits(0,15.0);
  YLimits(0,15.0);
  ZLimits(0,15.0);
  Image("Mats",WHITE,BLACK);
  MatColors(GRAY,BLUE);
  Plot3DMats();
  DrawBlockEdges();
}

```



```

    ClipZBelow(7.5);
    EndImage;
}

endspy

*
*****
*
* MATERIAL STRENGTH RECORDS
*
epdata
*
*****
*
* Steel (RHA)
*
*****
*
  matep 1 JO=USER AJO=1.0e10 BJO=0.0 CJO=0.0 MJO=1.e99 NJO=1.0 TJO=1.e99
        POISSON=0.283
*
  matep 2 JO=USER AJO=1.0e10 BJO=0.0 CJO=0.0 MJO=1.e99 NJO=1.0 TJO=1.e99
        POISSON=0.283
*
  mix 3
*
ende
*
*****
*
* TRACER RECORDS
*
tracer
endt
*
*****
*
* EOS RECORDS
*
eos
*
*****
*
* RHA
*
mat1 mgrun USER R0=7.85 CS=4.5e5 S1=1.49 G0=2.17 CV=5.12e10
*
*****
*
*Steel
*
*
mat2 mgrun USER R0=7.85 CS=4.5e5 S1=1.49 G0=2.17 CV=5.12e10
*
ende
*
*****
*
* DIATOM RECORDS
*
diatom
package 'Block1'
material 1
xvel 70710.68
yvel 70710.68
insert par
  p1 = 6.439 6.439 6.0
  p2 = 8.561 8.561 6.0
  p3 = 4.318 8.561 6.0
  p4 = 6.439 6.439 9.0
endi
endp

```

```

package 'Block2'
material 2
xvel -70710.68
yvel -70710.68
insert par
  p1 = 8.561 4.318 6.0
  p2 = 10.682 6.439 6.0
  p3 = 6.439 6.439 6.0
  p4 = 8.561 4.318 9.0
endi
endp

enddiatom

*****
*
* CELL THERMODYNAMICS RECORDS
*
cellthermo
  mmp0
  ntbad=999999999
endc
*
*****
*
* CONVECTION RECORDS
*
convct
  convection=1
  interface=smyra
endc
*
*
*****
* * FRACTURE RECORDS
*
fracts
  stress
  pfrac1 -18.0e9
  pfrac2 -18.0e9
  pfmix -1e12
  pfvoid -1e12
endf
*
*****
*
* EDIT RECORDS
*
edit
*
  shortt
    time=0. dt=1.
  ends
*
  longt
    time=0. dt=1.
  endl
*
  restt
    time=0 dt=5e-6
  endr
*
  histt
    time=0. dt=1.0e-7
    htracer all
  endh
*
ende
*
*****
*
* BOUNDARY CONDITION RECORDS

```

```
*  
boundary  
  bhydro  
    block 1  
      bxbot=2  
      bxtop=2  
      bybot=2  
      bytop=2  
      bzbot=2  
      bztop=2  
    endb  
  endh  
endb
```

*CTH 2" Plate Penetration*

```

*****
*
*eor* cthin
*
*****
*
* TITLE RECORD
*
Penetration 2 inch RHA
*
*****
*
* CONTROL RECORDS
*
control
  mmp
  tstop=100.0e-6
endc
*
*****

* Non-AMR calculation

mesh
  geom=3dr
  x0 0.0
  x1 dx=0.1 dxl=0.1 w=18
  endx
  y0 0.0
  y1 dy=0.1 dyl=0.1 w=10.4
  endy
  z0 0.0
  z1 dz=0.1 dzl=0.1 w=10.4
  endz
* active region
  xact= 0, 18.0
  yact= 0, 10.4
  zact= 0, 10.4
endmesh

* Spymaster input

spy

PlotTime(0,1e-6);
Save("VOLM,M,P,VX,VY,VZ,CS,VOID,DENS,DENSM,VMAG");
SaveTime(0,1e-6);

%ImageFormat(1024,1024); % uncomment for 1024x1024 image size
% default is 800x800

define main() {
  pprintf(" PLOT: Cycle=%d, Time=%e\n",CYCLE,TIME);
  XLimits(0,15.0);
  YLimits(0,15.0);
  ZLimits(0,15.0);
  Image("Mats",WHITE,BLACK);
  MatColors(GRAY,BLUE);
  Plot3DMats();
  DrawBlockEdges();
  ClipZBelow(7.5);
  EndImage;
}

endspy

*
*****
*

```

```

* MATERIAL STRENGTH RECORDS
*
epdata
*
*****
* RHA
  matep 1 JO=USER
        AJO=1.0e10
        BJO=0.78e10
        CJO=0.004
        MJO=1.e0
        NJO=0.106
        TJO=0.1536473
        POISSON=0.283
* DU Ti 0.75%
  matep 2 JO=USER
        AJO=1.79e10
        BJO=1.21e10
        CJO=0.007
        MJO=1.0
        NJO=0.25
        TJO=.129
        POISSON=0.3
*
  mix 3
*
ende
*
*****
* TRACER RECORDS
*
tracer
endt
*
*****
* EOS RECORDS
*
eos
*
*****
* RHA
*
mat1 mgrun USER R0=7.85 CS=4.5e5 S1=1.49 G0=2.17 CV=5.12e10
*
*****
* DU Ti 0.75%
*
mat2 mgrun USER R0=18.62 CS=2.487e5 S1=1.56 G0=2.32 CV=1.22e10
*
ende
*
*****
* DIATOM RECORDS
*
diatom

package 'Block'
  material 1
  iter 3
  insert box
    p1 = 7.87 0.0 0.0
    p2 = 12.95 10.4 10.4
  endi
endp

package 'Penetrator'
  material 2
  iter 3

```

```

xvel 1.2e5
insert cylinder
  cel = 0.2 5.2 5.2
  ce2 = 7.4865 5.2 5.2
  radius = 0.3835
endi
insert sphere
  ce= 7.4865 5.2 5.2
  radius = 0.3835
endi
endp

enddiatom

*****
*
*   CELL THERMODYNAMICS RECORDS
*
cellthermo
  mmp
  ntbad=999999999
endc
*
*****
*
*CONVECTION RECORDS
*
convct
  convection=1
  interface=smyra
endc
*
*
*****
* * FRACTURE RECORDS
*
fracts
  stress
  pfrac1 -18.0e9
  pfrac2 -20.0e9
  pfmix -1.0e12
  pfvoid -1.0e12
endf
*
*****
*
*   EDIT RECORDS
*
edit
*
  shortt
    time=0. dt=1.
  ends
*
  longt
    time=0. dt=1.
  endl
*
  restt
    time=0 dt=5e-6
  endr
*
  histt
    time=0. dt=1.0e-7
    htracer all
  endh
*
ende
*
*****
*
*   BOUNDARY CONDITION RECORDS
*

```

```
boundary
  bhydro
    block 1
      bxbot=1
      bxtop=1
      bybot=1
      bytop=1
      bzbot=1
      bztop=1
    endb
  endh
endb
```

*CTH Semi-infinite Plate Penetration*

```

*****
*
*eor* cthin
*
*****
*
* TITLE RECORD
*
Semi infinite penetration
*
*****
*
* CONTROL RECORDS
*
control
  mmp
  tstop=100.0e-6
endc
*
*****

* Non-AMR calculation

mesh
  geom=3dr
  x0 0.0
  x1 dxf=0.05 dxl=0.05 w=15
  endx
  y0 0.0
  y1 dyf=0.05 dyl=0.05 w=4
  endy
  z0 0.0
  z1 dzf=0.05 dzl=0.05 w=4
  endz
* active region
  xact= 0, 15.0
  yact= 0, 4.0
  zact= 0, 4.0
endmesh

* Spymaster input

spy

PlotTime(0,1e-6);
Save("VOLM,M,P,VX,VY,VZ,CS,VOID,DENS,DENSM,VMAG");
SaveTime(0,1e-6);

%ImageFormat(1024,1024); % uncomment for 1024x1024 image size
% default is 800x800

define main() {
  pprintf(" PLOT: Cycle=%d, Time=%e\n",CYCLE,TIME);
  XLimits(0,15.0);
  YLimits(0,15.0);
  ZLimits(0,15.0);
  Image("Mats",WHITE,BLACK);
  MatColors(GRAY,BLUE);
  Plot3DMats();
  DrawBlockEdges();
  ClipZBelow(7.5);
  EndImage;
}

endspy

*
*****
*

```



```

* MATERIAL STRENGTH RECORDS
*
epdata
*
*****
* Steel
matep 1 JO=USER AJO=0.81e10 BJO=0.5095e10 CJO=0.014 MJO=1.03 NJO=0.26
      TJO=0.156666
      POISSON=0.299
* Tungsten
matep 2 JO=USER AJO=1.365e10 BJO=0.1765e10 CJO=0.016 MJO=1.0 NJO=0.12
      TJO=0.318411
      POISSON=0.281
*
  mix 3
*
ende
*
*****
* TRACER RECORDS
*
tracer
endt
*
*****
* EOS RECORDS
*
eos
*
*****
* Steel
*
mat1 mgrun USER R0=7.85 CS=4.5e5 S1=1.49 G0=2.17 CV=5.12e10
*
*****
* Tungsten
*
mat2 mgrun USER R0=17.76 CS=4.03e5 S1=1.237 G0=1.67 CV=1.57e10
*
ende
*
*****
* DIATOM RECORDS
*
diatom

package 'Block'
material 1
numsub 8
iter 3
insert box
  p1 = 5.1 -10.0 -10.0
  p2 = 20.0 10.0 10.0
endi
endp

package 'Penetrator'
material 2
numsub 8
iter 3
xvel 1.5e5
insert cylinder
  ce1 = 0.1 2.0 2.0
  ce2 = 5.1 2.0 2.0
  radius = 0.25
endi
endp

```

```

enddiatom
*****
*
* CELL THERMODYNAMICS RECORDS
*
cellthermo
  mmp
  ntbad=999999999
endc
*
*****
*
*CONVECTION RECORDS
*
convct
  convection=1
  interface=smyra
endc
*
*
*****
* * FRACTURE RECORDS
*
fracts
  stress
  pfrac1 -18.0e9
  pfrac2 -20.0e9
  pfmix -1.0e12
  pvoid -1.0e12
endf
*
*****
*
* EDIT RECORDS
*
edit
*
  shortt
    time=0. dt=1.
  ends
*
  longt
    time=0. dt=1.
  endl
*
  restt
    time=0 dt=5e-6
  endr
*
  histt
    time=0. dt=1.0e-7
    htracer all
  endh
*
ende
*
*****
*
* BOUNDARY CONDITION RECORDS
*
boundary
  bhydro
    block 1
      bxbot=1
      bxtop=1
      bybot=1
      bytop=1
      bzbot=1
      bztop=1
    endb
  endh
endb

```

*CTH Taylor Impact*

```

*****
*
*eor* cthin
*
*****
*
* TITLE RECORD
*
Taylor Impact- Cu cylinder 210m/s, D=0.762cm L==2.347cm
*
*****
*
* CONTROL RECORDS
*
control
  mmp
  RIGID=0
  tstop=100.0e-6
endc
*
*****

* Non-AMR calculation

mesh
  geom=3dr
  x0 0.0
  x1 dxf=0.025 dxl=0.025 w=3.0
  endx
  y0 0.0
  y1 dyf=0.025 dyl=0.025 w=3.0
  endy
  z0 0.0
  z1 dzf=0.025 dzl=0.025 w=3.0
  endz
* active region
  xact= 0, 3.0
  yact= 0, 3.0
  zact= 0, 3.0
endmesh

* Spymaster input

spy

PlotTime(0,1e-6);
Save("VOLM,M,P,VX,VY,VZ,CS,VOID,DENS,DENSM,VMAG");
SaveTime(0,1e-6);

%ImageFormat(1024,1024); % uncomment for 1024x1024 image size
% default is 800x800

define main() {
  pprintf(" PLOT: Cycle=%d, Time=%e\n",CYCLE,TIME);
  XLimits(0,2.0);
  YLimits(0,2.6);
  ZLimits(0,2.0);
  Image("Mats",WHITE,BLACK);
  MatColors(GRAY,BLUE);
  Plot3DMats();
  DrawBlockEdges();
  ClipZBelow(7.5);
  EndImage;
}

endspy

*
*****

```

```

*
* MATERIAL STRENGTH RECORDS
*
epdata
*
*****
*
* Cu Impactor
*
*****
*
  matep 1 JO=COPPER
*
  matep 2 JO=URANIUM AJO=1.E+30 BJO=1.E+30
*
  mix 3
*
ende
*
*****
*
* TRACER RECORDS
*
tracer
endt
*
*****
*
* EOS RECORDS
*
eos
*
*****
*
* RHA
*
mat1 mgrun COPPER
*
*****
*
*Steel
*
*
mat2 mgrun URANIUM_TI
*
ende
*
*****
*
* DIATOM RECORDS
*
diatom

  package 'Rod'
  material 1
  yvel -0.21e5
  insert cylinder
  ce1 = 1.5 0.5 1.0
  ce2 = 1.5 2.847 1.0
  radius = 0.381
  endi
endp

* package 'Plate'
* rigid
* insert box
* p1 0.05 0.0 0.05
* p2 1.95 0.125 1.95
* endi
* endp

package 'PlateiVIZ'
material 2

```

```

insert box
  p1 0.0 0.0 0.0
  p2 3.0 0.5 3.0
endi
endp

enddiatom

*****
*
* CELL THERMODYNAMICS RECORDS
*
cellthermo
  mmp0
  ntbad=999999999
endc
*
*****
*
*CONVECTION RECORDS
*
convct
  convection=1
  interface=smyra
endc
*
*
*****
* * FRACTURE RECORDS
*
*fracts
* stress
* pfrac1 -9.44e9
* pfrac2 -7.0e9
* pfmix -1e20
* pfvoid -1e20
*endf
*
*****
*
* EDIT RECORDS
*
edit
*
  shortt
    time=0. dt=1.
  ends
*
  longt
    time=0. dt=1.
  endl
*
  restt
    time=0 dt=5e-6
  endr
*
  histt
    time=0. dt=1.0e-7
    htracer all
  endh
*
ende
*
*****
*
* BOUNDARY CONDITION RECORDS
*
boundary
  bhydro
    block 1
    bxbot=0
    bxtop=0
    bybot=0

```

```
        bytop=0
        bzbot=0
        bztop=0
    endb
endh
endb
```

*CTH -9.3° Yaw Plate Penetration*

```

*****
*
*eor* cthin
*
*****
*
* TITLE RECORD
*
Yaw -10
*
*****
*
* CONTROL RECORDS
*
control
  mmp
  tstop=100.0e-6
endc
*
*****

* Non-AMR calculation

mesh
  geom=3dr
  x0 0.0
  x1 dx=0.125 dxl=0.125 w=20.0
  endx
  y0 0.0
  y1 dy=0.125 dyl=0.125 w=10.0
  endy
  z0 0.0
  z1 dz=0.125 dzl=0.125 w=15.5
  endz
* active region
  xact= 0, 20.0
  yact= 0, 10.0
  zact= 0, 15.5
endmesh

* Spymaster input

spy

PlotTime(0,1e-6);
Save("VOLM,M,P,VX,VY,VZ,CS,VOID,DENS,DENSM,VMAG");
SaveTime(0,1e-6);

%ImageFormat(1024,1024); % uncomment for 1024x1024 image size
% default is 800x800

define main() {
  pprintf(" PLOT: Cycle=%d, Time=%e\n",CYCLE,TIME);
  XLimits(0,15.0);
  YLimits(0,15.0);
  ZLimits(0,15.0);
  Image("Mats",WHITE,BLACK);
  MatColors(GRAY,BLUE);
  Plot3DMats();
  DrawBlockEdges();
  ClipZBelow(7.5);
  EndImage;
}

endspy

*
*****
*

```

```

* MATERIAL STRENGTH RECORDS
*
epdata
*
*****
* RHA
  matep 1 JO=USER
        AJO=1.0e10
        BJO=0.78e10
        CJO=0.004
        MJO=1.e0
        NJO=0.106
        TJO=0.1536473
        POISSON=0.283
* DU Ti-0.75%
  matep 2 JO=USER
        AJO=1.79e10
        BJO=1.21e10
        CJO=0.007
        MJO=1.0
        NJO=0.25
        TJO=.129
        POISSON=0.3
*
  mix 3
*
ende
*
*****
* TRACER RECORDS
*
tracer
endt
*
*****
* EOS RECORDS
*
eos
*
*****
* RHA
*
mat1 mgrun USER R0=7.85 CS=4.5e5 S1=1.49 G0=2.17 CV=5.12e10
*
*****
*Uranium
*
mat2 mgrun USER R0=18.62 CS=2.487e5 S1=1.56 G0=2.32 CV=1.22e10
*
ende
*
*****
* DIATOM RECORDS
*
diatom

package 'Block'
material 1
  iter 3
  xvel -0.61631e4
  yvel 0.20806e5
  insert par
    p1 = 1.787 0.4999 0.25
    p2 = 16.169 4.76 0.25
    p3 = 1.605 1.114 0.25
    p4 = 1.787 0.4999 15.25
  endi

```



```

endp

package 'Penetrator'
material 2
iter 3
xvel 1.21e5
insert cylinder
  ce1 = 0.5 3.345 7.75
  ce2 = 7.7865 3.345 7.75
  radius = 0.3835
endi
insert sphere
  ce= 7.7865 3.345 7.75
  radius = 0.3835
endi
endp

enddiatom

*****
*
* CELL THERMODYNAMICS RECORDS
*
cellthermo
  mmp
  ntbad=999999999
endc
*
*****
*
*CONVECTION RECORDS
*
convct
  convection=1
  interface=smyra
endc
*
*
*****
* * FRACTURE RECORDS
*
fracts
  stress
  pfrac1 -18.0e9
  pfrac2 -20.0e9
  pfmix -1.0e12
  pfvoid -1.0e12
endf
*
*****
*
* EDIT RECORDS
*
edit
*
  shortt
    time=0. dt=1.
  ends
*
  longt
    time=0. dt=1.
  endl
*
  restt
    time=0 dt=5e-6
  endr
*
  histt
    time=0. dt=1.0e-7
    htracer all
  endh
*
ende

```

```
*  
*****  
*  
* BOUNDARY CONDITION RECORDS  
*  
boundary  
  hydro  
    block 1  
      bxbot=1  
      bxtop=1  
      bybot=1  
      bytop=1  
      bzbot=1  
      bztop=1  
    endb  
  endh  
endb
```